DSE - Maritime Flyer

A remotely piloted aircraft system (RPAS) that will increase the safety and security of a maritime environment

J.T. Busch	4141083	K. Langemeijer	4165209
R.A.C.M. van Casteren	4215966	M.T. Latour	4203607
A.E. Demir	1544446	D.J. van Oorspronk	4220838
R. Hammink	4090764	J.S. Visscher	4107934
S. van der Helm	4221362	D.E. van der Hoff	4139925

Final Report

Design Synthesis Excercise

TU Delft Delft University of Technology

Aerospace Engineering

June 30, 2015

Preface

This report is the final report of the Design Synthesis Exercise of group 6. The Design Synthesis Exercise is a mandatory project which marks the end of the bachelor Aerospace Engineering at the Delft University of Technology. In this challenging project all knowledge gained over the past three years of the bachelor must be applied.

Before this final report could be realised several reports has been written including a project plan, baseline report, and mid-term report. Each report is written at a specific design phase of the project. This project represents the design of a remotely piloted aircraft system flying in maritime environment. The following report is to be read as a stand-alone report and contains all of the tasks that have been completed from the last ten weeks.

Advice and support was given during the project for which many thanks can be given. Primarily we want to thank our tutor Dr. Ir. Erik-Jan van Kampen and coaches Jan Rohac and Shaafi Kaja Kamaludeen. Furthermore we want to thank everyone who's expertise helped us to complete this project.

Delft, June 30, 2015

List of Symbols

Symbol	Unit	Description
α	$^\circ$	Angle of attack
γ	$^\circ$	Launch angle
ϵ	-	Damping coefficient
η	-	Efficiency
λ	m	Wave length
λ	-	Taper ratio
Λ	$^\circ$	Sweep Angle
μ	$Pa \cdot s$	Dynamic viscosity
μ_b	-	Dimensionless mass coefficient
ρ	kg/m^3	Density
σ	Pa	Stress
τ	Pa	Shear stress
a	1/rad	lift curve slope
a_0	1/rad	two dimensional lift curve slope
A	-	Aspect ratio
A	m^2	Area
b	m	Total wing span
b^*	m	Pure wing span
c	m	Chord
C	bit/s	Channel capacity
CD	$bits$	Colour depth
CR	-	Compression ratio
C_D	-	Drag coefficient
C_{D_0}	-	Zero-lift drag coefficient
C_{l_α}	1/rad	Lift curve slope
C_l	-	Two dimensional lift coefficient
C_L	-	Lift coefficient
C_m	-	Moment coefficient
C_{n_β}	$1/rad$	Yaw response to sideslip
C_{n_r}	$1/rad/s$	Yaw response to yaw rate
C_p	-	Pressure coefficient
C_{Y_α}	$1/rad$	Response to angle of attack change for the vertical wingtip
d	m	diameter
D	b/s	Data rate
e	-	Oswald Factor
E_b	W	Received signal power
F	N	Force
FR	fps	Frame rate
g	m/s^2	Gravitational acceleration
G_t	-	Transmitter Gain
G_r	-	Receiver Gain
h	m	height
h	m	Altitude
H_e	Nm	Hinge moment

Symbol	Unit	Description
I	kgm^2	Mass moment of inertia
I	m^4	Area moment of inertia
I	A	Current
IR	pix	Imaging resolution
K_Z^2	-	Dimensionless mass moment of inertia about z-axis
l	m	length
L	N	Lift
L	-	Signal loss
M	Nm	Moment
M	-	Mach number
M	Nm	Moment
m	kg	Mass
n	-	Arbitrary number
n	-	Load factor
N	N	Normal force
N_0	W	Noise Power
p	rad/s	Roll rate
P	W	Power
PD	m	Pixel depth
P_b	W	Battery power
P_{req}	W	Required power
P_{ic}	W	Power required for the imaging communication/live stream
Q	Ah	Battery capacity
Re	-	Reynolds number
s	m	Displacement
S	m^2	Wing Surface Area
SNR	-	Signal-to-Noise Ratio
SW	m	Swadth width
t	$hours$	Mission time
T	N	Thrust
T	K	Temperature
T_f	-	Mission time fraction, duty cycle
U	V	Voltage
V	m/s	Velocity
V	N	Shear force
Vol	m^3	Volume
w	rad/s	Frequency
w	m	width
W	N	Weight
Z	-	Zoom

Contents

1 Introduction

Current port authorities and local police only have limited methods of reaching incident areas, such as four wheel drive vehicles, on horseback, and maritime vehicles. With these modes of transportation it may be difficult and expensive to ensure the safety of maritime environments. Aerial surveillance poses a more economic solution to this problem, as the situation can generally be assessed instantly and a more specific response can be executed. For these reasons, a remotely piloted aircraft system (RPAS) can be ideal to assist the police and port authorities to quickly and safely assess incidents in the maritime environment. The purpose of this project is to design an RPAS that can be deployed to survey various maritime regions by providing video feedback, and thus solving various problem scenarios.

A project plan, baseline report, and mid-term report have been written. The conclusion of the mid-term report was the trade-off and selection of a final design for the detailed design phase of this project. The design that was chosen to be worked on in detail is the flying wing. This report covers the detailed design of this concept for each of its subsystems, including operations and production. Using an N^2 chart and the required calculations for each subsystem, it is possible to determine how all subsystems are integrated. This is important as it determines the interrelation of every subsystems, as well as the iterations that need to be made for each subsystem to find the optimal characteristics for the RPAS. The requirements determined in the baseline report are used as design objectives. Risk analysis and sustainability is also integrated throughout the design process. All major aspects of the flying wing are covered to determine the best design for this particular mission.

The structure of this report will be as follows. In chapter 2, the project will be described and the mission analysed. This is followed by the functional flow diagram and functional breakdown structure in chapter 3. The preliminary design of four concepts and the final trade-off is explained in chapter 4. Next, the final design and subsystem integration is summarised in chapter 5. In chapters 6 to 12 the different subsystems are elaborated upon. Costs of the production process is described in chapter 16. Following this, the risk analysis is done in chapter 17. Finally, a conclusion and recommendations for future work is given in chapter 18.

2 Project Description and Mission Analysis

In this chapter a short summary is given about the maritime flyer project and an analysis of the mission is done. Firstly, the assignment is described and the possible scenarios are explained. Next, a project objective statement is presented to give a clear indication of the goal that needs to be achieved. Furthermore, budgets and resources are discussed and elaborated upon. Finally, a market analysis is done to give an indication about the supply and demand for this and similar products.

2.1 Assignment

The given assignment for this design synthesis exercise (DSE) is to "*design a remotely piloted aircraft system (RPAS) that will increase the safety and security of a maritime environment*" [1]. The system design must consist of the aircraft and payload, as well as the ground station and communication systems for the entire project. This project should consider situations where a rapid deployment of an RPAS is vital in order to achieve quick and efficient data collection in order to improve safety procedures of authorities.

The three scenarios that are defined in which the RPAS will be used, are stated below [2]. For all of these scenarios, the RPAS should be capable of providing a live video feed relayed to the ground station, when it is within a 10 *km* radius of the ground station. The scenarios take place in a maritime environment, an example of which is shown in figure 2.1.

Seaside recreation
The beaches and dunes are visited by numerous people for recreational purposes throughout the year. Any unusual occurrences and incidents are reported to local authorities. As a response, the RPAS can be deployed in order to identify the urgency of the situation through rapid observation. Three situations are given for this scenario: a kite surfer in distress, an incident in the dune area, and a fight breaking out on a beach.

Places of interest
For this scenario, two possible situations are proposed:
Anchorages - Any illegal activities taking place, like dumping of waste materials, are to be detected and sent to the monitoring post by the RPAS.
Inspection flight - At one of five identified points of interest an illegal activity is said to take place. The RPAS is deployed to detect what vessels are involved, and at what location the activity is occurring.

Protesters boarding a ship
In the case of unwanted passengers on a ship within the port, it is necessary to have an aircraft that can fly above this ship and identify the intruders. For example if there is a protest on a cargo ship and the intruders are spread over the entire deck, the aircraft should be able to identify each individual separately. Facial recognition will not be necessary for this scenario, only location, number of people present at the situation, and the colour of their clothes should be identifiable.

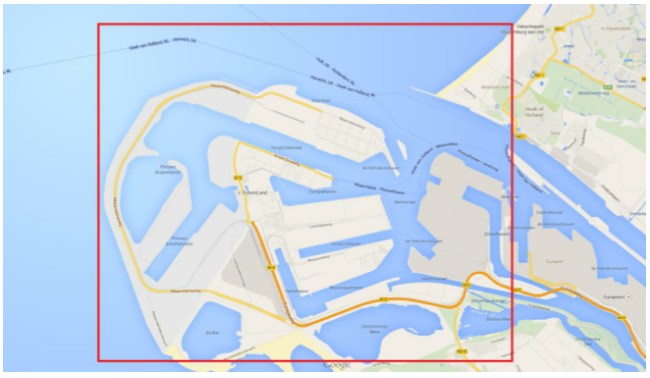

Figure 2.1: Example of a maritime environment [1]

2.1.1 Project objective statement

This section describes the steps taken for defining the project objective statement (POS) and provides the statement itself. A POS is a single sentence that encompasses all aspects of the project and gives the specific direction and goal of the project.

The POS for the design of the RPAS is as follows:

DSE group 6 will design an RPAS capable of providing real-time surveillance in maritime environment within 10 kilometres, and that is capable of storing video surveillance material from 10 to 20 kilometres range.

2.2 Budget and resources

Budgets play a large role in the design of the RPAS as it tells the designer that a certain value for a certain parameter may not be exceeded. All the budgets are initial and are considered rough estimates. Contingencies are taken into account for the budgets, in order to deal with uncertainty in various stages of design.

Cost
The maximum budget for the production of the RPAS is €100,000. The total costs may not exceed this value. The budgets for each section are summarised in table 2.1 and are discussed below.

Table 2.1: Cost budget

Development section	**Cost allocation** [€]
Labour	0
Payload	5,000
Production	50,000
Ground station	30,000
Legislation	1,000
Contingency	14,000
Total	100,000

This RPAS is designed for specific scenarios in which imaging takes a prominent role. The payload is therefore important to budget since it includes the imaging system. Many different types of imaging sensors exist. The price varies depending how advanced the camera is. In this stage the specific camera is not known yet. Therefore, as a start, €5,000 is set as the budget for this system, because the payload or imaging sensor is estimated to be 5% of the total costs. Furthermore, production of the RPAS will have the highest portion of the total budget. Included are all the production tools and materials. For production, €50,000 are reserved. The ground station is a large component of the whole mission therefore the budget for the ground station has a rather high portion of the total budget. The budget is determined using an average price of a van including the costs to fit the van with technical components to operate the RPAS. These costs are based on the 3I project [2], the ground station for the maritime flyer is still to be determined. In total €30,000 is budgeted for the ground station. Furthermore there are no labour costs, as this project is designed by students for their DSE. Eventually the RPAS must be eligible to fly, so the RPAS has to be certified by legislation. This procedure to get certification documents will introduce new costs, and is budgeted at €1,000. Lastly there is a contingency put in the budget. These are costs which arise due to an aspect becoming slightly more expensive than budgeted for. The project budget is limited to €100,000, so a contingency of €14,000 was decided upon.

Mass
The mass budget is important in the conceptual phase of the RPAS design. The mass estimates are quite rough with a contingency of 20%. This contingency is used because the RPAS may not exceed 20 kg, and the mass is expected to grow throughout the design process. In this case the RPAS will be designed for a 16 kg mass. In the end, due to the expected growth of the mass as the design matures, it will be exactly designed for the 20 kg requirement. [3]

Next, the mass of the payload and fuel have to be estimated. The payload system is estimated to be in a range of 3-4 kg for a complex video system [4, p. 10]. In this case 3 kg is used, since the contingency can account for a slight increase. Furthermore, the mass of the fuel or power supply is estimated to be 3 kg as well. This mass ranges from 10% to 50% of the total weight depending on the endurance [4, p. 21]. The required endurance for our mission is 4 hours. This gives the mass estimation of 3 kg.

Furthermore, the operative empty weight could be estimated to be 10 kg taking a 20% contingency into account. Note these are conceptual estimations, so they are likely to increase during the whole design process. The final

design should eventually not exceed a maximum take off weight of 20 kg.

The technical performance management (TPM) graph for the mass budget is given in figure 2.2. Note that the first point in the graph indicates the contingency during the first stage of the conceptual design, which is equal to a contingency of 20%. This contingency will decrease as the maturity of the design increases. By week 10, the target is exactly the same as the requirement, as the week after is already used for finalization of the project.

Table 2.2: Mass Budget

Section	**Mass** $[kg]$
Payload	3
Fuel/Power	3
OEW	10
Contingency	4
Total (MTOW)	20

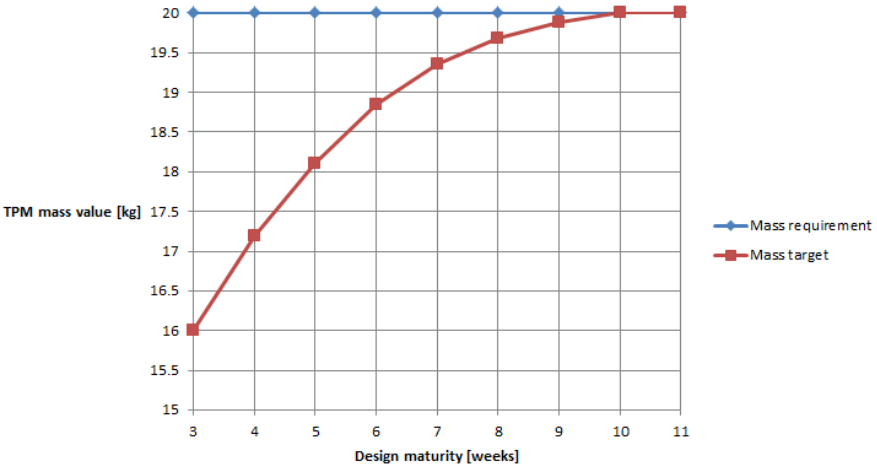

Figure 2.2: Technical performance measurement graph for the mass

Figure 2.2 depicts the TPM graph for the total mass of the RPAS. However, similar contingencies may be used for the masses of the separate subsystems.

Power

For preliminary design an indication of the power budget is needed. Due to the fact that RPAS are a relatively new subject to the market, not much is known about preliminary estimation of the power budget. Therefore, the power budget will be estimated by both looking at the market and by making a rough estimation of all devices using power on board of the RPAS. A difference will be made between electrical powered RPAS and RPAS with other types of propulsion. The power budgets are presented in table 2.3.

The power budget is split up in the following categories:

- Communications
- Payload
- Control surfaces and operation
- Electrical propulsion

Communications involves all the up- and downlink power usage for all systems. This includes the data links needed for the video streaming, but also all control commands from the pilot and gps information that has to be sent to the ground station.

Payload consists of the power requirements due the payload, for example power requirements for the operation of the camera or video storage. The control surfaces and operation category contains all actuators and processor power required for the RPAS.

This is a very rough estimation of how the power budget should look like. An estimation for an RPAS of previously estimated mass would be around 100 W of total power usage. Communication power budget is based on the assumed high bit rate and range requirement combined with the used frequency spectrum. [4]. For the payload certain cameras were considered and this was used to determine the required power [4]. This resulted in a very rough estimation of 60 W out of a total of the 100 W budget. For control surfaces and operation an estimation of 5 W out of 100 W total was decided. Using this as an estimate this would result in a power budget as shown in table 2.3.

Table 2.3: Estimated power budget for a 100 W RPAS

Categories	**Power usage RPAS** $[W]$
Communication	25
Payload	70
Control Surfaces, Operation	5
Total	100

2.3 Market analysis

To make the maritime flyer a success seen from an economical point of view it is important to investigate its position on the market. This will be done by performing a market analysis in which the supply and demand sides of the market will be examined. For the supply side the competitors will be examined. After this the product target price will be determined for the maritime flyer and finally potential customers of the RPAS are investigated.

Competitors
For a new product to come on the market it is important to investigate whether this product will differ enough from already existing products so that potential customers decide to choose the new product over another already existing product. For the maritime flyer this difference can for example follow from having the same characteristics as an already existing RPAS, but having the benefit of being cheaper. In table 2.4 five alternative RPAS solutions are presented [5] [6] [7] [8] [9]. In this table MTOW is the maximum take-off weight of the RPAS's.

Table 2.4: Alternative remotely piloted aircraft surveillance systems

	Unit	*Maritime Flyer*	Apid One Ranger	ScanEagle	HBS FX79	Draganfly Tango	Integrator
Range	$[km]$	20	100	1296	50	25	1225
Endurance	$[h]$	4	6	24	2	0.83	24
MTOW	$[kg]$	18	180	22	2.8	3.94	61.2
Ceiling	$[m]$	200[1]	N/A	5950	N/A	640	5950
Cruise speed	$[m/s]$	28	25	30	N/A	16.7	28.3
Price	[€]	100,000[2]	N/A	450,000	4,400	22,000	12,550,000

(a) Boeing ScanEagle [6] (b) Apid One Ranger [5] (c) Integrator UAV [9]

Figure 2.3: Three examples of RPAS's from table 2.4

From table 2.4 it can be seen that four of the five alternative RPAS's have a range at least twice as large as the maritime flyer. Looking at the mission requirements of the maritime flyer it can thus be concluded that these RPAS's are over-designed. The only RPAS which has about the same range as the maritime flyer, the Draganfly Tango, has an endurance of only 50 min. This RPAS can carry about one-fifth of the required MTOW but it is also costs about one-fifth of the production price of the maritime flyer. Also the HBS FX79 has a bigger range than the maritime flyer but again a smaller endurance. The Apid One Ranger, which is an unmanned rotor-craft, has about the required endurance, but it is nine times heavier than the required MTOW. The RPAS which comes closest to the requirements of the maritime flyer is the ScanEagle. However, looking at the range and endurance requirement it can be said that this RPAS is over-designed. A major difference between the maritime flyer and the other RPAS' is that the maritime flyer is especially designed for the maritime environment it will operate in.

It can be concluded that the maritime flyer not only will be a new product on the market, but that it also will be a unique product. It is able to fly for four hours in a range of twenty kilometres with a weight of less than 20 kg. As said earlier the only alternative which comes close to these characteristics is the ScanEagle.

[1] For the maritime flyer this altitude is the maximum cruise altitude
[2] The value denoted is in fact the production cost for one maritime flyer RPAS

Product price
A targeted product price can be determined from the references in table 2.4. The price given in the table is the budget available for the production of one product/prototype only. Labour costs nor development costs were taken into account in this budget. This is applicable to the DSE, but will not apply to any other commercial situation. To determine the product price for the maritime flyer, the price of competitors should be taken into account as well as a trade-off between the profit margin and the desired number of maritime flyer's sold.

The costs of the five competitors range between €4,400 and €12,550,000. This price difference reflects the difference in the characteristics of the RPAS'. Due to these differing characteristics, it is hard to set a competition price. For the maritime flyer to be commercially attractive it is important that it is either cheaper than its best alternative or that it is more expensive but better than its best alternative. As mentioned before the best alternative for the maritime flyer is the ScanEagle. Comparing the characteristics of the two RPAS' it can be concluded that the weight of the ScanEagle is equal to the maritime flyer but that it has a longer endurance and range. From the characteristics point of view this means that the ScanEagle is more attractive than the maritime flyer. Potential clients will however also evaluate the product on the total costs, which will be lower for the maritime flyer.

Additionally the price of a product depends on the trade-off between the profit margin and the desired number of products sold. If a product has a very high profit margin, but it has a competitor which is cheaper or a competitor which is better and more expensive, there is a chance that the client decides to buy the competitor's product. The best way to determine what potential clients moves to choose the maritime flyer above other alternatives is to perform a market research. This however is outside the scope of the DSE project. With a profit margin of 50% the price of the maritime flyer will be €150,000. This is only a third of the price of one ScanEagle. It is expected that most clients would buy an RPAS to provide surveillance through a cheaper alternative. With this product price, the maritime flyer is thus more attractive than the ScanEagle.

Potential Customers
In this section potential customers for the maritime flyer will be investigated. This will be done by looking at the potential missions the maritime flyer will be able to fulfil. The maritime flyer is in the first place designed to be able to provide real-time surveillance in a maritime environment within a range of 10 km and store surveillance material from 10 km to 20 km range. The three scenarios the maritime flyer is designed for, which are the seaside recreation, surveillance on places of interest, and protesters boarding a ship are not strictly related to be used by a very specific customer. Potential customers are listed below:

In most ports in the world surveillance is done by using boats as the Rotterdam Port Authority does.

The surveillance performed by boats can be more cheaply executed by the maritime flyer. Police forces assigned to provide surveillance and security in recreational coastal areas can also apply the maritime flyer for providing quick response surveillance in case of emergency. It is also possible for security companies to buy an RPAS which can be rented to companies or authorities who ask for surveillance and security.

As the maritime flyer can be launched and recovered without a runway, as explained in chapter 14, it can be operated from a boat. As a result coast guards can use the maritime flyer to examine vessels. An example is the deck of a large container ship. A current issue is the illegal human trafficking taking place on the Mediterranean Sea. The migrants are sailing in overcrowded ships causing dangerous situations. In order to determine what action is required by the border control, a maritime flyer can be flown to these ships to provide images.

3 System Functions

The mission and project have been described. To give a better indication of the functions of the RPAS, some diagrams are produced. There are two ways to designate the necessary functions of the RPAS: through a functional flow diagram (FFD) and a functional breakdown structure (FBS). The FFD shows the logical order of these functions while the FBS shows their hierarchical breakdown. This section will present these two diagrams.

3.1 Functional flow diagram

The functional flow diagram (FFD) is a representation of the functions and their order that the system has to complete. The process of operating the RPAS is visualised by using blocks placed in chronological order. In these blocks the different functions which have to be performed are described using verbs. The functional flow diagram can have OR junctions, as well as AND junctions. In case of an OR junction, there are multiple options to operate the system. In case of an AND junction, the functions may be performed in parallel. In the first row the main functions are horizontally visualised in a chronological way. Underneath this row these main functions are elaborated on in more detail. The FFD is depicted in figure 3.1 below.

The FFD makes it easier to visualise the functional flow of the RPAS system. If an error occurs during use of the system, the FFD can be used to narrow down the location of the functional error. The high level functions can be assessed at first, followed by the lower levels to check where errors or functional inaccuracies lie. This FFD can be continuously adjusted to the changing or additional functions that may arise and be used throughout the project to visualise the flow of the functions.

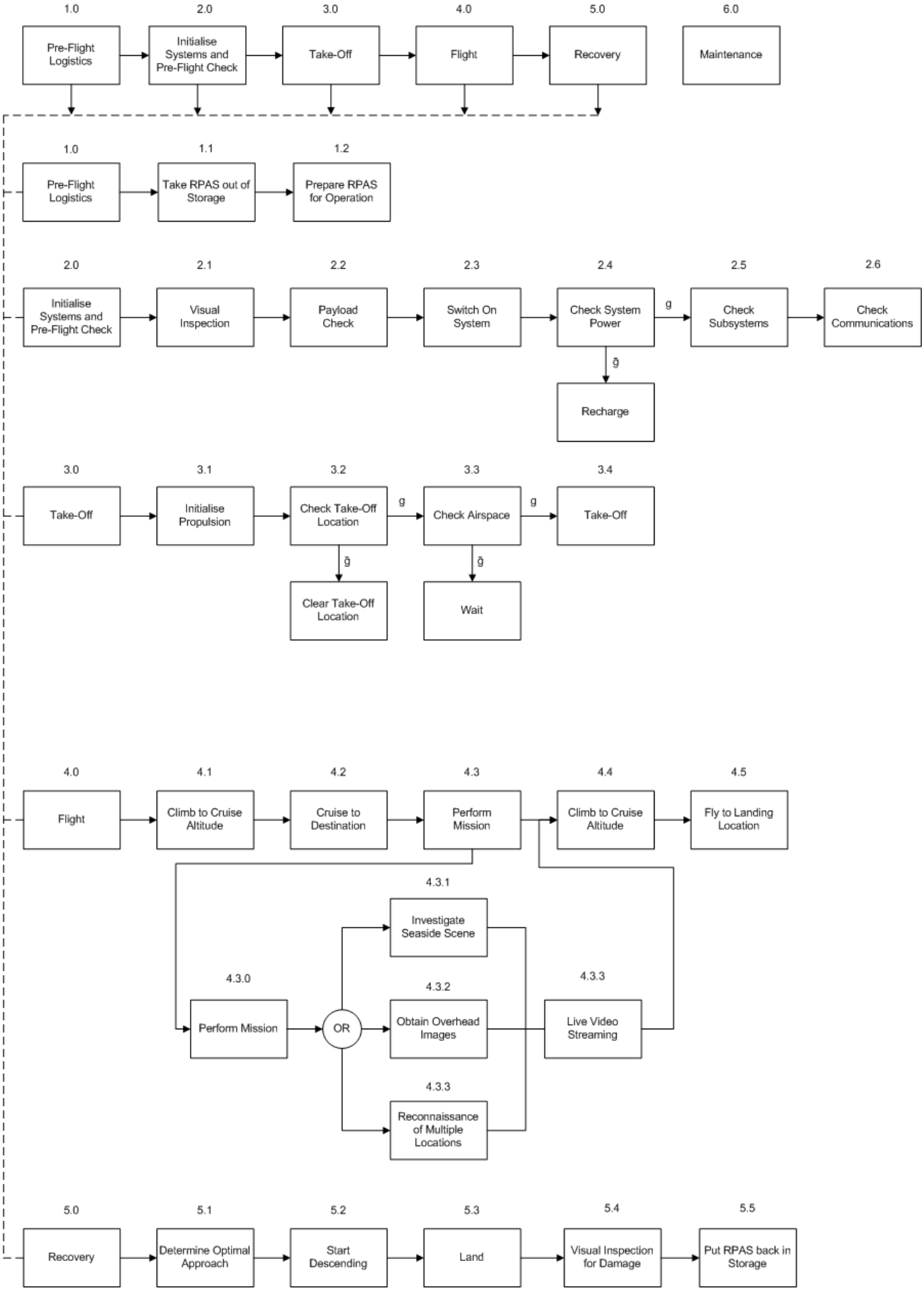

Figure 3.1: Functional Flow Diagram for the Maritime Flyer

3.2 Functional breakdown structure

The functional breakdown structure (FBS) shown in this section represents the minimum required functions that the RPAS has to fulfil. The FBS structures the main functions of the product hierarchically in the form of an AND tree. In the FBS diagram, the different basis functions are located in the higher level while the sub-functions are located in the lower levels of the tree.

The top level functions in the FBS diagram are limited to the system itself. Broader sub-functions can be specified into multiple functions that belong to the same sub-function. The final FBS diagram can be seen in figure 3.2.

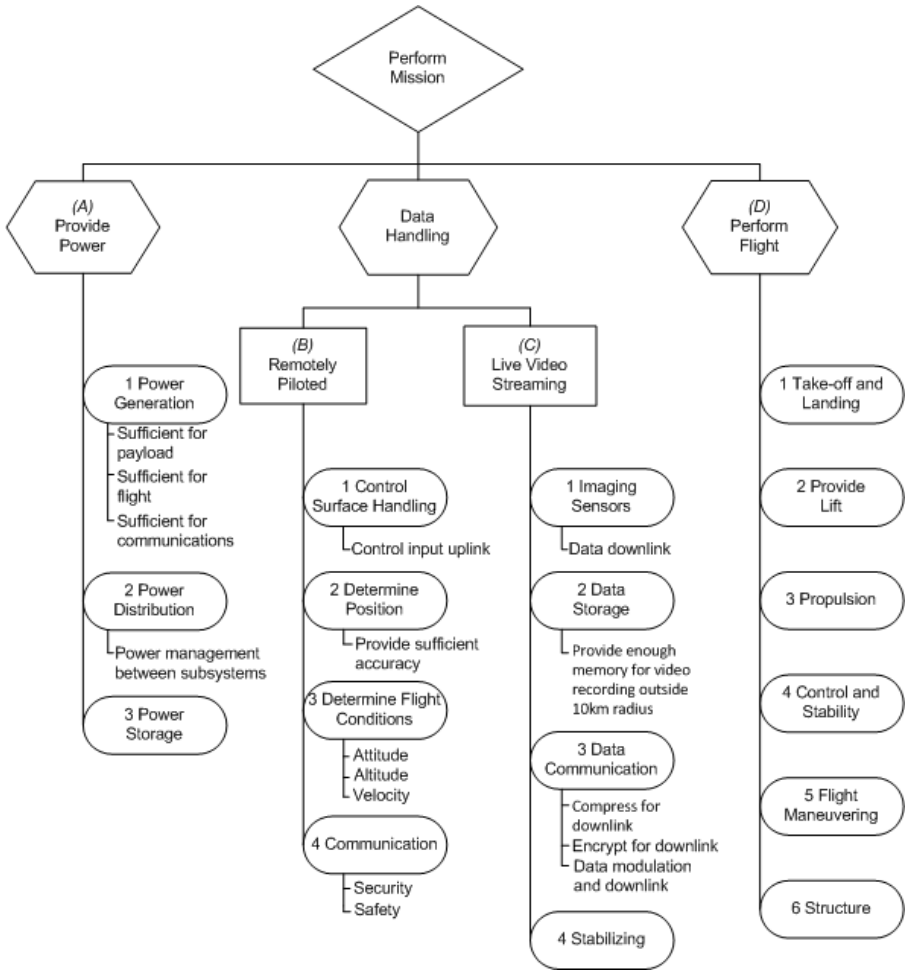

Figure 3.2: Functional Breakdown Structure for the Maritime Flyer

4 Preliminary Design Phase

Following the functional analysis of the mission, requirements for the RPAS are determined. This is a long list of requirements for all subsystems of the RPAS, it will be discussed further in chapter 5. It is now possible to start with the preliminary design phase of the project. This part of the project entails that four preliminary designs are to be thought of and worked out to a certain extent. Design option trees (DOT) were used to explore possibilities for the design of the RPAS. Initially, seven conceptual designs were thought of, which are the flying wing, glider, airship, conventional, kite, rotorcraft, and tube. For preliminary design it was necessary to limit the amount of designs. From these seven, four were chosen to continue to the preliminary design phase. These four designs are the kite, conventional configuration, flying wing, and the airship.

This section will cover into some detail the process of preliminary design for these four concepts. First the kite concept will be elaborated upon, followed by the conventional configuration. Next, the flying wing will be explained, after which the airship will be expanded on. After all the designs have been shown, a trade-off will take place to decide which of the designs will be used for the detailed design phase of the project.

4.1 Kite

The first of the four chosen concepts is the kite configuration. Instead of conventional methods, this configuration uses a non-rigid material for the wing. For the wing a Technora sailcloth will be used. This is a commonly used material for sails and is suitable for the maritime environment the kite will operate in. In figure 4.1 a top and side view of the kite can be found.

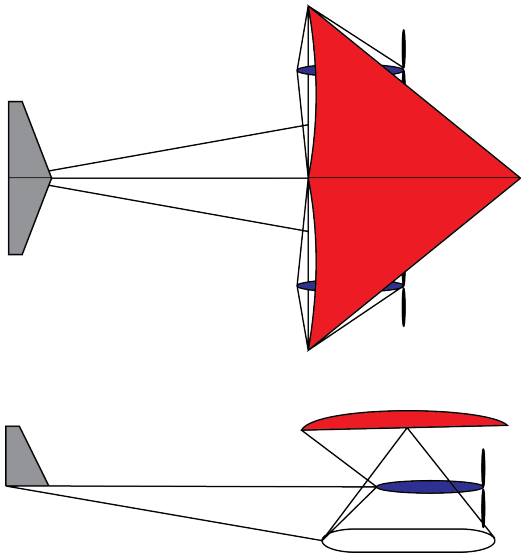

Figure 4.1: Preliminary concept design kite

For the struts and the internal structure of the wing carbon fiber will be used because of high strength-to-weight ratio. In order to be as sustainable as possible, two electrical engines will be used. An on board battery will provide the power required by the two engines. For the take-off and landing of the kite a clip-on landing gear will be used. In this way different types of landing gears can be attached like wheels, skids, and pontoons. The kite is modular which means that it is easily detachable and packable.

An advantage of the kite concept is the relatively low weight. Because of this low weight more and heavier payload can be carried. Because of the modularity the smaller and lighter parts are portable. A disadvantage of this lower weight however is that the kite will be sensitive to the wind gusts present in the maritime environment. Due to the non-rigid wing material it will be hard to attach control surfaces to the wing. Due to the usage of relatively cheap materials, it is easy to stay within budget.

4.2 Conventional configuration

The second concept chosen is the conventional configuration. A top and side view of this concept can be found in figure 4.2.

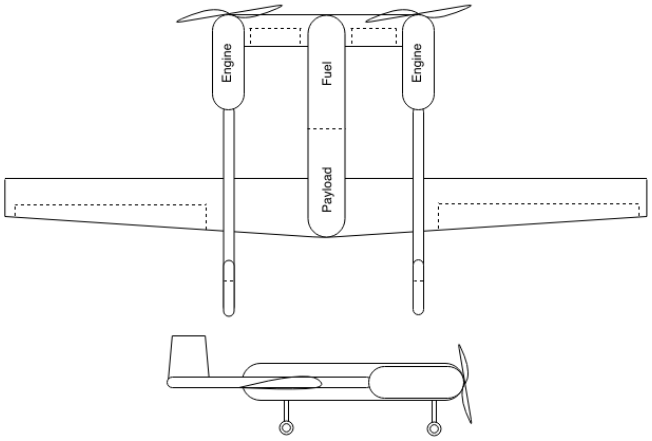

Figure 4.2: Preliminary concept conventional configuration

In the figure the flight direction of the RPAS is upward for the top figure and to the right for the bottom one. This means that unlike the name of the concept it uses a canard configuration for providing longitudinal stabilisation of the RPAS. This way of stabilisation comes with advantages as well as disadvantages. The main advantage of a canard over a horizontal stabiliser at the back is that it uses positive lift to provide the required moment about the centre of gravity instead of using a negative force. This increases the aerodynamic efficiency, which has a positive effect on the endurance of the RPAS. Another advantage is the increase in the manoeuvrability. However, compared to the stabiliser at the back of the aircraft it is more difficult to provide longitudinal stability. In order to come up with a lightweight design carbon fibre will be used for the structural parts of the concept as well as the material for the wings. For the propulsion of the RPAS a combustion engine will be used. Because of the use of relatively cheap materials and the already proven design, it is expected that the costs of this concept will stay within budget.

4.3 Flying wing

The third concept chosen is the flying wing. The main characteristic of a flying wing is that it does not have a separate horizontal wing surface to provide longitudinal stability. In figure 4.3 an impression of the flying wing can be found.

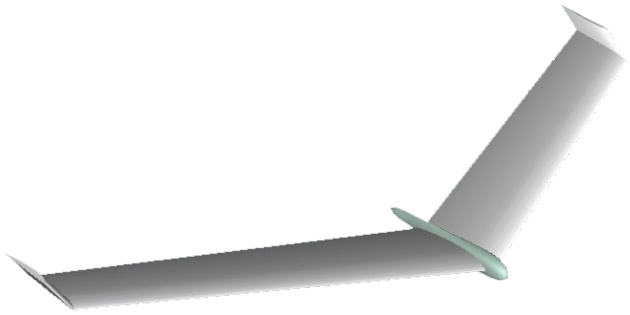

Figure 4.3: Preliminary concept flying wing

For the flying wing it is decided to launch and recover it by using external systems as a catapult and recovery net. This means that for this concept it is not needed to incorporate a landing gear which is beneficial for its weight and aerodynamic efficiency. Together with the high aerodynamic efficiency of a flying wing configuration it is expected that the required endurance will be easily met by this concept. A disadvantage of this concept is that it is a challenge to stabilise it. This stabilisation will be done by using sweep for longitudinal stability as well as vertical stabilising winglets for yaw stability. The low drag of the flying wing will have a positive

influence on the size of the engine required. For the propulsion a combustion engine will be used. Due to the relatively complex design of the flying wing it is however expected that it is hard to stay within the budgeted cost limit.

4.4 Airship

The last concept chosen is the airship. What makes the airship different from the other concepts is that it is a so called lighter-than-air aircraft. This means that no power is required to stay in the air. A drawing of this concept can be found in figure 4.4.

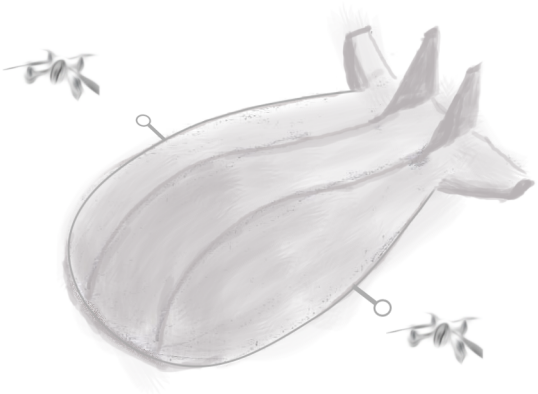

Figure 4.4: Preliminary concept airship

In order to propel the airship and provide the imaging quadcopters will be used which can be attached and detached to the airship during the mission. For the airship a semi-rigid structure is used to maintain the shape of the airship and to make it possible to attach the quadcopters. The airship will be a hybrid airship which means that it not only uses lighter-than-air characteristics to stay in the air, but that its shape provides a lifting force as well. A disadvantage of the airship is that it needs a large volume of helium to provide the so called aerostatic lift. Due to the large size of this concept it makes it sensitive to wind gusts. Due to the high drag as a consequence of the size the flight velocity of the airship will be significantly lower than the other concepts. On the other hand, because no or very little power is required to generate the lift required, the airship will have a higher endurance than the other concepts.

4.5 Trade-off

All four designs have now been worked out and a trade-off can take place. From this trade-off the winning design is chosen to be worked out in the detailed design phase. This section consists of two trade-offs, an initial one followed by an iteration due to high sensitivity of the initial. The method and trade-off criteria and weights are described for each iteration, followed by the trade-off results.

4.5.1 First trade-off

Defining the trade-off criteria is the first step in the trade-off. Secondly the sensitivity analysis and the trade-off method are defined. With the criteria known weights are assigned and the actual trade-off is performed.

Trade-off criteria
The first step in this trade-off is to define the trade-off criteria. This criteria should reflect the most important characteristics of the design. Part of the criteria will flow from the customer's needs and the other part will follow from characteristics set by the team. The criteria are defined and small descriptions are added to describe what the criteria are.

Sensitivity analysis
The trade-off will be performed by two independently working groups. The outcome of these two groups is compared and analysed. If the outcomes are largely similar, it is a good indication that the trade-off is performed objectively and correctly. Secondly the effect of setting the weights is analysed. For every criterion it will be checked what the sensitivity is with respect to the weights. If a small change in the weight induces large changes in the outcome, then it may be beneficial to split the criterion in smaller ones, or to make absolutely sure that the assigned weight is correct.

Trade-off method
For the trade-off method it is decided to use numerical values as well as a colour map. This combination is used to make it easier to determine if a certain concept is feasible or not. The values and colours can be found in table 4.1.

Table 4.1: Trade-off Values

Value	Definition	Colour
0	Unacceptable	Red
1	Below average	Orange
2	Average	Yellow
3	Good	Green

Performing the trade-off
As explained before the trade-off is performed by two groups which will be denoted by group 1 and group 2. This process is started by assigning weights to each criterion and after this the actual trade-off is performed. Determining the weights was done using the analytical hierarchy process (AHP). This is a more scientific method to compute weights, which consists of ranking criteria relative to each other. This is called pairwise comparison. These values are illustrated using a pairwise matrix.

Now that the weights by the two groups are assigned, the actual trade-off is done. This is done by each group using their own weights for the criteria. To make sure that the trade-off method is accurate and valid, it is essential to perform a sensitivity analysis. This is done by group 1 performing the trade-off using the weights of group 2 and vice versa. From this it was found that group 2 using the weights of group 1 leads to the same final ranking of the concepts. However group 1 using the scores of group 2 gave different scores. Though the method is deemed reliable, the grading and weighting is found to be unreliable due to evident differences between the two groups. Therefore an iteration should be performed.

4.6 Trade-off iteration

Since the results of the trade-off performed by the two separate groups were considered to be too different, an iteration in trade-off process shall be performed. Three steps were proposed to make the trade-off better and more uniform.

- Improve the definitions of the criteria
- Redefine trade-off criteria
- Improve trade-off procedure

The three steps are discussed and the trade-off will again be performed.

Improvement of criteria definitions
The definitions that defined the trade-off criteria had a lot of inconsistencies. Therefore the two groups interpreted these definitions in a different way which resulted in inconsistent answering of the trade-off table. Most problems occurred due to the fact that the criteria definitions were not specific enough. The other problem consisted of the fact that it was not specified how the grading for the trade-off criteria would work for the different concepts. There was no reference value implemented so this resulted in different trade-off results as well. To improve on this all criteria need an explanation on how to use the grading for this specific criteria.

Redefine trade-off criteria
In order to make sure each group interprets the trade-off criteria in the same and correct way, the criteria are redefined. This is done by combining criteria which were too similar. Also the definitions of some criteria were changed because they were too vague.

Improve trade-off procedure
Another reason for the inconsistency between the trade-offs is the fact that both groups used different grading to express the same opinion about certain criteria. To counteract this concise definitions are given in the descriptions of the criteria. Also the way of grading, whether it should be done absolute or relative to each concept, is given in the description as well.

Second trade-off execution
Now that all the problems with the first trade-off are solved, the weights for the new criteria have to be established. The weights are again determined by two groups and compared in order to determine the sensitivity

of the method with respect to the weights. Using the newly defined definitions for the criteria and the AHP template, the following weights were determined for the first group and second group, as can be seen in table 4.2.

Table 4.2: Weights determined by using AHP template

Parameter	Weight group 1	Weight group 2
Endurance	9.63	10.71
Costs requirements	4.5	7.02
Payload capacity	12.42	12.69
Suitable for maritime	13.86	16.02
Flight stability	4.86	4.05
Redundancy	9.27	6.39
Feasibility risk	13.5	13.77
Environmental impact	1.8	2.07
Durability	2.7	3.87
Time to destination	6.66	4.68
Take-off and landing	4.86	2.88
Transportation	1.8	1.8
Ease of maintenance	4.14	4.05

As can be seen from table 4.2, there is consistency between the weights of the two groups.

Using the new trade-off criteria and weights, the scores for all the concepts are again filled in, and the overall scores of the design were computed. In order to properly compare the sensitivity of the trade-off method with respect to the weights, for both sets of weights of both groups the same scores were given as input. This will isolate the sensitivity of the method with respects to the weights. The results for the trade-off with the weights as determined by the first group are given in figure 4.5. The results for the trade-off with the weights from the second group are given in figure 4.6.

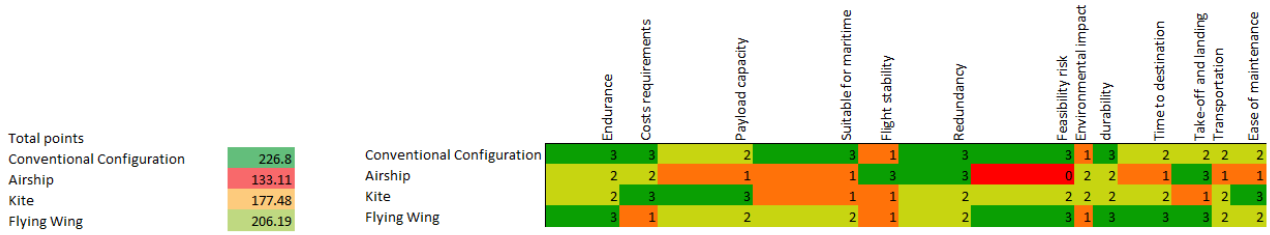

Figure 4.5: New trade-off matrix first group

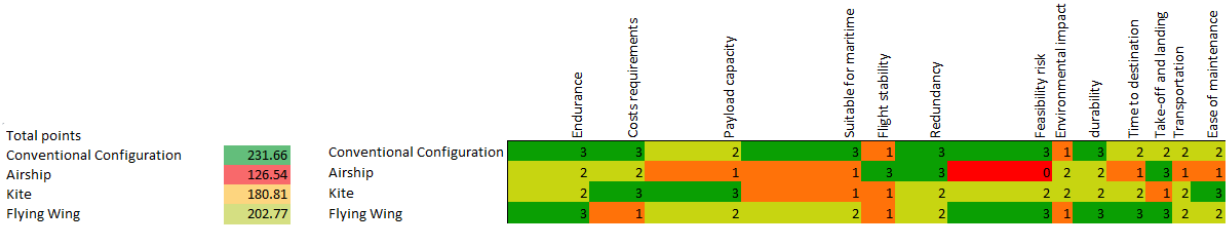

Figure 4.6: New trade-off matrix second group

4.6.1 Performing sensitivity analysis

One of the things that can be noticed in both groups is that the suitability for the maritime environment is consequently the highest weight. Logically, this is also the most important criterion the design has to fulfil. However, due to this weight the method is very sensitive to this criterion. Giving the flying wing a score of 3 instead of 2 for this criterion gives the flying wing almost the same overall score as the conventional configuration.

The same goes for payload capacity and feasibility risk. For this reason there should also be a qualitative and not only a quantitative trade-off between the two winning concepts.

4.7 Final design choice

In the final trade-off the kite and airship score significantly lower than the other two concepts and are therefore eliminated. The difference in total score between the remaining two options are minute with respect to the sensitivity of the method. Therefore the final choice of design is made using a qualitative reasoning, rather than a quantitative analysis. From the trade-off tables it can be concluded that both the flying wing and the conventional design are feasible options.

The conventional design has the highest score making it a very good choice. However a very similar product already exists in the Netherlands. Therefore the design will face an experienced competitor when entering the market.

The main reason the flying wing scores lower on suitability for maritime environment than the conventional configuration is due to the corrosion of the aluminium structure. This criterion is very important, but the material for the flying wing can easily be replaced by a different material. Furthermore the flying wing has a higher aerodynamic efficiency, longer endurance, and a lower fuel consumption than the conventional design. Manoeuvrability is also extremely good, making it capable of tight turns and quick changes in location.

By using the quantitative as well as the qualitative reasoning it is decided that the flying wing will be used for the detailed design.

5 Final Design

Following the results of the trade-off, it is concluded that the flying wing is chosen for the detailed design phase of the project. A render of the final design is given in figure 5.1. This section will give an overview of the subsystems as well as the compliance of the final design with the requirements. First all subsystems will be divided and elaborated upon. This is followed by an N^2 chart which indicated the integration of all the subsystems. Furthermore, this integration is explained with respect to the iterations that must occur during the design phase. Finally, the list of requirements along with the design's compliance to them with them is given.

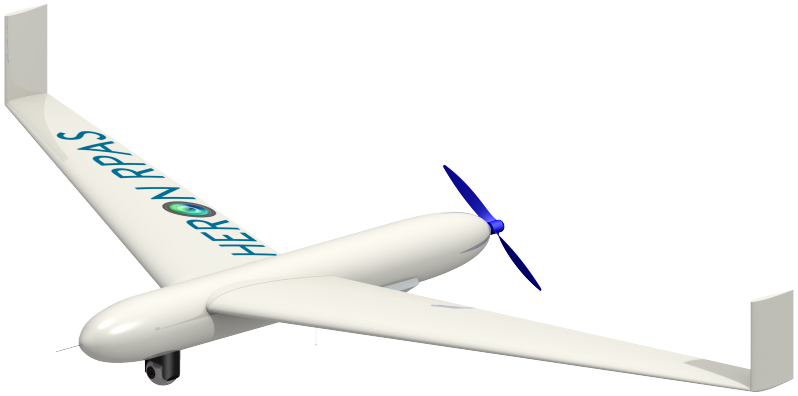

Figure 5.1: Render of the HERON RPAS

5.1 Subsystem division

Now that the final design is chosen, the detailed design process can begin. In order to have a clear overview of all the work to be performed, the entire design will be separated in subsystems. Seven subsystems were determined for the flying wing, and for each of these, certain characteristics will need to be calculated. Since the group will be divided over these seven subsystems, communication is of great importance. Due to the fact that many characteristics of different subsystems will be related and dependent of each other. The first of the seven is the aerodynamics subsystem. In this subsystem all parameters relevant to the aerodynamic characteristics are determined. The subsystem stability and control ensures that the RPAS is controllable and stable. In addition the RPAS needs to be able to carry all the loads, the subsystem structures and materials is responsible for this. The communication subsystem will determine the methods used for streaming video and controlling of the RPAS. To be able to operate, several subsystems require electrical power which will be taken care of by the power subsystem. For the RPAS to be able to move from one place to another, the propulsion subsystem will determine the required propulsion unit. In order to be able to meet the requirements for the imaging, a suitable camera will be selected by the payload subsystem. Finally all the actions that have to take place outside piloting the RPAS is covered by the operations subsystem. This includes launch, recovery, maintenance, certification, and insurance.

5.2 N^2 chart

To make it easier to visualise the integration of the different subsystems and their effects on each other an N^2 chart was made. The diagonal contains all the subsystems present in the design. Horizontal lines indicate and output while vertical lines indicate inputs. The N^2 chart can be found in figure 5.2.

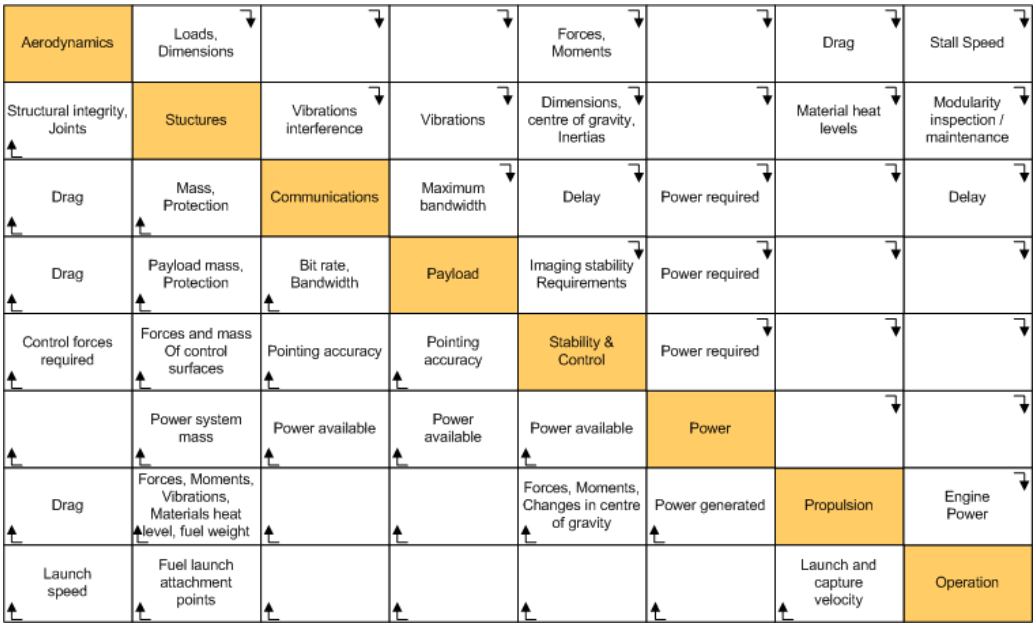

Figure 5.2: N^2 chart for subsystem integration of flying wing

Integration of subsystems
Throughout the report references to other subsystems are given as there is a high integration between them, as shown in figure 5.2. To give an overview of the relationship between subsystems, every chapter will start with a table containing the data from the N^2 chart for each subsystem. The parameters will be given along with the specification if they are inputs or outputs. For inputs, the source will be given, while for outputs the destination for the value is given.

5.3 Compliance with design requirements

With a finalised design, it is possible to return to the requirements set at the beginning of the design process and determine if they have been met. To assist in this process, a compliance matrix is used to give an overview of all the requirements and if they have been completed. Identifiers are used which specify the origin, level, and version of the requirement. The first tag of the identifier explains where the requirements come from, as shown in 5.1. The second indicates if it is a system or a subsystem requirement. In case it is a subsystem requirement, the third tag is used to indicate which subsystem the requirement is about. The different third tags are shown in table 5.2. The first number of the tag indicates which number of requirements it is. The second number indicates the version number of the requirement. The list of requirements is given on page 25 and 26. On the right, a checkmark indicates that the requirement has been met while 'Fail' specifies that it has not.
While most requirements have been met, there are five requirements that have not. Due to insufficient time, encryption of the control system and imaging system have not been completed. Furthermore, with the weight of the RPAS consisting mostly of internal system that are difficult to recycle, a 50% recyclable RPAS was not achieved. Power of the RPAS comes from the engine as well as lithium ion batteries, which means a 20% power generation from renewable sources was not achieved. Finally, calculating the probability of failure to a definitive value was outside the scope of the project, thus the requirement was not achieved.

Table 5.1: Requirement identifiers

Identifier	Meaning
CUST	Customer requirement
FUNC	Functional requirement
SELF	Self defined requirement
CERT	Requirement for certification/legislation

Table 5.2: Subsystem identifiers

Identifier	Meaning
A	Payload
B	Power
C	Propulsion
D	Structures and materials
E	Communications
F	Avionics

Table 5.3: List of requirements

Identifier	Requirement	Status
	Endurance	
CUST-S-1.0	The RPAS shall have an endurance of 4 hours.	✓
	Range	
CUST-S-2.0	The RPAS shall have a minimal range of 20km.	✓
	Cost	
CUST-S-3.0	The total costs of the RPAS shall not exceed €100000.	✓
	MTOW	
CUST-S-4.0	The MTOW of the RPAS shall not exceed 20kg.	✓
	DSE	
SELF-S-1.0	The detailed design of the RPAS shall be done in less than 10 weeks.	✓
	Remotely Piloted	
FUNC-SUE-1.0	Control input uplink shall have a delay of maximum 100 milliseconds.	✓
FUNC-S-1.1	Geographical location of the RPAS shall be determined with an accuracy of at least 5 meters.	✓
FUNC-S-2.1	Altitude of the RPAS shall be determined with an accuracy of at least 5 meters.	✓
FUNC-S-3.1	Velocity of the RPAS shall be determined with an accuracy of at least 5 meters per second.	✓
FUNC-S-4.1	Attitude of the RPAS shall be determined with an accuracy of at least 10 degrees.	✓
FUNC-S-5.0	Sampling rate of the flight condition data shall be at least 20Hz.	✓
FUNC-S-6.0	Control input data shall have an encryption of at least 128 bits.	Fail
FUNC-SUF-1.0	The RPAS shall be able to fly autonomously if connection is lost.	✓
FUNC-SUE-2.0	The RPAS shall have at least one redundant communication system.	✓
	Comply with certifications for flying	
CERT-S-1.0	The RPAS shall be designed according to ICAO regulations[10].	✓
CERT-S-2.0	The RPAS shall be able to fly fully autonomous in case of emergencies or lost connection.	✓
	Provide Power	
FUNC-SUB-1.0	The RPAS power system shall have a redundancy system.	✓
FUNC-SUB-2.0	The RPAS power system shall be able to distribute power to all subsystems.	✓
FUNC-SUB-3.0	The RPAS power system shall be able to regulate the electrical properties to suit each subsystem need.	✓
FUNC-SUB-4.0	The RPAS power storage shall be able to provide enough power to meet the requirements set by other subsystems.	✓
	Conduct Imaging	
CUST-S-5.0	The number of persons on a scene shall be extracted from the video feed.	✓
CUST-S-6.0	The colour of clothes shall be extracted from the video feed.	✓
CUST-S-7.0	Ship names shall be readable.	✓
CUST-S-8.0	Structures on ground level with dimensions of 2 meter shall be identifiable in the video.	✓
FUNC-SUA-1.0	The imaging system shall be able to store the recorded data.	✓
FUNC-SUA-2.0	The imaging system shall be able to compress the recorded data.	✓
FUNC-SUA-3.0	The imaging system shall be able to encrypt the data for downlink with at least 128 bits.	Fail
FUNC-SUA-4.1	The imaging system shall have a pointing accuracy of at least 5 degrees.	✓
FUNC-SUA-5.0	The RPAS shall be able to record video during dawn and dusk in low light conditions.	✓
CUST-S-9.0	A realtime video link shall be available to end-users on the ground within a 10km radius.	✓

Table 5.4: List of requirements

Identifier	Requirement	Status
	Perform Flight	
FUNC-S-5.0	The RPAS shall be launched from or nearby the ground station.	✓
FUNC-S-6.0	The RPAS shall be recovered near the ground station.	✓
FUNC-S-7.0	The RPAS shall produce a lift force.	✓
CUST-S-10.0	The RPAS shall be controlled remotely.	✓
FUNC-S-8.0	The RPAS shall be able to fly autonomously.	✓
FUNC-S-9.0	The RPAS shall be longitudinally (artificially) stable.	✓
FUNC-S-10.0	The RPAS shall satisfy level 1 handling requirements.	✓
FUNC-S-11.0	The RPAS shall be able to change flight direction.	✓
FUNC-S-12.0	The RPAS shall be able to change altitude.	✓
	Suitable for Maritime Environment	
SELF-SUD-1.0	The material of the RPAS shall be resistant to salt water corrosion for the entire lifetime of the aircraft.	✓
SELF-SUC-1.0	The propulsion system shall be able to operate in humidity levels of higher than 75%.	✓
SELF-S-2.0	The RPAS shall be able to operate in humidity levels of up to 100%.	✓
SELF-S-3.0	The RPAS shall be able to operate with wind speeds of on average 7.0 meters per second.	✓
SELF-S-4.0	The RPAS shall stay in flight with wind gust up to 14.0 meters per second.	✓
SELF-S-5.0	The RPAS shall be able to operate under rainy conditions.	✓
	Sustainability	
SELF-S-6.0	The mass of the RPAS shall contain at least 50% recyclable materials.	Fail
SELF-S-7.0	The power generation for the RPAS shall consist of at least 20 % renewable sources.	Fail
SELF-S-8.0	The RPAS lifetime shall be at least 5 years.	✓
SELF-S-9.0	The RPAS design shall facilitate any part replacement to be completed within 1 day.	✓
	Safety	
SELF-S-10.0	The RPAS shall have a minimal environmental impact.	
CERT-S-3.0	The RPAS shall be compatible with the safety regulations.	✓
CUST-SUF-1.0	The RPAS shall be able to detect static and dynamic objects.	✓
CUST-SUF-2.0	The RPAS shall be able to avoid static and dynamic objects.	✓
SELF-S-11.0	The RPAS shall minimize harm to the surroundings in case of failure.	
SELF-SUE-1.0	The RPAS shall try to recover remote connection in case of a loss in communication.	✓
SELF-SUF-1.0	The RPAS shall be autonomous in case of communication loss.	✓
SELF-S-12.0	The RPAS shall be detectable by detection equipment complying with the avionic standards.	✓
SELF-S-14.0	The ground station shall be manned by at least 2 pilots.	✓
SELF-S-15.0	The RPAS shall have a probability of a catastrophic failure less than 10^{-2} per 1000 flying hours.	Fail
	Structure	
FUNC-SUD-1.0	The RPAS structure shall be able to survive the landing impact.	✓
FUNC-SUD-2.0	The RPAS structure shall have a fatigue life of at least 5 years.	✓
FUNC-SUD-3.0	The RPAS structure shall provide shielding for vulnerable subsystems.	✓

6 Aerodynamics

The RPAS market is rapidly expanding. This is mainly due to the increasing demand for safety and security for military and homeland security missions. The first flying wings exist for along time now, therefore the concept is quite old. However flying wing configurations are new in the RPAS market. Since RPAS wing planforms and cruise velocities range from commercial airliner size down to micro flyers, the aerodynamics vary extremely.

Regarding the dependence of the various subsystems and therefore clarifying the iteration process, all inputs and outputs are shown in table 6.1. Note that the total wing span of the aircraft is defined as b, whereas the span of the wing excluding winglets and fuselage is indicated by b^*.

Table 6.1: Inputs and outputs for aerodynamics

Parameter	Value	Unit	Input	Output	Comments	Source/Destination
$MTOW$	18	$[kg]$	X		Maximum take-off weight excluding contingency	Structures and Materials
Λ	25	$[°]$	X		Leading edge sweep angle	Stability and Control
$\Lambda_{0.25c}$	22.5	$[°]$	X		Quarter-chord sweep angle	Structures and Materials
Λ_{tr}	15.0	$[°]$	X		Trailing edge sweep angle	Structures and Materials
$d_{fuselage}$	0.2	$[m]$	X		Fuselage diameter	Structures and Materials
$b_{winglet}$	0.035	$[m]$	X		Winglet contribution to total span	Structures and Materials
M_{roll}	21.2	$[Nm]$	X		Rolling moment about the X-axis	Stability and Control
$c_{L_{cruise}}$	0.34	[-]		X	3D Lift coefficient	Structures and Materials
$c_{D_{cruise}}$	0.014	[-]		X	3D Drag coefficient	Propulsion
V_{cruise}	28	[m/s]		X	Cruise velocity	Structures and Materials, Operations
V_{stall}	15	[m/s]		X	Cruise velocity	Operations
λ	0.35	[-]		X	Taper ratio computed using figure 6.9	Structures and Materials
S	1.1	$[m^2]$		X	Wing area computed using equation 6.1.4	Structures and Materials
b^*	3.3	$[m]$		X	Pure wing span	Structures and Materials
b	3.57	$[m]$		X	Total wing span including fuselage and winglets	Structures and Materials
c_{elevon}	0.2c	$[m]$		X	Elevon chord as function of chord	Structures and Materials
b_{elevon}	0.82	$[m]$		X	Elevon span	Structures and Materials
l_{elevon}	0.85	$[m]$		X	Elevon length along trailing edge	Structures and Materials
M_{elevon}	21	$[Nm]$		X	Moment generated per elevon at full deflection ($\delta_e = 20°$)	Structures and Materials

6.1 Flow characteristics

The first step in determining the aerodynamic characteristics is to analyse the flow itself and thereby computing the Reynolds and Mach number using equations 6.1.1 and 6.1.2. Input parameters and their corresponding values are shown in table 6.2. Critical parameters in this table include the velocity and chord range, which correspond to the minimum and maximum values of reference RPAS in Appendix A.

$$Re = \frac{\rho \cdot c \cdot V}{\mu} \tag{6.1.1}$$

$$M = \frac{V}{a} \tag{6.1.2}$$

It is convenient for future computations to reduce the calculated Reynolds and Mach range to a specific number. Consequently an average is taken with an accuracy represented in the number of significant digits. Therefore a Reynolds number of 600,000 at Mach 0.08 will be used.

Table 6.2: Parameters for equations 6.1.1 and 6.1.4

Input parameter	Value	Unit	Input	Output	Comments
ρ	1.225	$[kg/m^3]$	X		Air density at sea-level
μ	$1.5111 \cdot 10^{-5}$	$[m^2/s]$	X		Kinematic viscosity of air at $20°C$
a	343.59	$[m/s]$	X		Speed of sound at $20°C$, sea-level
V	$25 - 35$	$[m/s]$	X		Velocity range
c	$0.2 - 0.4$	$[m]$	X		Chord width range
g	9.81	$[m/s^2]$	X		Mean gravitational acceleration
$MTOW$	18	$[kg]$	X		Maximum take-off weight excluding contingency
Re	$330,885 - 926,477$	[-]		X	Reynolds number computed using equation 6.1.1
M	$0.07 - 0.1$	[-]		X	Mach number computed using equation 6.1.2

The lift to be provided by the flying wing has to correspond to the air density, MTOW and velocity range shown in table 6.2. The equivalent coefficient to be designed for can thus be calculated using equation 6.1.3 and 6.1.4.

Note that the MTOW used is excluding contingency. This is done in line with the system engineering approach to prevent overdesign, which would yield an even higher MTOW. In other words, designing for a MTOW including contingency results in a higher structural mass and therefore making a lower MTOW unlikely. However, the required lift coefficient is augmented in an iteration in case that the MTOW increases during the design process.

$$MTOW = \frac{L}{g} \tag{6.1.3}$$

$$C_L = \frac{L}{\frac{1}{2}\rho V^2 S} \tag{6.1.4}$$

6.2 Airfoil analysis and selection

The design of the airfoil starts with listing the required aerodynamic characteristics for the flying wing. These characteristics are in a certain range for Reynolds- and Mach number, lift- and moment coefficients, where the airfoil shall perform the best in terms of stall characteristics, low drag, high lift, easy to manufacture, and sensitivity regarding to dust and dirt. After that the most applicable airfoil is chosen.

The first NACA airfoil family is defined using four-digits introduced by NACA itself. Each digit in the digit series represents a certain airfoil parameter. The exact setup of the digit series is illustrated using the NACA 1234 airfoil. The first digit (1) represents the maximum camber in tenths of chord, the second (2) indicates the position of the maximum camber in tenths of chord, the last two numbers (34) together indicates the maximum thickness of the airfoil in percentage of chord [11].

After constructing the four-digits NACA airfoils, a more elaborate naming convention was required to generate more complicated shapes. This NACA airfoil series can be demonstrated using the NACA 12345 airfoil. The first digit (1) defines the camber of the airfoil. This digit is multiplied by 1.5 to get the design lift coefficient in tenths of the chord length. The second digit (2) indicates the position of maximum camber divided by 20 in tenths of chord. Next, the third digit (3) is a binary digit. The airfoil consist of a normal camber line, if the third digit is equals zero. A number one represents a reflex camber line. The last two numbers (45) indicates just as the four-digit NACA airfoils the maximum thickness as percentage of the chord length [11].

One of the largest challenges in designing a flying wing is the stability and control. Since in general the stability of an aircraft is mainly dependent on the wing characteristics and therefore the aerodynamics, the first design iteration starts in the aerodynamics department. Most of the airfoils have a pitch-down moment at positive angles of attack, that is counteracted by a horizontal tail or canard as can be seen in figure 6.1.

Figure 6.1: Longitudinal stability of a conventional aircraft

However flying wings are tailless-aircraft that have to be stable without any horizontal tail surface. There are two different centres that have to be taken into account when designing a flying wing, the aerodynamic center and the center of gravity. In case the center of gravity location is after the aerodynamic center location, lift will generate a pitch-up moment as can be seen in figure 6.2.

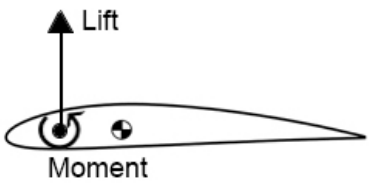

Figure 6.2: Aerodynamic stability of a flying wing when center of gravity is after the aerodynamic center

Figure 6.2 shows that using pitch-down moment combined with a pitch-up moment due to the lift could be made stable, the moments have to be the same magnitude but should be counteracting. Benefit of this configuration

showed is that almost every arbitrary high-lift airfoil can be chosen. However if there is any flow disturbance and the angle of attack increases, a pitch-up moment will cause the airfoil to be unstable. Due to the fact that an increase in angle of attack will generate a larger lift force, therefore $C_{m_\alpha} > 0$ and thus unstable. An unstable aircraft is not desired, and therefore, this configuration will not be selected.

The aerodynamic center and the center of gravity can be located the other way around. In figure 6.3 the aerodynamic center location is after the center of gravity location. Lift will generate a pitch-down moment, in order to counteract the pitch-down moment a pitch-up moment from the airfoil is required in order to be stable.

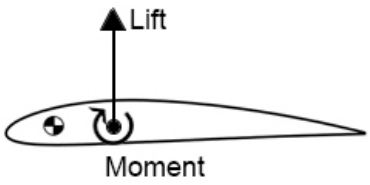

Figure 6.3: Aerodynamic stability of a flying wing when the aerodynamic center is after the center of gravity

Figure 6.3 shows that there is a moment equilibrium in case that both moments have equal counteracting magnitude. One of the advantages of this configuration is that in case of any flow disturbance, the airfoil will remain stable. If the angle of attack increases also the lift force becomes larger, in this particular configuration a pitch-down moment is generated and therefore the airfoil is stable ($C_{m_\alpha} < 0$). The disadvantage of this configuration is that there is a scarcity of airfoils that have a positive pitching moment (pitch-up moment) at a large range of angles of attack. A solution for this could be a elevator or aileron deflection that generates a pitch-up moment as a result that the lift coefficient will be lower. Another way of compensating the pitch-down moment is applying a combination of sweep and twist to the wing.

For the airfoil analysis, the focus is on airfoils that have the tendency to pitch-up at a broad range of angles of attack. In the analysis the NACA four-digits and five-digits are compared in terms of airfoil characteristics as can be seen in table 6.3.

Table 6.3: Advantages and disadvantages of the 4-digit and 5-digit NACA series [12]

Airfoil series	**Advantages**	**Disadvantages**
4-Digit	Good stall characteristics	Low maximum lift coefficient High pitching moment
5-Digit	Higher maximum lift coefficient Low pitching moment	Poor stall behavior

Stability for a flying wing is a crucial part of the design and is interrelated to the aerodynamics of the wing. As can be seen in table 6.3 the disadvantage of a four-digit NACA airfoil is the high pitching moment, to correct for this moment a large sweep and twist is required. Low pitching moments can be generated by using a five-digit NACA airfoil, those five-digit airfoils have the ability to apply a reflex. Using a reflex airfoil the wing could be stable without using sweep or twist, as a result that the lift force will be lower.

Airfoil selection

Besides the aerodynamic coefficients such as lift and drag, the moment coefficient is also one of the important parameters. The moment coefficient has a big impact on the longitudinal stability of the RPAS.

For the flying wing there are four NACA five series airfoils analysed. Those airfoils are selected on their lift, drag, and moment characteristics. Those aerodynamic characteristics can be influenced by changing airfoil design parameters such as camber, and thickness.

- Camber - The effect of applying camber to the airfoil is reaching higher values of lift coefficient in correspondence of lower angle of attack. Increasing camber will increase the pitching moment of the airfoil, in general an increasing pitch-down moment. However it is not only the maximum camber that affects the aerodynamic characteristics, but also the location of maximum camber. Relocating the camber towards the nose will increase the $C_{L_{max}}$ but is not favourable for the stall characteristics, also vice versa this is true [13].
- Thickness - The effect of the maximum thickness of the airfoil and its location have an influence on the $C_{L_{max}}$, stall characteristics, and drag. When the maximum thickness is shifted back, the following aerodynamic characteristics will change: Lower minimum drag, lower $C_{L_{max}}$, and higher drag increase.

When shifting the location of maximum thickness forward, vice versa is true. From structural point of view, thick airfoils are beneficial since there are lower wing bending stresses [13].

Using this information the airfoils shown in figure 6.4, from top to bottom NACA 22115, NACA 23115, NACA 32115, and NACA 42115 are chosen.

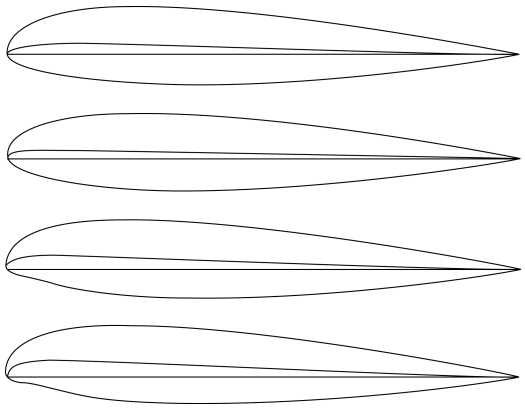

Figure 6.4: Selected NACA 5-digit airfoils from top to bottom: NACA 22115, NACA 23115, NACA 32115, and NACA 42115 [14]

6.3 Aerodynamic coefficients

Now that a selection is made of four different airfoils, the analysis of their characteristics can be performed. To this extend the acquired 2D data firstly is converted to 3D.

Finite wing corrections
A infinite 2D wing can be seen as a finite wing with an unlimited aspect ratio. Therefore aerodynamic characteristics from a infinite wing (2D) differ significantly from the finite wing (3D). A finite wing correction is applied to correct those aerodynamic characteristics.

Adding a third dimension by transforming an airfoil into a wing, alters the pressure distribution over the wing. Due to the difference between the upper and lower pressure, a circular motion is introduced about the wingtips. The circular motion, called a vortex, is causing downwash that is influencing the local airflow. Drag will increase by this induced downwash [15].

Firstly the lift produced is corrected for a finite wing using equation 6.3.1. This equation determines the change in slope of the $C_L - \alpha$ curve and can only be used for a wing in incompressible airflow with an aspect ratio of at least 4 [15]. In this equation $a = dC_L/d\alpha$ and $a_0 = dc_l/d\alpha$ in $[1/rad]$.

$$a = \frac{a_0}{1 + \frac{a_0}{\pi A e}} \; [1/rad] \tag{6.3.1}$$

The value to be determined for a varies with different values for the aspect ratio and Oswald factor. Consequently the slopes can be determined for the proposed NACA 5 airfoils, shown in figure 6.4. To this extend the $C_l - \alpha$ plot is linearised and the zero-lift angle of attack is determined. All values used are shown in table 6.4.

Table 6.4: 3D Lift Slope Parameters for $A = 10$ and $e = 0.90$ [11]

Parameter	NACA 22115	NACA 23115	NACA 32115	NACA 42115	Unit	Comments
$\alpha_{L=0}$	-0.75	-0.80	-1.6	-2.0	[°]	Zero-lift angle of attack
a_0	0.10	0.10	0.10	0.099	[1/°]	2D lift slope (C_{l_α})
a	0.086	0.084	0.083	0.083	[1/°]	3D lift slope (C_{L_α})

Aerodynamic characteristics in 3D
Next the finite wing correction is applied to the 2D data, the 3D lift and drag coefficients are calculated and described in this section. After that the way of constructing a lift drag polar is shown for both 2D and 3D.

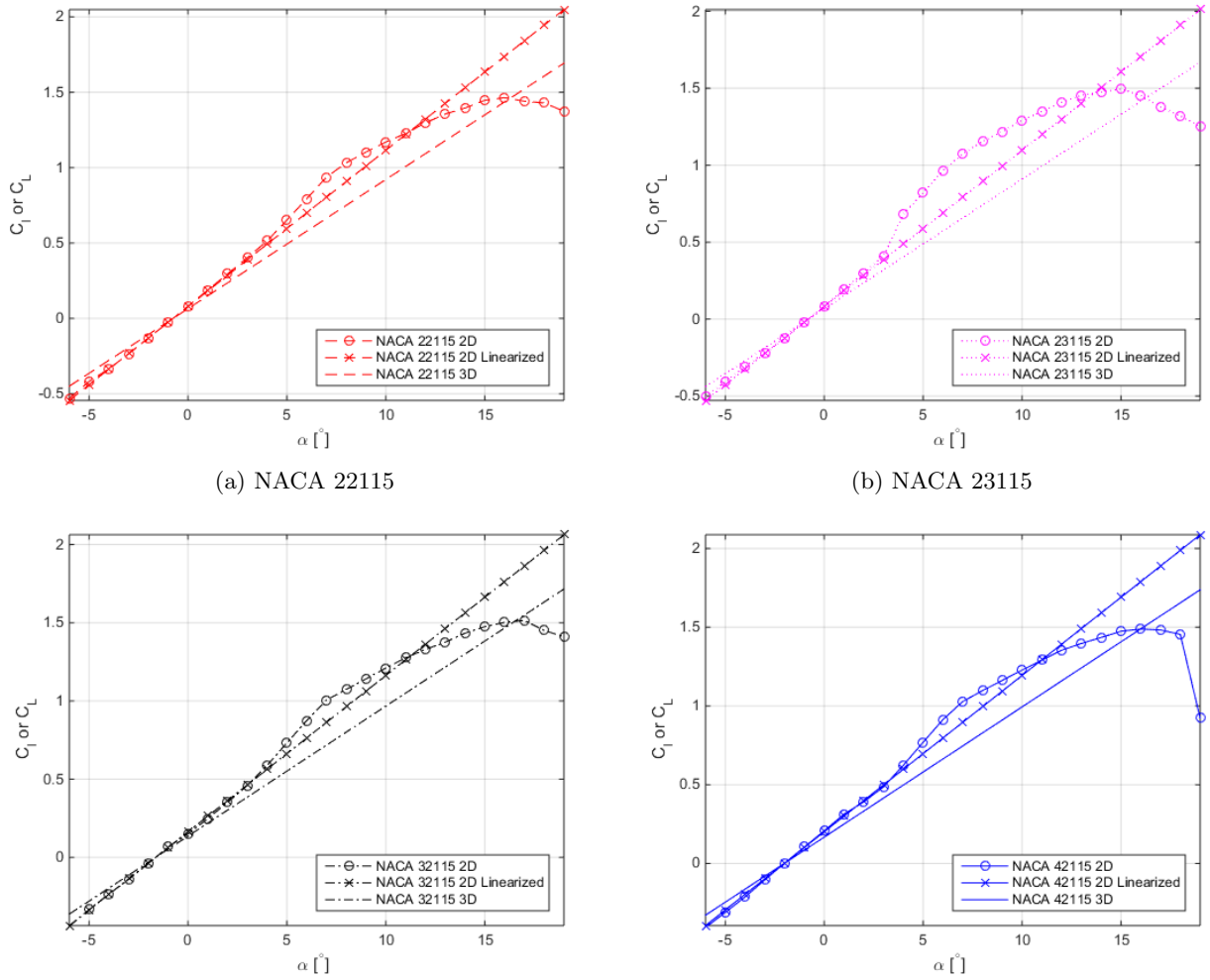

(a) NACA 22115

(b) NACA 23115

(c) NACA 32115

(d) NACA 42115

Figure 6.5: Prandtl's lifting line theory for NACA 5 airfoil series, Re=600,000, M=0.08, n_{crit}=9.0

Throughout this section the same symbols and colours are used for each airfoil. The 2D airfoil data shown in figure 6.5 is gathered from XFLR5. XFLR5 is an analysis tool for airfoils, wings and planes operating at low Reynolds Numbers. From the 2D data a linearised function is defined which is a linear approximation of the lift coefficient, indicated as 2D linearised in figure 6.5. From the 2D linearised function, a 3D lift coefficient is generated using equation 6.3.1. The 3D lift slope of the four airfoils is lower compared to the 2D lift slope, however the difference is minute due to the high aspect ratio. Interesting to point out is that all four the graphs in figure 6.5 show a small bump corresponding to an increase in lift in the 2D data, this irregularity will be explained in section 6.7.

After calculating the lift gradients for the different airfoils, the drag coefficients are estimated. In figure 6.7 the lift drag polars can be seen, where again the same symbols and colours are used. The 3D drag coefficient can be calculated using equation 6.3.2 [16]. This equation is used for a 3D drag calculation for a finite wing only, therefore e is the span efficiency in this equation.

$$C_D = C_d + \frac{C_L^2}{\pi A e} \tag{6.3.2}$$

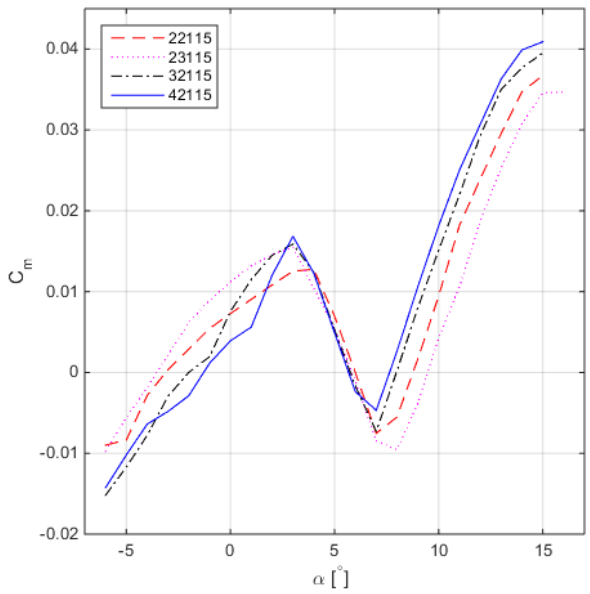

Figure 6.6: Moment coefficient, Re=600,000, M=0.08,n_{crit}=9.0

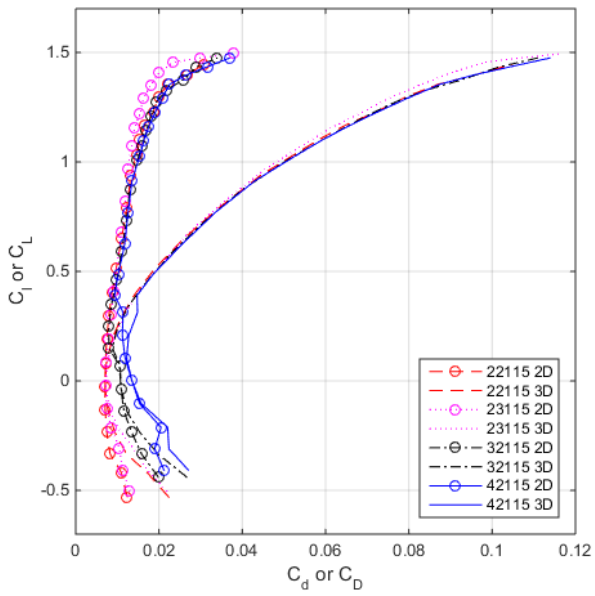

Figure 6.7: Lift drag polar, Re=600,000, M=0.08,n_{crit}=9.0

Figure 6.7 displays the change in drag when transforming from 2D to 3D. One can observe that the difference between the various airfoils in the 2D drag polars are reduced when going from 2D to 3D. Noteworthy is the drag at zero lift, which is equal for 2D and 3D.

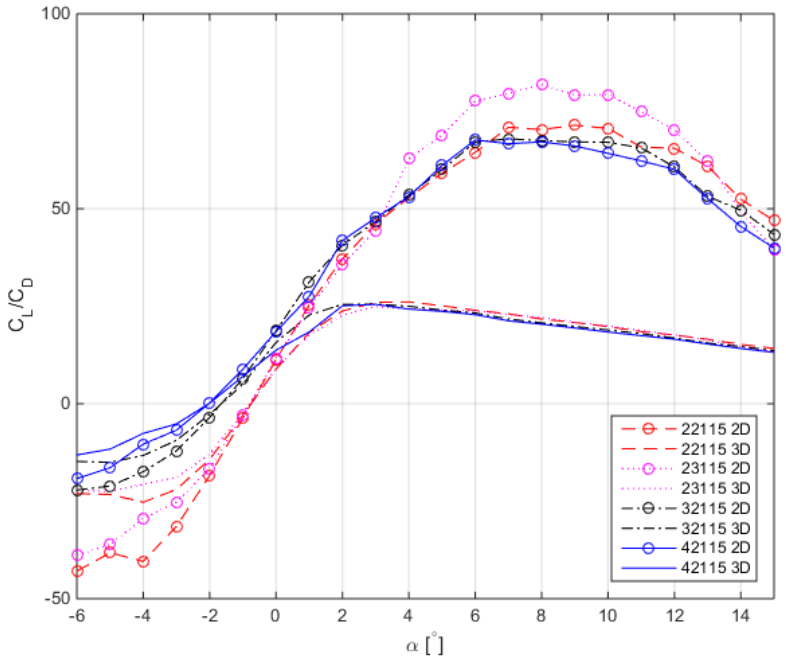

Figure 6.8: Lift over drag ratio, Re=600,000, M=0.08, n_{crit}=9.0

After computing 3D lift and drag, different lift over drag ratios are determined for a range of different angles of attack, the results are displayed in figure 6.8. What can be noticed is that the lift over drag in 3D is at maximum in the range from 2 to 4 degrees angle of attack for all airfoils.

After analysing the design lift coefficients and comparing the lift, drag, and moment coefficients for the different airfoils gathered from XFLR5, there is decided that the NACA 22115 is the best airfoil for the mission. As can be seen in table 6.4 resulted from figure 6.5, the lift slope C_{l_α} for the four chosen airfoils approximately the

same. The only difference between the airfoils is the design lift coefficient as described in the NACA five-digit description. As can be seen in the drag polar in figure 6.7, the difference between the airfoils is small. However for small lift coefficients and in particular when lift is equal to zero, the NACA 22115 is performing the best. One of the most important criteria where the airfoil selection is based on it the moment coefficient. As can be seen in figure 6.6, the range for a positive moment coefficient (pitch-up moment) is largest for the NACA 22115. This is preferred since the positive moment coefficients occur on angles of attack where the flying wing is most of the time flying. On top of that, the lift over drag is slightly higher at angles of attack larger than 3 degrees, exactly at which angles of attack the flying wing will be flying. The final conclusion where the choice is based has to do with the production of the airfoil. As can be seen in figure 6.4, the third and fourth airfoil (NACA 32115 and 42115) are more complex shaped airfoils. These airfoils will therefore likely to have higher production costs as compared with the upper two (NACA 22115 and 23115).

6.4 Planform parameters

Considering the fact that the airfoil is now chosen, one can now scale the remaining parameters which determine the design of the wing.

Wingtip devices and effective aspect ratio
The aspect ratio is of critical importance to the endurance of the aircraft, since it is one of the main drivers for the drag. The lift induced drag decreases with a larger aspect ratio. The total drag of a finite wing is given by equation 6.3.2 [16].

Another way of minimising the induced drag of the wing is applying wingtip devices such as winglets, endplates, or fences. Since there are winglets on the wingtips of the flying wing for rudder control, the induced drag component is therefore minimised.

Wingtips reduce the intensity of tip vortices and keep the outboard wing surface as free as possible from lift-spoiling effects. A properly designed wingtip device can create the same effect of a larger wing aspect ratio as a simple wing extension without extra weight and bending load. A properly designed winglet device can yield an effective aspect ratio of about 20% higher compared to a wing without wingtip devices [17]. The 20% increase in aspect ratio is only implemented for the aerodynamic characteristics, and is not applied on the geometrical properties of the wing.

Taper ratio
Applying taper to a wing gives a number of significant aerodynamic and structural advantages. Determining a suitable wing taper involves a trade-off between structural advantages and adequate resistance to tip stall.

Numerical lifting line theory and lifting surface methods show that the use of linear taper can reach span efficiency factors close to 1, which means close to an elliptical lift distribution [18]. A rectangular wing planform, taper of 1, has a larger downwash angle at the tip compared to the root. Therefore, the effective angle of attack at the tip is lower compared to the root. Therefore the tip will tend to stall later than the root [11]. In order to reduce the induced drag, the planform has to be tapered such that the planform approximates the ideal, elliptical span load distribution. The taper ratio can be calculated using equation 6.4.1.

$$\lambda = \frac{c_{tip}}{c_{root}} \tag{6.4.1}$$

For every arbitrary wing aspect ratio, there is an optimal taper ratio where the wing efficiency is maximal as can be seen in figure 6.9. From d on the vertical axis of figure 6.9 the wing span efficiency factor can be calculated using equation 6.4.2.

$$e = \frac{1}{1+d} \tag{6.4.2}$$

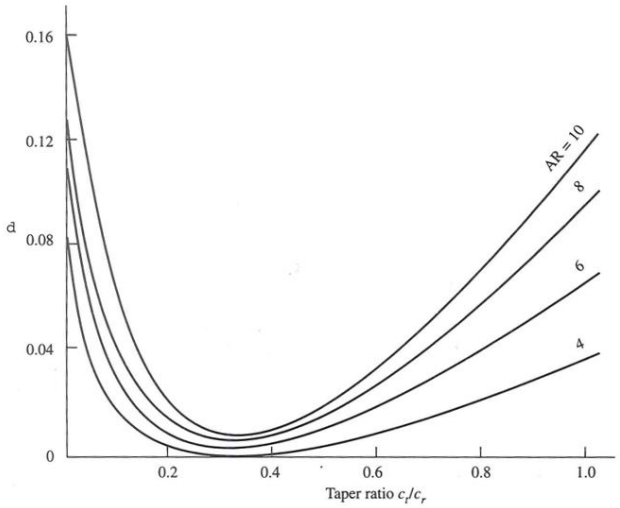

Figure 6.9: 'Induced drag factor as a function of taper ratio for wings of different aspect ratios' [19]

Sweep angle
Applying sweep reduces the airflow experienced by the wing by the cosine of the leading edge sweep angle. Therefore, this approach is used when it is desired to fly at a higher velocity. In addition sweep can be beneficial for the stability and control of the aircraft since it influences the position of the aerodynamic center, center of gravity and the arm for the forces generated by the control surfaces.

The latter reason is leading for the design of the maritime flyer since the flying wing configuration does not include a second lifting surface like a tail. The sweep therefore is determined by the stability and control department. Regarding the reduction in velocity, the cosine of the leading edge sweep angle is taken into account for the computations of the performance of the aerodynamic design.

6.5 Aerodynamic design parameters

The aerodynamic design of the flying wing is done in an iterative manner. The decisions driving the design are discussed in this section. The basis parameters are shown in table 6.5.

Table 6.5: Basis Parameters for optimal C_L/C_D for NACA 22115

Parameter	Value	Unit	Input	Output	Comments
g	9.81	$[m/s^2]$	X		Mean gravitational acceleration
$MTOW$	18	$[kg]$	X		Maximum take-off weight excluding contingency
ρ	1.225	$[kg/m^3]$	X		Air density at sea-level
e	0.9	[-]	X		Oswald factor [11]
V	25	$[m/s]$	X		Cruise velocity
A	12.5	[-]	X		Aspect ratio
Λ	25	[°]	X		Leading edge sweep angle
α_{opt}	3	[°]		X	AOA
$C_{L_{opt}}$	0.4	[-]		X	3D Lift coefficient
$C_{d_{opt}}$	0.0087	[-]		X	2D Drag coefficient
$C_{D_{opt}}$	0.013	[-]		X	3D Drag coefficient
L/D	25	[-]		X	3D Lift over drag ratio
S	1.4	$[m^2]$		X	Wing area computed using equation 6.1.4
b^*	4.2	$[m]$		X	Pure wing span computed using equation 6.5.1

The computed pure wing span in table 6.5 is considered too high considering the logistics of the aircraft in components on the ground. Especially when taking into account the extra 0.20 m fuselage diameter and 0.035 m width per winglet which together add up to the total wing span of 4.47 m. Therefore a reduction in aspect ratio is proposed to lower the total wingspan, using equation 6.5.1.

$$A = \frac{b^2}{S} \tag{6.5.1}$$

The result of decreasing the aspect ratio is shown in table 6.6.

Table 6.6: Iteration 1 parameters for optimal C_L/C_D for NACA 22115

Parameter	Value	Unit	Input	Output	Comments
A	10	[-]	X		Aspect ratio
α_{opt}	3	[°]		X	AOA
$C_{L_{opt}}$	0.4	[-]		X	3D Lift coefficient
$C_{d_{opt}}$	0.0087	[-]		X	2D Drag coefficient
$C_{D_{opt}}$	0.014	[-]		X	3D Drag coefficient
L/D	24	[-]		X	3D Lift over drag ratio
S	1.4	$[m^2]$		X	Wing area computed using equation 6.1.4
b^*	3.7	$[m]$		X	Pure wing span computed using equation 6.5.1

The pure wing span is still considered to be excessive and will be further reduced by increasing the cruise velocity, this is shown in table 6.7.

Table 6.7: Iteration 2 parameters for optimal C_L/C_D for NACA 22115

Parameter	Value	Unit	Input	Output	Comments
V	28	[m/s]	X		Cruise velocity
S	1.1	$[m^2]$		X	Wing area computed using equation 6.1.4
b^*	3.3	$[m]$		X	Pure wing span computed using equation 6.5.1

The various iterations have had an impact on the aerodynamic performance of the flying wing. In order to still provide sufficient lift, the cruise angle is changed from 3° till 3.4°. To conclude, the final planform parameters are shown in table 6.8. Note that in the computations of the aerodynamic performance the effective aspect ratio is used, which incorporates the 20% increase due to the winglets as determined in section 6.4.

Table 6.8: Final parameters using NACA 22115

Parameter	Value	Unit	Comments
g	9.81	$[m/s^2]$	Mean gravitational acceleration
$MTOW$	18	$[kg]$	Maximum take-off weight excluding contingency
ρ	1.225	$[kg/m^3]$	Air density at sea-level
e	0.9	[-]	Oswald factor [11]
α_{cruise}	3.4	[°]	Cruise angle of attack
$C_{L_{cruise}}$	0.34	[-]	3D Lift coefficient
$C_{l_{max}}$	1.465	[-]	2D Maximum lift coefficient
C_{d_0}	0.007	[-]	Zero lift drag coefficient
$C_{d_{cruise}}$	0.0087	[-]	2D Drag coefficient
$C_{D_{cruise}}$	0.014	[-]	3D Drag coefficient
L/D	27	[-]	3D Lift over drag ratio
V	28	[-]	Cruise velocity
A	10	[-]	Aspect ratio
A_{eff}	12	[-]	Effective aspect ratio due to winglets
Λ	25	[°]	Leading edge sweep angle
λ	0.35	[-]	Taper ratio computed using figure 6.9
S	1.1	$[m^2]$	Wing area computed using equation 6.1.4
b^*	3.3	$[m]$	Pure wing span computed using equation 6.5.1
b	3.57	$[m]$	Total wing span including fuselage diameter and winglets

6.6 Control surface sizing

Control surfaces of a flying wing are used to both stabilise the RPAS and provide control in the form of control moments needed for manoeuvre. In this section the elevon surface sizing is performed since the function of an aileron and rudder is combined in one control surface. For the first iteration the basic parameters are set on an initial value as will be explained in this section.

In order to roll or bank the RPAS, the elevons move opposite of each other. To control the pitch of the RPAS, the elevons move together. In this way a smaller elevon surface is already sufficient. Elevons needs to be located at the tip of the wing to be as effective as possible for roll and pitch, because of the attachment of the wingtips the elevon starts 5.0 cm from the tip. The initial design parameters of the elevon are determined from statistics. Based on statistics, about 15% to 25% of the wing chord is devoted to the aileron [20], therefore the average

of 20% is taken for the first iteration. The control moment required from the elevons is required in every flight condition, therefore the elevons are designed for stall conditions.

After initialising the first design parameters, the effectiveness of an elevon deflection is investigated. Large elevon deflections comes with larger structural loads, therefore the lift coefficients for different angles of attack for elevon deflections between 0° and 25° are investigated as can be seen in figure 6.10.

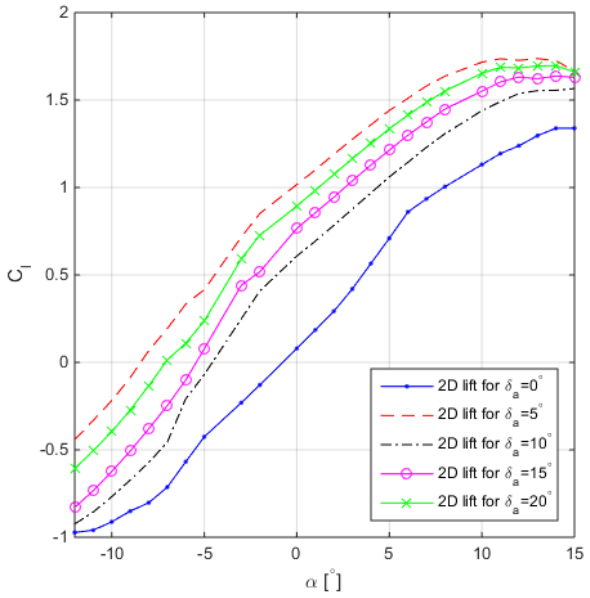

Figure 6.10: 2D Lift coefficients for various elevon deflections, Re=380,000, M=0.04, n_{crit}=9.0

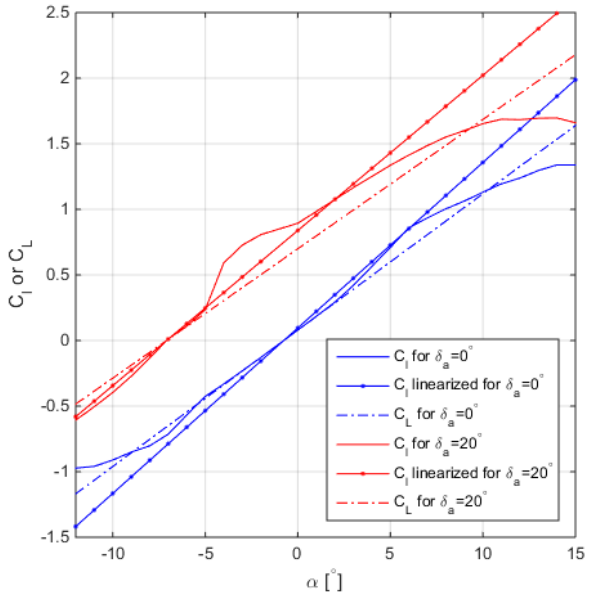

Figure 6.11: Lift coefficient with and without full elevon deflection, Re=380,000, M=0.04, n_{crit}=9.0

As can be seen in figure 6.10, the elevon effectiveness decreases with increasing elevon deflection. When a control surface is deflected more than about 20° to 25°, flow separation over the wing tends to occur and the effectiveness will drop [20]. The same phenomenon can be seen in figure 6.10, where the effectiveness decreases with increasing deflection angle. Therefore the maximum elevon deflection is set at 20° after analysing 2D data from XFLR5.

Using these first iteration parameters, the elevon sizing starts with comparing the lift coefficients for 0° and 20° elevon deflection. In figure 6.11 the NACA 22115 airfoil for both 0° and 20° elevon deflection is shown for 2D and 3D. For the elevon sizing, again the normal lift equation multiplied by the arm as can be seen in equation 6.6.1.

$$M_{roll} = \frac{1}{2}\Delta C_L \rho S V_{stall}^2 \cdot arm \tag{6.6.1}$$

The initial values and the results after iterations can be seen in table 6.9. The results from the iterations can be used for designing the structure of the RPAS.

Table 6.9: Iteration parameters for elevon sizing using NACA 22115 airfoil

Parameter	Value	Unit	Input	Output	Comments
V_{stall}	15	$[m/s]$	X		Stall speed
c_{elevon}	0.2c	$[m]$	X		Elevon chord as function of chord
b^*	3.3	$[m]$	X		Pure wing span
b_{elevon}	0.82	$[m]$		X	Elevon span
l_{elevon}	0.85	$[m]$		X	Elevon length along trailing edge
M_{roll}	21.2	$[Nm]$		X	Moment generated per elevon at full deflection ($\delta_e = 20°$)

6.7 Relevant drawbacks

Two well known disadvantages of the chosen airfoil and planform combination include stalling and the location of the transition point. Both are essential to the performance of the final design and are therefore closely analysed. In addition, the wing-fuselage interaction is discussed.

Stall characteristics
A low velocity is desired for manoeuvres like recovery. One would therefore like to fly at high values of C_L, hence at large angle of attack. To prevent the aircraft from stalling, firstly the stall speed will be considered. Equation 6.1.4 is rewritten to compute the stall speed using the maximum lift coefficient.

$$V_{stall} = \sqrt{\frac{L}{C_{L_{max}} \frac{1}{2}\rho S}} = \sqrt{\frac{MTOW \cdot g}{C_{L_{max}} \frac{1}{2}\rho S}} \tag{6.7.1}$$

Before equation 6.7.1 can put to use, a transition needs to be performed for the maximum lift coefficient from 2D to 3D. The most reliable approach is to carry out a wind tunnel experiment. However due to the limitations of the DSE, this is left as a recommendation for further research. An approximation of this value can be made by using equation 6.7.2 [21].

$$C_{L_{max}} = 0.9\, C_{l_{max}} \cdot \cos \Lambda_{0.25c} \tag{6.7.2}$$

Using the values in table 6.10, the stall speed is computed at 15 m/s. This value equals exactly half of the optimal cruise speed and will be used in the launch and recovery analysis.

Table 6.10: Parameters for stall speed in equations 6.7.1 and 6.7.2

Parameter	Value	Unit	Input	Output	Comments
g	9.81	$[m/s^2]$	X		Mean gravitational acceleration
$MTOW$	18	$[kg]$	X		Maximum take-off weight excluding contingency
ρ	1.225	$[kg/m^3]$	X		Air density at sea-level
$\Lambda_{0.25c}$	22.5	$[°]$	X		Quarter-chord sweep angle
$C_{l_{max}}$	1.465	[-]	X		2D maximum lift coefficient at $\alpha = 16°$
S	1.1	$[m^2]$	X		Wing area computed using equation 6.1.4
V_{stall}	15	$[m/s]$		X	Stall speed at sea-level

A negative effect of the proposed sweep, taper, and aspect ratio is that the stall starts at the wing tips causing an unexpected roll of the aircraft. A downward twist from root to tip may be applied to counteract this effect. The application of this technique is also called a washout. The required angle highly depends on the (in)stability gained from other configuration choices, but will never be considerably large as seen from reference aircraft [22]. A wind tunnel test is proposed to inspect whether a washout is required. If applied, a range from 0° to 5° can be expected [22].

Transition point
Transition points are located at the point where the boundary layer around an airfoil changes from laminar to turbulent flow. The state of the boundary layer is generally in one state. It can be laminar where the fluid is undisturbed and in well-ordered layers, or turbulent where the fluid is disturbed and chaotic [23]. The exact location of the transition point has a major influence on the aerodynamic characteristics. Therefore two situations are described in which the transition point is changed with respect to the clean airfoil.

The first situation changes the transition point to improve the aerodynamic characteristics. As can be seen in figures 6.5a and 6.6, the slope of the coefficients change over different angle of attack. The lift coefficient for example shows a small increase in lift slope at four degrees, at the same angle of attack the slope of the moment coefficient changes sign. This is due to separation effects on the wing due to the low Reynolds number. For low Reynolds number, an adverse pressure gradient can cause the laminar boundary layer to separate. After separation a shear layer, which for slightly higher Reynolds number transforms into a turbulent boundary layer, reattaches again [24].

In particular for the moment coefficient graph in figure 6.6, the instant change in sign of the slope is not preferred since stability changes can be expected. In figure 6.12 different transition points can be noted on the top of the airfoil. However also on the bottom of the airfoil, transition points can be noted almost at the trailing edge.

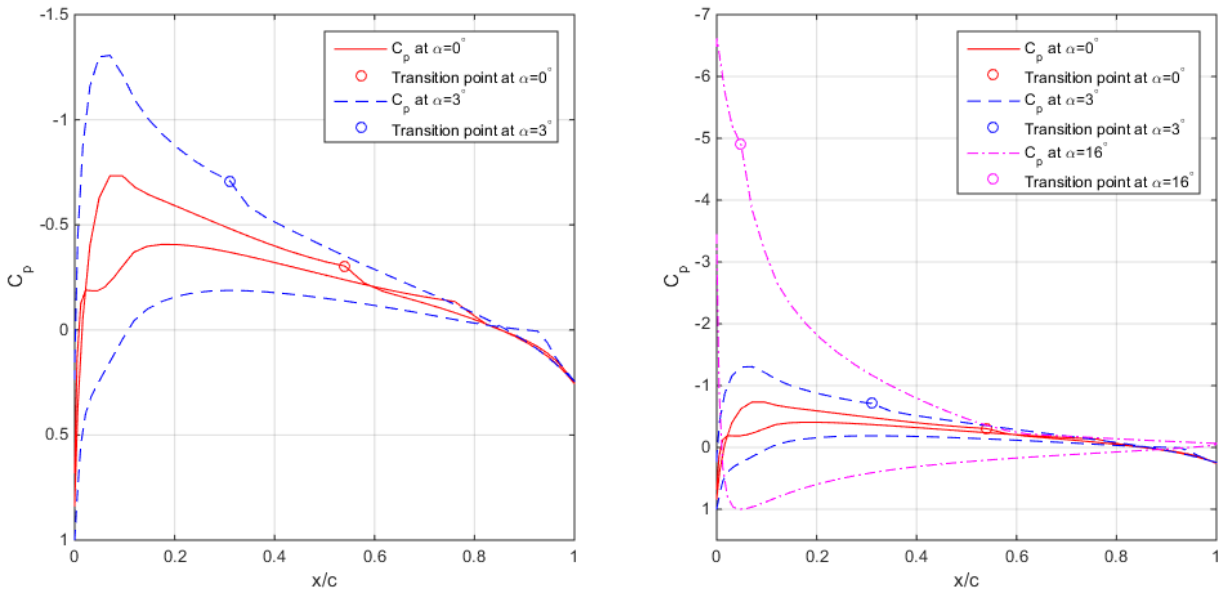

Figure 6.12: Pressure coefficient distribution for NACA 22115, Re=600,000, M=0.08, n_{crit}=9.0; for 0° to 3° and 0° to 16°

Applying a forced transition on the bottom of the airfoil alters the aerodynamic performance of the airfoil. As can be seen in figures 6.13 and 6.14, forcing the transition point alters the aerodynamic performance of the airfoil compared to the free transition.

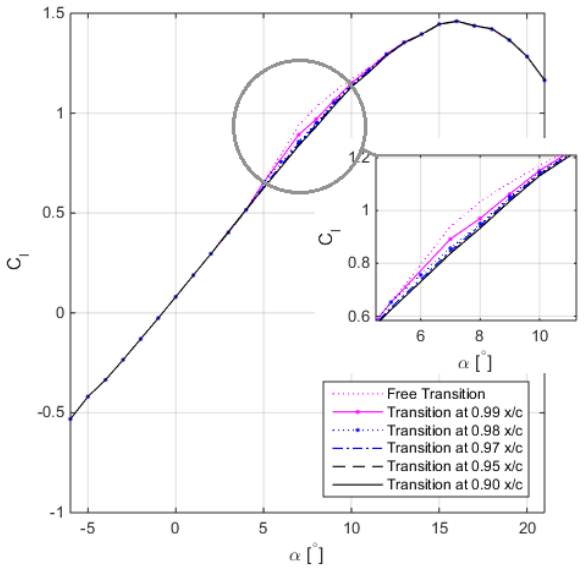

Figure 6.13: $C_l - \alpha$ curve for various transition points, Re=600,000, M=0.08, n_{crit}=9.0

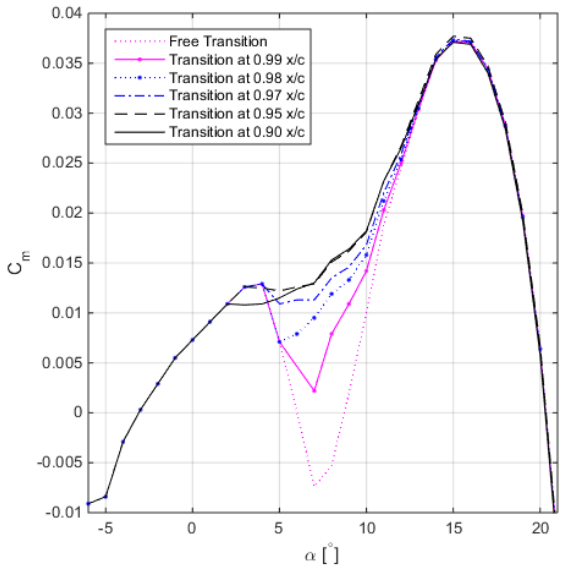

Figure 6.14: $C_m - \alpha$ curve for various transition points, Re=600,000, M=0.08, n_{crit}=9.0

The second situation shows the impact of the transition point moving forward to the nose. Due to increasing angle of attack, transition points move forward to the nose as can be seen in figure 6.12. A second condition that causes the transition point to move forward is in case of dust or dirt on the nose of the airfoil. Due to dust and dirt the transition point for both the top and bottom tend to move to the nose. Since there is always a possibility that the airfoil is getting dirt, there must be accounted for this accounted in the design. The forced transition points are chosen to be 5% and 10% for top and bottom respectively.

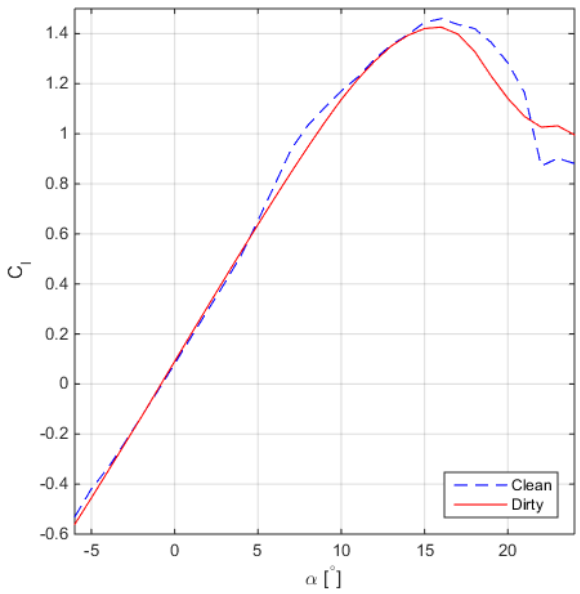

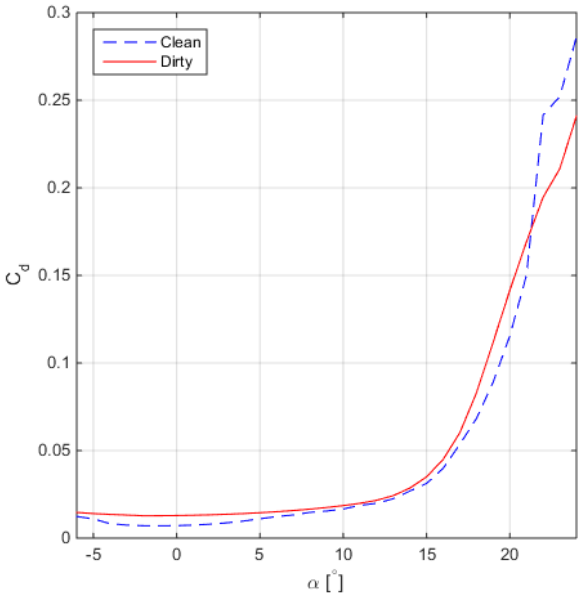

Figure 6.15: $C_l - \alpha$ curve for a clean and dirty airfoil, Re=600,000, M=0.08, $n_{crit,clean}$=9.0, $n_{crit,dirty}$=2.0

Figure 6.16: $C_d - \alpha$ curve for a clean and dirty airfoil, Re=600,000, M=0.08, $n_{crit,clean}$=9.0, $n_{crit,dirty}$=2.0

Figures 6.15 and 6.16 shows both the lift and drag coefficient of the airfoil for a clean and dirty airfoil. For the dirty airfoil the forced transition is applied and $n_{crit,dirty} = 2.0$. As can be seen there is a small difference in lift and $C_{l_{max}}$ remains almost unchanged. What is important to mention is that the drag coefficient with zero lift is larger. The drag coefficient is larger for angles of attack smaller than the stall angle.

Wing-fuselage interaction

In recent years there has been much research into the wing-fuselage interaction for many types of aircraft. The effect of this is generally large because the ratio between the surface area of the fuselage and wing is often different compared to an RPAS. For an RPAS, the influence of the fuselage is smaller than that of civil aviation due to the relative small size of the fuselage in proportion to the wing.

Due to the presence of a fuselage, the lift distribution of the model alters. Especially at the location of the fuselage the local lift will decrease. To compensate for this effect, there is a difference between the total wing span and the pure wing span. The total wing span b, is the wing span of the total RPAS including wing and fuselage. The pure wing span b^* is the wing span of the wing. The wing is therefore designed with the pure wing span. However the most reliable approach is to carry out a wing tunnel experiment that is able to visualise the wing-fuselage interaction, this is left as a recommendation for further research.

6.8 Verification and validation

For calculating the aerodynamic properties of the concepts using a wing configuration the analysis tool XFLR5 is used. With this tool airfoils and wings can be analysed. For the wing design and analysis the lifting line theory, vortex lattice method, and 3D panel method are used [25]. Although such a tool may not be set as a true estimate for the aerodynamic properties, with respect to verification the program could be regarded as verified because the model has been confirmed. XFLR5 can not be assumed as a true value for the physical reality as it is not based on a computational fluid dynamics model, which is much more accurate for physical phenomena. Therefore the estimations which were made with XFLR5 should be validated before assuming them accurate enough.

A similar NACA 5-digit airfoil is selected for validation, since experimental windtunnel data for the chosen NACA 22115 airfoil was not available. The data points from NACA are extracted from the graphs in Appendix B and are displayed by circles in graphs 6.17a until 6.17c. Although the airfoil and Mach number are similar to the previously computed cases, it is noted that the Reynolds number for this experiment was significantly higher.

The computed value using data from XFLR5 is done in the same manner as before and is displayed by the dashed line in red in figures 6.17a through 6.17c. The approximation for this similar airfoil approaches the experimental values, denoted by magenta circles, with little error. However, one has to note that there is a

slight overestimation of performance for the calculated 3D values. This is shown in a minute addition in lift.

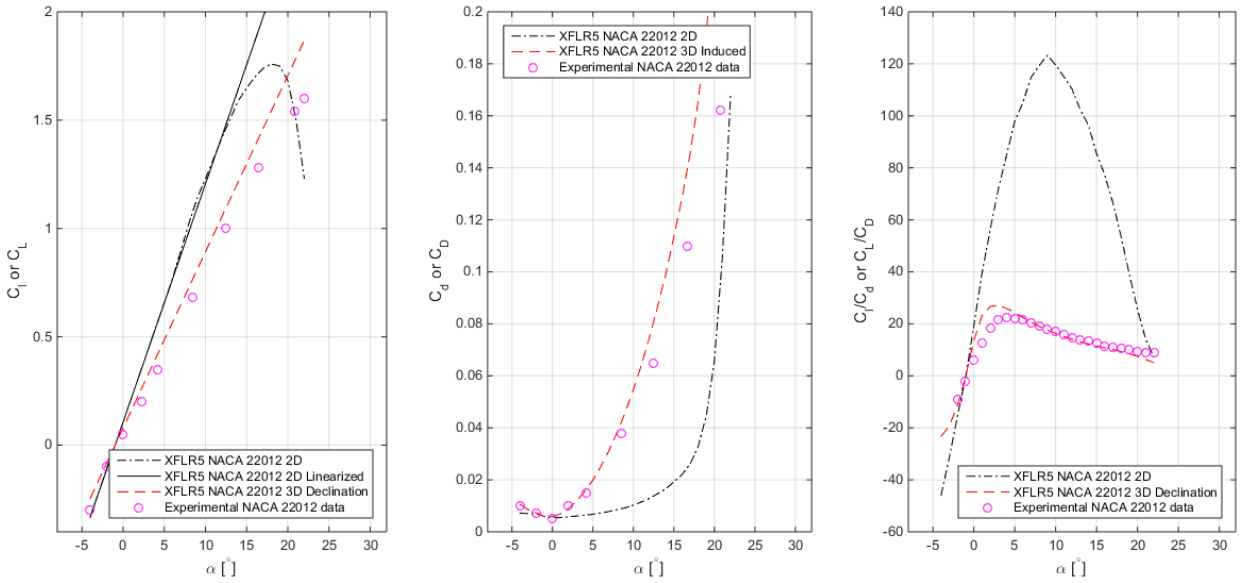

(a) Lift coefficient (b) Drag coefficient (c) Lift-to-drag ratio

Figure 6.17: NACA 22012 for Re=3,150,000, M=0.06, A=6

Before the data acquired from XFLR5 can be considered validated, one also has to analyse lower Reynolds numbers. To this extend, an airfoil is chosen with similar thickness to the chosen NACA 22115. The comparison is displayed using similar lines and symbols for experimental and computed data. The acquired data points are extracted from the graphs in Appendix B.

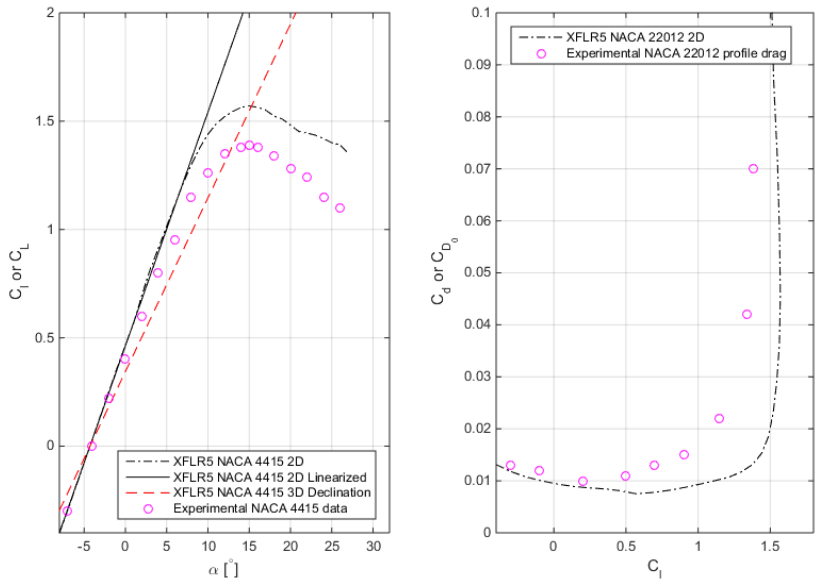

(a) Lift coefficient (b) Lift-to-drag ratio

Figure 6.18: NACA 4415 for Re=654,000, M=0.06, A=6

The lower Reynolds range seems to change the accuracy of the XFLR5 data. However, the estimate implies a conservative approach with respect to the approximated lift and a too low drag. Therefore we might expect a higher drag than previously estimated.

In this design stage XFLR5 is used for preliminary estimations, which are used for further design and analysis. In the later stage the CFD simulation should be validated. For validation a scale model could be tested in a wind tunnel. This data should then be compared with the CFD data.

7 Stability & Control

In this section the stability and control of the RPAS are elaborated upon. First the static longitudinal stability is figured out, which is then used to determine the centre of gravity limit and the overall location of the aerodynamic centre. After that the control surfaces of the RPAS are sized. All inputs and outputs used throughout the chapter are given in table 7.1.

Table 7.1: Inputs and outputs for stability and control

Parameter	Value	Unit	Input	Output	Comments	Source/Destination
S	1.1	$[m^2]$	X		Wing area	Aerodynamics
b	3.57	$[m]$	X		Wing span	Aerodynamics
λ	0.35	[-]	X		Taper ratio	Aerodynamics
c_r	0.494	$[m]$	X	X	Root Chord	Aerodynamics
c_t	0.173	$[m]$	X	X	Tip Chord	Aerodynamics
Λ	25	$[°]$		X	Sweep	Aerodynamics, Structures
I_{xx}	5.036	$[m^4]$	X		Moment of Inertia about X-axis	Structures
I_{zz}	6.042	$[m^4]$	X		Moment of Inertia about Z-axis	Structures
$c.g.$	0.12	$[m]$		X	Required location of centre of gravity	Structures
m	18	$[kg]$	X		Mass	Structures
I_{zz}	-	$[kgm^2]$	X		Mass moment of inertia about Z-axis	Structures
M_{roll}	21.2	$[Nm]$		X	Rolling moment about the X-axis	Aerodynamics
V_a	28	$[m/s]$	X		Airspeed	Aerodynamics
V_d	42	$[m/s]$	X		Dive speed	Structures

7.1 Static stability

In this section an analysis is done on the static longitudinal stability of the RPAS. The results of the analysis will give constraints for the centre of gravity location.

7.1.1 Static longitudinal stability

To analyse static longitudinal stability, a model has been made. In figure 7.1 the model is shown of the RPAS reduced to the most significant influences on stability. For this analysis only the vertical forces acting on the wing are considered. The horizontal forces, thrust and drag, are assumed to have sufficiently small arms with respect to the centre of gravity of the flying wing to be negligible in this analysis.

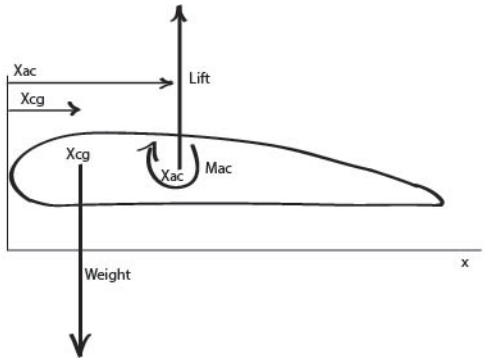

Figure 7.1: Static stability of the flying wing

The flying wing needs to have its aerodynamic centre (a.c.) behind the centre of gravity (c.g.) for longitudinal stability, as explained in section 6.2. In order to be able to position the a.c. behind the c.g. and have a moment equilibrium, it is necessary that the flying wing has a positive pitching moment (pitch up) about its a.c., as is drawn in figure 7.1. The methods to generate such a positive pitching moment for the flying wing, and which method is chosen, will now be expanded on.

7.1.2 Moment coefficient of wing

Two main methods are considered for generating the required positive moment of the flying wing. The first of these methods is adapting the wing profile itself to create an inherent positive moment. The second of these methods is finding an appropriate combination of wing sweep and wing washout.

Positive moment wing profile
The second method for generating the positive moment is by choosing a wing profile with an inherently positive pitching moment around its aerodynamic centre. This way, effectively no sweep or washout is required to generate the positive pitching moment. This will be beneficial for the effectiveness of the lift generation of the wing. Typically this requirement on the used airfoil means that a reflex airfoil is required. Reflex airfoils generate most of its lift at the leading edge, and not so much lift at the trailing edge, such that the positive moment is created.

Wing sweep and wing washout
If a wing profile is chosen that does not have an inherently positive pitching moment around its a.c., a combination of wing sweep and wash out can still be used to generate the required pitch up moment for the entire flying wing. The wings will be swept back, and towards the tip of the airfoil, the wing will twist downwards. Effectively, the angle of attack of the wing at the tip will be lower than the angle of attack of the root. The diminished lift at the tip, which is behind the c.g. due to sweep, causes the required pitch up moment of the flying wing.

Chosen method
After discussions with the aerodynamics and structures department, the conclusion was made that a positive moment wing profile is chosen, due to the fact that it is more easily manufactured resulting in a cheaper design. The design of this profile will be done by the aerodynamics department.

7.1.3 Determining the aerodynamic centre

Now that it is known that the wing profile will have a positive moment, it is important to start looking into the exact location of the aerodynamic centre. This information is important for the structures department, as the structures department must make sure that the centre of gravity is sufficiently ahead of the aerodynamic centre.

The aerodynamic centre is dependent on the wing sweep, wing planform and the airfoil of the wing. The airfoil and planform of the wing are given by the aerodynamics department, as can be found in section 6. The only parameter remaining is the sweep. The sweep is initially taken from the reference flying wings as found in appendix A, and determined to be 25 °. The stability requirements can be met with this amount of sweep, as explained in section 7.4.2, and the structures and aerodynamics department confirmed that the amount of sweep is attainable.

To determine the location of the aerodynamic centre, a numerical method is produced. Then this numerical method is verified using an analytical method. When the location of the a.c. is known, the limit for the c.g. is determined.

Numerical Method
First, the wing was divided into n sections, using the wingspan given for the wing planform. Then, using the taper ratio, λ, and the wing span, b, the local chord over the wing is calculated. The running variable y is used to indicate the position on the wing. This is done by using equation 7.1.1 and can be seen in figure 7.2. The parameters used are given in table 7.2.

$$c_i = \frac{2S}{(1+\lambda)b} \cdot (1 - \frac{2(1-\lambda)}{b} \cdot y_i) \tag{7.1.1}$$

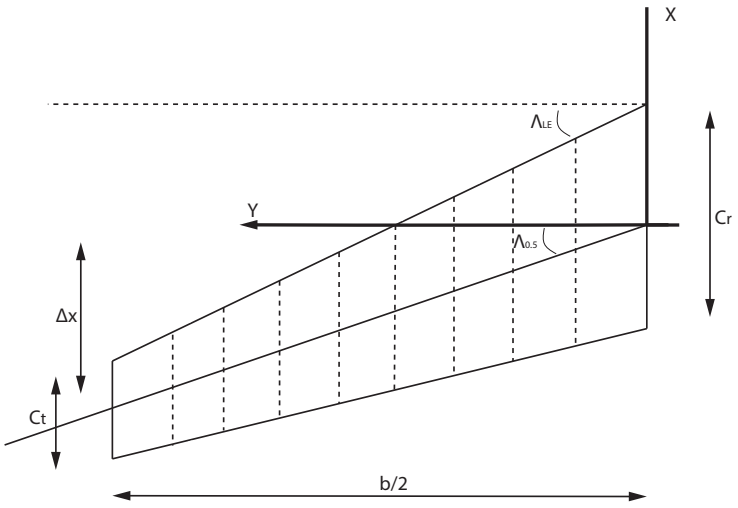

Figure 7.2: Visualization of numerical method

Table 7.2: Parameters in equation 7.1.1

Parameter	Unit	Comments	
S	1.1	$[m^2]$	Wing span
λ	0.35	[-]	Taper ratio
b	3.57	$[m]$	wing span
y_i	-	$[m]$	y location of wing section i
c_i	-	$[m]$	chord length at wing section i

For each section on the wing, the local aerodynamic centre is known, because it is dependent on the wing profile. Using this fact, the aerodynamic centre for the whole wing can be calculated.

Due to the tapering of the wing, the wing sweep changes depending on what chordwise location is chosen to define the wing sweep at. To be able to calculate the aerodynamic centre for the whole wing, an equation has to be made that relates the half chord wing sweep to a sweep on any chordwise position. The half-chord sweep is taken as the central wing sweep, and the other wing sweeps are defined with respect to this point. The derivation is done in several steps. The first step is finding a relationship between the leading edge sweep and the half chord sweep, as given by equation 7.1.2. As a reference, figure 7.2 can be used.

$$\Delta x = \frac{b}{2} \cdot tan(\Lambda_{0.5})$$

$$\Lambda_{LE} = tan^{-1}\left(\frac{b \cdot tan(\Lambda_{0.5}) + \frac{1}{2}c_r - \frac{1}{2}c_t}{\frac{b}{2}}\right) \tag{7.1.2}$$

Now that the relation between the leading edge sweep and half chord sweep is known, the variation of the sweep throughout the wing may be computed by noticing that it varies linearly over the wing's chord. The relationship for computing the sweep at a distance x from the half chord is given by equation 7.1.3.

$$\Lambda_x = \Lambda_{0.5} + \frac{\Lambda_{LE} - \Lambda_{0.5}}{\frac{1}{2}c_r} \cdot x$$

$$\Lambda_x = \Lambda_{0.5} + \frac{tan^{-1}\left(\frac{L \cdot tan(\Lambda_{0.5}) + \frac{1}{2}c_r - \frac{1}{2}c_t}{\frac{b}{2}}\right) - \Lambda_{0.5}}{\frac{1}{2}c_r} \cdot x \tag{7.1.3}$$

In equation 7.1.3, the running variable is x. It is defined to be the distance from the half-chord of the wing, as expressed as a portion of the root chord multiplied by the root chord. For example, the leading edge sweep may be obtained by filling in $0.5 \cdot c_r$ for x. All the different sweeps are indicated by Λ.

Knowing the transformation of sweep angles across the chord of the wing, the numerical method for determining the aerodynamic centre may be computed. As a reference frame, figure 7.2 is used.

The calculation of the aerodynamic centre is done by an area-weighted average of the individual aerodynamic centres for the numerical sections of the wing. This is represented by equation 7.1.4.

$$ac = \frac{ac_1 \cdot A_1 + ac_2 \cdot A_2 + ... + ac_n \cdot A_n}{\sum_i A_i} \tag{7.1.4}$$

An equation may be established for all the location of the aerodynamic centres, measured from the trailing edge of the root of the wing. For this, the sweep will be used at the aerodynamic centre of the wing profile. For this, equation 7.1.3 may be used to determine this sweep. The equations for the aerodynamic centre show a clear pattern, as shown by equation 7.1.5.

$$\begin{aligned} ac_1 &= ac_1 \\ ac_2 &= ac_1 - \Delta y \cdot tan(\Lambda_{ac_1}) \\ ac_3 &= ac_2 - \Delta y \cdot tan(\Lambda_{ac_1}) = ac_1 - 2\Delta y \cdot tan(\Lambda_{ac_1}) \\ &\cdot \\ &\cdot \\ ac_n &= ac_1 - (n-1)\Delta y \cdot tan(\Lambda_{ac_1}) \end{aligned} \tag{7.1.5}$$

The pattern may be substituted into equation 7.1.4 to find the total aerodynamic centre of the wing, as given in equation 7.1.6. Consecutively the aerodynamic stability of the entire wing can be calculated by numerically dividing the wing into n sections, and applying the equations mentioned in this section.

$$\begin{aligned} ac &= \frac{ac_1 \cdot A_1 + (ac_1 - \Delta y \cdot tan(\Lambda_{ac_1})) \cdot A_2 + ... + (ac_1 - (n-1)\Delta y \cdot tan(\Lambda_{ac_1})) \cdot A_n}{\sum_i A_i} \\ &= \frac{ac_1 \cdot \sum_i A_i}{\sum_i A_i} - \frac{\Delta y \cdot tan(\Lambda_{ac_1}) \cdot A_2 + ... + (n-1)\Delta y \cdot tan(\Lambda_{ac_1}) \cdot A_n}{\sum_i A_i} \\ &= ac_1 - (\Delta y \cdot tan(\Lambda_{ac_1})) \cdot \frac{A_2 + 2 \cdot A_3 + ... + (n-1) \cdot A_n}{\sum_i A_i} \end{aligned} \tag{7.1.6}$$

Table 7.3: Inputs for equation 7.1.4 and 7.1.6.

Input parameter	Value	Unit	Comments
ac_1	0.3705	$[m]$	Aerodynamic centre of section at root chord
Δy	-	$[m]$	Distance between numerical sections
A_n	-	$[m^2]$	Area of section n
Λ_{ac1}	22.6	[°]	Sweep angle at a.c. of the root

Analytical method

As a verification method, another way of calculating the aerodynamic centre was used. This was done by using equation 7.1.7, which is found in [26].

$$MAC = \frac{2}{3} c_r \cdot \frac{1 + \lambda + \lambda^2}{1 + \lambda} \tag{7.1.7}$$

Table 7.4: Basis Parameters for optimal C_L/C_D for NACA 22115

Input parameter	Value	Unit	Comments
c_r	0.494	$[m]$	Root chord
λ	0.35	[-]	Taper ratio
MAC	0.3591	$[m]$	Mean Aerodynamic chord

This equation is used to calculate the mean aerodynamic chord. The aerodynamic centre of this chord is the aerodynamic centre for the whole wing. The numerical method presented in the previous section is then used to find the distance to the aerodynamic centre for this chord length.

Results
The two methods for calculating the aerodynamic centre prove to be almost the same, with differences less than 0.1%. This can be seen in figure 7.3, where for the wing planform the location of the aerodynamic centre is plotted against the wing sweep.

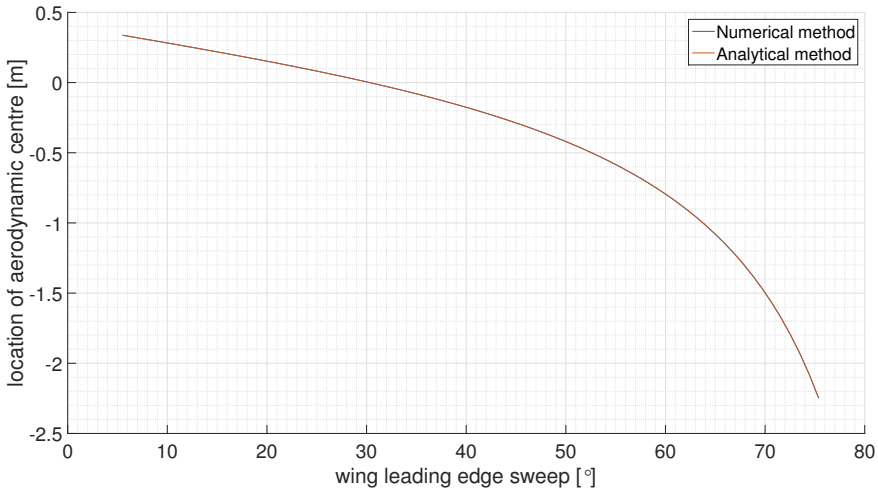

Figure 7.3: Location of aerodynamic centre vs wing half chord sweep

With the leading edge sweep angle of 25°, the location of the a.c. is 0.0819 m from the trailing edge. Using a typical value for the static margin, 10% of the mean aerodynamic chord [27], the location of the centre of gravity should be at least 0.12 m ahead of the trailing edge of the root chord. This value is handed to the structures department to comply with.

7.2 RPAS classification

Now that the static longitudinal stability of the RPAS has been covered, it is important to consider aspects of its dynamic stability and control. In order to consider these aspects, it is important to first determine exactly what type of aircraft the RPAS is considered to be, what type of mission it flies, and what level of flying qualities it should adhere to.

The RPAS will be classified according to the method specified in [28]. The RPAS may classified as a Class I aircraft, which means it is light and small. Furthermore, it is set to be in flight category A, which consists of *"Those nonterminal Flight Phases that require rapid maneuvering, precision tracking, or precise flight-path control..."*. [28] Lastly, the RPAS shall have level 1 flying qualities, which means that the flying qualities are *"clearly adequate for the mission Flight Phase"*. [28]

The classification of the RPAS will ultimately lead to constraints with respect to its dynamic behaviour, which can be used for sizing of the winglets and control surfaces in the following sections.

7.3 Winglet sizing

To ensure lateral stability for the flying wing, winglets are a necessity. The sizing and airfoil shape of these winglets has significant influence on the stability of the RPAS. First the airfoil shape for the winglets will be determined. After that the appropriate sizing and winglet planform will be given.

7.3.1 Winglet Airfoil

To determine an appropriate airfoil, a few requirements have been set.

- The airfoil shall have minimum drag at 0° angle of attack
- The airfoil shall produce no lift at 0° angle of attack

The winglets should minimise the amount of drag contribution to keep the flying wing design aerodynamically efficient. To fulfil the requirement of producing no lift at a 0° angle of attack, a symmetric airfoil is required. For symmetric airfoils, the NACA 4-digit series is extensively used. The only variable property of the NACA 4-digit series when designing an symmetric airfoil is the thickness at 30% chord, which therefore needs to be determined.

To make a decision on the airfoil thickness, the effect of the thickness on the airfoil properties have to be determined. In XFLR5 the C_l/α and C_l/C_d curves of the wing profiles with 10%, 12%, 14%, and 16% chord thickness are plotted.

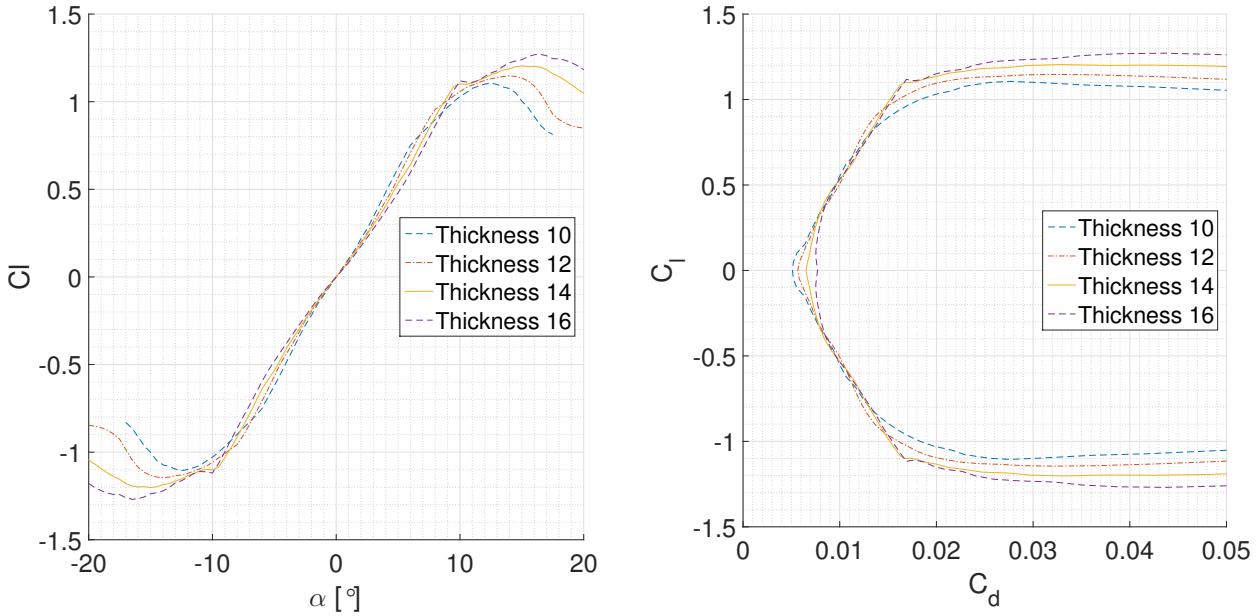

Figure 7.4: $C_l - \alpha$ and C_l/C_d curve of the symmetric airfoil with varying thickness

As can be seen in figure 7.4, most profiles provide the least drag at 0 angle of attack. This can be seen in the characteristic drag bucket presented in the C_l/C_d graph. All profiles have lowest drag at 0° angle of attack, except for the profile with 16% thickness, which is why this airfoil eliminated from the trade-off.

The profile with 10% thickness has a very rapid increase in drag at maximum lift coefficient, as can be seen in the C_l/C_d graph. When looking at the $C_l - \alpha$ graph, the maximum lift coefficient is also lower than the other profiles. Because it is important to have the wingtip profile stall as late as possible, and because a low increase in drag for an increase of angle of attack is preferred, the 10% thickness airfoil is deemed insufficient for the wingtip.

Only the 12% and 14% thickness profiles remain as a choice. As can be seen in the $C_l - \alpha$ graph, the 12% thickness profile has a lower $C_{L_{max}}$ than the 14% thickness profile. Because stall has to be delayed as much as possible, while keeping the drag at a minimum for 0° angle of attack, the profile with 14% thickness is selected. The resulting profile is a NACA 0014 airfoil.

When it shows in later stages, for example through wind tunnel tests, that the winglets can easily cope with the disturbances, the 12% thickness profile can be selected to reduce the production of drag.

7.3.2 Winglet planform

To determine the winglet planform, a MATLAB model was created to asses the lateral stability. This was then used to determine the damping coefficient and natural frequency as a function of winglet area. Using the flying qualities as requirements resulted in constrains for the damping coefficient and natural frequency of the RPAS.

7.3.3 MATLAB model

The flying wing model was first analysed in XFLR5 for all the stability modes. It showed that the Dutch roll was the most problematic eigenmode in terms of frequency and damping. Using [29], a reduced state-space

system was found, as can be seen in figure 7.3.1.

$$\begin{bmatrix} C_{Y_\beta} - 2\mu_b D_b & -4\mu_b \\ C_{n_\beta} & C_{n_r} - 4\mu_b {K_Z}^2 D_b \end{bmatrix} \begin{bmatrix} \beta \\ \frac{rb}{2V} \end{bmatrix} = \vec{0} \tag{7.3.1}$$

This matrix contains coefficients that describe the motion of an aircraft during Dutch roll. These coefficients have to be approximated for the flying wing. All the coefficients and descriptions can be found in table 7.5.

Table 7.5: Stability coefficients needed for Dutch roll

Parameter	Description
C_{Y_β}	The derivative of the sideforce with a change in angle of sideslip
μ_b	Dimensionless mass coefficient
D_b	Dimensionless time derivative
C_{n_β}	Change in moment around Z-axis with respect to change in angle of sideslip
C_{n_r}	Change in moment around Z-axis with respect to a yaw rate
K_z^2	Dimensionless mass moment of inertia about Z-axis
β	Angle of sideslip
$\frac{rb}{2V}$	dimensionless yaw rate

Determination of C_{Y_β}
The C_{Y_β} of the RPAS is approximated by only considering the contribution of the vertical wing tips of the RPAS, since these will give the largest contribution. [29] The equation for obtaining C_{Y_β} is given in equation 7.3.2. The parameters are summarised in table 7.6.

$$C_{Y_\beta} = C_{Y_\alpha} \frac{S_v}{S} \tag{7.3.2}$$

With this approximation, the C_{Y_β} is simply equal to the three dimensional C_{L_α} of the wing tip, multiplied with the wing tip surface area ratio. This value was approximated by determining the 2D C_{l_α} first with XFLR5. Then, using equation 6.3.1, the approximated 3D C_{L_α} was calculated.

Determination of μ_b
The μ_b of the RPAS is the dimensionless mass coefficient. Using [29, p. 109], this coefficient is defined as in equation 7.3.3. The parameters in equation 7.3.3, their values, and the final outcome are given in table 7.6.

$$\mu_b = \frac{m}{\rho S b} \tag{7.3.3}$$

Determination of C_{n_β}
The C_{n_β} can be computed using equation 7.3.4, found in [29, p. 205].

$$C_{n_\beta} = C_{Y_\alpha} \left(1 - \frac{d\sigma}{d\beta}\right) \left(\frac{V_v}{V}\right) \frac{S_v l_v}{S b} \tag{7.3.4}$$

The terms modelling the downwash and decrease in airspeed at the vertical wingtips are assumed to be zero, because these effects are minimal for a flying wing configuration. The equation can therefore be reduced to equation 7.3.5. Table 7.6 gives all the values and the coefficients in equation 7.3.5. Note that table 7.6 does not give any value for the wing tip surface area, S_v. This is because this surface area will be the running variable in the following computations, and will be sized in these computations.

$$C_{n_\beta} = C_{Y_\alpha} \frac{S_v l_v}{S b} \tag{7.3.5}$$

Determination of C_{n_r}
The C_{n_r} can be computed using equation 7.3.6. [29]. The effect only considers the contribution by the wing tips, because these have a higher impact than the fuselage and engines. The parameters in equation 7.3.6, their values, and the final outcome are given in table 7.6.

$$C_{n_r} = -2 C_{Y_\alpha} \frac{S_v l_v}{S b} \frac{l_v}{b} \tag{7.3.6}$$

Determination of K_z^2
The K_z^2 is the dimensionless moment of inertia, and is simply defined as given in equation 7.3.7. [29]. The parameters in equation 7.3.7, their values, and the final outcome are given in table 7.6.

$$K_Z^2 = \frac{I_{zz}}{mb^2} \tag{7.3.7}$$

Table 7.6: Inputs and outputs for equations 7.3.3 - 7.3.7

Parameter	Value	Unit	Input	Output	Comments
μ_b	4.04	[-]		X	Dimensionless mass coefficient
m	18	$[kg]$	X		Mass
ρ	1.225	$[kg/m^3]$	X		Air density
S	1.1	$[m^2]$	X		Wing planform surface area
b	3.57	$[m]$	X		Total wing span
C_{n_β}	0.13	$[\ 1/rad\ ]$		X	Yaw response to sideslip
C_{Y_α}	3.609	$[1/rad]$	X		Sideforce response to angle of attack change for the vertical wingtip
$d\sigma/d\beta$	0	[-]	X		Sidewash in air flow at wingtips
V_v/V	1	[-]	X		Speed ratio at vertical wingtips
S_v	-	$[m^2]$	X		Surface area wingtips
l_v	0.439	$[m]$	X		Distance of aerodynamic centre of wing tips to centre of gravity
C_{n_r}	-0.0348	$[1/rad/s]$		X	Yaw response to yaw rate
K_Z^2	0.0308	[-]		X	Dimensionless mass moment of inertia about z-axis
I_{zz}	6.04	[-]	X		Mass moment of inertia about z-axis
C_{n_r}	-0.0068	$[1/rad/s]$		X	Yaw response to yaw rate

Results
In this section the results of the previously modelled state-space system will be given. The goal is to determine the state-space systems eigenvalues, so that the damping coefficient and natural frequency can be determined. This is done by solving the state-space system using the characteristic equation of the state-space system. This equation is given in 7.3.8.

$$A\lambda^2 + B\lambda + C = 0 \tag{7.3.8}$$

The coefficients for the characteristic equation are determined by taking the determinant of the state-space matrix, and equating it to zero. This results in the coefficients as seen in 7.3.9. The parameters are given in table 7.6.

$$\begin{aligned} A &= 8\mu_b^2 K_z^2 \\ B &= -2\mu_b(C_{n_r} + 2K_z^2 C_{y_\beta}) \\ C &= 4\mu_b C_{n_\beta} + C_{Y_\beta} C_{n_r} \end{aligned} \tag{7.3.9}$$

Using these coefficients in combinations with equation 7.3.10 and 7.3.11 the damping coefficient (ξ) and natural frequency (ω) can be determined. These equations are obtained from [29].

$$\xi = \frac{B}{2\sqrt{AC}} \tag{7.3.10}$$

$$\omega = \frac{V}{b}\sqrt{\frac{C}{A}} \tag{7.3.11}$$

The results from these equations are plotted against a variation of wing tip surface resulting in the following plots, as seen in figure 7.5.

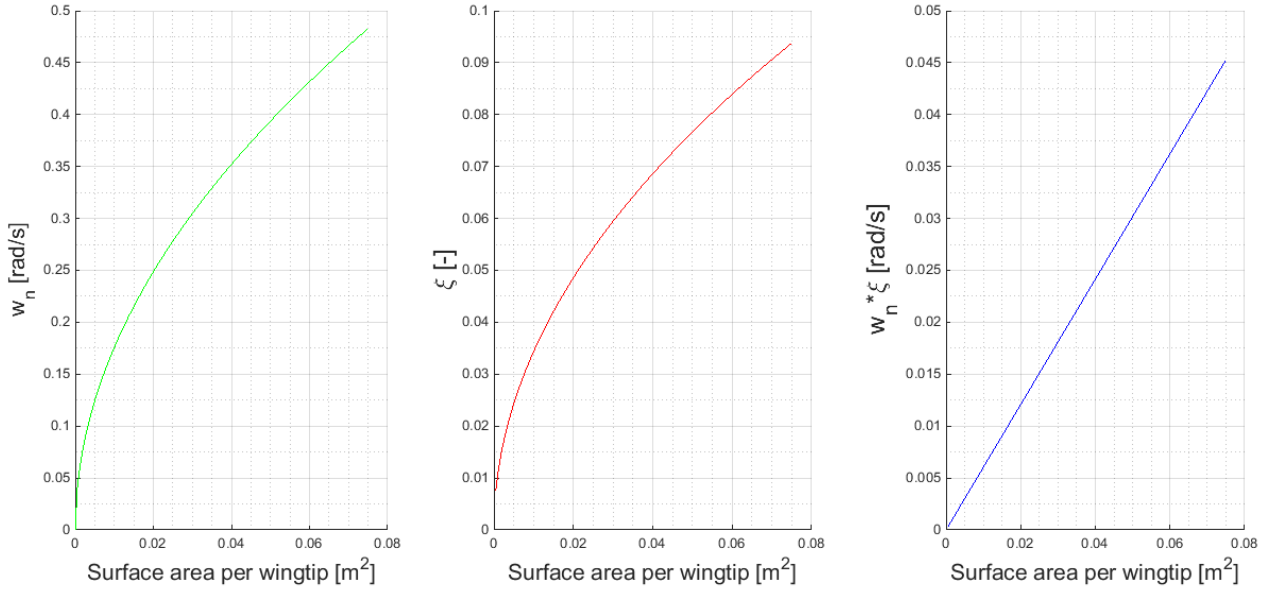

Figure 7.5: Results stability analysis of the wingtip

Using the plots, an estimate of the required wing tip area can be made. This was done by using the classification described in section 7.2. However, to have level 1 flying qualities without any artificial stabilisation is a very stringent requirement. Even adhering to level 2 flying qualities would result in wingtips that are unrealistically large. For this reason, the wing tips will be designed for level 3 flying qualities. However, because the goal was to obtain level 1 flying qualities, it will instead be investigated whether this can be achieved with artificial yaw damping, as is discussed in section 7.4.2. The results are that each wing tip needs a surface area of 0.05 m^2.

7.4 Control surfaces

To be able to control the flying wing, control surfaces have to be implemented into the design. For pitch and roll, elevons along the trailing edge of the RPAS wing will placed. For yaw control, rudders are applied to the winglets of the flying wing. Due to the fact that in general flying wings are difficult to stabilise, and that the Reynolds number is lower than conventional aircraft, control surfaces on flying wings have to be relatively bigger than conventional standards. [30]. This section will be split into a section that is concerned with the sizing of the elevons, and a section that concerns the sizing of the rudders.

7.4.1 Elevon sizing

A program will be coded in MATLAB to aid in the sizing of the elevons. The program will ultimately make use of the fact that for proper control of the RPAS, a certain amount of roll angle should be attainable in a given amount of time.

A rear view schematic of the RPAS, that describes the situation presented in this section is given in figure 7.6. The symbols used in this figure are summarised in table 7.7.

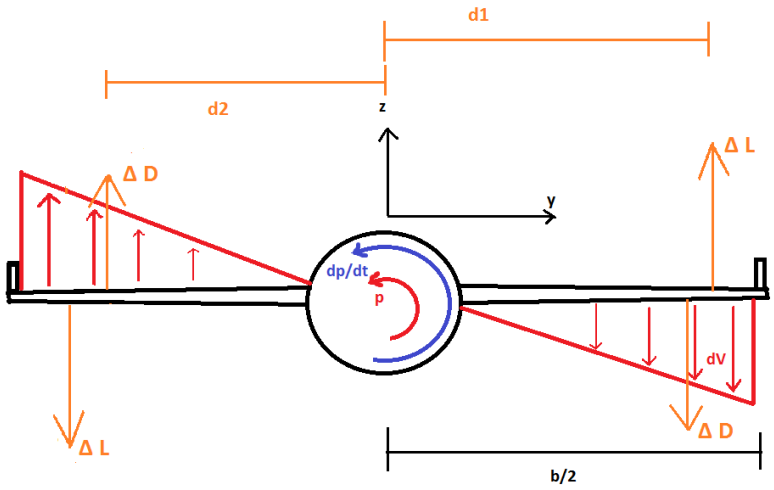

Figure 7.6: Schematic depiction of forces, velocities and accelerations during roll

Table 7.7: Symbols used in figure 7.6

Input parameter	Unit	Comments
p	$[rad/s]$	Roll rate
dp/dt	$[rad/s^2]$	Roll acceleration
ΔL	$[N]$	Additional lift generated by elevon
ΔD	$[N]$	Additional vertical drag generated by rolling aircraft
$d1$	$[m]$	Distance from acting point of additional lift to centre of gravity of RPAS
$d2$	$[m]$	Distance from acting point of additional drag to centre of gravity of RPAS
dV	$[m/s]$	Velocity field generated by rolling of the RPAS.

The basic idea behind the rolling motion of the RPAS is that when the RPAS will start rolling, the wings will experience a vertical velocity. This vertical velocity is dependent on the distance of a point on the wing from the centre of gravity, as given by equation 7.4.1.

$$dV = p \cdot d \tag{7.4.1}$$

Where d is an arbitrary distance away from the centre of gravity of the RPAS.

Using vector addition, this additional vertical velocity will, together with the forward velocity of the RPAS, generate an increase or decrease in the angle of attack of the RPAS. This increase or decrease in angle of attack will cause the wings to generate a lift force to oppose the rolling motion of the RPAS. After some time this opposing lift force will be equal to the additional lift generated by the elevons, causing the roll rate to stop accelerating and becoming constant. A second effect opposing the rolling motion of the RPAS is the additional drag generated, which will also be considered. [29]

A simplified differential equation, which models the roll rates and accelerations of an aircraft is given by equation 7.4.2. This equation is simplified because it assumes the Earth is flat, the Earth is non-rotating, and that there is complete decoupling from the rolling mode of the RPAS with the other modes of the RPAS (such as yaw). In reality these assumptions don not hold. For the RPAS, the flat, non-rotating Earth introduces reasonably little error, because the velocities attained by the RPAS are low. [29]. The assumption that roll is decoupled from other modes of the RPAS does introduce some error, but this can only be solved by getting accurate predictions of all the stability parameters of the RPAS, for example through wind tunnel experiments on a scaled model of the RPAS.

$$\dot{p} = \frac{2\Delta L \cdot d_1 - 2\Delta D \cdot d_2}{I_{xx}} \tag{7.4.2}$$

I_{xx} in equation 7.4.2 is the mass moment of inertia about the X-axis of the RPAS, which is given by the structures department. The other variables are given in table 7.7.

Before expanding equation 7.4.2, it is necessary to obtain an equation for the chord distribution along the wing. This is given by equation 7.4.3. The variables are summarised in table 7.8.

$$c(y) = c_r - \frac{c_r - c_t}{\frac{b}{2}} \cdot y \tag{7.4.3}$$

Table 7.8: Symbols used in figure 7.6

Input parameter	Unit	Comments
$c(y)$	$[m]$	Chord at a distance y from the centre of gravity of the RPAS
c_r	$[m]$	Root chord of the wing
c_t	$[m]$	Tip chord of the wing
b	$[m]$	Wing span

The term $\Delta D \cdot d_2$ in equation 7.4.2 can now be expanded on, by using the theory of the additional vertical velocity experienced by the wing. The contribution from the additional lift force is worked out in equation 7.4.4. It consists of an integral over the length of the wing that computes the additional lift generated.

$$\begin{aligned}(\Delta D \cdot d_2)_{lift} &= \int_0^{\frac{b}{2}} C_{L_\alpha} \Delta\alpha(y) \cdot y \cdot \frac{1}{2}\rho V^2 \cdot c(y) \cdot dy \\ &= \int_0^{\frac{b}{2}} C_{L_\alpha} \frac{p \cdot \mathrm{y}}{V} \cdot \mathrm{y} \cdot \frac{1}{2}\rho V^2 \cdot \left(c_r - \frac{c_r - c_t}{\frac{b}{2}} y\right) \cdot dy \\ &= \frac{1}{192} C_{L_\alpha} p \cdot b^3 \cdot \rho V \cdot c_r + \frac{1}{64} C_{L_\alpha} p \cdot b^3 \cdot \rho V \cdot c_t \end{aligned} \tag{7.4.4}$$

Similarly, the contribution to $\Delta D \cdot d_2$ in equation 7.4.2 that is caused by the additional drag force is given by equation 7.4.5. The drag coefficient is approximated to be that of a flat two dimensional plate.

$$\begin{aligned}(\Delta D \cdot d2)_{drag} &= \int_0^{\frac{b}{2}} C_D \frac{1}{2}\rho V(y)^2 \cdot y \cdot c(y) dy \\ &= \int_0^{\frac{b}{2}} C_D \frac{1}{2}\rho (p \cdot y)^2 \cdot y \cdot \left(c_r - \frac{c_r - c_t}{\frac{b}{2}} y\right) dy \\ &= \frac{1}{640} C_D \cdot \rho \cdot p^2 \cdot b^4 \cdot c_r + \frac{1}{160} C_D \cdot \rho \cdot p^2 \cdot b^4 \cdot c_t \end{aligned} \tag{7.4.5}$$

Equations 7.4.4 and 7.4.5 may be substituted in equation 7.4.2 to obtain the final differential equation. This is given in equation 7.4.6. The newly introduced parameters are given in table 7.9.

$$\dot{p} = \frac{2\Delta L \cdot d_1 - 2\rho \cdot p^2 \cdot b^4 \cdot C_D \left(\frac{c_r}{640} + \frac{c_t}{160}\right) - 2C_{L_\alpha} p \cdot b^3 \cdot \rho V \left(\frac{c_r}{192} + \frac{c_t}{64}\right)}{I_{xx}} \tag{7.4.6}$$

Table 7.9: Symbols used in equation 7.4.6

Input parameter	Unit	Comments
C_{L_α}	[-]	Derivative of lift coefficient with respect to alpha
C_D	[-]	Drag coefficient of a two dimensional plate
$\Delta\alpha$	$[rad]$	Change in angle of attack
V	$[m/s]$	Airspeed
ρ	$[kg/m^3]$	Air density

It was decided to solve equation 7.4.6 numerically with a first order Runge-Kutta scheme. As an example, for a $\Delta L \cdot d_1$ of 5 Nm, the roll rate and roll angle are plotted in time. This is given in figure 7.7.

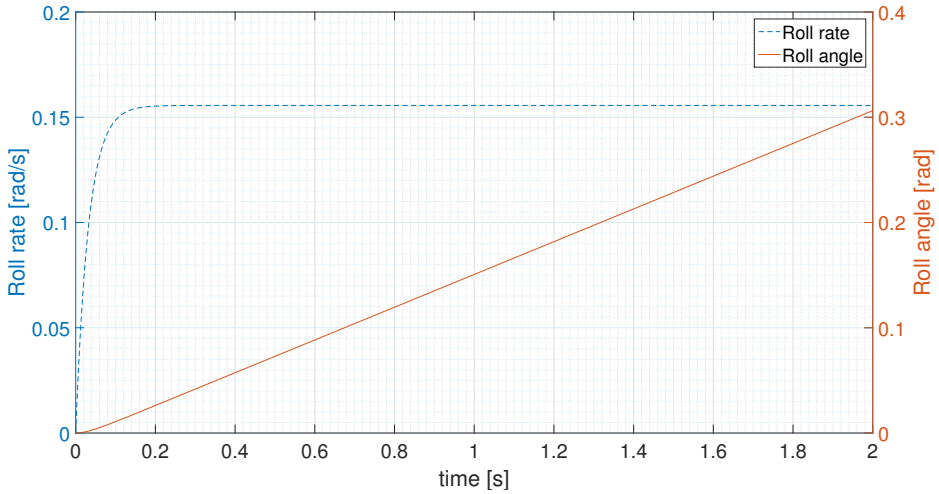

Figure 7.7: Roll rate and roll angle in time

An important parameter for lateral controllability of the RPAS is the time it takes for the RPAS to get to a 60 degree roll angle. [28] For a range of values of $\Delta L \cdot d_1$, the time it takes to get to a 60 degree angle is plotted. This is given in figure 7.8.

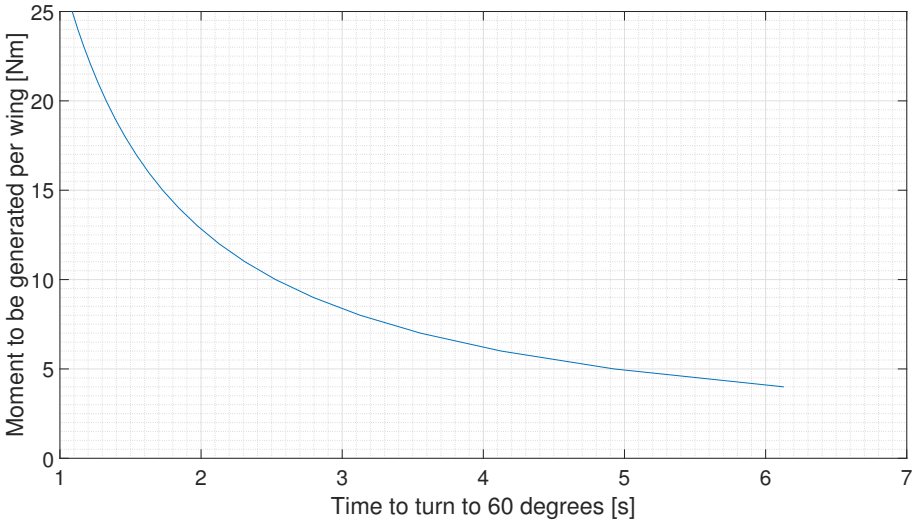

Figure 7.8: Time to roll to 60 degree angle vs moment generated

Using [28, p. 163], an appropriate time to roll can be determined. Using the qualification of the RPAS as determined in section 7.2, it becomes apparent that the RPAS is required to attain a roll angle of 60 degrees in 1.3 seconds. From figure 7.8 it becomes clear that the elevons must therefore generate a moment of 21.2 Nm. This result will be handed to the aerodynamics department as M_{roll}, such that they can size the dimensions of the elevons.

7.4.2 Rudder sizing

The rudder will mainly be implemented to counteract the jitter the RPAS shows in lateral direction. A state-space system is created of the simplified lateral equation of motion of the RPAS, as given in equation 7.3.1. The state-space model is implemented into MATLAB and the response of the RPAS is simulated to an initial input of 25° on the angle of sideslip. The dynamic response of the angle of sideslip and the yaw rate of the RPAS is given in figure 7.9.

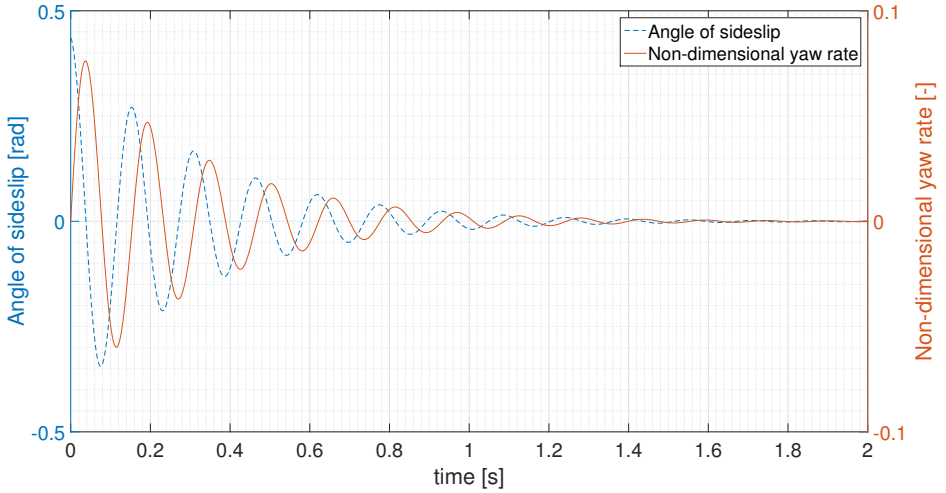

Figure 7.9: Simplified lateral response of the RPAS to a 25° input on angle of sideslip

Although the behaviour is stable, for proper control of the RPAS, this is not the behaviour that is desired for good quality images. For this reason, it is decided that the rudder shall provide active lateral damping to dampen the motion of the RPAS more quickly. To see the effect of the rudder, first the rudder size must be determined. A typical value of 20% of the wing tip chord will be reserved for the rudder. In order to make a model of the damper, the rudder effectiveness must be computed. To determine the rudder effectiveness a plot is made using XFLR5 that gives C_l of the winglet profile at different flap deflections. As can be seen in figure 7.10, the linear part of the curve can be found in between an angle of -10° and 10°. Approximating this with a linear regression a slope can be found. This slope reflects the $C_{Y_{\delta r}}$ coefficient needed, which is the rudder effectiveness.

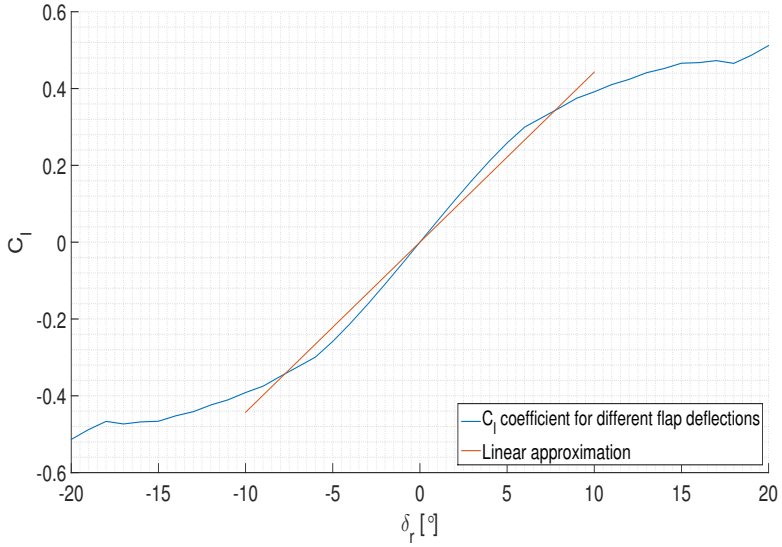

Figure 7.10: C_l curve with respect to flap deflection

Now that the rudder effectiveness is known, the yaw damper can be modeled. The effect of an example of such a damper is shown in figure 7.11. This damper uses the signal of the measured yaw rate of the RPAS and sends it back to the control system of the rudder in a closed loop. It can clearly be seen that the response of the RPAS improves greatly with such a damper, and therefore it is decided to implement a similar active control system.

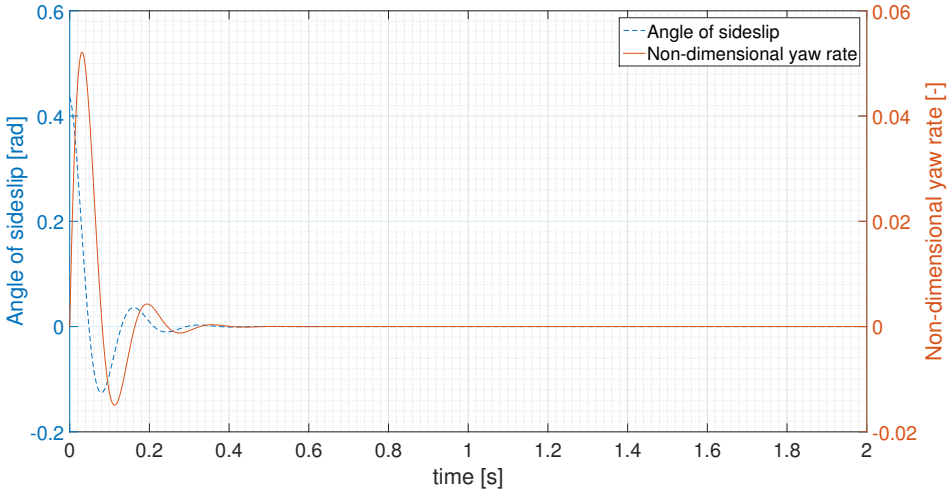

Figure 7.11: Simplified lateral response of the RPAS to a 25° input on angle of sideslip with active damping

7.5 Servo selection

Now that the control surfaces are discussed, the servos that will control these surfaces must be selected. This will be done by estimating the hinge moment acting on the control surfaces.

7.5.1 Rudder servo

For the estimation of the maximum hinge moment of the rudder, figure 7.10 is used, which estimates the change in lift coefficient due to a change in flap deflection. If it is assumed that the change in lift acts completely on the rudder, and that this change in lift acts on the quarter-chord point of the rudder itself, an estimation of the hinge moment about the front of the rudder can be made. Note that both the assumption that all of the change in lift acts on the rudder, and the assumption that the hinge is completely at the front of the rudder result in slight over estimations of the hinge moment. Furthermore, the C_l as depicted in figure 7.10 provides the two dimensional lift coefficients, which also results in an overestimation. This is favourable, because that means the servo selected to provide the hinge moment will surely be able to provide the required torque. The hinge moment may now be calculated using equation 7.5.1. The used coefficients and their values are given in table 7.10. Note that the hinge moment will be designed for the dive speed of the RPAS, as the hinge moment will be highest at this speed.

$$H_e = \Delta C_{l_{max}} \frac{1}{2} \rho V^2 S_{rudder} \cdot 0.25 \cdot c_{rudder} \tag{7.5.1}$$

Table 7.10: Inputs and outputs for equation 7.5.1

Parameter	Value	Unit	Input	Output	Comments
H_e	0.043	$[Nm]$		X	Hinge moment for rudder
$\Delta C_{l_{max}}$	0.51	[-]	X		Maximum change in lift coefficient for deflection of rudder
V	42	$[\frac{m}{s}]$	X		Maximum speed attained by RPAS
S_{rudder}	0.009	$[m^2]$	X		Surface area per rudder
c_{rudder}	0.173	$[m]$	X		chord length of rudder

With the computed hinge moment, a reference servo may be selected, which can be used in the mass and power budgets. However, because hinge moments are virtually impossible to estimate without the use of wind tunnel tests, it should be noted that the selection of this servo is subject to change. [31].

The chosen reference servo is the TGY-306G. [32] The specifications of this servo are summarised in table 7.11.

Table 7.11: Specifications for the TGY-306G servo

Parameter	Value	Unit
Mass	21	$[g]$
Voltage	4.8-6.0	$[V]$
Torque	24-30	$[Ncm]$
Operating speed	0.07-0.06	$[sec/60°]$

The rudders will both be controlled by a separate servo, which means a total of 2 servos of the type TGY-306G will be present to control the rudders.

7.5.2 Elevon servo

To estimate the maximum hinge moment of the elevon, the previous calculated needed roll moment is used. This value is determined in section 7.4.1. This resulted in a total needed elevon moment per elevon of $21.2Nm$ around the X-axis of the RPAS. The elevon parameters can be found in table 7.12. To calculate the lift produced on the elevon equation 7.5.2 is used.

$$L = \frac{M_{roll}}{d} \tag{7.5.2}$$

This results in a lift produced on the elevon of 17.5 N. Then using equation 7.5.3 the maximum hinge moment can be calculated.

$$H_e = 0.2 \cdot MAC \cdot L_e \tag{7.5.3}$$

The coefficients in equations 7.5.2 and 7.5.3 are given in table 7.12.

Table 7.12: Inputs and outputs for equation 7.5.1

Parameter	Value	Unit	Input	Output	Comments
H_e	0.2275	$[Nm]$		X	Hinge moment for elevon
d	1.2	$[m]$	X		Distance to elevon a.c.
M_{roll}	21.2	$[Nm]$	X		Produced moment around RPAS X-axis due to elevon deflection
MAC	0.052	$[m]$	X		Mean chord of the elevon
L_e	17.4	$[N]$		X	Lift produced due to elevon deflection

Using the resulting hinge moment a reference servo, the TGY-589MG [33], was selected. The specifications of this servo are shown in table 7.13.

Table 7.13: Specifications for the TGY-589MG servo

Parameter	Value	Unit
Mass	40	$[g]$
Voltage	6-7.4	$[V]$
Torque	63.7-78.5	$[Ncm]$
Operating speed	0.10-0.09	$[sec/60°]$

It was decided, for redundancy reasons, to split the elevon surfaces designed by aerodynamics into two and having them controlled by separate servos. This means there will be a total of 4 servos of the TGY-589MG type to control the elevons. During normal operation the split elevon surfaces get the same deflection. In case of failure of one of the elevons, controlability can still be ensured. However, due to the reduced amount of controlling surface the RPAS will be significantly less control able.

7.6 Verification and validation

Some of the methods used in this chapter require some verification and validation to prove that they work. These methods will be discussed in this section.

The first thing that will be validated are the stability parameters used for sizing the winglets. The stability parameters will be verified using the stability analysis method from XFLR5, which gives as an output the stability parameters. The results of the comparison are given in table 7.14. The values produce sufficiently low error to be considered verified. Of course, to get more accurate estimations of these parameters it is essential to do wind tunnel testing to validate and if necessary update the used parameters.

Table 7.14: Validation of stability parameters

Parameter	**Computed value**	**XFLR5 value**	**Error**
C_{Y_b}	-0.1936	-0.18067	6.7%
C_{n_b}	0.0257	0.02043	20.5%
C_{n_r}	-0.0068	-0.00777	-14.2 %

The method used for determining the moment required to be generated by the elevons used a simplified differential equation that models the rolling of the RPAS, including the roll damping. To verify that the roll damping is reasonable, the roll damping will be made non-dimensional, as defined in [29], and compared to a method of estimating the roll damping using the aspect ratio and taper ratio of the wing, as described in [34].

The non-dimensional roll damping obtained from the differential equation is -0.62. The non-dimensional roll damping obtained from the preliminary estimation in [34] is approximately -0.5. This is a difference of about 20%. Because the method in [34] is only preliminary, the difference is assumed to be small enough to be reasonable, and it does show that the order of magnitude of the calculation is correct. Furthermore, an overestimation of the roll damping will make sure that the elevons will still be capable of providing the required forces, whereas an underestimation would mean a degradation in real life performance. It is recommended to also validate the results of the roll damping with (scaled) wind tunnel testing.

8 Propulsion

In this chapter the selection of the engine for the RPAS will be discussed. To be able to choose the best suitable engine first the required power will be determined. For this power suitable engines will be searched for and a trade-off will be done. For the selected engine the dimensions of the required propeller will be determined. After this the vibration and noise pollution as well as sustainability will be discussed and finally verification and validation will be done.

8.1 Required propulsive power

In this section the required propulsive power is be calculated. This is done by using an iterative process, because the values of some of the parameters are not known exactly upfront. Due to changes in these parameters two iterations are performed which can be found below.

8.1.1 First iteration

The first step in the engine selection process is to make a plot of the required power versus the flight velocity. From this plot it can be determined what amount of power is needed to fly at a certain speed. To make the plot, equation 8.1.1 [35, p. 73] is used.

$$P_{req} = \frac{1}{2}\rho V^3 S C_{D0} + \frac{W^2}{\frac{1}{2}\rho V^2 S}\left(\frac{1}{\pi e A}\right) \tag{8.1.1}$$

By filling in the input data given in table 8.1 into equation 8.1.1 the power versus velocity plot can be made and is found in figure 8.1. In order to be able to start somewhere on designing the propulsion part of the Maritime Flyer, the parasitic drag obtained from XFLR5 in the very beginning of the detailed design process is used.

Table 8.1: Required Power Input and Output

Parameter	Value	Unit	Input	Output	Comments
C_{D0}	0.071	[-]	X		Parasitic drag from XFLR5
ρ	1.225	$[kg/m^3]$	X		Density
S	1.12	$[m^2]$	X		Wing area
W	176.6	$[N]$	X		Weight
π	3.1415	[-]	X		Pi
e	0.9	[-]	X		Oswald factor
A	9.96	[-]	X		Aspect ratio
V	[4 - 40]	$[m/s]$	X		Velocity range
P_{req}	2,097	$[W]$		X	Required power

From this graph it can be directly seen what power is required to fly at a certain velocity. For the flying wing the cruise speed is set to be 28 m/s and from the requirements it is defined that the RPAS should be able to operate with wind speeds of on average of 7 m/s. With equation 8.1.2, the required cruise speed in case of headwind is calculated. On base of this velocity and using figure 8.1 the required power is determined to be $P_{required}$ = 2,097 W.

$$V_{max} = V_{cruise} + V_{wind} = 28 + 7 = 35 m/s \tag{8.1.2}$$

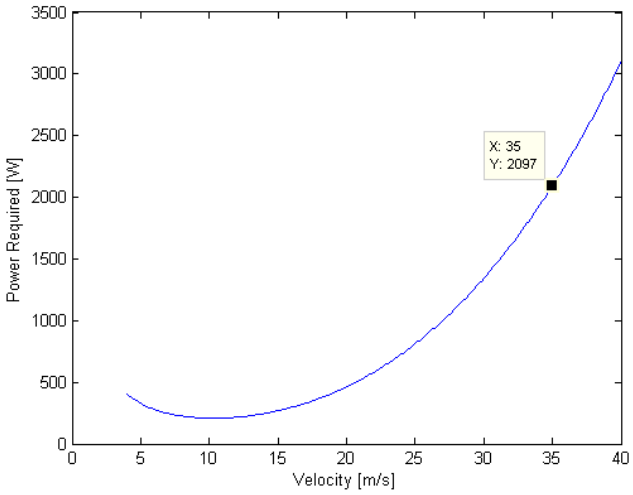

Figure 8.1: Power versus velocity for the first iteration

To choose an engine which can deliver the required power, the propulsive efficiency should be taken into account. From reference it can be found that at normal flight speeds a propulsive efficiency range of [0.85 - 0.9] is given [35, p. 357]. Taking into account that the efficiency could be low, the lowest possible efficiency was chosen, which is 0.85. Dividing the required power by this efficiency gives a power needed of 2,467 W. This is the power that the engine needs to provide before the thermal and propeller efficiency have been applied to it.

As a precaution, it is decided that a safety factor will be added to the power required. This is to ensure that the engine will produce enough power even if an error with the engine occurs or a design change occurs that negatively effects the required power. The value decided upon was 1.2. Deciding on this value was done by looking at the probability of the engine failing and the effects of reduced propulsive power. Internal combustion engines have been in use for more than 100 years [36, p. 29] and have been perfected to perform in their respective areas. It can therefore be assumed that the reliability of internal combustion engines is extremely high, and the probability of failure extremely low. This can be taken into account with the safety factor. As the probability is not completely zero, some amount of safety has to be taken into account. Alongside this, a reduction in propulsive power must be analysed for the safety factor. Looking at the graph in figure 8.1 and keeping in mind a stall velocity of 15 m/s, it can be seen that the power required to stay in flight is relatively low compared to cruise velocity power. This means that the safety factor needed is not that high. However it cannot be 1, and by noting that a twenty percent decrease in power will just allow the RPAS to fly at cruise speed, it is taken taken to be a good value for the safety factor. With this safety factor, a final power requirement of 2,960 W is obtained, as shown in equation 8.1.3.

$$P_{eng} = \frac{P_{req}}{\eta_p} \cdot S.F. = 2,960W \tag{8.1.3}$$

To summarise all values used in determining the power required, table 8.2 is given.

Table 8.2: Engine power input and output for the first iteration

Parameter	Value	Unit	Input	Output	Comments
P_{req}	2,097	$[W]$	X		Theoretical required power
η_p	0.85	[-]	X		Propulsive efficiency
S.F.	1.2	[-]	X		Safety factor
P_{eng}	2,960	$[W]$		X	Engine power

A clear indication of the propulsive power required for the RPAS has been determined, and now the engine selection process can start. The first step is to search a range of engines which are suitable for the RPAS. Because most of the time the power of an engine is given in horsepower, the required power is rewritten to horsepower using a conversion factor, this is shown in equation 8.1.4.

$$P_{engine} = 2,960 \cdot 1.3 \cdot 10^{-3} = 3.97hp \tag{8.1.4}$$

8.1.2 Second iteration

After looking at reference material, it is found that the value of the parasitic drag coefficient is quite high for an RPAS. This parameter has a significant influence on the required horsepower, so therefore it is decided to perform an second iteration. The parasitic drag coefficient range given in table 8.3 is found to be typical values for model aircraft and aircraft flying below Mach 0.3 [37, p. 12] [38, p. 7]. In order to make sure that the engine is capable of providing enough power to propel the RPAS, the highest value of C_{D_0} is taken to calculate the required power. This power is again calculated by using equation 8.1.1 and the other parameters being unchanged.

Table 8.3: Parasitic drag from reference

Parameter	Value	Unit	Input	Output	Comments
C_{D_0}	[0.025-0.045]	[-]	X		Parasitic drag range from reference
P_{req}	1,346	$[W]$		X	Required power

As explained before, the power required in case of headwind is taken, so the velocity of 35 m/s is used to determine the power required.

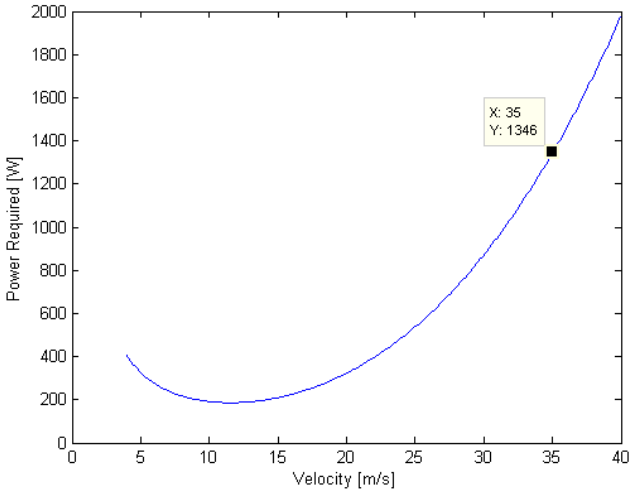

Figure 8.2: Power versus velocity iteration 2

Again using the same value for the propulsive efficiency and the safety factor and using equation 8.1.5 the power which the engine should deliver is calculated. The input parameters and result are summarised in table 8.4.

$$P_{eng} = \frac{P_{req}}{\eta_p} \cdot S.F. = 1,900W \tag{8.1.5}$$

Table 8.4: Engine power input and output for the second iteration

Parameter	Value	Unit	Input	Output	Comments
P_{req}	1,346	$[W]$	X		Theoretical required power
η_p	0.85	[-]	X		Propulsive efficiency
S.F.	1.2	$[W]$	X		Safety factor
P_{eng}	1,900	$[W]$		X	Engine power

In order to be able to find suitable engines for the calculated engine power, the power is rewritten to horsepower using a conversion factor as can be seen in equation 8.1.6.

$$P_{hp} = 1,900 \cdot 1.3 \cdot 10^{-3} = 2.55hp \tag{8.1.6}$$

8.2 Engine selection process

In this section the engine selection is described. With the calculated engine horsepower it is possible to give the engine characteristic requirements. After this engine options are presented. Finally the fuel consumption is calculated and the fuel tank is designed. This procedure is done for both the first and the second iteration.

Number of cylinders
Now that the amount of horsepower required is known, the type of engine which satisfies this can be specified. This is because there are a lot of different types of engines available on the market. The first distinction can be made in the number of cylinders of the engine which ranges usually from 1 to 4 cylinders for RPAS engines. For these engines, an increase in the amount of cylinders means an increase in the delivered horsepower. Based on the calculated required horsepower, it is decided to go for a single cylinder engine. This is because multiple cylinders would mean that the engine delivers more horsepower than required and therefore results in a decrease in efficiency. Another advantage of single cylinder engines is that they are easier to cool than multiple cylinder engines. A disadvantage of a single cylinder engine is that the level of vibration is generally higher than multiple cylinder engines. However this does not counterbalance the fact that a multiple cylinder engine would mean an increase in the fuel consumption, and therefore in the weight, and as mentioned before a decrease in the efficiency.

Engine Selection
In table 8.5 five engines are presented which are in the range of the required horsepower calculated above [39] [40] [41] [42] [43].

Table 8.5: Engine Specifications

	Unit	NGH GT25	O.S. 95AX	DLE-20RA	RCG 26cc	O.S. GT22
Output	$[hp]$	2.7	2.86	2.5	2.6	2.66
RPM range	$[rpm]$	1,600-11,000	2,000-16,000	1,700-9,000	1,500-8,000	1,800-9,000
Price	[€]	174.51	247.94	N/A	135.95	339.29
Weight	$[g]$	960	745	870	1,122	999.2
Fuel type	[-]	Gas	Glow	Gas	Gas	Gas

By using the different characteristics of these five engines, an analysis can be done to be able to choose the best suitable engine. The result of the analysis can be found in table 8.6. When looking at the engine characteristics, it can be seen that the DLE-20RA has too little horsepower to provide enough power. Furthermore do the NGH GT 25 and the O.S. 95AX have too much horsepower compared to the remaining two engines. The best suitable engines left are the RCG 26cc and the O.S. GT22. Based on the comparison between these two engine characteristics, it is decided to choose the O.S. GT22. Although this engine has more horsepower and is more expensive than the other engine, it has lower weight and a larger rpm range. This engine can be found in figure 8.3.

Table 8.6: Analysis of engines

	NGH GT25	O.S. 95AX	DLE-20RA	RCG 26cc	O.S. GT22
Analysis	+ price − hp	+ weight − hp	+ weight − hp	+ hp − weight	+ hp − price
Applicable	No	No	No	No	Yes

Figure 8.3: O.S. GT22 [43]

Fuel consumption and tank
Now that an engine has been chosen, the fuel consumption must be estimated and the fuel tank will have to be sized. A low fuel consumption is required to improve sustainability of the design as well as decrease the amount of fuel that needs to be stored on board. This in turn will keep the design weight as low as possible and within the mass budget.

To estimate the amount of fuel needed by the engine for the endurance requirement of four hours, some calculations were done. An easy way of determining the fuel flow per hour of the engine is to use the brake specific fuel consumption (BSFC). The BSFC is a value for the fuel consumption of an engine with respect to the amount of horsepower it delivers [44]. The fuel consumption of an engine in pounds per hour is given in equation 8.2.1.

$$F.C.P. = P_{hp} \cdot BSFC \tag{8.2.1}$$

Where $F.C.P.$ is the fuel consumption in pounds per hour, HP is the amount of horsepower the engine delivers, and $BSFC$ is as defined above. For two-stroke gasoline engines, the BSFC is assumed to lie at 0.55 [44]. To rewrite it to a fuel flow in litres per hour, a conversion factor from pounds to kilograms must be used, as well as dividing that value by the density of gasoline. The density of gasoline is assumed to lie between 0.71 and 0.77 kg/L, the average will be taken at 0.74 kg/L [45, p. 33]. With the given engine, a horsepower of 2.66 is taken and multiplied by the BSFC of 0.55. It is then converted to litres per hour as shown in equation 8.2.2. The input and output data for this equation can be found in table 8.7.

$$F.C. = \frac{P_{hp} \cdot BSFC \cdot c_{pk}}{\rho_{gas}} = 0.897\ L/hr \tag{8.2.2}$$

Multiplying this value by four hours gives the total amount of fuel needed in litres, which is equal to 3.587 L. The weight of the fuel can be determined by multiplying the number of litres by the density of gasoline, 0.74 L/kg, giving a weight of 2.65 kg.

Table 8.7: Fuel consumption input and output

Parameter	Value	Unit	Input	Output	Comments
P_{hp}	2.66	$[hp]$	X		Horsepower
BSFC	0.55	$[lb/hp{\cdot}hr]$	X		Brake specific fuel consumption
c_{pk}	0.4536	[-]	X		Pounds to kilogram conversion factor
ρ_{gas}	0.74	$[kg/L]$	X		Gasoline density
F.C.	0.897	$[L/hr]$		X	Fuel consumption
W_{fuel}	2.65	$[kg]$		X	Fuel weight

8.3 Engine selection process iterated

In the selection process described before it was not taken into account that electrical power can be generated by using an engine with a generator attached to it. As described in chapter 13 it has a benefit in weight when a power generator on the engine is used instead of only using a battery for providing electrical power. With this in mind engines are searched for which have a power generator attached to it or which have the possibility of attaching a power generator. These engines can be found in table 8.8 [46] [47].

Table 8.8: Engine specifications with generator

	Unit	3W 28i	RCV 35cc
Output	$[hp]$	3.35	2.7
RPM range	$[rpm]$	1,500-8,500	2,000-10,000
Price	[€]	1,000	N/A
Weight	$[kg]$	1.2	1.9
Fuel type	[-]	Gas	Heavy fuel
Combustion	[-]	two-stroke	four-stroke
BSFC	$[lb/hp{\cdot}hr]$	0.55	0.58
Fuel density	$[kg/L]$	0.74	0.804

Because in this iterated selection process it is not searched for an engine which gives the exact required amount of horsepower the trade-off criteria will differ from the criteria used before. It should be noted that the amount of horsepower lies within reasonable limits. It is tried to find a two-stroke and a four-stroke engine which have the possibility of attaching an electrical power generator and have the same fuel type. However, it was not possible to find a four-stroke engine which complies to these requirements. In the weights given in table 8.8 the weight of the generator is not included. It is assumed that the same generator will be used which weighs about 500 g [46]. However, for the 3W 28i, the manufacturer offers the whole package, and in case of the RCV 35cc the generator has to be attached by the customer itself.

For each of the two engines the minimum required amount of fuel will be calculated by using equation 8.2.2 and the flight duration. For the heavy fuel a density of 0.804 kg/L [48] is used as can be seen in table 8.8. The specific fuel consumption of 0.58 $lb/hp{\cdot}hr$ is given in the engine specifications [47]. In table 8.9 the different characteristics of the two engines can be found.

Table 8.9: Analysis of engines with generator

	Unit	3W 28i	RCV 35cc
Fuel consumption	$[L/hr]$	1.129	0.8835
Fuel volume required	$[L]$	4.52	3.53
Fuel weight required	$[kg]$	3.340	2.840
Total weight	$[kg]$	5.093	5.241
Total weight + reserve fuel	$[kg]$	5.833	6.045

In table 8.9 the total weight is the weight of the engine added by the weight of the generator and the minimum required fuel weight. As can be seen in the table there is only a small difference in the total weights of the engines with the minimum required fuel included. However, to make sure that the engine will have enough fuel to fulfil the mission, one litre reserve fuel is added. This means for the 3W 28i an extra fuel weight of 740 g and for the RCV an extra fuel weight of 804 g. After this the total weight of the 3W 28i is lower than that of the RCV. Furthermore, the 3W 28i is offered as a package with the generator already mounted on the engine. For the RCV the generator has to be bought and attached by the customer. Because of these reasons it is decided to choose the 3W 28i to use as propulsion unit for the maritime flyer. The engine, with the power generator attached, can be found in figure 8.4. The required fuel tank volume is determined in chapter 9.

Figure 8.4: 3W 28i with power generator [46]

8.4 Propeller selection

With an engine having been selected, the propeller must now be looked into and a viable option must be determined. There are many variables that effect the performance of a propeller, which makes it difficult to choose one. Characteristics of the propeller such as its pitch and diameter must be carefully chosen with respect to the engine's rpm and propulsive power. During the selection process, cost must also be taken into account, as a self-designed propeller may be too expensive to produce with respect to the cost budget.

To start the design and selection procedure, some background research was done on propellers and their characteristics. It was found that propellers are described by their pitch and their diameter and are presented in this way online and in books. An example of this is 18 x 8, which indicates a propeller with a diameter of 18 inch, and a pitch of 8 inch. The diameter is defined as the diameter of the circle that the propeller produces when making a revolution. Pitch is more difficult to understand and is the distance covered along the rotational axis in one revolution [49]. An example is given in figure 8.5.

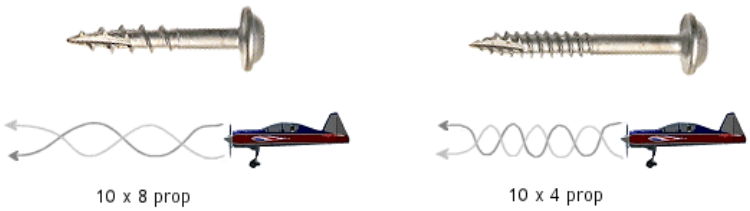

Figure 8.5: Pitch of a propeller

Research also indicated that the efficiency of the propeller depends on the rotational speed as well as the velocity. As cruise velocity will be the most used speed during the RPAS's lifetime, the propeller should be most efficient at this speed. To visualise this, a graph was made relating the pitch of the propeller with the RPM of the engine as shown in figure 8.6. Using the cruise velocity of 28 m/s and equations 8.4.1 and 8.4.2, the required pitch for a certain velocity can be determined. Because the pitch for propellers is given in inches, in equation 8.4.2 a conversion factor from meters to inches is used.

$$RPS = \frac{RPM}{60} \tag{8.4.1}$$

$$p = \frac{V \cdot 39.37}{RPS}[inch] \tag{8.4.2}$$

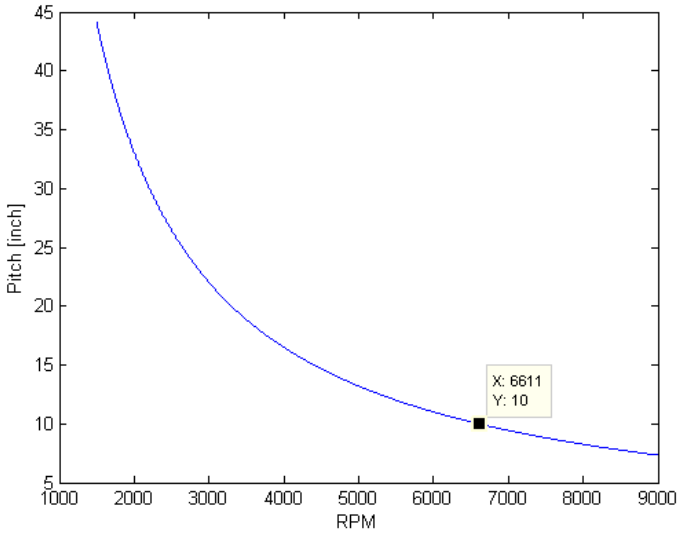

Figure 8.6: Relationship between pitch and RPM for a velocity of 28 m/s

From figure 8.6 it can be determined that in order to fly at a velocity of 28 m/s at about 6,700 RPM a 10 $inch$ propeller pitch is required. This can either be a two bladed propeller or a three bladed propeller. However, because a two bladed propeller is more efficient than a three bladed propeller, it is decided to use a two bladed propeller [50]. From the supplier two propellers with 10 $inch$ pitch are recommended [46]. These two bladed propellers are the 16 x 10 and the 18 x 10. From reference an increase in the diameter results in an increase of the efficiency [51]. Therefore it is decided to use a 18 x 10 propeller. In figure 8.7 the chosen propeller is shown. This propeller is a push propeller made from carbon fiber because of the weight advantage over wood. The specifications can be found in table 8.10.

Figure 8.7: Selected 18 x 10 push propeller [52]

Table 8.10: Selected propeller characteristics

	Unit	Value
Weight	$[kg]$	0.113
Price	[€]	35

8.5 Vibration and noise pollution

When searching for a propulsion system for the RPAS, it is essential to investigate the vibrations induced by its operation and the amount of noise pollution it will put out. Only vibrations induced by the engine will be looked at, as this is closer to the payload and may have a negative impact on stability of the imaging system. Noise pollution is produced by the engine, RPAS aerodynamics, and the propeller, however "*In most propeller driven airplanes the propeller generated noise tends to dominate* [11, p. 316]". This means that for noise pollution, only the propeller noise will be looked into.

To make sure that the RPAS does not vibrate too much and affect the stability of the images being taken, vibrations induced by the engine must be kept to a minimum. This can in the first place be done by using the optional two level anti-vibration engine mount provided by the supplier [46]. On the other hand, most engines operate at relatively high RPM's for their highest efficiency. A compromise must be made between the two to give the highest efficiency possible for the lowest vibrations. A propeller pitch of 10 inch was chosen for the RPAS as this was necessary for a cruise velocity of 28 m/s and a non-maximum throttle. It should be noted that this RPM setting is relatively low compared to the maximum capable by the engine. Decreasing this value would reduce vibrations in the RPAS but would come at the cost of decreased efficiency of the propulsion system. Efficiency plays a large role in being able to fly for four hours and it is therefore decided that the RPM's will not be decreased any further. What should be taken into account alongside just the vibrations of the engine are the interaction of frequencies and the natural frequencies of the RPAS. Vibration of the engine should not coincide with the natural frequency of the rest of the RPAS, as that would induce constructive interference and may have a very negative impact on structural integrity. This can not be tested before completion of the RPAS and must be carefully validated once the RPAS is completed.

Next to be covered is the noise pollution of the propulsion system. As stated above, the propeller is the main source of noise and will be investigated. The number of blades influences the noise level produced by the propeller [11]. With two blades, the amount of noise is highest, and with more blades this noise decreases [11, p. 687]. While it is important to keep the noise pollution to a minimum, it is not as important in the mission area for the Maritime Flyer. In a maritime environment such as the Port of Rotterdam, noise levels can be considered to be less significant. For this reason, it is decided that the current number of blades is adequate and not subject to change due to its higher amount of noise.

8.6 Sustainability

During the design of the propulsion system, sustainability must be taken into account. This includes keeping the design eco-friendly as well as making it durable. Having a sustainable design is quite difficult for the internal combustion engine due to its emissions. However, it can be taken into account during operation of the RPAS as well as during production of the propellers and fuel tank.

Operation of the aircraft requires gasoline to use the internal combustion engine, of which the main harmful emissions are carbon monoxide CO, unburned hydrocarbons HC, and nitrogen oxides NO_x [53, p. 483]. These emissions should be monitored if possible during operation of the RPAS and try to be kept at a minimum. Possible alternatives to gasoline which have a lower environmental impact can also be considered if it does not have an impact on the endurance. Furthermore, hydrogen fuel cells as well as electrical power must be considered in the long run if their specific energy increases by a significant amount; the RPAS must stay under 20 kg. Next, durability of the engine must also be high to ensure that it will last for the RPAS's lifetime. To guarantee this, proper inspection and maintenance can be done on a periodic basis. This will ensure that the combustion process is done in a clean and correct way, without any errors that may potentially be catastrophic. Inspection will also be able to identify flaws in the propulsion system and make it possible to fix them on time.

Next to operation, production of the propulsion system can also be done in a sustainable way, for example producing the propellers and the fuel tank. The materials used to make these parts can be chosen with respect to their eco-friendliness and durability. Materials that are recyclable provide an advantage over materials that

can not be reused after their lifetime. The parts may be purchased from a reseller and if that is the case, the material from which the parts are made must be checked for the sustainability of their production process. Parts that require intensive machine labour from environmentally unfriendly processes must be excluded and a better alternative has to be chosen. Composites are extremely popular for the RPAS due to their low density and high strength. The possibilities of bio-composites must be investigated as they provide composites made from environmentally friendly materials [54]. Furthermore, to ensure durability of the parts, the production process needs to focus on using the correct composition of materials to ensure that the parts are able to survive the entire lifetime of the RPAS.

8.7 Verification and validation

For the verification of the used computational models the equations used are calculated analytically in order to check whether the computed values are correct. Furthermore code verification is done by checking every line for syntax errors. In this way errors are detected in an early stage and can be solved directly. The plots made by the computational model are validated by comparing them with similar plots in reference materials as books or scientific articles.

The calculated required engine power is validated by looking at reference RPAS's with similar characteristics. In order to validate the used propulsive efficiency of the engine, wind tunnel tests can be performed or test flights can be done. Also the performance of the propeller chosen can be validated by performing wind tunnel tests or test flights. However, doing wind tunnel tests or test flights is outside the scope of this DSE project. For the calculation of the required amount of fuel it is very hard to come up with a detailed number. This is because the fuel consumption of the engine depends on a lot of different factors and engine settings. For the determination of the fuel required for the maritime flyer the specific fuel consumption coefficient for a two-stroke engine is used. To validate the fuel consumption of the engine, test flights should be done. The amount of fuel at the start and end of the flight should be measured and with the known flight time the fuel consumption can be calculated.

9 Structures and Materials

This chapter elaborates on the structure of the RPAS. It includes the structural analysis, materials and manufacturing aspects of the RPAS.

9.1 Interface and structural layout

The structural design of the RPAS is initialised by selecting a rough layout. With this layout dimensions and materials can be selected to accommodate the loads acting on the aircraft. The RPAS is mainly subdivided into the wing and the fuselage. The structural layout of the wing includes the material inside the wing, the skin, and the winglets. The fuselage contains the fuselage skin, the fuel tank, the camera, the communication systems, the engine, the batteries, an on-board computer, autopilot, antenna, and an estimation of the wiring. The fuselage and the wing are connected by a joint, which will guide the loading from the wing through the fuselage to the other wing.

In order to come up with a final structural layout, first a loading analysis was done to see what forces the RPAS should be capable of withstanding. Additional load factors are determined for safety. Secondly, a structural analysis was done to make a preliminary structural design. Next, the materials and manufacturing methods were selected according to the budget constraints and the structural design. Finally, a mass and cost budget model is developed which keeps track of the weight and costs of all contributing components in order to assure that the budgets are not exceeded. The methods used in all these analyses are then verified and validated to assure the quality of the design and sustainability is checked throughout the process and validated at the end.

The structural department is closely interrelated with other departments. All inputs and outputs are summarised in table 9.1 to keep an updated overview during the process. For the mass and centre of gravity of all departments, a separate table can be found in section 9.5

Table 9.1: Inputs and outputs of structures

Parameter	Value	Unit	Input	Output	Comments
ρ	1.225	$[kg/m^3]$	X		Air density at sea-level
C_{L_α}	4.9	$[rad^{-1}]$	X		Lift slope (Chapter 6)
C_L	0.3	[-]	X		Lift coefficient at cruise (Chapter 6)
S	1.1	$[m^2]$	X		Wing area (Chapter 6)
$\bar{c}$	0.36	$[m]$	X		Mean aerodynamic chord (Chapter 6)
g	9.81	$[m/s^2]$	X		Gravitational acceleration
V	28	$[m/s]$	X		Cruise speed (Chapter 6)
b	3.3	$[m]$	X		Span (wings only) (Chapter 6)
F_w	1	$[kg]$	X		Wing weight
Λ	22.5	$[deg]$	X		Quarter-chord sweep (Chapter 7)
F_{launch}	787.6	$[N]$	X		Launch load (Chapter 14)
$F_{recovery}$	1300.5	$[N]$	X		Recovery load (Chapter 14)
$m_{component}$		$[kg]$	X		Mass of each component * (Table 9.8)
$x_{cg_{component}}$		$[m]$	X		X-coordinate centre of gravity *(Table 9.8)
$cost_{manhour}$	25	$[e]$	X		Cost of one man hour with average salary (Section 14.7)
W	18	$[kg]$	X	X	Maximum take-off weight (iterated in this section)
σ_{max}	72	$[Mpa]$		X	Maximum normal stress in wing skin
τ_{max}	50	$[Mpa]$		X	Maximum normal stress in wing skin
$x_{cg_{RPAS}}$	0.867 - 0.902	$[m]$		X	X-coordinate center of gravity of RPAS * (Table 9.8)
I_x	5.036	$[kgm^2]$		X	Mass moment of inertia about the X-axis *
I_z	6.042	$[kgm^2]$		X	Mass moment of inertia about the Z-axis *

* The mass moments of inertia are extracted from the CATIA model.

9.2 Loading analysis

9.2.1 Load factors

The RPAS has to withstand all forces which it is subjected to. First the maximum loading cases of the RPAS have to be analysed before the structure can be determined. To determine the maximum loading the mission is divided into three sections, launch, recovery and flight. The loads during these mission elements strongly depend on the speed, manoeuvres and the overall configuration of the RPAS. Next the three mission elements will be analysed separately.

Launch
During launch a force is applied on the RPAS. This force is determined to be 787.6 N, which is analysed in section 14.1. In that section the launch mechanism is explained. The RPAS will have to withstand this force. This force will be exerted on the fuselage. Therefore the fuselage will have to be able to withstand this force.

Recovery
For recovery the RPAS will be subjected to a force by the net capture system. Further detail of this system is explained in section 14.1. This force is estimated to be 1300.5 N. This force does not specifically act on a certain point on the RPAS. It will be distributed from fuselage nose to the side and on the wing. If the RPAS would fly directly with its nose in the net, the maximum load will be found at the fuselage nose. Therefore the fuselage nose shall have to withstand this force. However there is a possibility the RPAS will fly in the net with side slip. In this case the force will be more distributed along one half of the wing, because one half of the wing will touch the net faster. Therefore the wing should also withstand this force distributed along the half wing span. Although the force will have a much higher impact near the wing root than the wing tip

Note that the loads of launch and recovery are subjected in longitudinal direction through the RPAS.

Flight
During flight more loads are subjected to the aircraft. The RPAS will be subjected to longitudinal load due to thrust and drag. Furthermore the most predominant load is in the direction of the lift and weight. This load is defined as the amount of g's the RPAS is exposed to. This load factor is defined as in equation 9.2.1.

$$n = \frac{L}{W} \tag{9.2.1}$$

To determine the maximum load factor a loading diagram is made. This diagram consists of the manoeuvring load and gust load. This diagram is found in figure 9.2. The maximum limit load for manoeuvring is found to be 5, calculated in chapter 15 . The negative limit load is 0.4 times the positive limit load, resulting in a negative limit load of -1.8. [55] The cruise speed of the RPAS is 28 m/s. The operational dive speed is roughly a factor 1.5 of the cruise speed which results 42 m/s. [55]

Next the gust envelope is determined. Wind gusts act on the RPAS for a short period of time. High loads can be subjected to the RPAS. The data of gust speeds is retrieved from the KNMI [56] at the measurement point in Hoek van Holland. A normal distribution is made with the maximum wind gusts of every day in the last 5 years. This distribution can be seen in figure 9.1. The average maximum wind speed on a day was 14 m/s. However if this wind gust would be used to design the RPAS, the RPAS can be operated only half of all the days. Therefore a wind gust of 20 m/s is used to design the RPAS. At 20 m/s the RPAS can be operated 90% of the days.

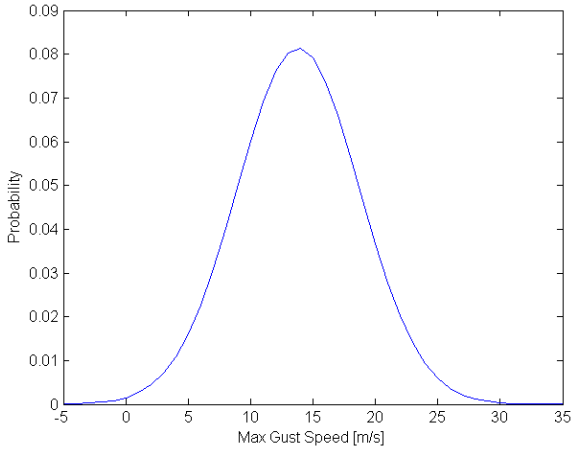

Figure 9.1: Maximum wind gusts

The gust load induces a change of angle of attack which creates a change in lift. Thus a load factor is experienced by the RPAS. The change of angle of attack depends on the direction of the wind gust. Figure 9.3 shows the effect of a wind gust to the angle of attack. Furthermore using equations 9.2.2 to 9.2.4 the load due to wind gust is calculated for cruise speed (28 m/s). The gust load increases linearly with respect to the 20 m/s wind gust, due to fact that the RPAS is flying near sea level the whole mission. The wind gust diagram can be found in figure 9.2.

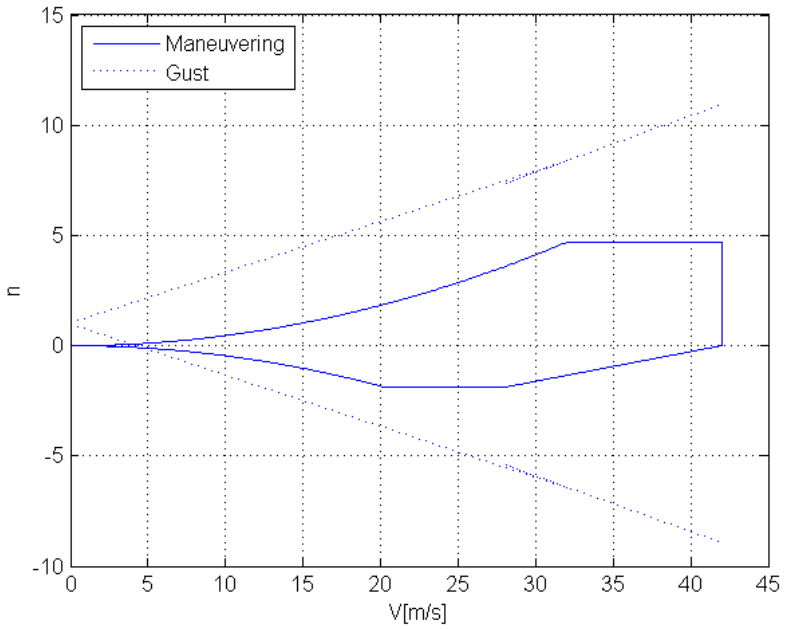

Figure 9.2: Load diagram

This load diagram shows that the wind gust is the limiting factor for the RPAS. The RPAS is a lightweight object and has a low wing loading, which increases the influence by gusts. The load factor at cruise is 7.4 and at dive speed 11. The calculations for cruise speed are shown in equations 9.2.2 to 9.2.6. The RPAS will not reach dive speed, therefore the RPAS will be designed for a higher speed than cruise but slightly lower than dive speed. The RPAS will be designed for a limit factor of 10 and thus, with a safety factor of 1.5, an ultimate factor of 15.

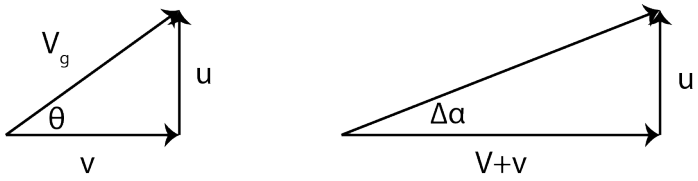

Figure 9.3: Wind effect on RPAS

$$\mu = \frac{2W}{\rho g \bar{c} C_{L_\alpha} S} = \frac{2 \cdot 175.58}{1.225 \cdot 9.81 \cdot 0.36 \cdot 4.9 \cdot 1.1} = 15 \tag{9.2.2}$$

$$K = \frac{0.88\mu}{5.3 + \mu} = 0.65 \tag{9.2.3}$$

$$\Delta\alpha = \tan^{-1}\left(\frac{Ku}{V+v}\right) = \tan^{-1}\left(\frac{0.65 \cdot 20}{28+0}\right) = 0.43 \tag{9.2.4}$$

$$\Delta L = \frac{1}{2}\rho V^2 S C_{L_\alpha} \Delta\alpha \tag{9.2.5}$$

The load factor results in:

$$n = 1 + \Delta n = 1 + \frac{\rho V^2 S C_{L_\alpha}}{2W}\Delta\alpha = 1 + \frac{1.225 \cdot 1.1 \cdot 4.9}{2 \cdot 175.58} \cdot 0.43 = 7.4 \tag{9.2.6}$$

9.3 Wing structure and materials

This section analyses the stresses inside the wing due to its loading. A structural wing design will be evaluated which results in the specific materials the wing will be made of.

9.3.1 Analytical wing model

The ultimate load is determined to be 15. This ultimate load is used to start with the design of a simplified structure. The lift distribution acting along the wing is the most predominant force subjected to the RPAS. This distribution is shown in figure 9.4. The lift force is distributed elliptically along the total span. The weight of the wing is acting along the total wing as well. Furthermore the fuselage is simplified as a point force acting in the middle of the fuselage.

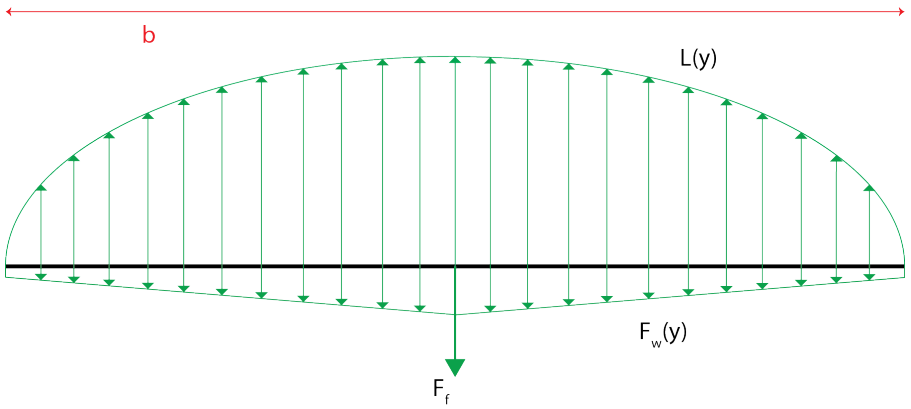

Figure 9.4: Wing load distribution

Due to the fact the wing is symmetrical along the zx-plane the load distribution is simplified to a half-wing. The other half will be subjected to exact the same loads as in figure 9.5a. To simplify the distributions more the force distribution are defined linear decreasing until the tip of the wing as in figure 9.5b. The fuselage is left out, because only the wing is analysed with the forces acting upon it.

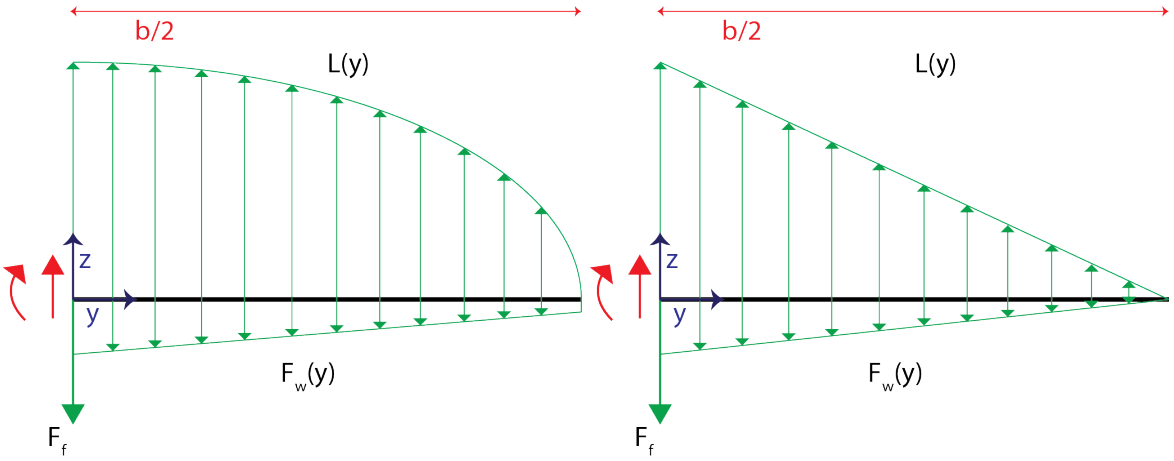

(a) Half-wing load distribution

(b) Simplified half-wing load distribution

The simplified wing loading model is given in figure 9.5b. This model is used to determine the moments and shear forces along the span. The results of the moments and shear forces will have a certain error due to assumptions and simplifications. In this stage a rough estimate of the forces along the span are made. In later stage these will be used to verify a complicated computational model. The following assumptions and simplifications were made:

- The model is made two dimensional. However the wing also embodies torque due to the fact the force does not act directly on the beam's axis of symmetry.
- The lift distribution is modelled linear. In physical conditions lift force is distributed more elliptical.
- The mass of the wing is distributed linearly along the wing.
- The force contributions of the winglets are neglected.

Note that these assumptions imply errors of the solution compared to the real physical model. The values of the parameters in this model are summarised in table 9.2.

Table 9.2: Values

Parameter	Value	Unit	Input	Output	Comments
W	176.6	$[N]$	X		Cruise Weight
b	3.3	$[m]$	X		Span
F_w	9.81	$[N]$	X		Weight of the Wing
n	15	[-]	X		Load Factor
$L(=nW)$	2649	$[N]$	X		Total Lift

The shear force and bending moment (M_x) at every location on the span are calculated. The shear force is calculated using equation 9.3.2. This equation was found by integrating the lift distribution from tip to root.

$$V(y) = \int_{y}^{1.5} L\,(y)dy - \int_{y}^{1.5} F_w\,(y)\,dy \tag{9.3.1}$$

$$V(y) = \left[\frac{L}{2} + \left(\frac{2}{9}y^2 - \frac{2}{3}y\right)L\right] - \left[\frac{F_w}{2} + \left(\frac{2}{9}y^2 - \frac{2}{3}y\right)F_w\right] \tag{9.3.2}$$

The bending moment is calculated using equation 9.3.3.

$$M_x = V\,(y) \cdot \left(\frac{1.5 - y}{3}\right) \tag{9.3.3}$$

The shear and bending moment along the half wing is calculated. This distribution is shown in figures 9.6a and 9.6b. The shear and moment at the root are roughly 1200 N and 600 Nm.

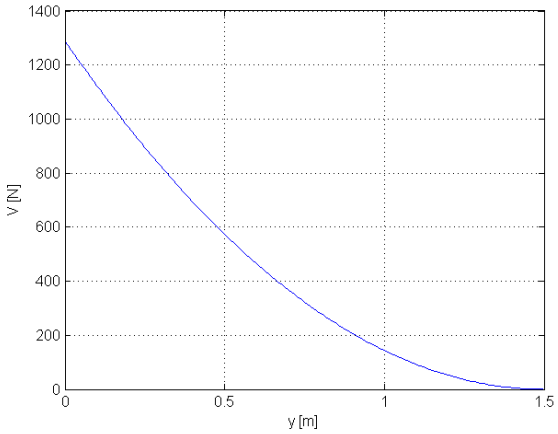

(a) Half-wing shear distribution

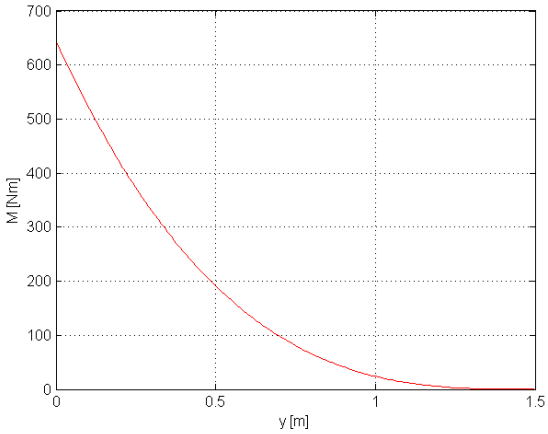

(b) Half-wing moment distribution

Figure 9.6: Half-wing distributions

Furthermore torsion is an important factor in the design of the wing. Therefore the torsion moment (My) is evaluated as well. For this analytical model the torsion at the root is calculated. This moment is not counter acted by the other half of the wing. Therefore the total lift is considered in calculating this moment in the wing. The lift is assumed acting on quarter chord of the mean aerodynamic chord. Using figure 9.7 and equation 9.3.4 an estimation of this torque is calculated.

$$T = -d \cdot \tan(\Lambda) \cdot L = -0.7 \cdot \tan(22.5) \cdot 2649 = -768Nm \tag{9.3.4}$$

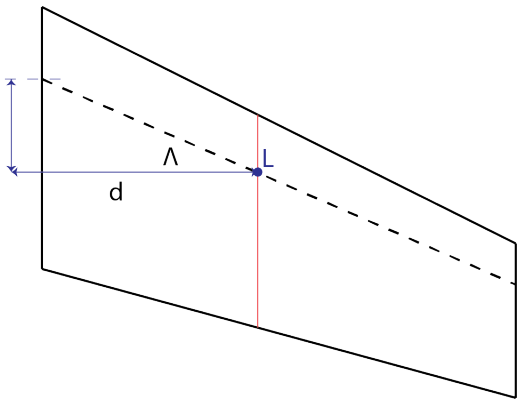

Figure 9.7: Torsion of wing

9.3.2 Computational model

Next a computational model of the lift distribution is analysed. This approaches forces and moments differently. In the computational model the span is divided in sections. First the lift distribution, which is discretised in XFLR, is imported. The following assumptions and simplifications are used for the computational model:

- The lift distribution is imported from the XFLR model.
- The weight of the wing is linear.
- The force contributions due to the of winglets are neglected.

The forces are determined for every section. The shear forces are calculated by summing the lift force cumulatively from tip to root. The moment is calculated by the lift force multiplied by the length of a section. These moment are cumulatively summed from tip to root. The lift, shear, bending moment and torsion moment distributions are shown in figures 9.8.

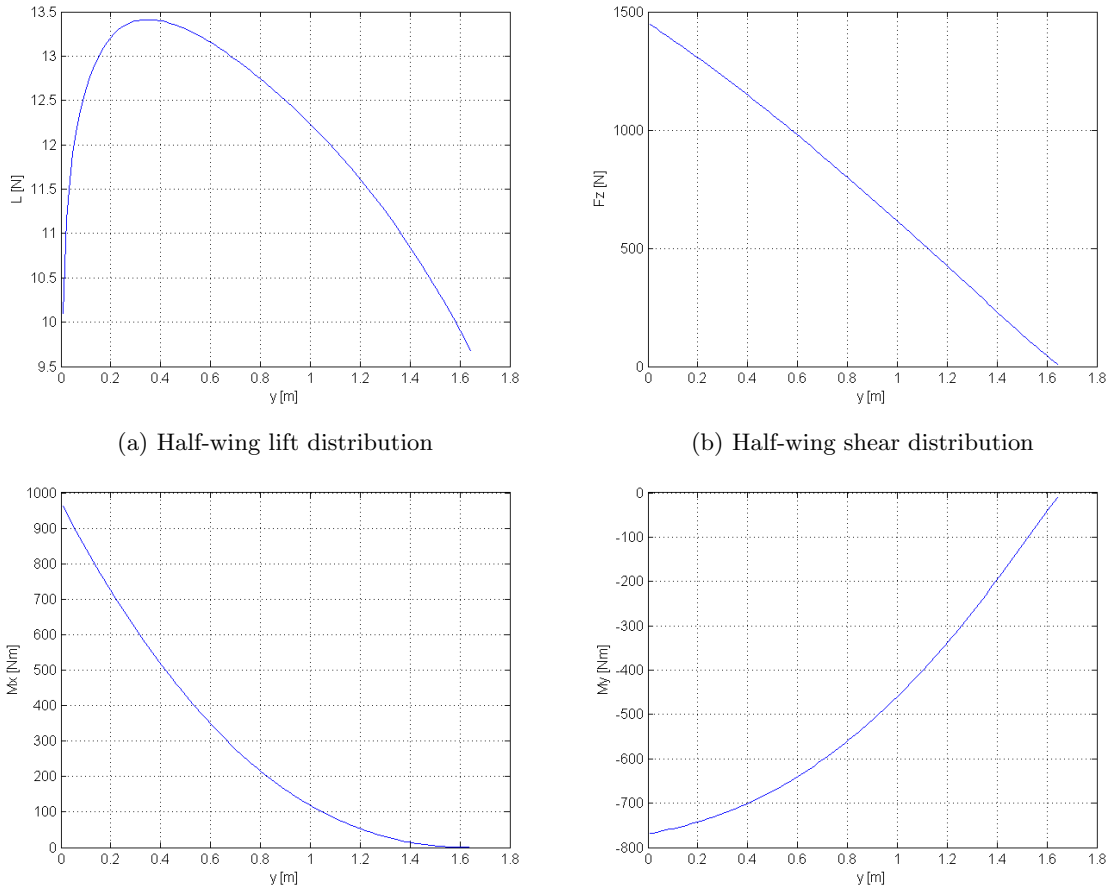

(a) Half-wing lift distribution

(b) Half-wing shear distribution

(c) Half-wing bending moment distribution

(d) Half-wing torque moment distribution

Figure 9.8: Force and moment distributions

9.3.3 Wing stress distributions

The maximum loads the wing is subjected to are summarised in table 9.3. In further design the values of the computational model are used, because they comply better with reality. Particularly due to the more realistic lift distribution. The analytical values show that the computational values are in the same order of magnitude. Therefore the computational model is verified.

Table 9.3: Maximum loads during flight

Location	**y=0 (Root)**	**y=1/6b**	**y=1/3b**	**y=1/2b (Tip)**
Shear Force Analytical $[N]$	1290	573	143	0
Shear Force Computational $[N]$	1450	900	750	0
Bending Moment Analytical $[Nm]$	645	191	24	0
Bending Moment Computational $[Nm]$	680	430	120	0
Moment Analytical $[Nm]$	-768	-	-	-
Moment Computational $[Nm]$	-770	-670	-420	0

The force and moment distributions determine the strength the structure has to have, because the forces and moments may not break the wing. Therefore the wing will be designed to withstand these forces. This is done by analysing the stress distribution along the span of the wing. Just as the force and moment distribution the stress distributions for the wing is analysed for half a wing.

Rod Design

The wing will be subjected to several forces. The wing loading acts lateral and the force due to launch and recovery acts longitudinal. Therefore a rod with a symmetrical shape is chosen to withstand all those forces. The rod has to fit in the wing from root to tip. The maximum thickness at root and tip is found to be respectively 6 cm and 2 cm. Therefore a circular tapered rod is used with these dimensions at root and tip. The material is

chosen to be carbon fibre and has an ultimate tensile/compressive stress of 110 MPa and ultimate shear stress of 260 MPa, which depends on the direction of the fibres and amount of fibres with respect to the polymer. Further explanation of the chosen material is elaborated in section 9.3.4. The minimum thickness over the span of half wing is found, which is shown in figure 9.9.

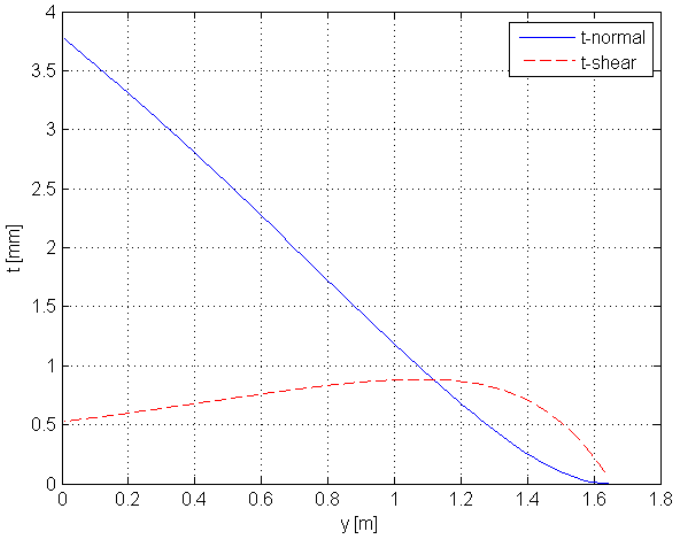

Figure 9.9: Thickness distribution

Skin Design

Furthermore the wing can be designed with no rod. In this case all stress will be distributed in the skin of the wing. Unlike the rod the skin thickness is constant along the span. The skin thickness is set to 0.5 mm. First the airfoil is simplified as a rectangle. This rectangle is assumed such that the cross-sectional area is similar to the true cross-sectional are of airfoil. This cross-sectional rectangle compared to the airfoil is shown in figure 9.10.

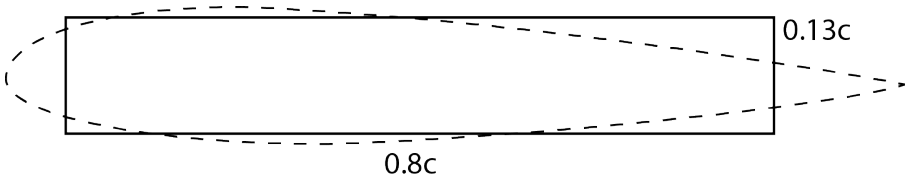

Figure 9.10: Airfoil simplification to rectangle

The normal stress and shear stress are calculated for this rectangle along the span of the half wing. The normal stress distribution is found at the maximum stress at each section using equation 9.3.5. The shear stress is calculated with the torsional moment at each section using equation 9.3.6. Both distributions are shown in figure 9.11.

$$\sigma = \frac{M_x z}{I_{xx}} \tag{9.3.5}$$

$$\tau = \frac{M_y}{2At} \tag{9.3.6}$$

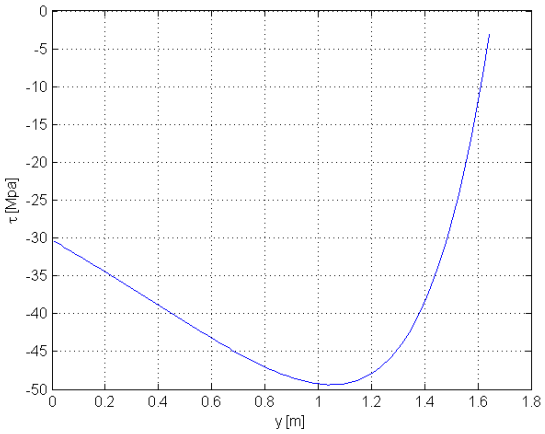

(a) Half-wing shear stress distribution

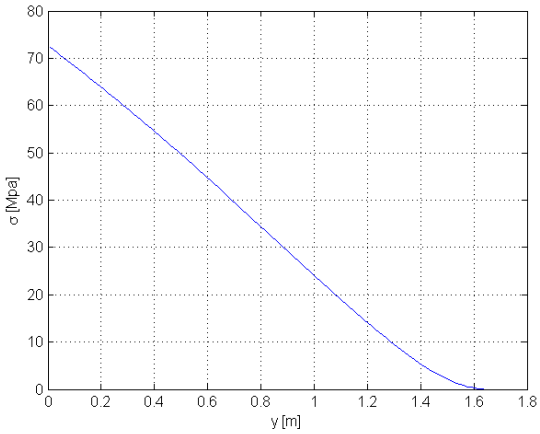

(b) Half-wing normal stress distribution

Figure 9.11: Half-wing stress distributions

Table 9.4: Maximum stress

Parameter	Value	Unit
σ_{max}	72	MPa
τ_{max}	50	MPa

Thus the rod or the skin can be used to withstand the stresses in the structure of the wing. Both structures are a possibility. However using the rod a skin is still needed for the shape of the wing. The thickness of the rod is roughly 8 times as high at the root compared to the skin. Therefore it is rather efficient to get rid of the rod and have solely a skin. Furthermore, for manufacturing reasons, the skin only is more efficient which will be explained in the next section.

9.3.4 Materials and stress

The wing is made out of a skin, a solid filling and a joint. Every part is made out of a different material. The skin is made out a carbon fibre reinforced polymer, the solid filling is a foam and the joint is made out of wood. Possible materials are summarised in table 9.5 with their properties [57] [58] [59].

Table 9.5: Material selection

Part	Unit	CFRP (0°)	CFRP (±45°)	Abachi Wood	ROHACELL HF 31
Density	$[kg/m^3]$	1600	1600	380	32
Tensile modulus	$[GPa]$	70	17	6.69	0.036
Tensile strength	$[MPa]$	600	110	60.8	1
Compressive modulus	$[GPa]$	70	17	-	0.036
Compressive strength	$[MPa]$	570	110	29.3	0.4
Shear modulus	$[GPa]$	5	33	-	0.013
Shear strength	$[MPa]$	90	260	-	0.4

The rod and the skin will be made out of carbon fibre reinforced polymer (CFRP), because it has high strength properties with respect to its weight. CFRP can be manufactured in several methods. The manufacturing has impact on the strength of the CFRP. Furthermore the percentage of carbon fibre and the direction its placed in respect to the loading determines the final strength of this composite. Furthermore the minimum thickness of one layer is roughly 0.125 mm.

The optimal fibre orientation for bending is 0°, because it has highest strength properties in that direction. However the optimal fibre orientation for torsional rigidity in carbon fibre composites are ± 45° which also has strength in the bending direction. The wing is subjected to bending and torsion, therefore several layers with different orientations are used for the skin. The rod would use only ± 45° orientated fibres.

Rod design

The minimum thickness of the rod was determined in figure 9.9 using the values of table 9.5. The minimum

thickness from root to tip is roughly 4 to 1 mm. This thickness is quite high compared to the diameter of 6 to 2 cm. This is rather inefficient. The manufacturing of the rod is quite easily done using filament winding. However the connection of the rod to the skin induces difficulties in manufacturing. The rod should therefore be just slightly smaller than the maximum thickness of the airfoil to fit in. The connection has to made with an adhesive, which makes the design less reliable. Furthermore the rod implies difficulties in the joint of the wing with the fuselage. Therefore the rod design does not suffice the structural design optimal. A design of the wing with solely a skin is chosen.

Skin Design

The stresses for skin are analysed with a skin thickness of 0.5 mm. With thickness of 1/8 mm for one layer, this determines the skin has four layers of fibres. The maximum stress the skin can be subjected to at a point is found in table 9.4. The ultimate strength for two different fibre orientations are found in table 9.5. Using these values the material stress strain curves are made, as shown in figure 9.12. The maximum stresses are shown in these figures as well. Hence the maximum stress does not exceed the ultimate stress of the carbon fibre reinforced polymer. Even for every fibre orientation the stress does not exceed the maximum allowable stresses. Furthermore the strength can be made optimal for this wing. A wing that is subjected to torsion and bending has a different optimal fibre orientation than 0° or 90° degrees. Multiple layers also give the option to put fibres in even more directions. Therefore the wing structure with a 0.5 mm thickness of carbon fibre can be made stiff enough to withstand the bending and torsion.

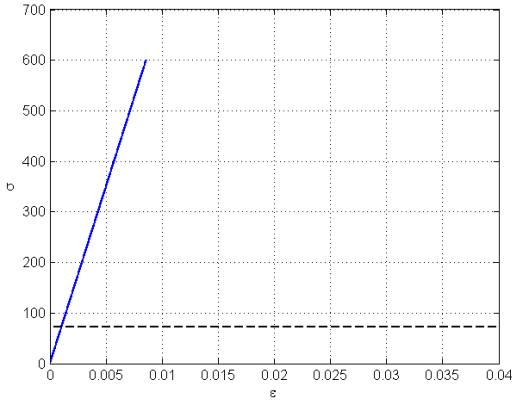

(a) Tensile stress-strain curve for 90°

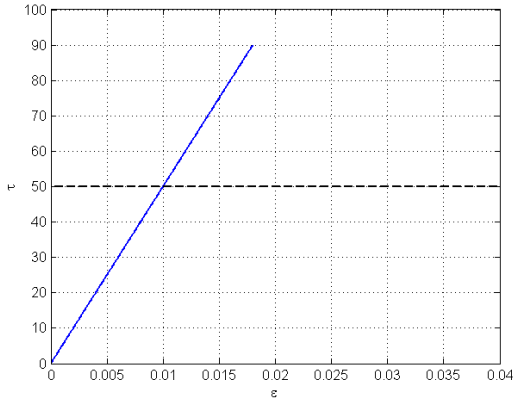

(b) Shear stress-strain curve for 90°

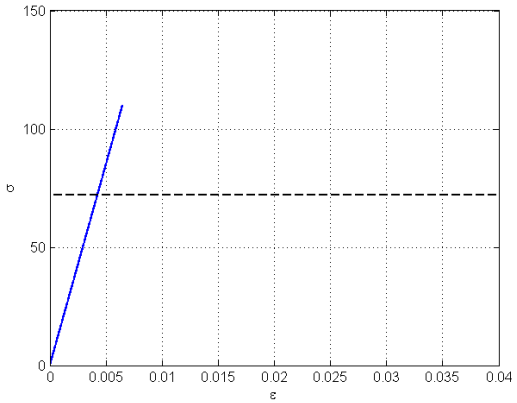

(c) Tensile stress-strain curve or 45°

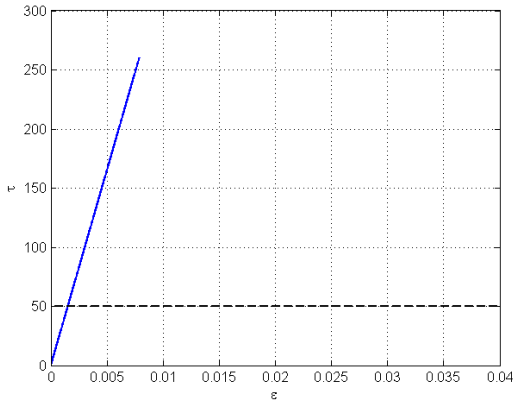

(d) Shear stress-strain curve for 45°

Figure 9.12: Stress-strain curves

An additional structural issue are the vibrations through the wing. The wing is likely to exhibit flutter. The carbon fibre reinforced polymer skin compensates this flutter, by having fibres in several directions. Flutter can not be analysed easily with computational tools. The flutter can be analysed by doing wing tunnel tests with the wing. Furthermore the foam inside the wing induces higher vibrational stiffness, because it adds weight to create higher rigidity.

Wing Joint

The skin is determined to be a 0.5 mm thick with CFRP. To keep the wing in its shape foam is used inside the

skin. The total wing is filled with foam except at the root where the wings are attached to each other and to the fuselage. The properties of the foam are summarised in table 9.5. This foam does not carry the loads, it merely to keep the wing its shape. All the loads of the wing are carried to the root. The wing at the root is therefore not filled with this foam, but filled with Abachi wood (Triplochiton scleroxylon [59]) as stated in table 9.5. The wood is sprayed with a water resistant coating to survive the maritime environment. The two half wings are slided in each other with one half wing is slided on the other half using an male and female joints. These joints are part of the wooden section of the wing. A minimum of three joints is needed, because then the forces and moments in all direction can be transferred to the other half wing and thus counteract each other. The wing slides through three webs which keep the wing in place. Than a bar is put in vertically so the wing does not slip. The joint of the wing section is shown in figure 9.13. The wooden part is shown in yellow. On either side it has a male or female joint. In order to attach the wings, a pin is used. Furthermore the cabling to send signals to the control surfaces are connected to the electrical plug which is embedded into the wood.

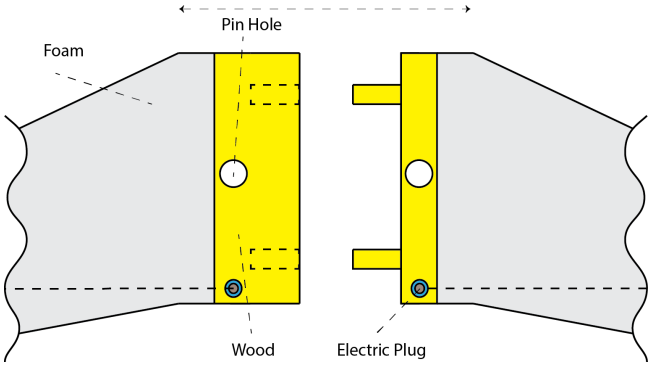

Figure 9.13: Wing structure of joint

Wing Control Surface
The wing is also equiped with control surfaces. These control surfaces are cut-outs from the wing. The structure of the elevons is shown in figure 9.14. The servos are placed inside the wing. Cabling is put through a small hole in the foam structure. This is connected to the servo to supply it with power. The servo turns the elevons which are hinged at the top. This hinge is made out of a strong tape which is put in between the layers of the carbon fibre skin. The foam and skin at the bottom is scraped out to let the elevons hinge downwards.

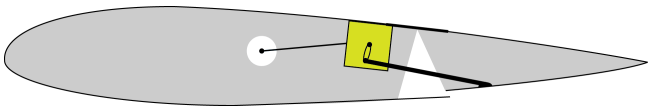

Figure 9.14: Wing structure at elevon

9.4 Fuselage structure and materials

Throughout this section the structure of the fuselage will be designed and analysed. Firstly the fuselage model, consisting out of the layout of the structure and the assumptions made, is presented. This is followed by the forces that apply to the fuselage, in accordance with these assumptions. The forces translate into a stress distribution, which finally lead to the selection of the material used and its thickness.

9.4.1 Fuselage model

The structural layout of the fuselage is determined by the materials and parts used. Hence, a preliminary estimate/selection is made to identify the shape of the fuselage and the material used in this construction. In most unmanned aerial vehicles, structural components are constructed out of composite materials as they provide high strength and stiffness in combination with low weight, opposed to metals/alloys [4]. A range of options suggested and investigated include skin only, sandwich skin only, skin in combination with stiffeners, and sandwich skin in combination with stiffeners. Due to an increased complexity induced by the use of stiffeners such as stringers and bulkheads, it is preferred to apply a simple structure, consisting out of a sole skin. Due to the allocation of antennas inside the fuselage, the material out of which the skin consists should allow the signals to propagate through the fuselage with minimal loss (dispersion, reflection, fragmentation). The construction will therefore be constructed out of a composite skin.

Assumptions

- The origin of the axis system is located at the most forward point of the fuselage, along its longitudinal axis.
- X is positive aft, Y is positive towards the right when viewed from above, Z is positive upward. The origin is located on the fuselage's longitudinal axis, at the most forward location.
- The fuselage is modelled as an open cylinder: the outer diameter equals 200 mm, the length of the cylinder equals 1650 mm.
- Thickness << radius, hence the thin-wall assumption is applied.
- All forces apply through the shear centre.
- Lateral forces are neglected.

9.4.2 Applied forces

The forces applied follow directly from the mass distribution established in the mass budget, and the lift applied. These values, extracted from section 9.5, are listed in table 9.6. In this table d represents the distance from the origin to the application point of the force along the X-axis.

Table 9.6: Magnitude, direction and location of forces exerted on fuselage

Identifier	**Origin**	**Force component** $[N]$		**X-location** $[mm]$
		X	**Z**	
W_1	Pitot tube	0,00	-0,49	0
W_2	Batteries	0,00	-1,84	50
W_3	Autopilot	0,00	-0,49	60
W_4	Raspberry Pi	0,00	-0,41	60
W_5	Camera system	0,00	-9,81	330
W_6	Upper frame front	0,00	-0,82	350
W_7	Wing system	0,00	-43,48	740
D	Total drag	20,00	0,00	740
L	Total lift	0,00	1719,10	740
W_8	Lower frame	0,00	-3,32	825
W_9	Fuselage	0,00	-12,75	825
W_{10}	IMU	0,00	-0,47	890
W_{11}	Wing joint	0,00	-3,70	903
W_{12}	Fuel and fuel tank	0,00	-43,45	950
W_{13}	Transponder	0,00	-0,98	1000
W_{14}	Upper frame back	0,00	-2,48	1070
W_{15}	GPU	0,00	-4,91	1070
W_{16}	Antenna and modem first	0,00	-12,26	1200
W_{17}	Video storage and processing	0,00	-0,49	1300
W_{18}	Double antenna and modem back	0,00	-7,85	1320
W_{19}	Engine, generator, and cap	0,00	-20,80	1550
T	Engine	-20,00	0,00	1575
W_{20}	Propeller	0,00	-1,11	1650

In order to acquire the stress distribution throughout the fuselage, multiple diagrams are constructed from this table. The diagrams include the normal force distribution, shear force distribution, and moment distribution and have been constructed for the forces applying in steady, symmetrical, horizontal flight. A graphic representation of these forces can be found in the free body diagram (FBD) shown in figure 9.15, which follows directly from table 9.6. Note that the figure is not to scale.

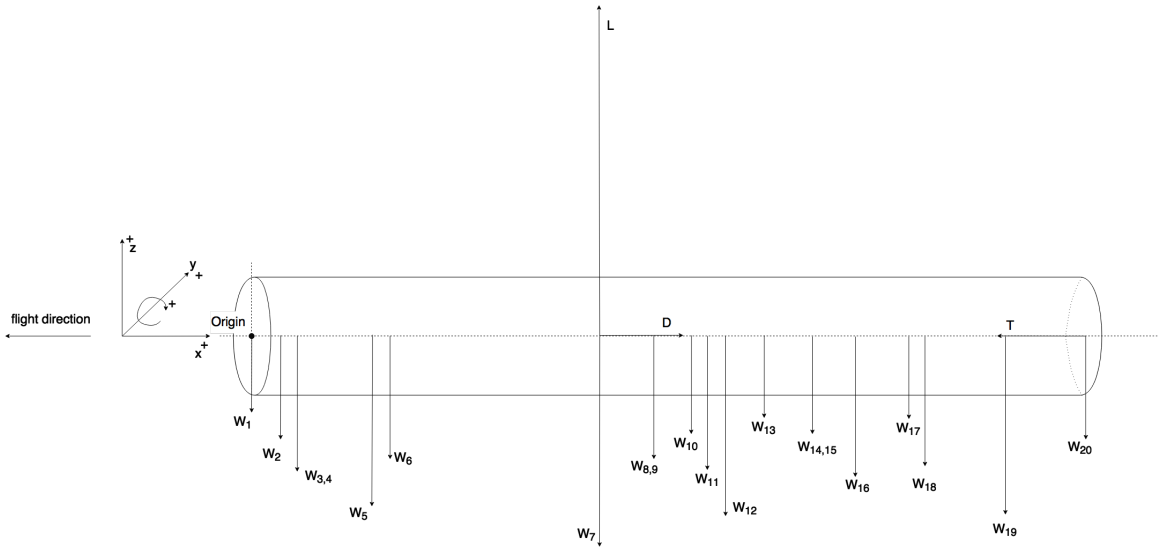

Figure 9.15: Free Body Diagram of the fuselage model

From the FBD follows the following for the frontal area of the fuselage model:

$$A_{frontal} = \pi(2rt - t^2) \tag{9.4.1}$$

Multiple cuts are made in the structure to calculate the resulting forces and moments (N_x, V_x, and M_x) according to equations 9.4.2, 9.4.3, and 9.4.4 below, which are based on cut "c" depicted in figure 9.16.

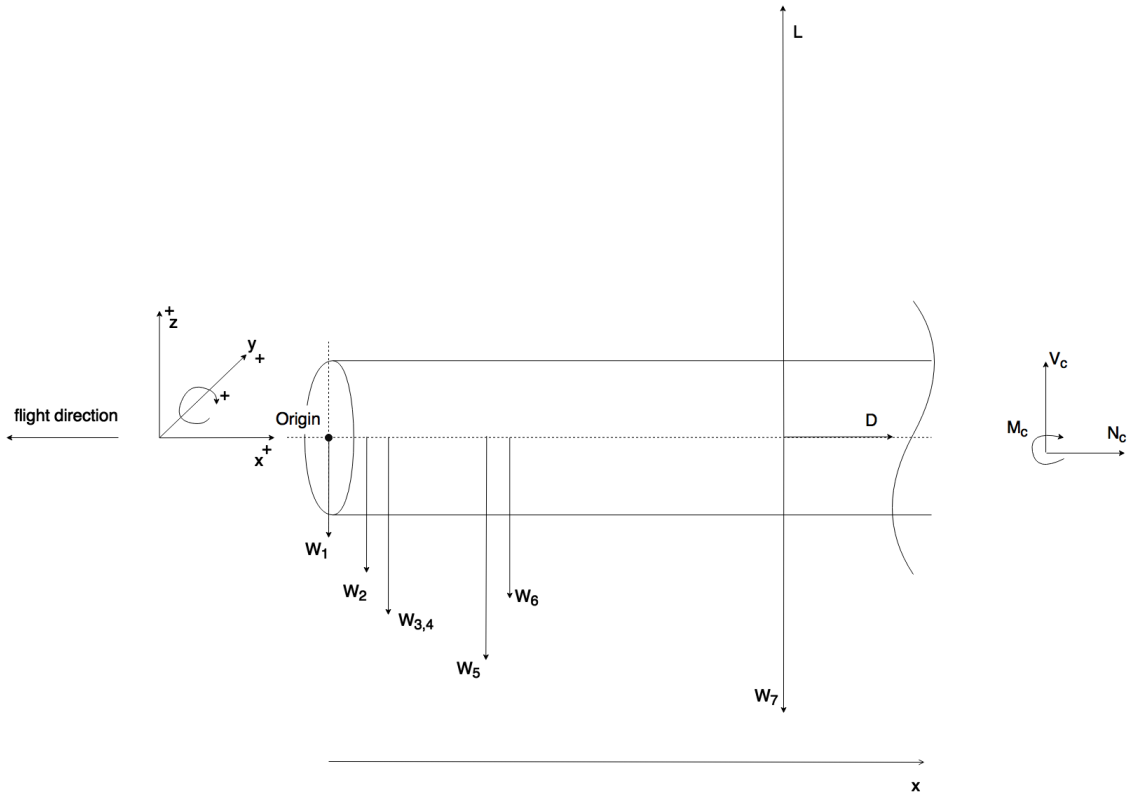

Figure 9.16: Cut "c" in the fuselage FBD

All following calculations will make use of $t = 0.0005\ m$. This is however a preliminary estimate and subject to change in section 9.4.5. The outer radius of the fuselage r equals $0.1\ m$. The previous results in $A_{frontal} = 0.3134 \cdot 10^{-3} m^2$.

$$\sum N = N_c + D = 0 \tag{9.4.2}$$

$$\sum V = V_c - W_1 - W_2 - W_3 - W_4 - W_5 - W_6 - W_7 + L = 0 \tag{9.4.3}$$

$$\sum M = M_c - W_1(x-d_1) - W_2(x-d_2) - W_3(x-d_3) - W_4(x-d_4) - W_5(x-d_5) - W_6(x-d_6) - W_7(x-d_7) + L(x-d_L) = 0 \tag{9.4.4}$$

Using these equations, the normal force, shear force, and moment distribution along the X-axis are calculated. The results can be found in figures 9.17a, 9.17b, and 9.17c respectively.

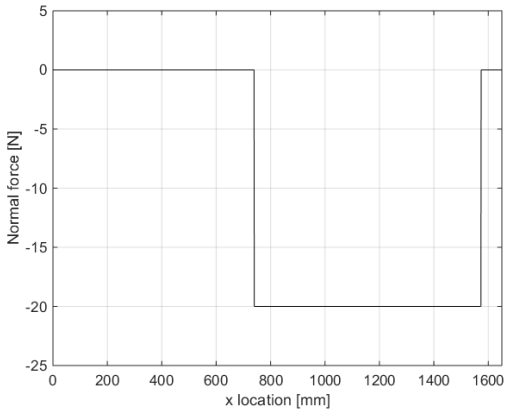

(a) Normal force distribution along X-axis

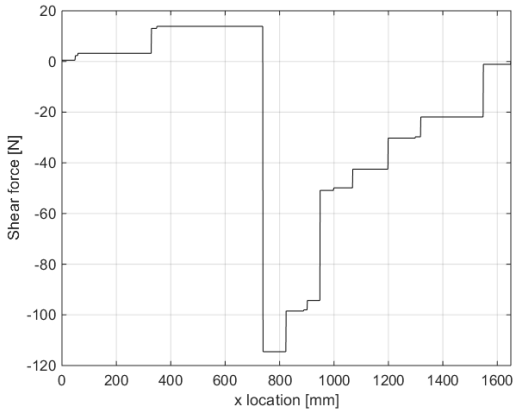

(b) Shear force distribution along X-axis

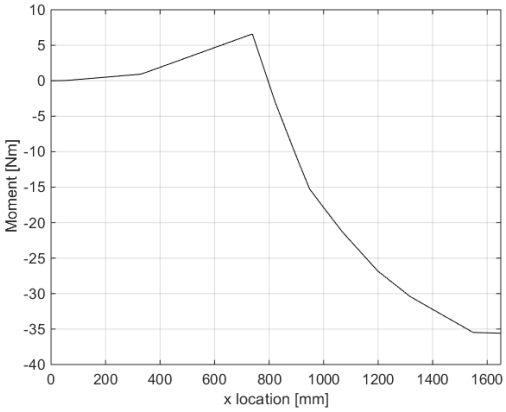

(c) Moment distribution along X-axis

Figure 9.17: Fuselage force and moment distributions

The maximum forces and moments can be extracted from figures 9.17a to 9.17c. These maxima are calculated for a load factor of 1. However, other load cases exist as described previously. The fuselage will be designed for the two most critical cases: at load factor n = 15, and at impact landing. The effect of the load factor translates into the lift force being multiplied by 15, as follows from equation 9.2.1. Both will be adressed in section 9.4.5.

9.4.3 Fuselage stress distributions

Now, the forces and moments determined in section 9.4.2 used to determine the normal stress due to normal force and bending and shear stress due to shear force.

Normal stress

The normal stress results from the summation of the normal stress induced by the normal force and the normal stress induced by the bending moments caused by the shear forces and moment at the wing attachment. The variables and the corresponding values are to be found in equations 9.4.5, 9.4.6, and 9.4.7.

$$\sigma_N(x) = \frac{N(x)}{A} \tag{9.4.5}$$

$$\sigma_M(x) = \frac{M(x) * y_{max}}{I_{xx}} \tag{9.4.6}$$

$$\sigma(x) = \sigma_N(x) + \sigma_M(x) \tag{9.4.7}$$

Shear stress
In addition to the normal stress, a shear stress acts on the fuselage caused by the shear forces. In order to determine this stress, the shear flow through a cross-section of the fuselage is calculated using equation 9.4.8.

$$q_s = -\frac{I_{xx}V_x - I_{xy}V_y}{I_{xx}I_{yy} - I_{xy}^2}\int_0^s t x \mathrm{d}s - \frac{I_{yy}V_y - I_{xy}V_x}{I_{yy}I_{xx} - I_{xy}^2}\int_0^s t y \mathrm{d}s \tag{9.4.8}$$

Due to symmetry in two directions ($I_{xx} = I_{yy}$, $I_{xy} = 0$) and the lack of a lateral shear force ($V_x = 0$), this reduces to the following:

$$q_s = -\frac{V_y}{I_{xx}}\int_0^s t y \mathrm{d}s \tag{9.4.9}$$

The shear flow is evaluated by making a cut at the bottom of the fuselage cross-section, along the line of action of the shear force in y-direction going through the shear centre. This is depicted in figure 9.18. This cross-section is evaluated through angle θ, rather than along distance s. This results in the following:

$$y = -\cos(\theta) \tag{9.4.10}$$

$$\mathrm{d}s = r\mathrm{d}\theta \tag{9.4.11}$$

$$q_s(\theta) = \frac{V_y}{I_{xx}}\int_0^\theta r^2 t \cos(\theta)\mathrm{d}\theta = \frac{V_y r^2 t}{I_{xx}}\sin(\theta) \tag{9.4.12}$$

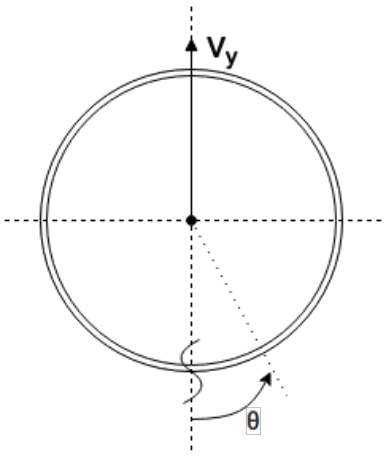

Figure 9.18: The allocation of the cut made on the fuselage cross-section for the shear flow analysis

The maximum shear flow is found at $\theta = \frac{\pi}{2}$ and $\theta = \frac{3\pi}{2}$. This shear flow is translated into a shear stress through equation 9.4.13.

$$\tau = \frac{q}{t} \tag{9.4.13}$$

Impact Stress
In addition to the forces induced during flight, the RPAS shall withstand the forces inflicted upon net recovery. In the most extreme case, the fuselage will take up all the loads inflicted, meaning zero force is absorbed by the frontal area of the wings. The force exerted on the total frontal area of the RPAS is determined in section 14.2

and is found to be equal to 1300.5 N in the positive x-direction. This force is applied to the frontal area of the fuselage model described in equation 9.4.1. The resulting normal force is calculated using equation 9.4.14.

$$\sigma_{impact} = \frac{F_{impact}}{A_{frontal}} \tag{9.4.14}$$

9.4.4 Stress concentrations

In this model the fuselage consists of an uninterrupted hollow cylinder, ignoring the holes created in the fuselage to provide enough space for the integration of the camera, gimbal system, and the attachment of the wings. These interruptions of the structure will cause elevated stresses in the areas around these features. It is however assumed that by including a safety factor in the thickness of the skin surrounding these features, the stress concentrations can be accounted for. This can be supported by the fact that the wing-to-fuselage attachment itself will have a significant strength, such that any loads are (partially) transferred into the combined structure. The exact magnitude of this safety factor is not determined at this stage as a more specific analysis and a more accurate model are required.

9.4.5 Materials and final dimensions

The material used to construct the fuselage is determined by its allowed weight and required strength. In addition to that, the material should allow for cheap and simple manufacturing. As the antennas will not be placed inside of the fuselage (refer to section 10), non-permeable materials can be used. It is preferred to make use of a material that is already used in the design of the RPAS to ensure equal properties throughout the structure. Additionally, larger batches of the same material can be bought, reducing the cost per kilogram of material.

The direction of the fibres is dependent on the prevailing forces and moments acting on the fuselage. The primary contribution to the forces and moments applying on the fuselage consists out of bending and impact. Hence, the fibres will be layed up in the 0° direction. The material properties of the carbon fibre reinforced polymer (0°) can be found in table 9.5. The CFRP layers each have a thickness of 0.125 mm. With the properties of the material known, the calculations in section 9.4.3 are executed for t in the range of [0.125 , 1.000] mm representing 1 to 8 layers of CFRP, at a load factor equal to 1 and 15. The results from these calculations are presented in table 9.7. Note that the calculated stresses are all maximums.

Table 9.7: Resulting maximum stresses for varying thickness at n = 15.

n	**-**	**1**								**15**							
t	**[mm]**	**0,125**	**0,250**	**0,375**	**0,500**	**0,625**	**0,750**	**0,875**	**1,000**	**0,125**	**0,250**	**0,375**	**0,500**	**0,625**	**0,750**	**0,875**	**1,000**
σ_M	$[MPa]$	9,06	4,53	3,02	2,27	1,81	1,51	1,29	1,13	567,70	283,85	189,23	141,92	113,54	94,62	81,10	70,96
σ_N	$[MPa]$	0,25	0,13	0,09	0,06	0,05	0,04	0,04	0,03	0,25	0,13	0,09	0,06	0,05	0,04	0,04	0,03
σ_{impact}	$[MPa]$	16,57	8,29	5,53	4,15	3,32	2,77	2,38	2,08	16,57	8,29	5,53	4,15	3,32	2,77	2,38	2,08
τ_V	$[MPa]$	0,35	0,18	0,12	0,09	0,07	0,06	0,05	0,04	0,35	0,18	0,12	0,09	0,07	0,06	0,05	0,04

From the table it follows that the most extreme loading on the fuselage originates from bending. The values in table 9.7 are compared to the mechanical characteristics of the CFRP material selected. From this it can be concluded that two layers ($t = 0.125\ mm$) would suffice, when regarding all maximum stresses individually. The values listed will however have a shared contribution to the total stress, which will at all times exceed the maximum value within the table. Thus an amount of four layers of CFRP ($t = 0.500\ mm$) is selected to provide a sufficiently large margin (approximately 4 for compressive strength). Additionally, this amount of layers will guarantee the fuselage will maintain its shape.

9.4.6 Fuselage joint

The fuselage and wing have to be joined. The joint section of the wing can be slided into each other with wooden fittings which transfer the loadings on the wing to each other. The bending loading of the wing withstands itself in the wing joint, this because the bending moments of both half wings cancel each other out. However the shear and torsion loads will be transferred to the fuselage. Figure 9.19 shows the structural layout of the fuselage joint. The fuselage joint consists of three thick webs which transfer the loads from the wing to the structure of the fuselage. These webs are made of the Abachi wood [59]. Furthermore at the outside of the fuselage loads are transferred to the skin as well. This configuration is shown, because the skin of the wing is designed to withstand all loadings. No rod is used which can be fitted in the joint. The pin holes are also fitted with pins to keep the wings in place. To fit the pins and connect the cabling of the fuselage to the wing a hatch can be opened at the top of the fuselage skin.

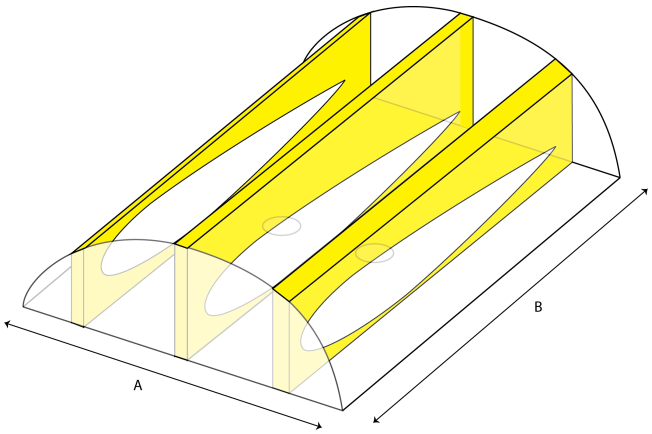

Figure 9.19: Fuselage structure of joint

9.5 Mass budget and centre of gravity

During the design process a few requirements are very restricting the design choices. One of those design requirements is the maximum take-off weight (MTOW) of 20 kg. If the mass budget would increase, it would influence the design of the RPAS and the transportability of the RPAS. In order to assure the mass budget is not exceeded, a MATLAB code is written which calculates the mass according to several design parameters. These parameters include mainly dimensions of sub components, material properties, and, when of the shelf products are implemented, a centre of gravity and mass. From these parameters a component mass, total mass and a total centre of gravity follows. A first estimation of the mass is based on a simplified model for initial indication of the centre of gravity. For the centre of gravity calculation the X-axis is assumed to start at the nose and is positive towards the propeller. Furthermore, it is assumed that for the fuselage the coordinates of the centre of gravity in the longitudinal wing direction and the nadir direction are zero. This assumption is based on the fact that the wing is symmetric and all systems in the fuselage are positioned in these directions at relatively short distance from the X-axis. Therefore, their influence on the centre of gravity shift is negligible. During the design process the mass budget is watched and verified with the CATIA model during. This first mass approximation model contains a hollow cylindrical shape representing the fuselage and a straight non tapered wing without sweep. The airfoil of this wing assumed to be elliptical and with the average chord line of the actual wing shape. From this model a rough indication of all mass components is made. Wherever needed, sub components are demanded to be designed lighter to meet the mass requirement. The masses of sub components are compared to similar components on similar RPAS. [22] After a few iterations the mass model is updated to a more detailed model figure 9.20.

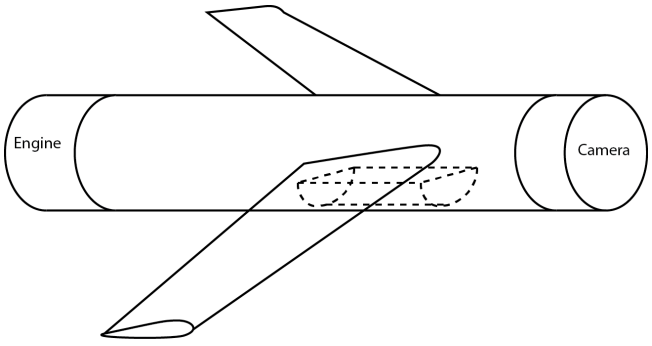

Figure 9.20: Change of cg w.r.t. sweep

The second mass model contains a cylindrical shape that functions as the fuselage. The fuselage accommodates the imaging system in the front, the engine in the back and the fuel tank in the middle. The fuel tank is placed at the centre of gravity of the RPAS model. This is done to prevent shifting of the centre of gravity during operation, as the amount in the fuel tank will decrease during operation. That would cause trouble for the stability and control of the RPAS.

The wing of this model is accurately modelled by dividing each wing in 1000 pieces and calculating the area, perimeter, and volume of each piece. For each piece the area and perimeter are calculated by taking the relative

chord value of the piece with respect to the imported standard airfoil with a 1 m chord line. That chord ratio of each piece is set by the position and taper of the wing with respect to the total length of the wing perpendicular to the fuselage. This is a linear relation. Then integrating the values for each piece over the total wing gives the result for the total wing and by using density values for the composite and the foam, the total mass is determined. By using the mass and centre of gravity of each piece a centre of gravity of each wing can be computed, to be used for total RPAS centre of gravity calculation. This centre of gravity is calculated with equation 9.5.1. [60]

$$x_{cg} = \frac{\sum m_i \cdot x_i}{\sum m_i} \tag{9.5.1}$$

After the centre of gravity is calculated it will be needed to account for the sweep. With equation 9.5.1 applied to the y-coordinate (positive in the direction of the right wing), the additional space in x-direction can be accounted for. This relation is shown in figure 9.21. By adding the additional space in x-direction to the x_{cg}-coordinate of the straight, tapered wing with airfoil, the x-location of the wing is determined.

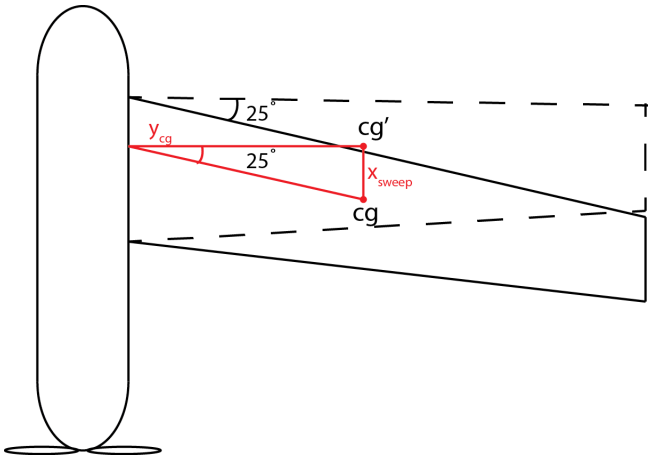

Figure 9.21: Change of cg w.r.t. sweep

At the end of the design process a complete RPAS design was implemented in MATLAB, showing all component masses and the x-coordinate of the centre of gravity. The final model used for calculating the centre of gravity is shown in figure 9.22.

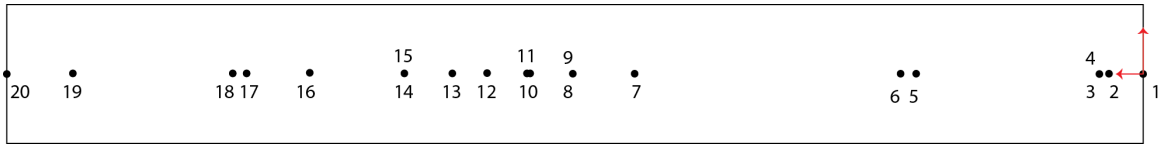

Figure 9.22: C.g. position of subsystems

The final configuration contains all sub components masses and centres of gravity. In this model the final position of the wing is determined according to the centre of gravity of the total mass of the RPAS. Using stability and control analysis from section 7, the centre of gravity was determined to lie at least 12 cm in in front of the leading edge of the wing at the root and preferably as close as possible to that point. By trial and error the x-coordinate of all components is found. This results in the leading edge of the wing starting at 0.528 m from the nose. The camera was moved from the nose to the belly of the RPAS for a better view. Figure 9.22 shows the final model. The masses of all components are shown in table 9.8.

By using equation 9.5.1 the centre of gravity with a full fuel tank is found to be positioned at 0.887 m. However, for an empty fuel tank the centre of gravity shifts to 0.867 kg. This shift in centre of gravity is even more critical when the RPAS is flying with a pitch up angle and the tank is filled with half of the total amount of fuel. In this critical situation the centre of gravity was set at the minimum distance of 12 cm from the trailing edge of the wing, resulting in 0.902 m. As that was the minimum distance required for control and stability, the centre of gravity lies further away from the trailing edge of the wing when the tank is filled completely. In order to stabilise this shift in centre of gravity, solutions like a bladder fuel tank, or an integrated movable fuel tank inside the fuselage could be implemented. However, this requires research that is out of the scope of this DSE

Table 9.8: Components mass budget and centre of gravity

Number	Component	Mass $[kg]$	X-coordinate center of gravity $[m]$
1	Pitot tube	0.050	0.000
2	Batteries	0.188	0.050
3	Autopilot	0.050	0.060
4	Raspberry	0.042	0.060
5	Camera system	1.000	0.330
6	Upper frame front	0.084	0.350
7	Wing, winglets, microphones, rudders, elevons and servos	4.432	0.740
8	Lower frame	0.338	0.825
9	Fuselage	1.300	0.825
10	IMU	0.048	0.890
11	Wing joint	0.377	0.903
12	Fuel and fuel tank	4.429	0.950
13	Transponder	0.100	1.000
14	Upper frame back	0.253	1.070
15	GPU	0.500	1.070
16	Antenna and modem first	1.250	1.200
17	Videostorage and processing	0.050	1.300
18	2x antenna and modem back	0.800	1.320
19	Engine, generator and engine cap	2.120	1.550
20	Propeller	0.113	1.650
	RPAS	17.574	0.887

and is therefore recommended for future investigation. Furthermore, to prevent splashing of fuel inside the fuel tank, division walls will be mounted inside the fuel tank. The division walls will be mounted vertically and have holes on the upper, lower, left, and right side. This will ensure that the fuel hose is always provided with fuel during every manoeuvre of the RPAS.

By summing up the values for all masses, a final mass of 17.574 kg is found. As the RPAS is designed for generating 18 kg of lift, there is still 0.426 kg left. Wires and additional plugs need to be taken into account when manufacturing the RPAS. The reason the mass was first set at 18 kg and not 20 kg, as was set by the maximum take off weight requirement, was due to 10% contingency in the mass budget. Eventually it turns out that all subsystems can be fit into the 18 kg. Weighing 2 kg less, the RPAS uses less fuel and is therefore more environmentally friendly than with a maximum take off weight of 20 kg. This satisfies the maximum take off weight requirement of 20 kg and maintains a sustainable design.

9.6 Manufacturing, assembly, and integration plan

The manufacturing, assembly and integration plan of the production of the RPAS is summarised in three separate flow diagrams: the production of the wing, the production of the fuselage and subsystem frame, and the assembly of the wing. In all figures the basic components are produced before assembling the parts. Production of the fuselage and subsystem frame can be done simultaneously with the production of the wing and the winglets. Assembling the subsystem frame, the fuselage, and the wing is done afterwards. For the production inspiration was taken from the model air plane sector as the RPAS has a similar layout and order of magnitude. [22]

For manufacturing the wing several options can be chosen. The composite of the wing can either be produced by shaping the carbon fibre with the use of a mould, or by cutting the foam first and using the foam as a mould, or by using filament winding. The problem with a separate mould for a carbon fibre shape is that it is very expensive and will only be profitable in case a large production series. As by market analysis the RPAS is expected to be produced in the amount of several dozens, it is beneficial to produce the wings by using the foam as a mould. The manufacturing of the wing is summarised in figure 9.23.

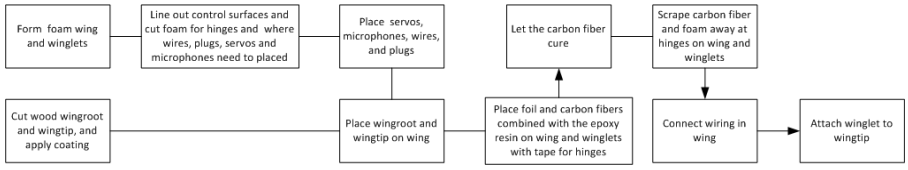

Figure 9.23: Flow diagram of the wing manufacturing

First, the wooden wingtips and wooden wingroots are cut out and impregnated with a water-resistant coating. This can be done simultaneously with cutting the winglet and wingfoam. The foam is cut in two halves. This way, it is easy to cut out the spaces for the servos, microphones, and wires and to mount them. The two halves are glued after placing the electronics. Then the control surfaces are cut out and a special type of model airplane tape is used as a hinge. Then the foam is covered with a foil and by using epoxy resin moulding the composite layers will be shaped around the wing foam. The skin will not be glued to the foam as that would require cutting the carbon fibre skin for inspection and maintenance. Once the carbon fibre has hardened and has reached its final shape, the wooden wingtips and wingroots can be mounted. For the plug in in the wooden wingtip, a hole needs to be cut in the composite skin. In the winglets a few holes need to be drilled into the wooden wingtips. Finally the winglets will be mounted to the wingtips with screws. Around the cuts local extra composite layers will be added to compensate for the stress concentrations due to the cut out. Furthermore the elevons are made by scraping carbon fibre away. In the carbon fibre layers tape is put in between the layers, which is left for the elevons. When the foam and carbon fibre is scraped away the elevon is able to turn. The servo is connected with a little bar to the elevon to turn it. An overview of this joint is shown if figure 9.14.

For manufacturing the composite fuselage a mould will be used, because the fuselage does not contain foam to be used as mould. As filament winding is used for unidirectional laminae, and for this RPAS woven laminae are preferred for multiple directional strength [61], the lay up method is chosen. The mould is applied with layers of carbon fibre and epoxy resin. After that process the carbon fibre is hardened by waiting a couple of hours. Next, several holes need to be cut in the cylindrical fuselage for the camera system, the wing joint, the antennas, and the engine mount. Then inside the fuselage a frame will be placed for mounting the subsystems.

The subsystem frame is made of aluminium as this is an isotropic material with high Young's Modulus compared to the density and is commonly used in aerospace engineering. [62] It is produced such that all subsystems are attachable and detachable to this frame. The frame has one lower sub-frame looking like a half a cylinder skeleton and two upper sub-frames in similar shorter shape. As shown in figure 9.24, the sub-frames are attached to each other by means of a sliding system. This makes maintenance of the mounting systems a lot easier as the subsystems can be detached after sliding out the frames.

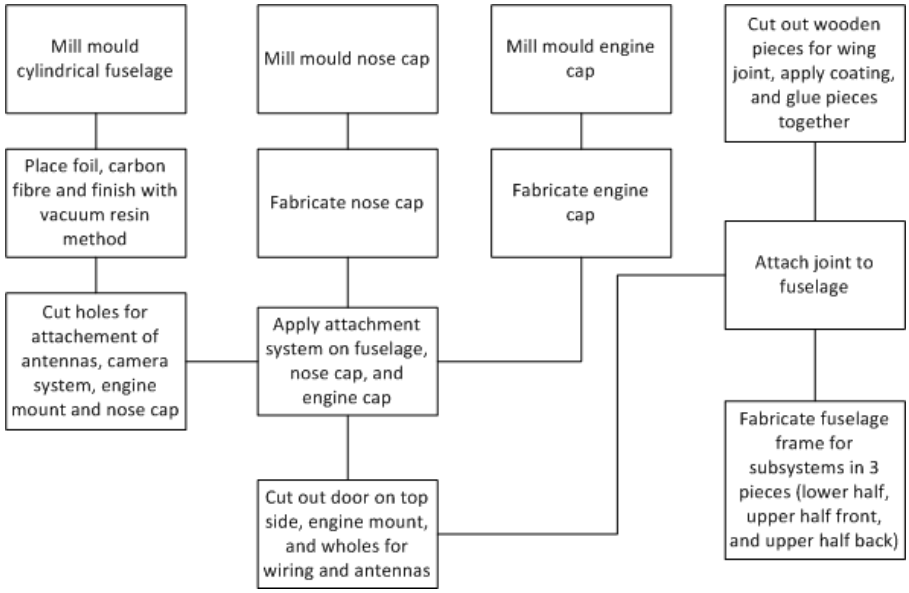

Figure 9.24: Flow diagram of the fuselage and subsystemframe manufacturing

In the end, the wings, the sub-frames, subsystems, the fuselage, and the front and back of the fuselage can all be assembled. The final assembly flow diagram is shown in figure 9.25. The last step of assembling, mounting the wings of the RPAS, is the only step that is performed every time the RPAS is deployed. Consecutively the RPAS is fit into a suitcase for transport to the operational location.

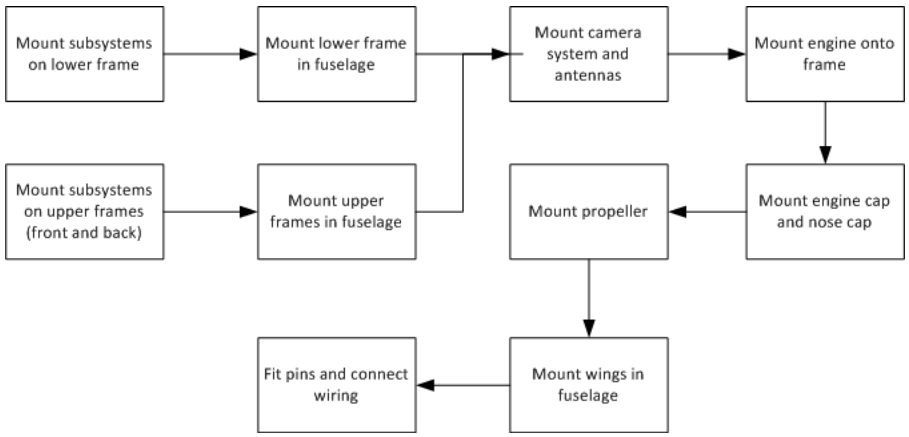

Figure 9.25: Flow diagram of RPAS assembly

9.6.1 Production costs materials and manufacturing of the wing and the fuselage

The cost of production of the fuselage structure, wing structure and assembly of the components is divided into the categories materials, tools, and man-hours. For man-hours an estimate of the salary is made of €25 per hour based on salary calculations of section 14.7 and a contingency factor of 25%. The final production price is based on this. A risk of unreliability lies in the salary price though, as this can differ from company to company. Therefore, a high Dutch standard of salary was taken into account. Table 9.9 shows a list of all costs that are made during production. For contingency some margins are added to assure not exceeding the budget that is further explained in section 16 about the total costs. As can be seen in the table, the final cost of the RPAS structure results in approximately €16,550.

Table 9.9: Production costs of the wing, fuselage, frame, and fuel tank.

Material	Component	Material Costs	Tool Costs	Labour Costs	Total Component Costs
	Fuel tank	€150			€150
	Fuel cables and filters	€30			€30
Aluminium [63]	Fuselage frame	€40	€50	€1000	€1090
Screws	Fuselage frame	€20			€20
Adhesives[64]	Fuselage	€20			€20
Foam [65]	Wing	€667.92	€50	€1000	€1717.92
Abachi wood [66]	Wing joint, root and tip	€10	€50		€60
Tape [64]	Hinges for elevons and rudders	€6.71	€50		€56.71
Carbon fibre rolls (100 meters) [65]	Wing and fuselage skin	€5838.25		€2000	€7838.25
Epoxy resin [65]	Wing and fuselage skin	€100		€2000	€2100
	Unforeseen costs	€2000		€2000 €4000	
	Total structural costs				€17082.88

9.7 Sustainability

The RPAS is composed of several materials. The carbon fibre reinforced polymer is one of the most predominant used materials in this design. This material is nowadays often used in aerospace structures. Besides the high strength to density ratio, it also a durable option. Carbon fibre strength degrades very slow in humid atmosphere. Although carbon fibre is durable, the waste is a problem. Eventually the RPAS will be at its end of life. The carbon fibre does not break down easily. Carbon fibres can be reused in other applications, however strength decreases a lot in recycling, as the fir The Rohacell foam is also very durable. Concerning the environment the Rohacell foam is non-hazardous and non-water-polluting, which is beneficial for the maritime environment. However the recycling of the Rohacell foam is a questionable. The foam must be combusted or disposed in a landfill [67]. Furthermore the structure consists aluminium. On contrary to carbon fiber aluminium is much easier to recycle. The properties of aluminium do not decrease after recycling. Aluminium can be reused by melting and forming it for other purposes. Also Abachi wood is used in the design. This is definitely a good choice in respect to the environment. Wood degrades in the environment very easy, which induces less waste.

10 Communications System

The communication system of the aircraft comprises of the on-board and ground station networks, linked together by the transmission channel(s) in between them. This system serves to enable control and feedback between the UAV's subsystems and the operators, as well as enable data access and provision. In this chapter important aspects of the design, as well as the detailed design itself of the communication system are presented.

10.1 Mission and design challenge

Relative to the mission, the communication system plays a crucial role and has direct impact on the mission performance. This is due to the fact that the mission itself is to conduct live surveillance, of which the purpose is to gather information by means of the payload and communicate live information to the interested parties on the ground. The second function is also defined in the mission objective statement with the term RPAS. Remote piloting is a function achieved by close cooperation between the navigation and sensing department and the communication department.

An ideal communication system serves to provide quick, accurate, secure and capable links between the subsystems. Yet there are many challenges that limit these factors and affect the communication performance of the system. Firstly, the transmission medium is one of the greatest limitations, this includes both wired and wireless transmissions, where the latter is generally more challenging to achieve. Requirement CUST-S-9.0 defines a live stream link with a distance of 10 km between the ground station and the UAV, while requirement CUST-S-2.0 sets the UAV to be controllable from a distance of 20 km. Video is a reasonable large information source for the relatively large transmission distance, which forms challenge for communication system design. Additionally, maritime weather conditions can pose limitations in terms of wireless transmission over air as well. Secondly, national and supranational regulations limit the system characteristics of wireless transmission.

10.2 Inputs and outputs

From the N^2 chart it can be observed that the communication system is relatively independent on the mechanical systems of the RPAS, while highly dependent on its electrical system and very significant in terms of the payload, operations and control of the RPAS. As several other systems, many inputs can also serve as an output of the system, depending on the importance and priorities set on the input/output per system. For example, the physical size of the antennas communication system might be an output to the structure of the system, yet there is also a constraint as input from the structure of the system. In the end, a compromise is made and more importance is given for it being an output of the communication system, as compared to other subsystems it plays a smaller role in terms of size occupation. Yet again, the aerodynamics of the UAV can be greatly affected by antenna shape, therefore it is decided to set external shape limitations as input from the aerodynamics department. A complete list of all inputs and outputs of the communication system can be found in the table 10.1.

Table 10.1: Inputs and outputs for communication system

Parameter	Value	Unit	Input	Output	Comments	Source/Destination
D_p	-	$[b/s]$	X		Payload down-link data rate	Payload
D_{cd}	-	$[b/s]$	X		Control up-link data rate	Navigation and Sensing
D_{cu}	-	$[b/s]$	X		Control down-link data rate	Navigation and sensing
C_c		$[m^4]$	X		Network costs	Costs
P_c	-	$[W]$		X	Power requirement	Power
V_c	-	$[V]$		X	Voltage requirement	Power
lll, hhh, www	-	$[mm]$		X	Antenna shapes/dimensions	Aerodynamics
m_c	-	$[kg]$		X	Network mass	Structures and materials

10.3 Design methodology and communication links

Generally the communication system is limited by the wireless communication performance of the subsystem, therefore primary focus has been set on the telecommunication aspects of the RPAS. Telecommunication can consists of several steps, as demonstrated in figure 10.1. The design of the communication system includes making decisions on the elements throughout this link such as the channel selection, modulation, encoding/encryption scheme, converters, antenna selections. It is important to note that designing every detail of the communication system is out of the scope of the DSE project, therefore focus is shifted only to the major influential and definitive characteristics that need to be determined. In the end however, a lot of decisions are limited by the market availability of a product. Therefore the design can be made by two different approaches, one being the scientific/idealistic approach, the other being the practical/design approach. A well balanced combination of both approaches guarantees a professional design of the communication system.[68] [69]

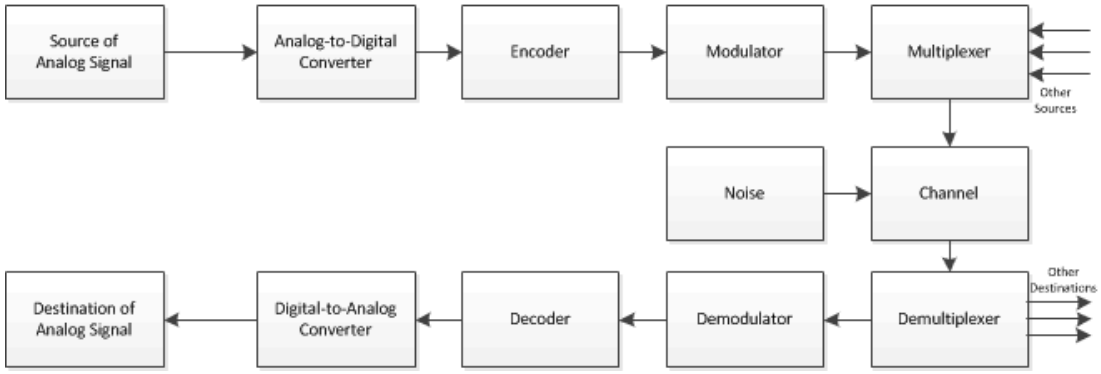

Figure 10.1: Overview of Telecommunication

With respect to risk analysis, the communication system poses a high risk system and therefore needs to be risk mitigated to meet the required confidence levels, which can be achieved by including redundancies. Particularly, the control communication failure poses a higher safety risk than the live stream failure, which only has a risk in not completing the mission. The design of the live stream communication is also a greater challenge than the control communication with respect to the sheer amount of data that needs to be transferred over a large distance. As a result, instead of a single link, two separate communication links are designed in order to guarantee both efficient data transmission as well as safe operation. In table 10.2 the characteristics of each link are defined. These have been estimated by briefly analysing the needs for the on-board system as well as the operator on ground.

The design of a communication system itself is out of the scope of this project, that is why it is aimed to find systems that are as ready as possible. With respect to this, the telecommunication design is limited to selecting the modems, which are generally a combination of modulator, de-modulator and antennas. A gimbal system, which is a motorised turret that provides a casing as well as the pointing accuracy for a sensor such as an antenna. As market research from the payload department reveals, it tends to be difficult to find a gimbal that meets low mass and costs for use on the aircraft. As a result it is noted that omni-directional antennas are preferred on-board, while ground antennas may be directional and motorised.

Table 10.2: Links characteristics

Link	Medium	Minimal distance	Data rate	Update rate	Risk	Security
Live Video	Air	10 km	High	Low	Low	Low
Flight Control	Air	20 km	Low	High	High	High

10.4 Transmission channels, data sources and sinks

The transmission channel is the medium through which the signal is transmitted. Every channel has its characteristics and effect on the communication link. Wired communication is generally a more energy efficient means of communication as less attenuation takes place than wireless communication, however many times this is not a possible option when the transmitter and receiver have a large distance between them. There are three different ways the electromagnetic wave can propagate, namely the ground-wave, sky-wave and line of sight (LOS) propagation. From market research it appears that the first two methods are not used as frequencies above 2 MHz and above 30 MHz are used for most similar communication systems. This leaves two channels

in the field of LOS communication, namely the direct link and the public network link. The first option uses a direct LOS link with a license free frequency, while the second one uses a public satellite network or ground network, like for instance the GSM/CDMA/3G network. Many maritime environments are prone to have low or no signal from these networks, such as large harbours, as there is a rather low amount of mobile phone users in such areas. As a result, it will be assumed that only direct LOS links can be used.

Data sources are devices from which data is put out, while data sinks are devices where data terminates. Analysing the on-board data sources and sinks, table 10.3 of signals has been compiled with their association to down-link/up-link, their accuracy and their update rate.

Table 10.3: Signals for Control, Navigation & Sensing

Signal	Up-link/Down-link	Precision	Update rate
Live video	Down-link	High	Low
Stored video	Down-link	High	Low
Payload power on/off	Up-link	Single	Low
Shutter on/off	Up-link	Single	Low
Zoom	Up-link	High	High
Pan	Up-link	High	High
Tilt	Up-link	High	High
Engine power on/off	Up-link	Single	Low
Engine throttle command	Up-link	Low	High
Engine RPM command	Up-link	Low	High
Elevon deflection command	Up-link	High	High
Rudder deflection command	Up-link	High	High
Engine throttle status	Down-link	Low	High
Engine RPM status	Down-link	Low	High
Airspeed	Down-link	High	High
Altitude	Down-link	High	High
Attitude	Down-link	High	High
Heading	Down-link	High	High
GPS Position	Down-link	High	High
Object detection front/left/right	Down-link	High	high
Transponder status	Down-link	Low	High
Computer health status	Down-link	Low	High
Power health status	Down-link	Low	Low
Engine health status	Down-link	Low	Low
Fuel gauge status	Down-link	Low	Low

10.5 Iterations: data rate and bandwidth

Before starting to specify the data rate and bandwidth, it is important to clarify one matter that can be confusing for parties of different technical background. There exist two definitions of the word 'bandwidth' in professional terminology, these vary in the field of computing and telecommunication and non-professional use. The communication definition of bandwidth is the absolute difference between the highest and lowest frequency that is used to transmit a signal, thus being the physical 'width' of the frequency 'band'. The more popular computing definition, which is also used by consumers, is in fact the same definition as the data rate, thus the amount of information, quantified by the number of bits, that can be sent and received per second. As a result, the first definition has a standard unit of Hertz while the second has the standard unit of bits per second. For the sake of consistency, the first definition of bandwidth will be used throughout the project, and the second bandwidth will just be termed data rate.

Each communication link consists of different data rates and bandwidths. While the bandwidth, as discussed in section 14.8 is limited by regulations, can be utilised maximally within the legal and capable limit, the data rate is defined by the data sources and sinks. Nevertheless, since these data sources and sinks are prone to change, this phase of the design involves several iterations.

The first iteration of the communication system design is very preliminary. The data rate values are extracted from the conceptual design of the payload, while a preliminary estimation of all the control signals and their size and rate is made with the aid of table 10.3. In the conceptual design, an 1080p HD resolution, 4-bit colour depth, 25 frame rate and 60:1 compression ratio has been chosen. For simplicity, each data source is assumed to be digital and signals are either a single bit or a floating point number, which has two levels of accuracy.

Each accuracy consists of a different number of bits, which can be calculated by looking at the number of significant figures and digits for the exponent are required. At the first iteration, all values have the same accuracy, presentable by 16 bits. Additionally, three different levels of update rate are defined, namely 10, 30 and 60 Hz, which are assigned to every signal by accounting the importance of the operator being updated about this value. This results in a payload data rate of 3.456 Megabits per second ($Mbps$) as well as a control data rate of 6 kilobit per second ($kbps$) as provided in 10.5.

For the second iteration, the value of the data rate for the payload has been updated. As live video streaming over a large distance is a challenge for the communication system design, it was requested by the communications department to keep the payload output data rate as minimal as possible, while still fulfilling the mission requirements. As a result, the payload has been chosen yielding the updated characteristics listed in table 10.3. The 25 frames per second (fps) can be converted into a lower frame-rate on-board as well, as such a high rate is not required by the payload, however this is not considered in the second iteration, as it requires video stream manipulation and adds delays. Additionally, the video format and video codec with the highest compression ratio, namely H.264/MPEG-4 AVC with a 60:1, can be used to minimise the data rate. Taking all these values into consideration, the data rate of the payload can be estimated to be approximately 1.5 $Mbps$, as can be calculated with the equation 10.5.1 and demonstrated on table 10.4 and on table 10.5. In equation 10.5.1 D_p presents the payload video datarate in bits per second, while IR presents the imaging resolution comprised of the vertical and horizontal pixel amounts, CD represents the colour depth in amounts of bits, FR represents the frame rate in frames per second and CF represents the compression ratio, which has no units.

$$D_p = IR \cdot CD \cdot FR \cdot CF \tag{10.5.1}$$

For the third iteration, the navigation and sensors department is consulted to correct the estimation of the data rate for the control signals. After some consultation with more professional individuals, it becomes clear that the 60:1 compression ratio has a certain risk involved, as it might lower the quality of the picture for the purpose of identifying the required objects of interest. This suggests that it is safer to incorporate a lower compression ratio, for a different video format and codec. From reference [70] other video formats for video streaming are WMV9, H.263 and MPEG-2, where the latter two have a compression ratio of 30:1. In order to account in the likelihood of having to use these video formats with half the compression ratios, the data rate is doubled. Also, in case it is not possible to adjust the frame rate, due to either payload limitations or in case this introduces additional delays, 50 fps is accounted for instead of 25 fps. This method is a safer approach for design of the communication system and gives a more professional solution than including an estimated safety factor. The final values for the data rates are 6 $Mbps$ for the live payload link and 3.382 $kbps$ for the control link.

It is important to note that the selection of precision and update rate in table 10.3 has been made with consideration of operational sensitivity for the value, while the high update rate signals usually require quick responses, high precision signals require more detail. Additionally, the selection for the numbers associated to the qualitative assessment of the signals has been estimated by considering floating point computing and calculating the amount of bits required for the set amount of digits for the significant and exponent of the number. Thus a high precision accounts for 4 digits for the significant, 2 digits for the exponent, and the low precision accounts for 2 digits for the significant and 1 digit for the exponent (while the signs account for 2 bits). This results in a high precision floating point number being 23-bits while the low precision one is 13-bits.

The final iteration takes place once all the systems have been determined. After applying the results from the third iteration into the link budget tool, some market research and more consultation with professionals has been done. It becomes clear that it is very difficult to find a suitable system in the market, as data rates not only differ immensely between theory and practice, but communication system providers also do not guarantee a certain data rate at a certain distance. Therefore the focus is shifted towards data handling in order to minimise the data rate and guarantee the required quality of images. These steps are considered in the following subsections. The results of these are also provided in table 10.5.

Table 10.4: Data rate iterations for live stream

Iteration	Image resolution	Frame rate	Colour depth	Compression rate	Data rate
1	1920 x 1080 pixels	25 fps	4 bits	60:1	3.456 [$Mbps$]
2	768 x 576 pixels	25 fps	8 bits	60:1	1.475 [$Mbps$]
3	768 x 576 pixels	50 fps	8 bits	30:1	5.898 [$Mbps$]
4	320 x 200 pixels	1 fps	8 bits	1:1	0.512 [$Mbps$]

Table 10.5: Data rate iterations for control

Iteration	Up-link/Down-link	Comments	Data rate
1	Up-link+Down-link	A preliminary list of 12 signals is used, assigned with 17-bit size for precision and assessed with the update rates 10, 30 and 60	6 [$kbps$]
2	Up-link+Down-link	The second iteration uses the same vlaues as the first	6 [$kbps$]
3	Up-link	The new list of signals from table 10.3 is used, a low update rate is assigned as 1 Hz, a high update rate as 10 Hz, a single precision is of 1-bit, a low precision is of 13-bit, and a high precision is of 23-bit size.	1.422 [$kbps$]
3	Down-link	Same computations apply as the up-link.	1.939 [$kbps$]

10.6 Data handling

Data handling involves the manipulation and adjusting of data supplied by data sources in order to change the unusable raw data format into a usable final data format. A lot of devices already include a data handler, however the UAV features a dedicated data handling subsystem as it tailors the specific needs of the communication system of the UAV itself.

10.6.1 Packetization

Packetization involves the grouping and multiplexing of data digitally before the wireless transmission. As already determined two data links exist, one for the live streaming and the other mainly designed for the flight controls. Therefore the first two packets that exist are the Live Video Packet for the down-link and the flight command packet for the up-link. In addition to this, there is a payload control packet for the up-link, the flight status packet for the down-link and the system status packet for the down-link. The contents of these digital packets are summarised in table 10.6.

Table 10.6: Data packetization

Packet	Link	Contents	Size	Update rate
Live video packet	Payload down-link	Live video feed, stored video feed	500 kb	1
Payload control packet	Control up-link	Payload power on/off, Shutter, zoom, pan, tilt commands	701 b	10 [Hz]
Flight control packet	Control up-link	Engine power on/off, engine throttle, engine RPM, Elevon deflection, rudder deflection commands	721 b	10 [Hz]
Flight status	Control down-link	Engine throttle, engine RPM, airspeed, altitude, attitude, heading, position, elevon deflection, rudder deflection, object detection front/left/right, transponder status	1,770 b	10 [Hz]
System status packet	Control down-link	Computer, power, engine health status and fuel gauge	169 b	1 [Hz]

10.6.2 Video processing

In the previous subsection, focus has been shifted on lowering the data rate of the video stream by video processing. As a result, a dedicated video processing unit (VPU) is involved in converting the large payload signal into a suitably-sized signal. After this step, the signal is multiplexed and modulated for the antenna to be sent. The inputs and outputs of this system is presented in the block diagram in figure 10.2. In this figure the video format compression ratio has not been taken into account, as the suitability of the video format is not set and can be varied according to results. It is important to note that the target tracking computer included in the payload uses the full resolution and frame rate of the PAL video stream, and the video processing unit is only designed to deliver the required live video for fulfilling requirements CUST-S-5.0, CUST-S-6.0, CUST-S-7.0 and CUST-S-8.0.

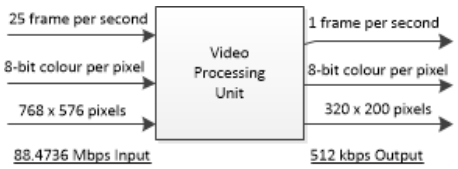

Figure 10.2: Video Processing Unit (VPU)

Related to the subject matter, it is important to be able to detect an object of interest and zoom into it for more detail. The resolution is adjusted to keep the data rate output minimal and still be able to report observations. The frame rate and colour depth is also adjusted, however these are set to fixed values. The minimal colour depth remains 8 bit, while the minimum frame rate is evaluated.

It has already been discussed that a large frame rate is not required, therefore the minimum frame rate is determined by means of looking at possible moving objects and the ability to track them. Brainstorming through possible scenarios in maritime areas, it results that the fastest possible moving object in the maritime environment would be a jet ski or car driving at speeds of approximately 140 km/h, thus around 40 m/s, which is a high estimation considering a research on the allowed maximum legal driving speeds on highways of several countries. If this speeding object crosses the coverage area of around 150 m length, as determined in the payload department, while the UAV is cruising at 28 m/s, the detection time for the object is slightly higher than 2 s. Using the sampling rate theorem, the frame rate of the video stream can even be re-framed to 0.5 fps, nevertheless to comply with the data being a video, a minimum frame rate of 1 fps is decided to be used.

Since the altitude of the RPAS is 200 m and the zoom feature of the payload provides a minimum field of view (FOV) of 1.6 °, the minimum swath width, which is the cover area dimensions at maximum zoom becomes 5 m, as calculated with equation 10.6.1. In this equation SW represents the swath width in meters, h represents the altitude in meters and FOV is the field of view in degrees. From the potential scenarios, the most critical scenario is identifying the number of passengers on a small inflatable boat or a kite surfer in need. This required identifying an inflatable boat and a kite surfer's kite without zoom, and the passengers with zoom. Assuming minimal top-down area of a single passenger of approximately 0.25 m [71], and an inflatable boat width and kite width of 1.5 m provides the required pixel width[72] [73]. Applying this, the required resolution of 100 x 100 at no zoom, and 20 x 20 at full zoom can be calculated with equation 10.6.2. In this equation, PD represents the pixel dimensions, which are in meters. However, to account for correct detection and redundancy, more than one pixel is required to identify an individual. After some research for video resolutions, it becomes clear that even the lowest common display resolution, namely QVGA 320 x 240, satisfies more than sufficient amounts of pixels of the targets. Without zoom the pixel dimensions become 0.469 x 0.625 m while with maximum zoom they are 0.016 x 0.021 m, which is certainly sufficient to even identify details such as limbs and items, like for example weapons. Considering operation however, it is simpler to conduct the imaging with less zoom, as the higher the zoom, the more the gimbal has to be directed to the target. Nevertheless, the automatic target tracking feature of the payload facilitates this task of the operator.

$$SW = h \cdot tan(FOV) \tag{10.6.1}$$

$$IR = \frac{SW}{PD} \tag{10.6.2}$$

It is also important to note that the image quality and sharpness of a camera cannot be fully judged by the resolution, colour depth and frame rate, and the specifications like for instance details on the video codecs, exposure (for lighting conditions) and sensor size and technology will also affect the quality of the image. However, since these topics are out of the scope of the project, they will not be considered in this report.

As a result, the VPU converts and formats the payload video output into a reformatted compressed video signal, which proceeds to the encoder and modulator. The final input and outputs of the VPU are displayed in red in figure 10.2.

10.6.3 Encryption and modulation

Encryption is the process of an encoder adding additional codes of data to a data packet in order to make the data exclusively readable by the receiver that has the specific decoder. This is an important procedure to ensure that no other individuals can abuse the communication link, or even try to hack the system. In table 10.2 the column safety describes how important it is for the channel to be secure in order to avoid drastic incidents, such as hacking, which could results in crashes. It can be observed that the control link, which is a high risk

system, has a high safety requirement, therefore encryption in this communication link is of high importance. Additionally, while safety is not of huge concern for the live video link, it can still inhibit minor security features. It is therefore favourable to have encoders within the communication link, however it is out of the scope of the project to select or design a specific encoder, yet it is bared in mind that this is a favourable feature that could be included in the modem.

Besides coding for encryption, there are also source and channel coding that matter in a communication link. The source code is related to the data packet and format of the data that will be sent, as it lowers the amount of data rate sent by means of formatting the data. This task is completed by the VPU for the live video, however an additional processor is assigned for processing the flight data packet, as well as the other packets. As encoders take place in processors, so do decoders, therefore both RPAS and ground station have their respective VPU and data processing unit. The channel code on the other hand is a coding that implements redundancy to the transmitted signal in order to decrease the bit error rate (BER). In theory, polar signalling and binary phase shift keying (BPSK) are preferred coding schemes as they produce a lower bit error rate. Both of these tasks are assigned to the processors, however are not designed in detail, as they are out of the scope of the project.

Another feature that is prime in the modem is the modulator and de-modulator. These components determine the modulation which is used for the signal. Modulation is a signal process that transforms a signal to a desired carrier configuration before sending it to the antenna. There are various modulation types that can affect the performance of the communication system, however since the modulation type of available modems are set by their manufacturers and not adjustable. Besides that, modulation is also out of the scope of the project, as it is a large topic for electrical and telecommunication engineers, therefore no favourable modulation is selected for the communication system. [68] [69]

10.6.4 Data handling block diagram

The data handling block diagram is a flow chart that highlights the data channels and their characteristics between the data processing components of communication system. In figure 10.3 most inputs and outputs to the on-board computer are shown. Since not all protocols for these are known, the interfacing remains a subject for latter consideration. However, all inputs and outputs are collected by means of their respective ports and busses, which connect to the Input/Output (I/O) Hub of the chipset. This data is then processed by means of the central processing unit (CPU) in combination with additional random access memory (RAM) depending on what program/software is installed on the programmable read-only memory. The PROM contains the BIOS as well as the operational modes installed on them. Data rates of most inputs and outputs are given, although the PFC, Data log, and video storage inputs and outputs are not set yet as they can be adjusted according to different requirements. Finally, an effort has been made to determine the required bus frequencies, nevertheless it becomes clear that this is of the scope of the project and can be considered as future task.

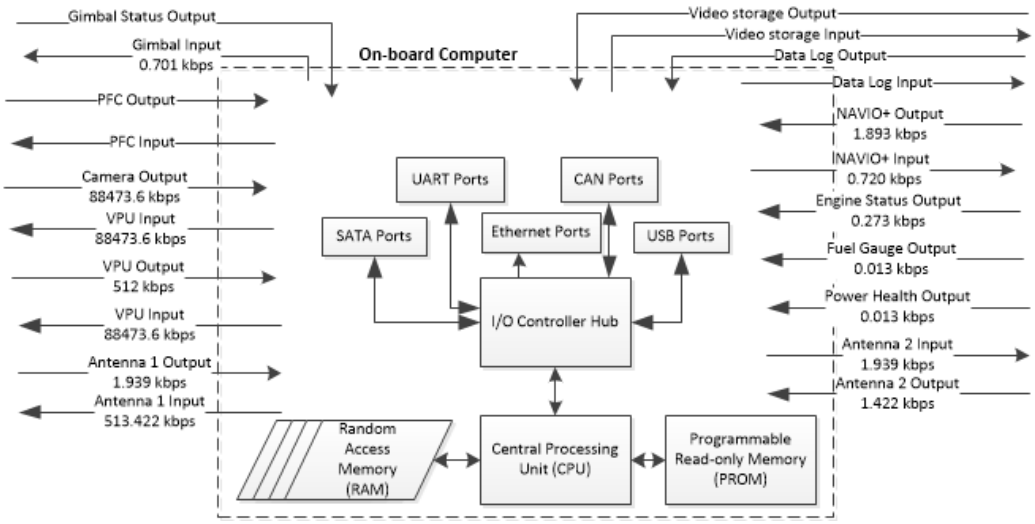

Figure 10.3: Data handling block diagram

10.7 Link budget

The link budget is a vital tool to account for the communication performance of the link and is used to determine the required design characteristics of the elements within the communication link. The signal-to-noise ratio

(SNR) specifically affects the likelihood of correct detection of the signal and therefore is of primary focus of the link budget. Equation 10.7.1 is the link budget equation, and demonstrates the components as well as the effect on the power level of the communication link, where the variables SNR are the signal-to-noise ratio, P is the power of the transmitter, L_l is the line loss due to losses in the cabling, G_t is t he transmitter gain, L_s is the space loss, L_a is the atmospheric loss, L_pr is the pointing loss of the receiver, G_r is the receiver gain, L_r is the receive loss, D is the data rate, k is the Boltzmann's constant and T_s is the system noise temperature. While gains and losses have no units, power is in Watts, system temperature is in Kelvin, data rate is in bits per second, $EIRP$ is the equivalent isotropic radiated power ($EIRP$) in $Watts$ and the Boltzmann's constant is in $m^2 \cdot kg \cdot s^{-2} \cdot K^{-1}$. This equation is presented in factor form, while the factors can also be expressed in decibels, changing the equation to a summation. [68] [69]

$$SNR = \frac{P \cdot L_l \cdot G_t \cdot L_s \cdot L_a \cdot L_{pr} \cdot G_r \cdot L_r}{D \cdot k \cdot T_s} = \frac{EIRP \cdot L_s \cdot L_a \cdot L_{pr} \cdot G_r \cdot L_r}{D \cdot k \cdot T_s} \tag{10.7.1}$$

The Shannon-Hartley theory, also referred as the Shannon limit defines the capacity of the communication channel. This is another important equation and can be used in addition to the link budget. The formula for the channel capacity is given in equation 10.7.2. C is the channel capacity in bit per second, B is the frequency bandwidth in Hertz while the SNR is the signal-to-noise ratio with no units. It is important to note that equation 10.7.1 is plugged into this equation in order to calculate the channel capacity. The data rate is also be taken instead of the channel capacity and $EIRP$ is made the subject of the equation, in order to calculate the ideal $EIRP$, as applied in the following section.

$$C = B \cdot log_2(1 + SNR) \tag{10.7.2}$$

From research it is found that there are three major levels at which telecommunication is regulated in the case of The Netherlands. The International Telecommunication Union (ITU), the Electronics Communications Committee (ECC), which is part of the European Conference of Postal and Telecommunications Administrations (CEPT), as well as the Radiocommunications Agency (Agentschap Telecom) which is part of the Dutch Ministry of Economic Affairs regulate the frequency allocation strictly. As frequency is strictly regulated, it is important to select a frequency that is legally allowed to be used for the purpose of communicating with the UAV. As the European regulations resemble the Dutch regulations, a communication system that is legal in the Netherlands is more likely to be legal in other European countries, however for legal compatibility with other countries the frequency allocation summarised in ITU's document [74] can be contemplated. The document on the license free frequencies in the Netherlands produced by Agentschap Telecom is browsed through in order to identify the possible frequency bands [75]. This results in the frequency bands 1.A, 1.B, 1.C, 1.D, 1.E, 1.E1, 1.E2, 1.F, 1.G, 1.H, 1.I, 1.K1, 1.K2, 1.L1, 1.L2, 1.M, 1.N, 1.O, 1.P, 1.Q, 1.R, 1.S, 2.A, 2.B, 3.A, 3.B, 3.C, 8.1.A, 8.1.B, 8.1.C, 8.1.D, 8.2.A, where the first digit presents the table number and the second and third alphanumeric character present the row, which specifies the details on the frequency band.

As can be seen from document [75], all frequencies have in addition to the frequency also a maximum bandwidth B and a maximum EIRP value. The EIRP is part of the link budget already, as it represents the transmitter power multiplied by transmitter gain and losses shown in equation 10.7.1. Some frequencies have additional restrictions in terms of duty cycle and power density. Both of these parameters affect the communication performance, however it is laborious to assess how significant they do so, therefore these frequencies pose a higher risk and are less favourable to use for the communication of the RPAS.

Using the frequency options and characteristics and the related equations, a Microsoft Excel Spreadsheet tool is created to calculate the link budget results in every frequency and analyse the results. This tool consists of three sections, one accounting for the down-link of the video stream, one for the down-link of the RPAS's status, and a third one for the up-link of the flight control signals.

10.8 Frequency selection and other characteristics

While the link budget tool is a useful tool to compute important values and characteristics, a judgement needs to made supported by scientific reasoning. Therefore a section for logical tests have been incorporated into the Excel spreadsheet.

Before discussing the tests, it is important to note that from all data rate iterations, it is chosen to use the third iteration for the live video link, namely the 6 $Mbps$, as in practice data rate values can be much less from theoretical values and as states earlier, it provides a safer approach, as it is similar to including a safety factor to the calculations. For the same reason, the same approach is also applied for the flight control link, where the highest data rate is used out of all iterations.

The first test checks whether the channel capacity is smaller than the data rate of the signal, because if this is the case, it is theoretically not possible to send the signal successfully via the specific channel due to the Shannon limit. This result automatically disqualifies a frequency as well.

The second test checks whether the legal constraint for the EIRP is smaller than the ideal EIRP, which was calculated with consideration of the Shannon-Hartley Law and the link budget. This test demonstrates whether a link at a certain frequency can achieve the best performance with the limitations on the EIRP. Failing this test also disqualifies a frequency to be eligible for this design.

The third test is made partially manually and partially automatic, as the free space loss is assessed for the frequencies. The channel loss comprises of the space loss plus the medium loss, which in this case is atmospheric loss. As the space loss varies per frequency and can be presented by equation 10.8.1, the atmospheric losses are addressed by the chart displayed in figure 10.4 [76]. Λ presents the wavelength of the electromagnetic wave in meters, while S presents the distance between the transmitter and receiver in meters. In figure 10.4 label A is man made noise, B is Galactic noise, C is Atmospheric noise, D is Solar noise, E is Sky noise, F is Cosmic noise and G is Rain noise. It can be observed that the higher the frequency, the lower the wavelength, therefore the lower the value L_s, which means the loss is higher. The figures also present a higher attenuation at higher frequencies therefore a lower L_a. In figure 10.4 the same result applies, and it can be seen that in lower frequencies galactic noise and man-made noise apply mostly. It becomes clear that the least noisy spectrum is between 0.1 GHz and 10 GHz for figure 10.4. These founds are taken into account for the selection of frequencies. Once the selection has been done a more precise estimation of these losses is made using the figures.

$$L_s = (\frac{\lambda}{4 \cdot pi \cdot S})^2 \tag{10.8.1}$$

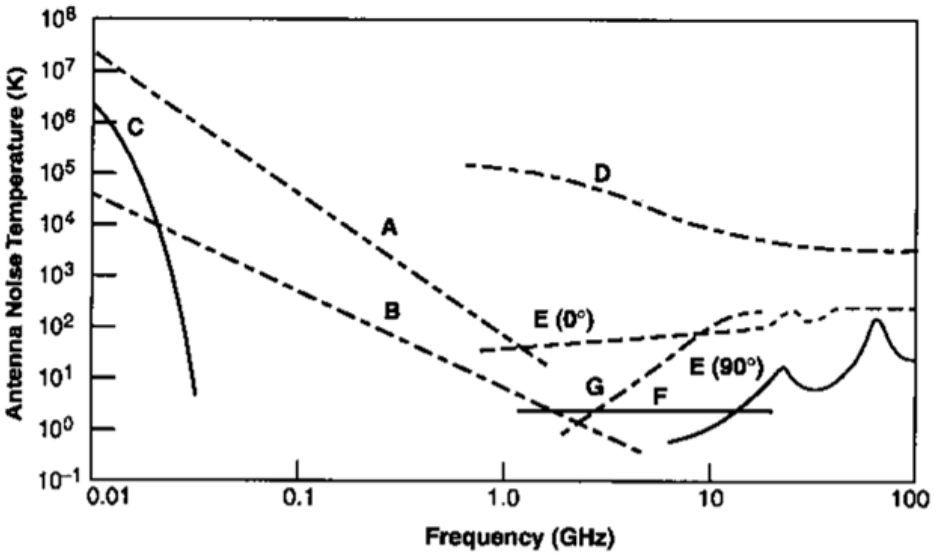

Figure 10.4: Medium-based losses

The results of the previous test are included in the link budget by colour coding a cell with green for criterion passed and red for criterion failed. After these tests, the remaining two tests are qualitative tests, and judge how well a certain frequency meets the ideal link. As the optimal link uses minimal EIRP to achieve them maximal signal-to-noise ratio (SNR), these values are coloured from worst (red) to best (green) in different shades. For this, the ideal SNR is compared with the actual SNR. Additionally the ideal EIRP is colour ranked. By using this method, the most eligible frequency bands for the communication links can be identified visually.

This analysis resulted in frequencies for Wifi, at 2.4 GHz and 5.8 GHz, corresponding to frequency band 1.M and 1.M in the regulations, being estimated as the most capable from all allowed license free frequencies. Additionally, a number of frequencies appear to supply sufficient data rate for the flight controls, however in theory it is assumed that lower frequencies are more likely to perform better at longer distances, due to less losses and disturbances. Taking this additional preference into account, frequencies at 434 MHz and 869 MHz corresponding to frequency band 1.E1, 1.E2 and 1.I appear to provide the most optimal solution.

It is important to note that in this method, estimation for certain variables of the link budget had to be made, and therefore pose a certain risk as well. Nevertheless, this method gives a good indication of what frequencies are more likely to fulfil the needs of the link. This result certainly facilitates the market research, as the search

can be limited to the desired estimated optimal frequencies. Although, the end result is very dependent on market research and availability and still prone to change, consultation with more experienced individuals in this field, such as the engineers in the MAVLab and ATMOS groups of the Technical University of Delft, confirm that these frequencies are commonly used for UAVs.

10.9 Communication system selection

Using the determined frequency bands and data rates, as well as the required transmission distance, the search for the modems and eventual antennas commences. Existing UAVs and RPAS are researched and it is discovered that for many the radio frequencies used for transmission are specified, but not details such as the modem manufacturers, models. Searching for individual providers, a number of communication system providers have been found, however most results do not specify the range of communication, while others do not mention the throughput of the system, which is the rate of data that is successfully received after transmission. It becomes clear that all systems that were found are missing pieces of information that guarantee the fulfilment of all criteria. Therefore a qualitative risk assessment is made to select the least risky communication system.

After market research, it is decided to give more priority to the range statement than specifications such as the EIRP and data rate. This is because the EIRP is not clearly defined in many cases and sometimes only the transmitter power is provided, while the data rate can never be fully guaranteed quantitatively and must be judged qualitatively. This research results in the selection of two Ubiquity systems and two ADCON systems, as provided in table 10.7 with their characteristics [77] [78] [79] [80] [81]. In table 10.7, f represents the frequency while s is the nominal range of the communication system.

Table 10.7: Selected Communication System

Company	**Model**	l, m, w $[mm]$	m_c $[kg]$	C_c [€]	f $[GHz]$	V $[V]$	P_c $[W]$	s $[km]$	D $[Mbps]$	**Link**
Ubiquiti	Nano Station M2	294 x 31 x 80	0.4	100	2.4	24	8	15	150	Live Video Down
Ubiquiti	Nano Bridge M2	543 x 440 x 725	2.346	100	2.4	24	5.5	30	150	Live Video down
ADCON	A733 addWAVE UHF	160 x 60 x 80	1.25	1890	0.434	6.2	n/a	20	n/a	Control up & down
ADCON	A850 Telemetry Gateway	182 x 260x 52	1.862	1240	0.434	n/a	n/a	20	n/a	Control up & down
ADCON	A440 Wireless Modem	119 x 79x 60	0.59	894	0.434	n/a	n/a	20	n/a	Control up & down

It is important to note that although the Ubiquiti Nano Station M2 is a directional antenna, it has been selected specifically out of all Ubiquiti antennas, as it meets the frequency characteristics and features a rather wide footprint in its antenna pattern. This allows the use of two of these devices in order to simulate an omni-directional antenna. The Nano bridge M2 on the other hand is a directional antenna that requires a motor, which can also be estimated to be around €100 looking at available motorised satellite dishes. The ADCON on the other hand is an omni-directional antenna and therefore only one is needed. The additional wireless modem and gateway are required for a functional duplex communication link. Also, for the ADCON system, since no clear throughput is specified, a qualitative assessment of the data rate is made.

10.10 Communication flow diagram

The communication flow diagram is a flow chart that demonstrates the flow of information between the operator and the subsystems. Technical details like the data rate are omitted in this diagram, as only the kind of information that travels through the channels is needed for the operator. The communication flow diagram can be found in figure 10.5 at the end of the chapter. HID refers to human input device and may refer to any ergonomic device that is used to control, such as a mouse, keyboard, joystick or pedals. It is not decided which HID to use for the operators however generally gimbals are controlled with a control stick, computers can be controlled by touchscreens, mice and keyboard, while flight control can be made with either control sticks or steering wheels in combination with pedals and levers. The dashed lines represent possible links, however not at nominal use. For example, the live video link can be used to transmit and receive control signals in case the control link fails. Additionally the director sometimes happens to have direct contact to the customers at site. Although it appears as if the control signals are fully dependent on the on-board computer, as they have to pass through it before reaching the flight control subsystem, this does not mean that they pose a higher risk thank the link between the payload and the payload transceiver. In fact, when designing the control network links, more emphasis is put on the safe delivery than the payload link, as it poses a higher impact than failure of the payload link.

10.11 Risk analysis, verification & validation

Throughout the design of the communication system risk has been assessed in both design choices and product selection. The selection of omni-directional antennas for the UAV reduce the risk of the system, as it is not dependent on a motor that directs the antenna towards the ground station. Additionally two communication links exist to take into account redundancy. The on-board computer can be adjusted manually, and also automatically adjusts its communication channels, in case a communication system failure occurs. In case the live video streaming link fails or is out of range, the payload camera is set to idle position, which is pointing directly downwards, while video stream is recorded onto the storage device, which is selected to be a flash memory of 16 GB, as these are storage devices are readily available and have very low weight and cost, as well as can be used to record more than 4 hours of video material, as well as log all the control signals. In case the control link fails and the aircraft is located out of 15 kilo meter range of communication, the autopilot takes over controls and will direct the aircraft towards 15 kilo meter range, where the Ubiquity communication link can be re-established. If the aircraft is located within the 15 kilo meter range, the control signal is switched to the live video link, and the ground station is alerted about this. Nevertheless the mission is not aborted, until the operator decides to do so. As already mentioned in the communication flow diagram section, more emphasis is put on the control link to make it less prone to failure than the payload link. Details on this involve many uncertainties at this level of design, therefore it is treated as a future consideration.

As already discussed, although certain technical steps have been taken to ensure risk mitigation in terms of designing the antenna, risk remains within the design. This is due to the fact that the design of the communication system is still highly dependent on the product, as not sufficient information is provided about it to verify successful operation. many aspects are also out of the scope of the project in order to verify the results. Nevertheless, many future steps can be taken in order to validate the use of this subsystem. For example, the modem, as well as the payload, can be placed at the required distance and even at the height, such as the tip of power plant, a wind turbine or a tower of 200 meters height. Although this location is static and not dynamic, by means of the Doppler effect, it can be calculated that speeds of 28 m/s do not cause any overlap for the radio frequencies, and therefore pose a potential means of validation.

The encryption of the signal always involves a risk, similar to how any personal computer can be hacked. Generally there are many solutions to these that are inexpensive and even freeware, although the more expensive alternatives might involve lower risk. They do not have to be a hardware solution, but can also be installed on a board computer as a software. Further studies on this can be conducted and although it is usually never impossible to hack a system, the risk of this can be reduced significantly, without affecting the communication system immensely.

The video processing unit can be validated on-ground as well, by feeding aerial images and checking the picture quality that is delivered. As already mentioned in the section about video processing, although the colour depth and resolution has been set, there are more variables that influence the picture quality, namely the video codec and the camera sensor itself. Many times the sensor technology has a large impact on how much colour can be observed in the picture. It is important not to use lower quality equipment such as displays in the ground station, which could lower the quality of the image even more. The payload VPU set-up can be validated on the ground in order to perhaps make adjustments of the imaging configurations in order to provide the best quality of imaging.

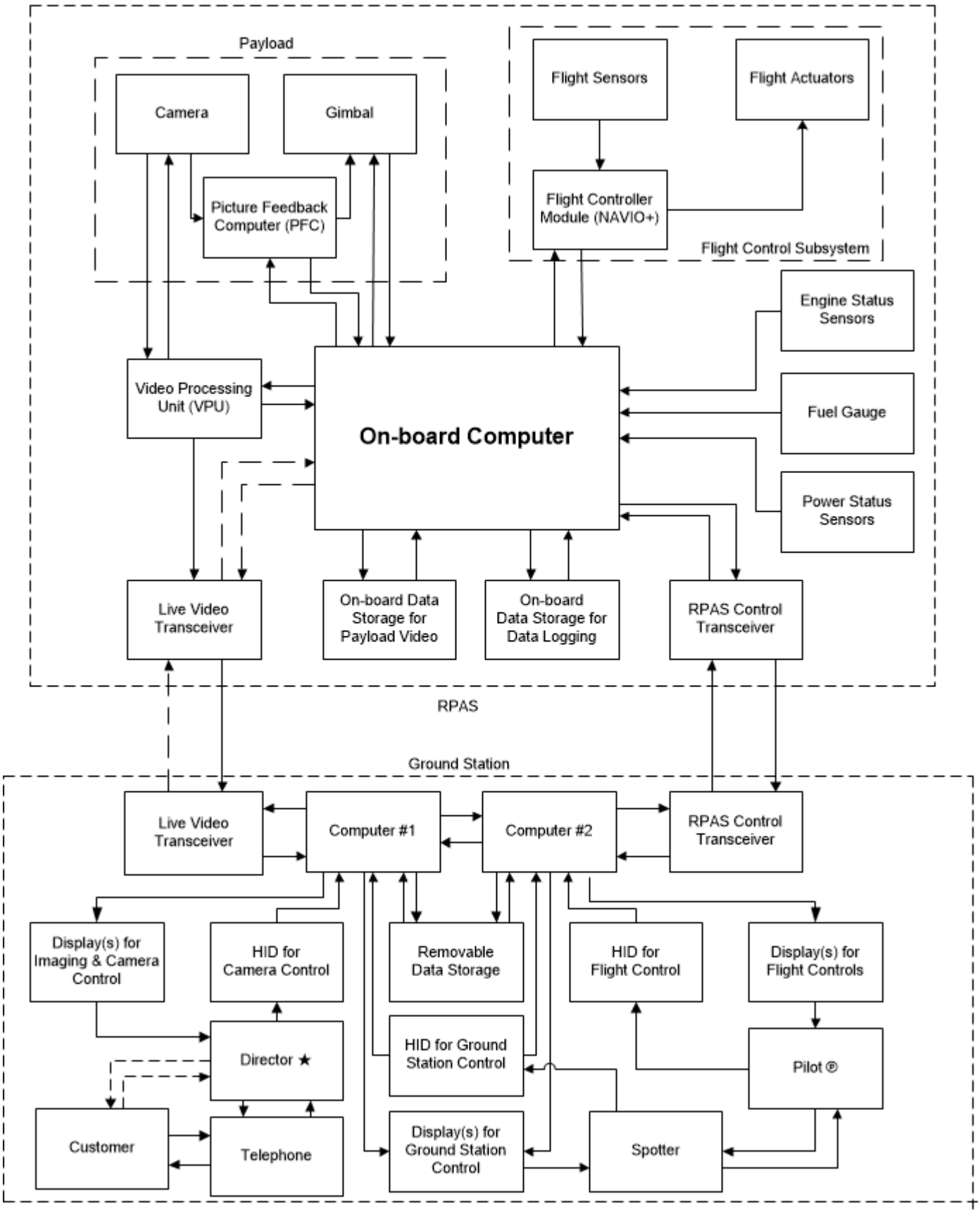

Figure 10.5: The Communication Flow Diagram

11 Payload System

Throughout this chapter the selection of the payload system will be explained. Firstly, the parameters of the payload in order to fulfil the mission will be determined and elaborated on. This is followed by an assessment made on the viability of an in-house developed system, which was proposed as the selected payload in the mid-term report. An analysis of the available systems is performed next. Lastly, a payload system is selected, which will be complimented with some concluding calculations on the system capabilities.

11.1 Payload parameters

Stated in table 11.1 below, are the payload parameters that will be vital in the payload selection process. These parameters all will comply with the mission requirements stated in section 5.3. Not all parameters are a result of these requirements, however they will be evaluated on during the payload system qualitative analysis.

Table 11.1: Payload system parameters and their origin

Payload parameter	Symbol	Origin requirement(s)
Resolution	R	CUST-S-5.0, CUST-S-7.0, CUST-S-8.0,
Field of view	FOV	-
Image size	S_i	CUST-S-9.0
Optical zoom	$Z_{optical}$	-
Digital zoom	$Z_{digital}$	-
Output format	-	CUST-S-9.0
Gimbal pointing accuracy	-	FUNC-SUA-5.1
Payload system cost	-	CUST-S-3.0
Power required	P_{req}	-
Weight	W	CUST-S-4.0
Dimensions (H X W X D)	-	-
Seperate GPS	-	-
Target tracking software	-	-

In order to determine the values of these parameters a range of equations treated below is applied. The assumptions made below shall be applied to these equations.

- The colour of clothing can be determined at a colour depth of 8-bit
- Ship names have minimum dimensions of 0.2 x 0.2 m, or area of 0.04 m^2 [82]

In addition to these items, the following is assumed for human dimensions based on data developed in 2004 on men and women ranging between the age of 20 to 60 years [83].

- The height of a human being equals 1.743 m
- The width of a human being equals 0.478 m
- The depth of a human being equals 0.301 m
- The frontal area of a human being equals 0.83 m^2
- The overhead area of a human being equals 0.45 m^2
- The lateral area of a human being equals 0.52 m^2

It is estimated that at a minimum of 9 pixels (3 x 3) is required to recognise a 0.2 x 0.2 m element, as from the above follows that this will be the smallest feature to be identified. Hence, the resolution of the camera should be at least 0.0044 m^2 per pixel. This resolution will be the result of a certain image size, field of view, and zoom capabilities of the camera. This will be determined in section 11.4. The other criterion in table 11.1 will be used in a qualitative analysis executed in the same section.

11.2 Viability of an in-house developed system

As proposed in the mid-term review report, the preliminary choice for a payload system was a system consisting out of separate modules that would form a in-house developed system. This is now re-evaluated in this section. The choice for an in-house developed system was mainly based on the lack of a low-cost payload system providing the desired imaging quality. However more advantages and disadvantages arose, listed in table 11.2 below.

Table 11.2: Advantages and disadvantages of an in-house developed imaging system

Advantages	**Disadvantages**
Low-cost components	High system complexity
High level of modularity	No information available on system reliability
	High technical risk

It was determined that the disadvantages outweigh the advantages of an in-house developed system. Due to the lack of information on the reliability of the system and validation data, costs may well exceed the budgeted amount. A high system complexity will also render high constructions/calibration costs of the system. Hence though all components are easily and cheaply bought, the total cost is likely to exceed the cost of a complete off-the-shelf imaging system. It was concluded that the latter is thus preferred over the modular in-house solution.

11.3 Available systems

Knowing the driving parameters required, an analysis was performed on available systems. These systems were mainly found through research on the imaging system market, and were complimented by the contributions of T. Manucci. The various options are listed below, in table 11.3. It is assumed that all systems have a colour depth of at least 8 bit.

Table 11.3: Available payload systems

Company **System** **Sensor**	**Unit**	**UAV Vision** **CM100** **DISC-120R**	**CloudCap** **TASE310**	**NextVision** **MicroCam-D2**	**VTULaPVO** **S120** **FCBEX980SP**	**MicroUAV** **BTC-101** **FCBEH3150**	**AtmoLAB**
Field of View	*deg*	62.9	39.7	32	42.2	53.4	-
Image size	*pix*	1280 x 720	1280 x 720		768 x 576	HD720p	768 x 494 / 752 x 582
Optical zoom		30x	30x	24x	26x	12x	10x
Digital zoom		2x			12x	12x	10x
Output format		YUV422	NTSC/PAL, 720P	NTSC/PAL	PAL	HD720p	NTSC/PAL
Gimbal pointing accuracy	°	0.022			0.05		-
Gimbal elevation	°	+- 115	[+45, -85]	[+45, -80]		[+20,-100]	+- 90
Gimbal azimuth	°	360 continuous	360 continuous	360 continuous	360 continuous	360 continuous	360 continuous
Slew rate	$°/s$	105	150		100	120	-
Payload system cost	€	38000		33000	9180		1900
Power required	W	12	20 (125max)	2.5	10 (20max)		-
Weight	kg	0.8	3	0.38	1.92	0.5	0.6
Dimensions (H X W X D)	mm	129 x 100 x 100	267 x 178 x 178	80 x 70 x 70	214 x 120 x 120	115 x 101 x 108	-
Seperate GPS		Excluded	Included	Excluded	Included	Excluded	Excluded
Target tracking		Included	Included	Excluded	Included	Excluded	Excluded
References		[84], [85]	[86]	[87]	[88]	[89], [90]	[91]

As insufficient imaging data is present for both the NextVision MicroCam-D2 and the AtmoLAB 360 Specter, the two systems are dropped from the comparison. The same applies to the CloudCap TASE310 and MicroUAV BTC-101 due to a lack of financial data. Thus, in the following section the imaging characteristics are determined for the UAV Vision CM100, and VTULaPVO S120.

11.4 Payload system selection

The variables in table 11.3 can be applied in order to determine what payload system complies with the criteria in section 11.1. Using equations 11.4.1 and 11.4.2 the coverage area of the imaging system can be determined. A graphical representation of the situation can be found in figure 11.1.

$$A = 2 \cdot \tan(\alpha) \cdot h \tag{11.4.1}$$

$$A_{\text{covered}} = A \cdot (A \cdot \frac{\beta}{\alpha}) \tag{11.4.2}$$

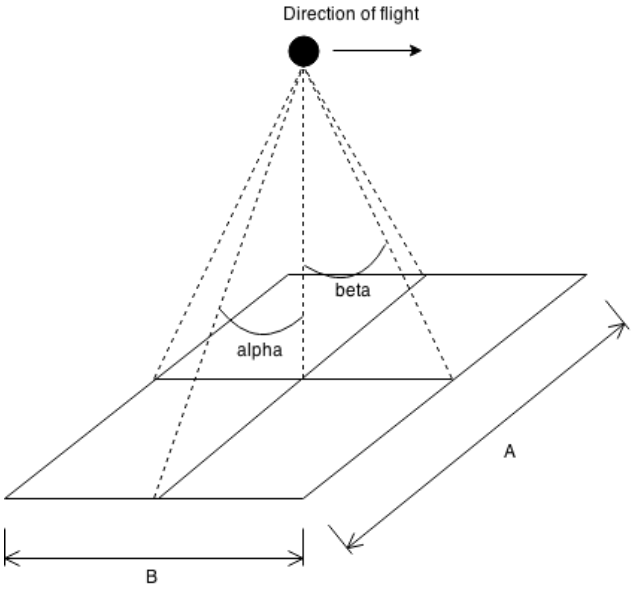

Figure 11.1: Graphical representation of imaging situation

Table 11.4: Imaging variables

Symbol	Variable
α	$\frac{\text{FOV}}{2}$
β	$\frac{\text{FOV}}{2}\frac{\text{image height}}{\text{image width}}$
A	Covered area width
B	Covered area height

This is applied in equation 11.4.3 and 11.4.4 to compute the resulting resolution without and with optical zoom respectively. The results, for altitude h ranging from 50 m to 500 m are shown in table 11.5.

$$R = \frac{A_{\text{covered}}}{S_i} \tag{11.4.3}$$

$$R = \frac{A_{\text{covered}}}{S_i \cdot Z_{optical}} \tag{11.4.4}$$

Table 11.5: Covered area and resolution (without zoom and with full optical zoom) for two payload systems at varying altitudes

	UAV Vision CM100			**VTULaPVO**		
h $[m]$	A_{covered} $[m^2]$	R (no zoom) $[m^2/pix]$	R (zoom) $[m^2/pix]$	A_{covered} $[m^2]$	R (no zoom)$[m^2/pix]$	R (zoom) $[m^2/pix]$
50	2104.06	0.002283	0.000076	1116.71	0.002524	0.000097
100	8416.26	0.009132	0.000304	4466.82	0.010098	0.000388
150	18936.58	0.020548	0.000685	10050.35	0.022719	0.000874
200	33665.03	0.036529	0.001218	17867.28	0.040390	0.001553
250	52601.60	0.057076	0.001903	27917.63	0.063110	0.002427
300	75746.31	0.082190	0.002740	40201.39	0.090878	0.003495
350	103099.14	0.111870	0.003729	54718.55	0.123695	0.004757
400	134660.11	0.146116	0.004871	71469.13	0.161560	0.006214
450	170429.20	0.184928	0.006164	90453.12	0.204475	0.007864
500	210406.42	0.228306	0.007610	111670.52	0.252438	0.009709

From this table it follows that both systems provide a sufficient resolution at a maximum altitude of 200 m and 150 m for the CM100 and VTULaPVO respectively. Also, when applying the optical zoom, both systems provide a sufficiently high image quality throughout the entire altitude range that is assumed to

Using the information in table 11.5, a qualitative analysis can be performed on the two systems. This analysis is described in table 11.6. In this table a criterion is graded with +, o , and -, representing a positive grade, an average grade, and a negative grade.

Table 11.6: Qualitative trade-off between the UAV Vision CM100 and VTULaPVO S120

Payload parameter	**UAV Vision CM100**		**VTULaPVO S120**	
Resolution	+	Resolution is above satisfactory	o	Resolution is satisfactory
Field of view	+	Field of view is relatively large	o	Field of view is average
Image size	+	Large image size	o	Image size is average
Optical zoom	+	Above average optical zoom	+	Above average optical zoom
Digital zoom	-	Below average digital zoom	+	Above average digital zoom
Output format	o	High quality output format, consequently high data rate	o	Sufficiently high quality output format, average data rate
Gimbal pointing accuracy	+	Very accurate pointing	?	Accuracy unknown, assumed to be average
Payload system cost	-	Very high product cost	+	Low product cost
Power required	o	Average power required	o	Average power required
Weight	+	Light system	o	Average system weight
Dimensions (H X W X D)	o	Average dimensions	o	Average dimensions
Separate GPS	-	GPS not present	+	GPS present
Target tracking	+	Target tracking present	+	Target tracking present

From the table above can be seen that both systems have a sufficiently high imaging performance. The imaging quality is thus no conclusive criteria. Two criteria that are however conclusive are the output format, and total cost of the system. Due to the challenge posed by the high range and related down-link of the RPAS, a lower data rate is preferred. This lower data rate can be found in the VTULaPVO S120. In addition to this, the cost of this system is lower than that of the CM100. The latter would contribute to more than a third of the allowed production cost, whereas the S120 contributes to this limited cost by less than 10%.

To conclude, the final selection comes down to the VTULaPVO S120, due to it's low cost whilst maintaining a sufficiently high imaging quality. The components of the system, camera and gimbal respectively, are shown in figures 11.2 and 11.3 below.

Figure 11.2: Sony FCBEX980SP [88]

Figure 11.3: VTULaPVO S120 [92]

12 Navigation and Sensing

Being able to properly perform a mission with the RPAS means it must be capable of more than just being able to fly. It is important that the user of the RPAS has information available about the RPAS and its environment. All the required information will be discussed in this section, including the means to obtain this information.

12.1 Required data

This section will introduce all the different types of data that need to be acquired from the RPAS and its surroundings.

12.1.1 Attitude determination

The attitude of the RPAS is an important piece of information. Knowing this information allows the RPAS to fly in a certain direction, and also helps in the control of the RPAS. The different types of attitude determination and the means to obtain these are discussed in this section.

Angular rates
Angular rates are important for the control of the RPAS. For example, as explained in section 7.4.2, for directional control the RPAS will implement a yaw damping system that uses feedback of the yaw rate of the RPAS to provide directional stability. Furthermore, for short periods of time, angular rates may be integrated in time to provide angles, which provide direct feedback to the pilot as to where the RPAS is heading. Angular rates may be measured using gyroscopes.

Angles
The angles themselves are important information for controlling the RPAS' heading and for manoeuvring to a certain position. The angles may be determined by using accelerometers and integrating them twice, or by using a gyroscope and integrating the measured angular rates once. Of course, for an even better determination, a combination of these may be used and filters, such as Kalman or complementary filters, may be used to reduce the effect of noise. Furthermore, because the RPAS is always flying in the Earth's magnetic field, it may also make use of magnetometers to determine its heading angle. Another method for determining Euler angles of the RPAS is using GPS receivers at different points in the RPAS, and comparing the phase of the signals at the different points to determine attitude. Finally, some angles that the RPAS has with respect to the wind may be important, such as angle of attack or angle of sideslip. These angles require separate sensors.

12.1.2 Altitude determination

The altitude of the RPAS must be determined for object avoidance and regulations. The altitude may for example be determined by using the static pressure of the air which is compared to the static pressure on the ground. Another option is using LIDAR altimeters, which use lasers to determine the altitude of the RPAS.

12.1.3 Velocities

Velocities are important information for a pilot. Velocities can be split into ground ("inertial") and air velocities. Air velocities are important information for aerodynamics, propulsion and handling characteristics of the RPAS. Ground velocities are important to know during phases where interaction between the RPAS and the ground takes place, for example during landing or take-off, or when surveying an area on the ground.

Air velocity
For air velocities, only horizontal velocity is important. Horizontal air velocity may be determined with the use of a pitot static tube.

Ground velocity
For ground velocity, both horizontal and vertical velocities are important. Horizontal ground velocity may be determined with the use of GPS. Furthermore, it can also be approximated by measuring air velocity and subtracting the average wind speed from it. Vertical ground velocity may be determined using the same

information from the pitot static tube, by measuring the rate of change of pressure from the static ports and relating it to vertical velocity.

12.1.4 Position determination

Position determination of the RPAS is important for performing the mission, because it must be possible to manoeuvre the RPAS to a certain location, and also for obstacle avoidance. The position of the RPAS may be determined by using a form of GPS, and also may be determined visually by using a camera pointed in the direction of flight of the RPAS. In case of loss of signal of the GPS, the information provided by the accelerometers may be integrated in time to obtain position information. [93]

12.1.5 Environment detection

Environment detection is important for safety reasons, the RPAS must know at all times what its surroundings are in order to be able to fly safely. Environment detection may consist of several systems.

Air traffic detection
Other air traffic in the proximity of the RPAS must be identified in order to safely avoid them. Air traffic detection may be done optically, for example by using cameras on-board of the RPAS. Furthermore, the RPAS may employ a system of microphones that detect the sound produced by other air vehicles [94]. Note that this only works when the other vehicles do not fly too fast, which is presumably the case at the altitude the RPAS flies on. The RPAS may also make use of transponder systems to detect other air vehicles. Another method of detecting the environment and especially air traffic in the environment is by using a radar system. A final method, which works when the RPAS is within field of view, is to have a spotter available that simply looks at the air around the RPAS for other air traffic. This spotter can assist the RPAS in the critical phases of the mission, during landing and take-off. However, the RPAS should also be sufficiently safe outside line of sight.

Object detection
Other objects in the environment can primarily be visually detected with the use of a camera. Furthermore, most of the large structures in the environment of the RPAS may be mapped and therefore known to the RPAS, and can be avoided by simply knowing the position of the RPAS and the position of the large structures.

Other dynamic objects
There is a final category of objects that exist, which is other dynamic objects. An important example of these other dynamic objects are birds flying around. Because these produce a minimal amount of sound, microphones will not pick up their sound. For obvious reasons, transponders will also not be useful in the detection of birds. The only option that remains is using visual identification of this category of objects, for example by using a frontal camera.

12.1.6 RPAS status sensing

It is important to also detect the internal status of the RPAS, because it gives information such as how much longer the mission may be performed, or how well the RPAS is operating. The status sensing options that are considered are those for control surface deflections, for fuel levels, for the power subsystem and for the engine subsystem.

Control surface deflections
A status parameter that could be measured by the RPAS is the amount of deflection the control surfaces have. This information could be used to determine whether the RPAS is tuned correctly and functioning properly. Furthermore, it can be used for fault prevention of the servo, in case a failure occurs in the servo and it turns the control surfaces beyond their maximum allowable values.

An alternative to measuring actual deflection is measuring current going to the servos on the control surfaces. If this is used in combination with predictions of dynamic flight behaviour of the RPAS, an estimate can be made if a failure occurs during flight whether the servo is at fault, because it is known whether there is still current flowing to the control surface.

Power level
Power levels are an important indication as to how much longer the mission can be performed. For that reason, the battery energy left can be monitored. One of the most often used methods for measuring left-over battery levels is measuring the output voltage, and relating it to the characteristic voltage curve of the battery, which gives an indication of the amount of energy left in the battery according to its output voltage. Another method that is sometimes used is coulomb counting, where the amount of current going out of and into the battery is measured and related to how much energy is consumed [95].

Fuel level
Fuel levels are the second important indication as to how much longer the mission can be performed. Different options, of varying precision and complexity, exist to measure the left over fuel. The fuel sensors may either measure the absolute amount of fuel tank left, or measure the fuel flow and compute how much fuel should be left. One of the options is an optical or heat sensor, which only measures when the left over fuel gets below a certain threshold. Another system uses a mechanical lever and a floating device, which floats on top of the left over fuel and thus indicates how much fuel is left. Another option is measuring the capacitance between the top and bottom of the tank to get an indication of the amount of fuel present. A final method is using a small rotor in the fuel duct to measure the fuel flow, and integrating it in time to get the amount of fuel consumed.

Engine status
Since the engine is such a critical part of the RPAS, it is important to sense its status, as it can indicate whether the engine is operating as it should. The most important engine sensors would be heat sensors, which make sure that the engine does not overheat. Furthermore, the throttle and RPM may be measured during operations.

12.2 Autonomous flight

Autonomous flight would be beneficial to reduce the load on pilots controlling the RPAS, and could possibly allow for more precise flight without human error. There are some additional hardware and software requirements for autonomous flight. The RPAS needs a stronger on-board computer to do the required computations for autonomous flight. Furthermore, the on-board computer needs to have autopilot software that is suitable for flying wings. The sensors required for autonomous flight are already mentioned above, but all the sensors do need to be integrated with the on-board computer and they need to be compatible with the software. There is the possibility to completely build the autopilot from the separate components, integrating and calibrating them and writing the required software for the autopilot. However, due to the fact that this is a very lengthy and labour intensive process, this option is not feasible in the given amount of time. Instead, options are considered that already have some of the components integrated, and for which software already exists.

The first option considered for autonomous flight was a complete package solution, which included all the required sensors, processors and software for autonomous flight. The product is from the company UAV Navigation, and is called VECTOR. [96]. However, after consultation with the company, UAV Navigation revealed that the price of the product is confidential information, but will be under €10,000. However, the maximum amount of €10,000 had to be assumed, and this unfortunately exceeded the cost budget of €5,000 that the navigation and sensing subsystem was assigned.

It became clear that complete autopilot packages would not fit within the budget, so a combination of integrated boards and separate sensors was considered instead. After a market analysis, a few promising technologies were selected that would be able to provide integration of sensors with an autopilot board. These technologies are ardupilot [97], paparazzi [98], NAVIO+ [99], and pixhawk [100]. All these technologies offer autopilot capabilities, but some do still require separate boards with processors.

All of these technologies offer similar features for similar prices, and therefore a product was chosen that simply meets all the requirements. After some discussion within the team, the NAVIO+ autopilot shield in combination with the raspberry pi was chosen as the autopilot system. The reasons for choosing the NAVIO+ autopilot are listed below.

- It has sufficient PWM outputs, namely 13, [99] which is a necessity due to the fact that there are as many as four control surfaces that all have two separate servos for redundancy in control. If no PWM output splitting is to be performed, the system requires at least 9 PWM outputs for the servos and the engine, which the NAVIO+ autopilot fulfils.
- It fits well into the cost budget. The costs of the NAVIO+ autopilot itself is under 200 dollars at the time of writing, and the Raspberry Pi that the NAVIO+ autopilot interfaces with costs less than 150 dollars.
- It has a built in magnetometer, which allows us to place the autopilot unit in the front of the RPAS where there is little magnetic interference and use the NAVIO+'s own magnetometers.
- The Raspberry Pi that the NAVIO+ autopilot interfaces with is more flexible than microcontrollers, it is easy to extend and is compatible with many programming languages.
- The NAVIO+ autopilot offers real time kinematics functionality, which means it uses the phase of the GPS' carrier wave signal to determine position, rather than the actual signal's information. This allows position determination at centimeter level.

- Kalman filtering becomes easy with the NAVIO+ autopilot, as open source Kalman filters for the NAVIO+ autopilot are readily available to be implemented, thus significantly increasing the accuracy of the estimates of the attitude and position of the RPAS.

12.3 Damping

The data acquired from the on-board sensors are critical for performing flight and therefore have to be of an adequate quality. Vibrations imposed on the structure by the engine can drive the induced measurement error to an unacceptable extend. To this extend the sensors might be fitted with rubber dampers. If testing shows that this is insufficient, a gimbal might me added to provide even more damping. Furthermore, the main sources that cause vibrations in the RPAS should also be eliminated. This is for example the engine, for which separate measures will be taken, as explained in section 8.5.

12.4 Additional sensor selection

Even though the NAVIO+ autopilot already has a large number of built-in sensors to determine attitude and position, it does not cover all of the sensors that were discussed previously. The additional selected sensors are listed below, and are also given as an overview in table 12.1.

1. Additional inertial measurement unit (IMU). The NAVIO+ autopilot already has an IMU, including a magnetometer, installed on-board. However, as explained in section 12.5, electrical interference is a big problem for magnetometers. For this reason, the NAVIO+ autopilot will be placed towards the nose of the RPAS, where there is minimal electrical interference for the magnetometer of the NAVIO+ autopilot. Furthermore, proper calibration of the integrated sensors of the NAVIO+ autopilot is not done by the manufacturer. Since this can be very difficult to do accurately, instead a separate IMU is preferred that is already calibrated by the manufacturer. This IMU can also be placed near the c.g. of the RPAS, as this way the IMU gets minimal disturbance inputs from rotational accelerations.
2. Pitot static tube. Although GPS with real time kinematics can quite accurately determine the velocity of the RPAS, this is the ground velocity. For aerodynamics reasons it is also important to know the airspeed of the RPAS. This will be done with a pitot static tube.
3. Transponder. Although the payload camera will be pointing forward during cruise, there should be other methods of detecting traffic around the RPAS. The first of these methods is by using a transponder on-board of the RPAS. The transponder will attempt to establish a connection with other air traffic in the area, provided they also have a transponder on-board. This can be used to map the surrounding air traffic.
4. Microphones. The second of the two methods that will be employed to detect other air traffic is using an array of microphones on the RPAS that will be able to detect the other air traffic in the surroundings.
5. Fuel gauge. Apart from knowing the position, attitude and surroundings of the RPAS, there is also a need to know the status of the RPAS. Sensors should be included to measure some of these status parameters. The first of these is the fuel gauge sensor, which tells the user approximately how much fuel is left in the RPAS.
6. Engine status sensor. In order to prevent the engine from overheating, the temperature of the engine should be fed back to the user of the RPAS. Furthermore, the RPM and throttle setting of the engine is important information to send back to the end user. However, to obtain these sensors the manufacturer of the engine should be contacted for best integration.
7. Battery power. To determine how much fuel is left to perform the mission, the left over battery energy should be measured and fed back to the user of the RPAS. Such a system is already included in the power system.

Table 12.1: Selected set of additional sensors

Product name	**Type**	**Quantity**	**Unit Weight** $[kg]$	**Unit Size** $[mm^3]$	**Unit cost** [€]
ADIS16485 [101]	6-degree IMU	1	0.048	$44x47x14$	$1697
Pitot-Static Tube for UAVs [102]	Pitot static tube	1	0.041	[1]	N/A
Knowles MR-23151-000 [103]	Microphone	4	0.09	$12.27x12.27x22.23$	4 x €32.32
Sagetech corporation mode S transponder [104]	Transponder	1	0.1	$58x17x78$	$3587
UAV Fuel level gauge [105]	Fuel sensor	1	0.050	$50x170x200$[1]	$500

[1] Size can be made according to customer's preference

12.5 Sensor interference

Interference of sensors can yield significant errors in the measurement data. To decrease this undesirable effect the sensors have to be located and oriented to minimise interference. Foreseen challenges include the interference of the magnetometer with electrical circuits and their corresponding fields. This is prevented by placing the magnetometers as far as possible from all batteries, computers, and cables. In addition, moving parts within the aircraft may generate noise and therefore interfere with the acoustical measurements. Therefore extra attention is paid to the placement of the microphones. The main contributor to the noise generation is the propeller. The microphones are therefore placed as far as possible from the engine. Moreover, filters may be applied to the measurement data since the rpm of the engine is known.

Taking into account the possible interference of sensors and minimum length of cables the ideal position of all sensors was determined. The overview is shown in table 12.2 and corresponds to the decisions made in section 12.4.

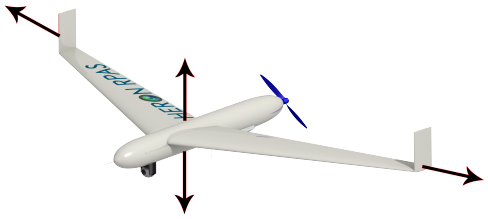

Figure 12.1: Microphone positions and directions

Table 12.2: Position of navigation and sensing components

Component	Position
Navio+	Inside nose
Additional IMU	C.g.
Pitot static tube	Outside nose
Transponder	Between c.g. and engine
Microphones	Arrows in figure 12.1
GPS receiver	Top of fuselage

12.6 Hardware and software

All of the information presented in this section may be summarised in a hardware diagram, as given in figure 12.2. The subsystem has interactions with the communication and power subsystems. The communication subsystems provides input data and receives output data. The power subsystem provides the necessary power. The servos have separate power inputs, because the autopilot board can not provide the required power to the servos.

Most of the software used by the NAVIO+ is built in to the system. It already has features such as real time kinematics computations and kalman filtering. However, because additional sensors are to be used, the software does have to be adapted manually. The exact programming of the autopilot is a recommendation for future work, as it will require the purchase of the system to experiment with.

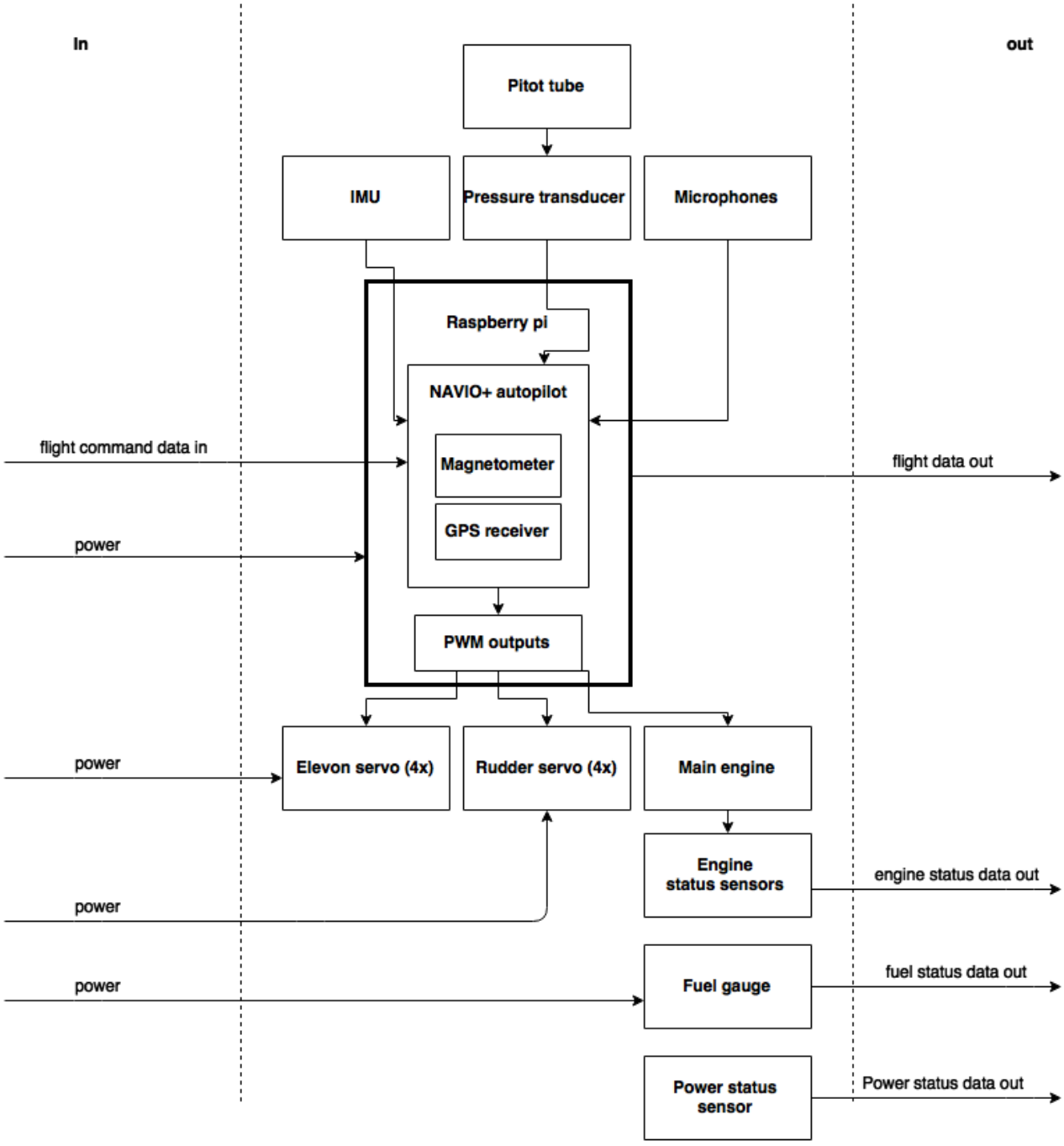

Figure 12.2: Hardware diagram for navigation and sensing

13 Power System

In this section the electrical power system will be explained in detail. A table is given that shows all inputs and outputs for the power system chapter. These inputs and outputs can be seen in table 13.1. The quantitative values given by each department can be found in the power budget, which can be seen in table 13.3.

Table 13.1: Inputs and outputs power subsystem

Parameter	Input	Output	Source	Destination
Power requirements	X		Communications	
Power requirements	X		Payload	
Power requirements	X		Stability and Control	
Power requirements	X		Navigation and Sensing	
Power generated	X		Propulsion	
Power system mass		X	Structures	

First the way of providing power is determined by doing a simple trade-off. After the trade-off a system is selected. Then the backup battery is determined and after that the power distribution in the RPAS is explained.

In this section the electrical power system will be explained in detail. First the way of providing power is determined by doing a simple trade-off. After the trade-off a system is selected. Then the backup battery is determined and after that the power distribution in the RPAS is explained. In table 13.1 all inputs and outputs for the whole section can be found.

Throughout the chapter equation 13.0.1 is extensively used, which relates power to voltage and current.

$$P = U \cdot I \tag{13.0.1}$$

Table 13.2: Parameters used in equation 13.0.1

Parameter	Unit	Comments
P	$[W]$	Power in Watts
U	$[V]$	Electrical potential in Volts
I	$[A]$	Current in Ampere

The power budget for the RPAS is used extensively throughout the chapter as well. This power budget is based on all information given by the subsystem departments. It can be found in table 13.3.

Table 13.3: Power budget

Subsystem	Power $[W]$	Voltage $[V]$
Payload Camera	10-20	9-26
Payload Computer	17	9-18
Actuators	-	4.8-6
Transceiver	16	24
Autopilot	6	5
Transponder	14	10-32
IMU	1	3-3.6
Fuel Gauge	1	4-9
Contingency	5	-
Total	80	-

13.1 Power supply determination

In this section a trade-off will be made between using an on-board power generator and batteries to provide the required power. To determine this, a very rough estimate is made for the mass needed to complete the mission. First an estimation is made for the total power consumption during the mission. This is done by using the power budget, which resulted in a total maximum power usage of 80 W including a 5 W contingency as can be seen in table 13.3.

13.1.1 Battery only

Estimating the mass using only battery power a continuous power consumptions of 80 W is used. Assuming the 4 hour mission time results in a total needed capacity of 320 Wh. Selecting the highest energy density batteries available as a reference, which are also used quite extensively in RC models, are lithium-ion based batteries. These batteries have a specific energy range of 130 - 180 Wh/kg [106].

Using this energy density, the dry battery mass for 320 Wh ranges between 1.78 kg to 2.46 kg.

13.1.2 Generator

For the mass estimation of a generator a suitable reference system is used to determine mass addition to the propulsive system. This mass addition consists mainly of the dry mass of the generator, the extra fuel needed to convert to electrical power and the mass of the battery. The reference system used is a 3W 28i equipped with a 100 W generator system. From the specifications it is determined that the added generator weights around 0.550 kg, as can be seen in table 13.5.

The amount of fuel needed for the required electrical capacity can be calculated using the specific energy for gasoline. The specific energy for gasoline is 12.33 kWh/kg. Taking into account the generator system efficiency of 75%, provided in the specifications of the reference system, the total amount of needed power is equal to 400 Wh. These specifications can be found in table 13.5. This results in an estimation of the fuel weight of 0.0324 kg.

A battery is also needed as a backup for the generator. The preliminary sizing of this battery will be based on the redundancy requirements, meaning that the RPAS in case of generator failure still has enough power to be operational for a required amount of time. This amount of time needed is calculated by taking the maximum range of the RPAS to the ground station, and calculating the time needed to travel this distance. The maximum range of the RPAS is considered to be 20 km. Assuming the RPAS is flying back with a cruise speed of 28 m/s, results in an amount of time needed of about 12 minutes.

When for example the generator fails, only the critical subsystems are used to reduce power consumption. This means that the payload camera and payload computer can be excluded from the power budget, which can be found in table 13.3. This results in a total power consumption of 43 W, including 5W contingency. This results in a needed capacity of 8.6 Wh. Using the specific energy density for lithium-ion batteries results in a battery mass ranging between 0.048 to 0.066 kg. This results in a total maximum mass for the system of 0.649 kg. A summary of these results is given in table 13.4.

Table 13.4: Summary of total mass of both power supply methods

	Generator	**Battery**	**Unit**
Mass	0.550 generator mass	1.78-2.46 battery mass	[kg]
	0.032 fuel	-	[kg]
	0.066 battery	-	[kg]
Total	0.649	1.78-2.46	[kg]

As can be seen, the mass estimate for a 4 hour flight with a generator results in approximately 0.649 kg. Using a battery supply results in an estimated mass of anything in between 1.78 and 2.46 kg. Based on these values a generator will be used as a power supply.

13.2 Generator system

The generator systems consists of a brushed DC generator connected to the crankshaft of the engine with a belt. The output of this DC generator is connected to a generator power unit (GPU). This unit converts the incoming variable voltage into a constant voltage and regulates the outgoing current. In discussion with the propulsion department a selection was made on the engine, which resulted in the 3w 28i, which can be seen in

figure 13.1. This engine includes a generator that can deliver up to 100 W of power. Elaboration on this choice can be found in section 8.3. The GPU has two outputs, one 6 V and one 12 V output which can both deliver a maximum current of 5A. The generator has a maximum power supply of 100 W at high RPM ranges. A backup battery interface is provided on the generator power unit. This is used to attach a backup battery that can power the critical subsystems in case of for example generator failure or when the rpm of the engine is too low to for the generator to provide power. Full specifications can be found in table 13.5.

Now that the power system is specified, the backup battery can be scaled and all other subsystems can be attached.

Figure 13.1: 3w 28i engine with generator system

Table 13.5: Generator system specifications [107]

Specification	Value	Unit
Maximum battery charging current	2	$[A]$
Maximum continuous battery current	8	$[A]$
Output Voltage	6 and 12	$[V]$
Continuous load current 6 and 12V	5	$[A]$
Maximum GPU efficiency	90 %	[-]
Maximum complete system efficiency	75%	[-]
Maximum peak load current	10	$[A]$
Complete onboard system mass	0.55	$[kg]$

13.3 Backup battery

Determining the choice for the backup battery type was done by looking at the specific energy densities of different battery types and the requirements of the GPU. A higher density is preferable resulting in less mass needed for a certain amount of energy on-board. A choice was made that lithium-ion based batteries are used. There are two types available, lithium-ion and lithium-polymer. The differences in both are relatively small, lithium-ion is a little heavier than lithium-ion polymer but is also less expensive. As a requirement for lithium-ion based batteries set by the GPU, the battery should consists of 3 cells. This results in a total voltage in between 10 V to 12.6 V.

13.3.1 Determining battery capacity and other characteristics

To determine battery capacity, a few scenarios are worked out and depending on these results a capacity is chosen. This is done because there is simply no clear limiting factor on the battery capacity.

The maximum charge rate the GPU can provide to the backup battery is 2 A as can be seen in table 13.5. It is preferable to use as much charging current as possible, which makes sure the battery is charged as much as possible. For lithium-ion based batteries the preferable charge rate lies in the range of 0.1 C to 1 C [106]. Limiting the charging current to this amount maximises the batteries lifetime and effectiveness. Using this charge rate as an indication, a battery of at least 2 Ah is needed to be able to charge with the full 2 A available.

To check if this capacity complies with the redundancy requirements of returning to home when engine or generator failure occurs, an estimation of the needed battery capacity for this operation is made. In case of generator failure, the engine is still working so an estimate of battery capacity is needed based on needed flight time to return to the ground station. To estimate the needed capacity the RPAS is assumed to be at a maximum range of 20 km. Assuming cruise speed when returning home the time to destination is roughly 12 min. The power consumption of the critical subsystems is approximately 43 W, resulting in a needed capacity of 8.6 Wh. However, a safety factor has to be incorporated as well to cope with efficiencies and also for redundancy. Doubling the capacity as a safety factor results in a needed capacity of 17.2 Wh. Using the nominal voltage of 3.7 V [106] per cell results in a total voltage of 11.1 V. Using this nominal voltage results in a needed capacity of 1.55 Ah. Concluding that the 2 Ah is enough for the RPAS to return to home.

Another determining condition for the battery capacity is that when operating normally, the payload has to be attached to the battery during low RPM stages. Also pre-flight check time is something to take into consideration when the RPAS is working fully on the battery.

For the first case, the total maximum consumption of the RPAS is estimated at 80 W. To determine how long the 2 Ah battery can sustain the whole RPAS, the efficiency of the GPU in between the battery and subsystems has to be estimated. This is estimated at 90%, which is based on the fact that the GPU efficiency of the DC-DC

converter is around 90% for the lowest input voltage of the generator. This can be seen in graph 13.2. Assuming this efficiency is the same for the battery, which has a lower voltage.

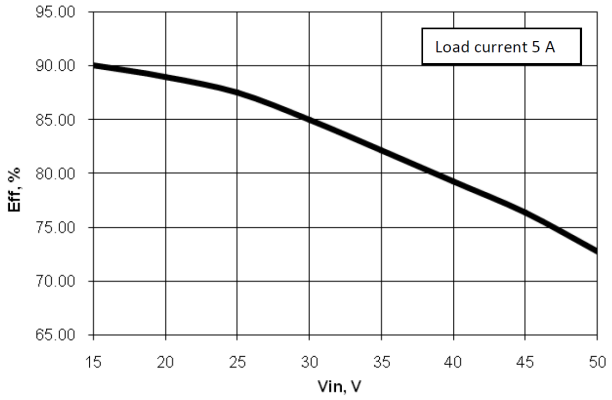

Figure 13.2: DC-DC conversion efficiency of the 6V output

This results in a power drawn from the battery of 89 W. Assuming the nominal voltage of 11.1 V, the amount of current drawn from the battery can be calculated. This results in 8 A. Calculating the time needed to completely deplete the 2 Ah battery, results in a total time to depletion of around 15 min.

So on a battery of 2 Ah the RPAS can fully function on the battery for 15 min without needing a recharge. The mass of the 2 Ah battery is estimated at 0.12 to 0.17 kg using its specific energy. Due to the unknown details of the flight envelope, no estimation of a reference capacity number can be given. However, with respect to the mass budget, 1 kg was assigned to the power subsystem. 550 g is used by the generator, leaving approximately 450 g for the batteries. This always leaves room for increasing the size of the battery.

For example doubling the battery capacity has advantages. The main advantage is obviously having a higher capacity. The higher battery capacity also means that the charge rate relatively to the battery size can be decreased, from 1 C to 0.5 C at maximum charge. A lower charging rate results in a longer lifetime and higher voltage of the battery, which is characteristic for lithium-ion batteries [106]. Drawbacks are that the battery is heavier and more expensive.

For the pre-flight check, an external power supply should be used to have a fully charged battery on launch. An interface is provided on the GPU to attach an external power supply, so that the battery can be fully charged before launch and all the subsystems can be checked without using the on-board battery.

A summary of the required battery characteristics are given in table 13.6.

Table 13.6: Battery specifics for battery selection

Characteristic	**Value**	**Comment**
Capacity	2+Ah	At least 2Ah is needed
Battery type	Lithium-ion/polymer	High energy density batteries types
Voltage/Cells	3 cells, 10-12.6V	Based on GPU specifications and lithium-ion characteristics.
Discharge rate	8A	The battery should be able to provide a 8A current
Weight	<0.45kg	Low battery mass is preferable

13.3.2 Battery selection

In this section a battery is selected that can be used on the RPAS. The required characteristics are extracted from table 13.6. A battery that complies with the requirements is the 2,200 mAh 3S 20 C Turnigy LiPo battery. The characteristics of the battery can be found in table 13.7.

Table 13.7: Battery specifications

Characteristic	Value
Capacity	2.2 Ah
Battery type	lithium-ion polymer
Voltage/Cells	3 cells
Constant discharge rate	44 A
Maximum discharge rate	66 A for 10 s
Mass	188 g
Costs	€8.79

Figure 13.3: Turnigy 2,200 mAh LiPo battery

13.4 Power distribution

The power distribution of the entire system is done by the GPU. There are two outputs on the GPU, one 12 V and one 6 V output. Both are limited to a 5 A max current. As can be seen in table 13.3, the payload, transponder and the transceiver require a voltage of 12 V or higher. The other subsystems, the actuators, autopilot, IMU and fuel gauge need 6 V or less.

To check compliance, the GPU has a maximum output of 5 A on both outputs. Using table 13.3 the currents on both outputs are calculated. The power consumption of the payload, transponder and transceiver is 67 W. This results in a maximum current drawn of 5.58 A. The subsystems attached to the 6 V output has a total power consumption of 13 W including the contingency. This results in a maximum current drawn of 2.16 A. As can be seen, the 12 V output has a higher total current than the allowed 5 A. By moving the transponder to the 6 V output and using a step-up DC-DC converter to provide the higher needed voltage, the resulted maximum current drawn of the 12 V output is 4.42 A. The maximum current drawn from the 6 V output is then 3.67 A. This complies with the GPU specifics, as can be seen in table 13.5.

The actuators however draw peak currents when deflecting, setting constrains on the system. In total, 6 actuators for the control surfaces can deflect simultaneously. The maximum current drawn is based on the stall current, that is given by the actuator manufacturer. The stall current is the highest current the actuator can draw, under maximum load with fastest deflection possible. The stall current at 6 V is estimated at 1 A [108]. This resulted in a maximum drawn peak current of 6 A. Adding this to the already flowing current on the 6V output, results in a total current drawn of 9.67 A

In the specifications it is stated that the maximum peak current is 10 A for 10 s. The turning time of these actuators is around 0.1 s. This check makes sure that the actuator deflection poses no limitations on the power system. The resulting subsystem connections to the GPU made can be found in table 13.8.

Table 13.8: Subsystem connections to GPU

Subsystem	12 V	6 V
Payload Camera	X	
Payload Computer	X	
Transceiver	X	
Actuators		X
Autopilot		X
IMU		X
Transponder		X
Fuel Gauge		X

13.4.1 Power Conversion

Some subsystems do not comply with the 12 V and 6 V outputs. Therefore, a DC-DC converter is needed to either lower or increase the incoming voltage to a suitable level.

For lowering the voltage there are two categories, switch-mode and linear DC-DC converters. Switch-mode store the energy and release it at a different voltage level, resulting in efficient voltage conversion without much losses. Drawbacks are that electromagnetic interference created will negatively influence nearby power using

subsystems. Linear DC-DC converters convert the voltage to a lower voltage by simply dissipating the difference in heat. Drawbacks are then that they are less efficient.

To make a choice on DC-DC converters, the more simple linear converters are used. Most voltage transformations on the RPAS only require a small reduction in voltage difference with low currents, resulting in low energy losses. This choice also results in lowering the electromagnetic interference, which is beneficial to other power consuming subsystems. The loss in power can be calculated using equation 13.4.1.

For increasing the voltage, only switch-mode like converters are a possibility, which ultimately results in electromagnetic interference. However, only a few are needed and when placed tactically, should have low impact on the other subsystems. An example of a DC-DC is a step-up converter, that boosts the input voltage to a higher output voltage. These step-up converters can have above 95% efficiency [109].

First, the lowering of the voltage is considered. This has to be done for the IMU and the autopilot.

$$P_{lost} = (U_{in} - U_{out}) \cdot I \tag{13.4.1}$$

First, the loss over the IMU is calculated. The IMU needs a 3.6 V input which can be found in table 13.3. This result in a of voltage difference of 2.4 V. Using equation 13.4.1 the resulted loss is 0.5 W. The difference in voltage for the autopilot is 1 V. This results in a loss of 1.2 W, using equation 13.4.1. The total loss in power is estimated at 1.7 W.

The subsystems in need for step up DC-DC conversion are the transceiver and the transponder. As can be seen in table 13.3, the voltage difference for the transceiver is 12 V with a total power consumption of 16 W. Assuming a 95% efficiency for the step-up DC-DC conversion a total loss in power is estimated at 0.8 W.

The voltage difference needed for the transponder is 4 V, consuming about 14 W. Assuming a 95% efficiency in DC-DC conversion results in a loss of 0.7 W. This results in a total loss of 1.5 W. A summary of the losses can be found in table 13.9.

Table 13.9: Losses due to DC-DC conversion

System	**Losses** $[W]$
IMU	0.5
Autopilot	1.2
Transceiver	0.7
Transponder	1.5

The total losses due to DC-DC conversion are then estimated at 3.2 W. This would increase the total power budget to about 83.2 W, still including contingency. Also losses over cables etc. are not taken into account. However, the generator has a maximum power generation of 100 W, thus still being capable of providing the required power. Also, the power budget is estimated at maximum power consumption at all times, which is never the case.

13.4.2 Electrical block diagram

In this section a drawn out plan of all power consuming hardware with their respective requirements is presented. All the required DC-DC converters are presented as well, with suitable specifications and losses created due to these converters. The electrical block diagram can be seen in figure 13.4.

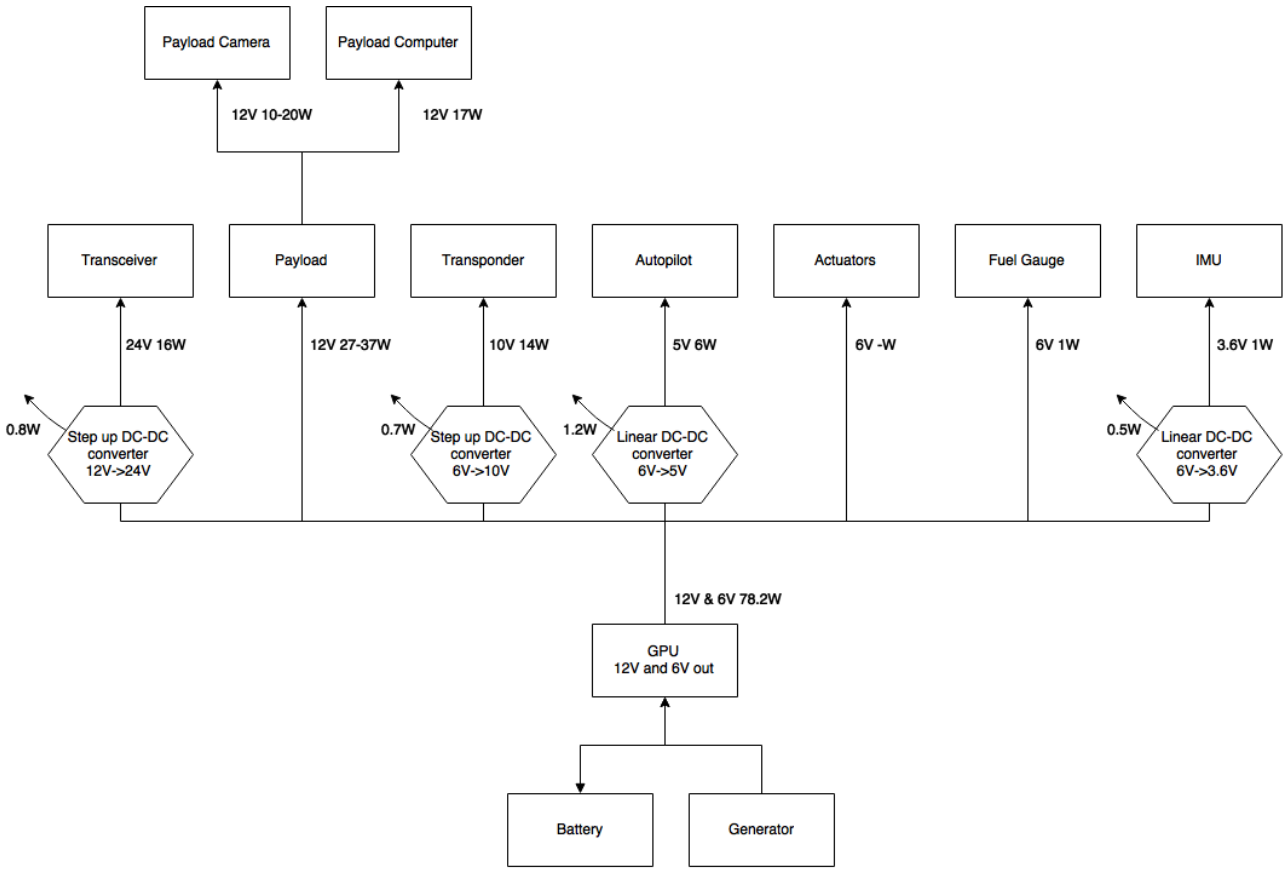

Figure 13.4: Electrical block diagram of the power subsystem

14 Operations

This section will contain information on the operational necessities for the flying wing design. This includes but is not limited to the operation of the RPAS at the ground station, maintenance of the RPAS, setting up of launch and recover systems, and so on. These aspects will be covered to give a clear indication of the operations needed for the RPAS to complete its mission.

14.1 Catapult launch system

During the preliminary design phase, it had already been determined that the flying wing design would be launched using a catapult system. A rail will be used along with a mechanism to propel the RPAS along this rail to a speed just above stall speed. The inputs from other subsections and the destination of the outputs of the launch system are given in table 14.1.

Table 14.1: Input and output parameters for the launch system

Parameter	Value	Unit	Input	Output	Comments	Source/Destination
Stall speed	15	$[m/s]$	X			
Mass	18	$[kg]$	X			
Clearance height	20	$[m]$	X			
Launch angle	22.5	$[°]$		X		
Clearance distance	48.3	$[m]$		X		
Rail length	5	$[m]$		X		
Launch velocity	20	$[m/s]$		X		
Launch acceleration	40	$[m/s^2]$		X		
Launch force	787.6	$[N]$		X		

Acceleration
A catapult system has many benefits for the mission, including mobility, its speed, efficiency, and manpower. Due to it being a relatively small launch method, it will be possible to launch from multiple locations, so the mission is not hindered by a fixed launch site. It is also a very fast and efficient system, the RPAS will not have to accelerate itself from start to lift off, and the catapult is extremely fast in 'shooting' the craft away. Many catapult systems, such as the one made by Arcturus, can be set up using one person in a short amount of time [110]. These catapult systems are transportable [111][110][112] and can be placed into the wind at the launch location to ensure an easier lift-off. However, due to the complex system, there is a higher chance an error or malfunction will occur during launch, leading to a higher technical risk.

First, theoretical calculations were made, starting with acceleration. Relating acceleration with final velocity gives equation 14.1.1.

$$v_f^2 = v_i^2 + 2 \cdot a \cdot d \tag{14.1.1}$$

Where v_f^2 and v_i^2 are the final and initial velocities respectively, and a and d are the acceleration and distance. The distance in this case is the length of the catapult system. Acceleration is assumed to be constant and occur over the entire length of the catapult system. Initial velocity is also assumed to be zero, and can be excluded from the equation. Rewriting equation 14.1.1 to make a the subject gives the following:

$$a = \frac{v_f^2}{2 \cdot d} \tag{14.1.2}$$

Different values of final velocity can now be entered, which can range from just above stall speed to above cruise speed. This can then be done for varying values of catapult length, which are taken from 2 m to 6 m. Two m was taken to be the shortest as an acceleration over one meter for a 20 kg RPAS would result in excessive g-forces. A maximum of six m was taken to ensure that the set up would not be too large and conflict with its

advantage of requiring little space. Using MATLAB to plot these values, a graph was able to be produced as shown in figure 14.1.

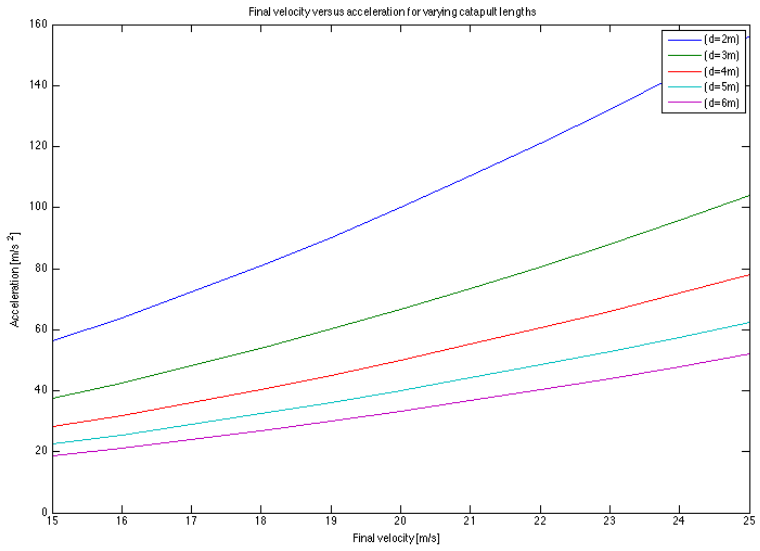

Figure 14.1: Final velocity over acceleration for different catapult lengths

Now there is a small trade-off between two factors. A lower acceleration would be better for the structure and a higher final velocity would make the launch system more efficient. The stall speed is 15 m/s, so a higher velocity than this is necessary. As a trade-off between the two, a launch velocity of 20 m/s is chosen. This lies well above the stall velocity and also makes it easier for the RPAS to accelerate to cruise velocity. The launch velocity can be verified and validated from values obtained for the ELI catapult system [1]. From figure 14.1, it can be seen that between 5 and 6 m distance, the acceleration is relatively small compared to the difference between 4 and 5 m. It is therefore chosen to choose a rail of 5 m long for the catapult system. The acceleration during launch is equal to 40 m/s^2.

Launch angle and clearance distance

Now that the length of the catapult system's rail has been determined, it is necessary to establish the launch angle of the RPAS. When finding this angle, it is essential to take into account the clearance distance, which is the distance in front of the catapult that must be clear of obstacles to ensure safety of the craft. The angle must also not be too high or the RPAS may have difficulty staying in flight after being launched. Furthermore, an angle that is too low will result in a very large clearance distance. Calculating the clearance distance can be done using simple trigonometry as shown in figure 14.2. In the figure, γ is the launch angle, h is the clearance height, and d is the clearance distance.

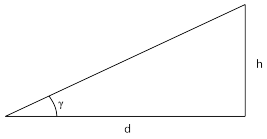

Figure 14.2: Clearance distance calculation

Using the tangent of the launch angle, an equation for the clearance distance can be determined. Equation 14.1.3 shows the calculation that needs to be done for varying launch angles to calculate the clearance distance. Clearance height h is taken to be 20 m, as this is a height at which the RPAS will be flying at an altitude where it is visible and not close to any potential obstacles.

$$d = \frac{h}{tan\gamma} \tag{14.1.3}$$

[1] Values have been acquired through personal communication

Equation 14.1.3 can then be used to create a graph relating the launch angle with the clearance distance. It is chosen to take a launch angle between 15 and 30 *deg*. A launch under 15 *deg* will make the clearance distance extremely large, and above 30 *deg* the RPAS may have difficulty sustaining flight after launch due to high angles of attack and quickly falling speed. A graph of clearance distance over launch angle was made and is shown in figure 14.3.

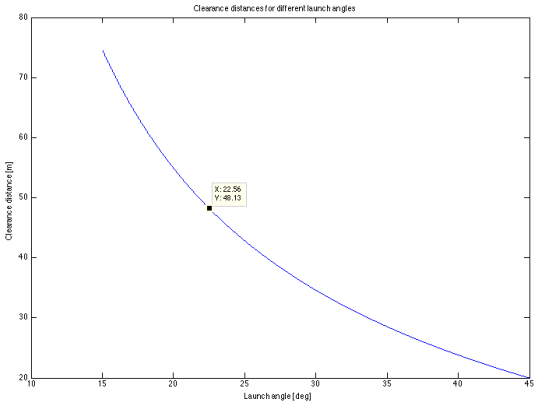

Figure 14.3: Clearance distance for varying launch angles

To find the most optimal combination of launch angle and clearance distance, the point most towards the bottom left of the curve is chosen, which in this case is shown in the figure as well. This ends up being a launch angle of 22.5 *deg* and a clearance distance of about 48 m.

Launch force

It is now also possible to determine the launch force, which can be done using figure 14.4 and using equation 14.1.5. The kinetic diagram should equal the forces on the free body diagram.

$$ma = F_{launch} - mgsin(\gamma) \tag{14.1.4}$$

$$F_{launch} = ma + mgsin(\gamma) \tag{14.1.5}$$

Using the launch angle of 22.5°, an acceleration of 40 m/s^2, and a mass of 18 kg, the force of the launch is calculated to be 787.6 N. This force will be acting longitudinally on the fuselage of the RPAS through the carriage and will be able to be sustained.

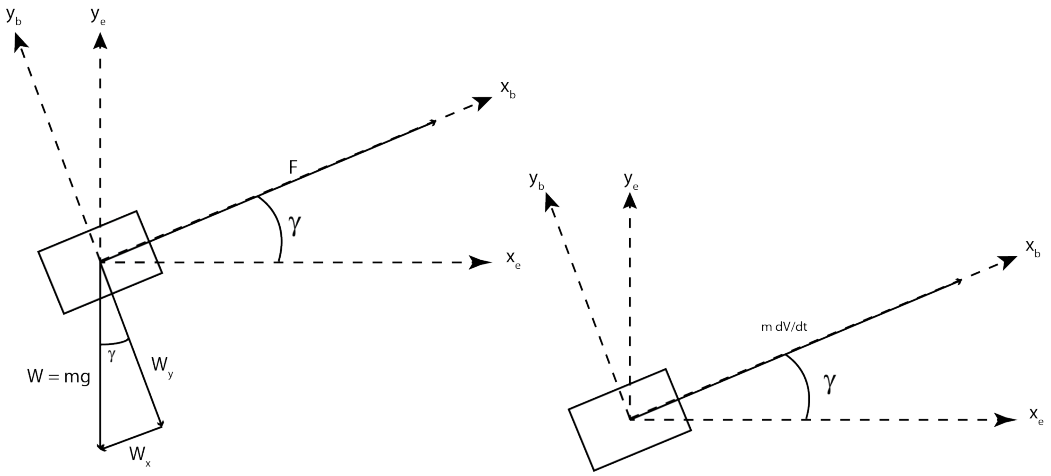

(a) Free body diagram for launch

(b) Kinetic diagram for launch

Figure 14.4: Kinetic and free body diagrams for launch

Catapult design

Now that the physical values have been determined for the launch, it is necessary to design the apparatus.

Reference catapult systems from ELI, Arcturus, UAV Factory, and Embention [111][110][112][113] will be used to determine a catapult design. These systems may also potentially be purchased as the launch system, but cost budgets will have to be taken into account in that decision.

One of the main reasons for choosing the catapult system was because of its mobility, which means that the design must incorporate mobility of the system. The length of the rail is 5 m, which is difficult to transport. It is decided that a modular system will be used where the catapult can be disassembled, this is also done with other catapults [111][110][112]. The rail will be able to be dismantled into multiple sections of one meter, allowing it to be transported in a rugged case or something similar. The cross section of the rail will resemble a hollow square with a hollow cylinder inside of it, as shown in figure 14.5. The outer structure will ensure that the carriage can slide over the top while the inner structure will ensure that pressure can be built up to launch the carriage. A cylinder is chosen as this is the strongest structure for internal pressure loading.

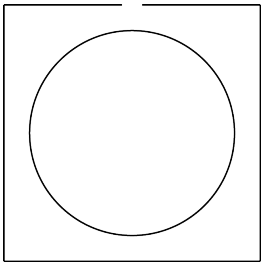

Figure 14.5: Launch rail cross section

This structure will need to be able to sustain the loads applied during launch of the RPAS, which means a stiff, strong, and reliable material will need to be used. Using the material property charts from Asbhy's Materials Selection in Mechanical Design, it is possible to make a selection for the materials with minimum weight and minimal deflection [114, p. 37]. From the graph, it can be seen that porous ceramics, engineering ceramics, and engineering alloys are suitable materials. Ceramics can be ruled out due to their low impact resistance, from which it can be determined that an alloy will be used. From these alloys, steel and aluminium are viable candidates. By comparing the two, it can be seen that the aluminium alloys have a higher Young's modulus for their relative density. Although steel may be stronger, it should be noted that aluminium has a density of almost 2.5 times less [114, p. 335-337]. Construction of the catapult must not be so heavy that many more people are needed to set it up. For this reason, it is decided that aluminium or an aluminium alloy will be used for the material of the catapult system.

Now that the material of the rail has been determined, the attachment carriage will have to be designed. This carriage will serve as the part that holds the RPAS in place during acceleration and releases it once the end of the rail has been reached. As can been seen in figure 14.6, both ELI airborne and UAV Factory have a similar design for supporting the RPAS during launch. For the maritime flyer, an identical design will be implemented. The four connection points will be attached at the hard points of the fuselage, where the wings connect with the body. This area is taken to be the most structurally strong, meaning it will be capable of supporting and distributing the loads induced by the launch. When launching, the c.g. must lie below or in front of the connection point to ensure that once the craft is launched, it does not pitch up.

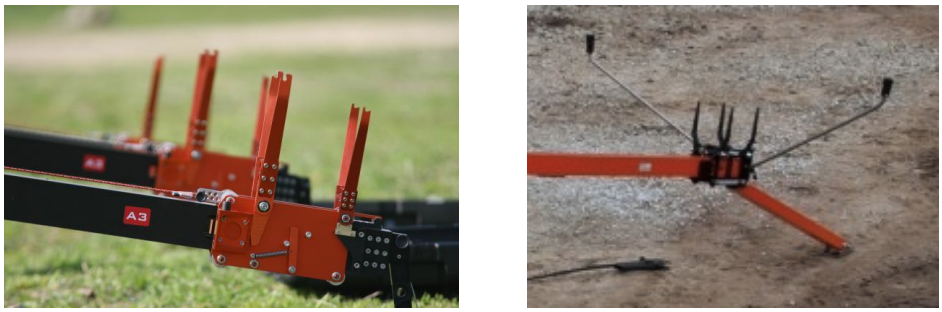

(a) Carriage for UAV Factory catapult [112] (b) Carriage for ELI airborne catapult [111]

Figure 14.6: Two different carriages for catapults

Comparing the prices from the ELI and UAV Factory launch systems, it is possible to give an estimation for the price of the catapult. The ELI catapult is priced at €16,000 while the UAV Factory launch system will

cost about €15,000. This catapult launch system is estimated to be €15,000 maximum.

Catapult operations
With a carriage and rail in place, the operations of the catapult system will now be explained. The catapult will be operated using a pneumatic system, which means compressed air or inert gas will be used to shoot the RPAS away. As seen in figure 14.7, the top right end of the rail will be the side where air or inert gas will be compressed using a compressor. The slider will be attached to a piece of strong string that will be attached to the carriage as shown by the dashed line in figure 14.7. The carriage will be locked in place, allowing pressure to build up in the end of the rail. Once the correct amount of pressure has been built up, the carriage can be unlocked. Due to the build-up of pressure, the slider will be shot downwards to the carriage, which will in turn launch the carriage up the rail. The RPAS will be started when placed on the carriage and full thrust will be provided during launch. Once the RPAS has reached the end of the rail, the four prongs holding the RPAS will release and rotate 180 degrees to a resting position. This will ensure that the propeller will not hit the carriage and be damaged.

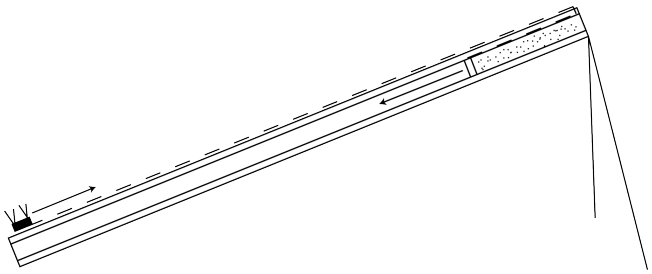

Figure 14.7: Design of the catapult system

Sustainability
When looking at the design and production of a launch mechanism such as the catapult system, sustainability must also be considered. This means that the design and production of the catapult must be done as eco-friendly as possible, and with a long lasting life in mind. Firstly, the materials used can be kept as sustainable as possible by using recycled aluminium, which can be remelted and used again for new aluminium [115]. Also, using aluminium will greatly increase the lifetime of the product, as the material is rugged and able to sustain systematic and random loads. What has to be noted is that the using a pneumatic system is not as sustainable as other launching methods. This is due to the fact that every launch will require compression of air or an inert gas, which may require large amounts of energy. To increase lifetime of the launch system further, it is essential that inspections are conducted and maintenance is provided when necessary. Jamming of the rail may cause serious damage to the catapult, so checks must be made to make sure everything is operating optimally.

14.2 Net capture system

For the maritime flyer it has been decided that a net capture system will be used for recovery. The concept consists of a large net made from a giving material that the RPAS will fly into and quickly come to a stop. An example is given in figure 14.8, which is the net capture system from Arcturus. It has been decided to use this method of recovery over conventional methods due to its mobility, its quickness, low required space, and ease of setting up. Contrary to conventional methods, the net allows capture of the RPAS in a separate location from launch. This is due to the fact that it takes up little space and can be transported easily to a recovery location. It is also a relatively 'soft' form of recovery compared to for example a belly slide, making it a more appealing capture method.

Figure 14.8: Example of a net capture system [110]

Net characteristics

Before calculating the force induced by capture, it is essential to define some characteristics for the net. Decreasing stress of the recovery impact can be done by spreading the loading over a larger area. Considering that the wing has the largest frontal area, it is chosen to try to spread the load over this component. The fuselage of the RPAS sticks out at the front, meaning the mesh should be big enough to let the fuselage through. To make sure that the payload is not damaged, only a vertical mesh will be used. The diameter of the fuselage is 20 cm so the mesh of the net is determined to be 25 cm. This characteristic also makes approaches with sideslip possible without highly loading one part of the RPAS more than another. Once a part of the RPAS has been hit, a moment about the c.g. is created that will return the aircraft to be perpendicular to the net, distributing the load of impact.

Furthermore, the dimensions of the net will have to be determined as well, which can be done using the frontal dimensions of the RPAS. As shown in figure 14.10 the frontal area of the RPAS has been simplified as a circle and two trapezoids. The width of the RPAS is equal to 3.57 m and the height is 48.9 cm, which means the net should be at least these dimensions. It is assumed that during recovery the RPAS will be controlled using visuals as it will be close enough to the pilot to see clearly. This means that control of the RPAS can be done with high accuracy. The net dimensions are to be bigger than this to allow for some error when approaching the net. Assuming a 50% error margin on each side of the RPAS gives a width of 6 m. Depending on the method of approach, the pilot may have difficulty evaluating the vertical location of the RPAS. Due to this, the height of the netting has a larger error, which makes it 2 m high. Figure 14.9 shows the net and its dimensions and figure 14.10 shows the frontal area of the RPAS with its dimensions.

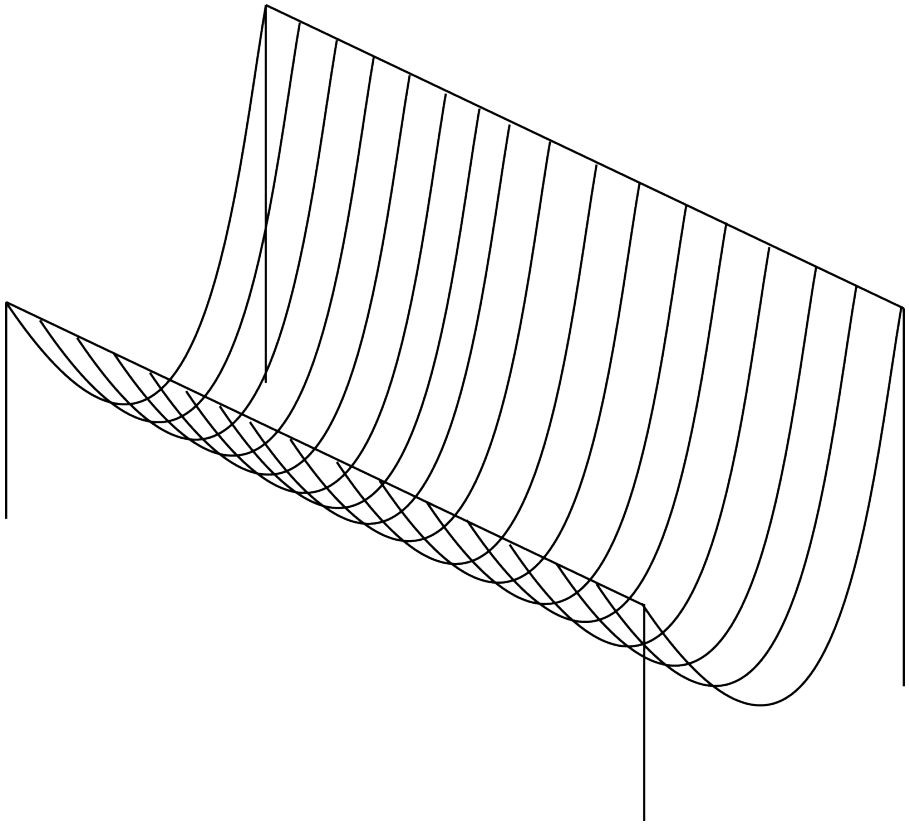

Figure 14.9: Dimensions of the net recovery system

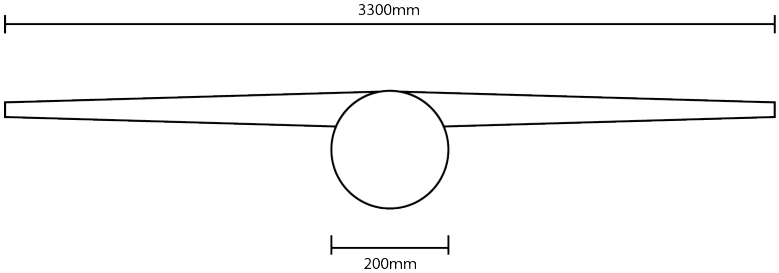

Figure 14.10: Simplified frontal area of the RPAS

To get an idea of the costs and materials used in this netting, safety netting is searched for. Safety netting is used on construction sites to save personnel if they fall or debris that falls from the construction site. This can be used as a rough estimation for the 20 kg RPAS that hits the net capture system. An Adjust-A-Net safety net for personnel that is a bit larger than the net needed costs USD 1,600 [116]. This helps to give an estimate for the recovery net required. The required net is smaller and requires less strength, meaning it will be cheaper. A price of USD 1,000 or €881 [117] is assumed as an initial price for the net.

Recovery force

Determining the force that the RPAS will sustain during recovery is essential for structural design of the fuselage and wings. A simple but reliable method will be used to determine the force, it has already been used in determining launch acceleration. Equation 14.1.1 can be rewritten to equation 14.2.1, where v_i is the approach speed for recovery, and v_f is the final velocity of zero. The distance d is the distance needed for the RPAS to come to a full stop.

$$a = \frac{-v_i^2}{2 \cdot d} \tag{14.2.1}$$

The acceleration obtained from this equation will give a negative value, which corresponds to the deceleration from reducing velocity to zero. Approach speed to the net should be as low as possible to decrease the force induced by the impact. With a stall speed of 15 m/s, the approach speed should be higher than this value. To show the effect of different approach velocities, a graph was made which relates the acceleration with the distance to stop for different velocities, as shown in figure 14.11.

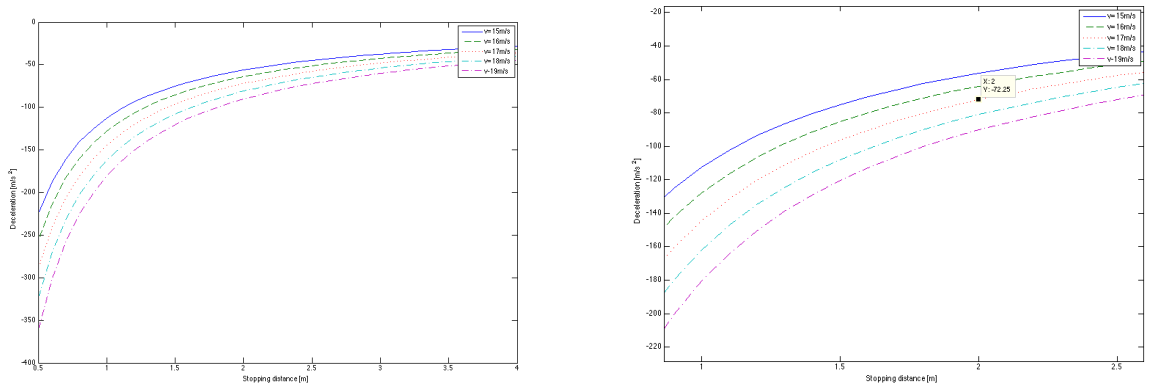

(a) Deceleration for varying velocities

(b) Zoomed in graph from figure 14.11a

Figure 14.11: Acceleration graphs for different approach velocities

In figure 14.11a, less than 1 meter distance gives a large change in acceleration for a change in velocity, so it is left out in figure 14.11b. Going over 2.5 m stopping distance showed a negligible change, and it is removed in figure 14.11b as well. From this figure, a value of 2 m for the stopping distance was chosen. This was done by trading off between an as low as possible approach velocity, a short stopping distance, and minimum acceleration.

Stall speed is determined to be 15 m/s, but keeping a slight margin over the stall speed so that gusts or incorrect readings do not cause the flying wing to stall, the approach speed is set at 17 m/s. Following this curve in figure 14.11b shows that a longer stopping distance decreases acceleration, as expected. A distance of one meter is extremely small and causes very high accelerations, which leads to forces exceeding the maximum shear force of the wing. However, the stopping distance cannot be too long as you decrease acceleration at the expense of mobility and set-up time of the recovery system. It is decided that the stopping distance will be 2 m. From equation 14.2.2, it is then possible to determine the force exerted over the entire frontal area of the RPAS. The frontal area is calculated using figure 14.10, and is determined to be 0.183 m^2.

$$F = m \cdot a = 18 \cdot -72.25 = -1,300.5N \tag{14.2.2}$$

Table 14.2: Recovery values

Parameter	Value	Unit	Input	Output
Mass		$[kg]$	X	
Frontal area	0.183	$[m^2]$	X	
Stall speed		$[m/s]$	X	
Approach velocity	17	$[m/s]$		X
Net size	6 x 2	$[m]$		X
Recovery force	1,300.5	$[N]$		X
Acceleration	-72.25	$[m/s^2]$		X

Recovery operations
Now that technical specifications of the recovery system have been determined, the operations required for recovery to occur are explained. Operations include all actions needed to set up the net and get the RPAS from flight to a stop in the net. First of all, the net will have to be set up in a suitable location. To ease the capture, the wing should be placed perpendicular to the direction of the wind so that the RPAS can use a headwind to decrease its ground speed and soften the landing. Supporting structures will be used to keep it stable during the recovery phase. This will be done by using long steel tubes which are supported by cables running from the top of the pole and driven into the ground by stakes, as is done with setting up a tent. The supports will be able to sustain the shear loads and moments sustained during capture. Once set up, there is not much that has to be done except fly the RPAS into the net. The spotter must be present to constantly check the airspace around the landing location to make sure there are no obstacles. Once near the net, the pilot should fly with visual rules to ensure an as accurate as possible landing. After flying into the net, the RPAS will land in between the front and back supporting structure in the net for easy retrieval. Once recovery is complete, the RPAS is removed and inspected, followed by the net and supporting structure being disassembled. The net can be folded to small dimensions while the supporting rods will have to be transported as they are.

Sustainability
For the recovery system it is also important to keep sustainability in mind, as the design should be eco-friendly as well as durable. Considering the environment, the materials from which the net as well as the supporting structure is made should be as environmentally friendly as possible. If possible, materials that are biodegradable and have the same properties should be used. Furthermore, strong and durable materials should be used as well as periodic inspections of the recovery system. This ensures that the net is always in pristine condition, which will be beneficial for the RPAS as well. A well-kept net will also be usable for a long period of time, which reduced waste produced. Keeping these aspects in mind during operation is a good way to keep up sustainability of the net capture system.

14.3 Operations and logistics concept

The operations and logistics concept of the RPAS gives a general overview of the logistical as well as the operational steps taken during a mission of the RPAS. This concept can be described in a number of ways, therefore first it has been thought through how it can be represented best. As a result, it is decided to use a similar concept as the operational flow diagram created for the preliminary design, however more detailed and in-cooperating flow elements and loops. The results can be demonstrated in figure 14.12.

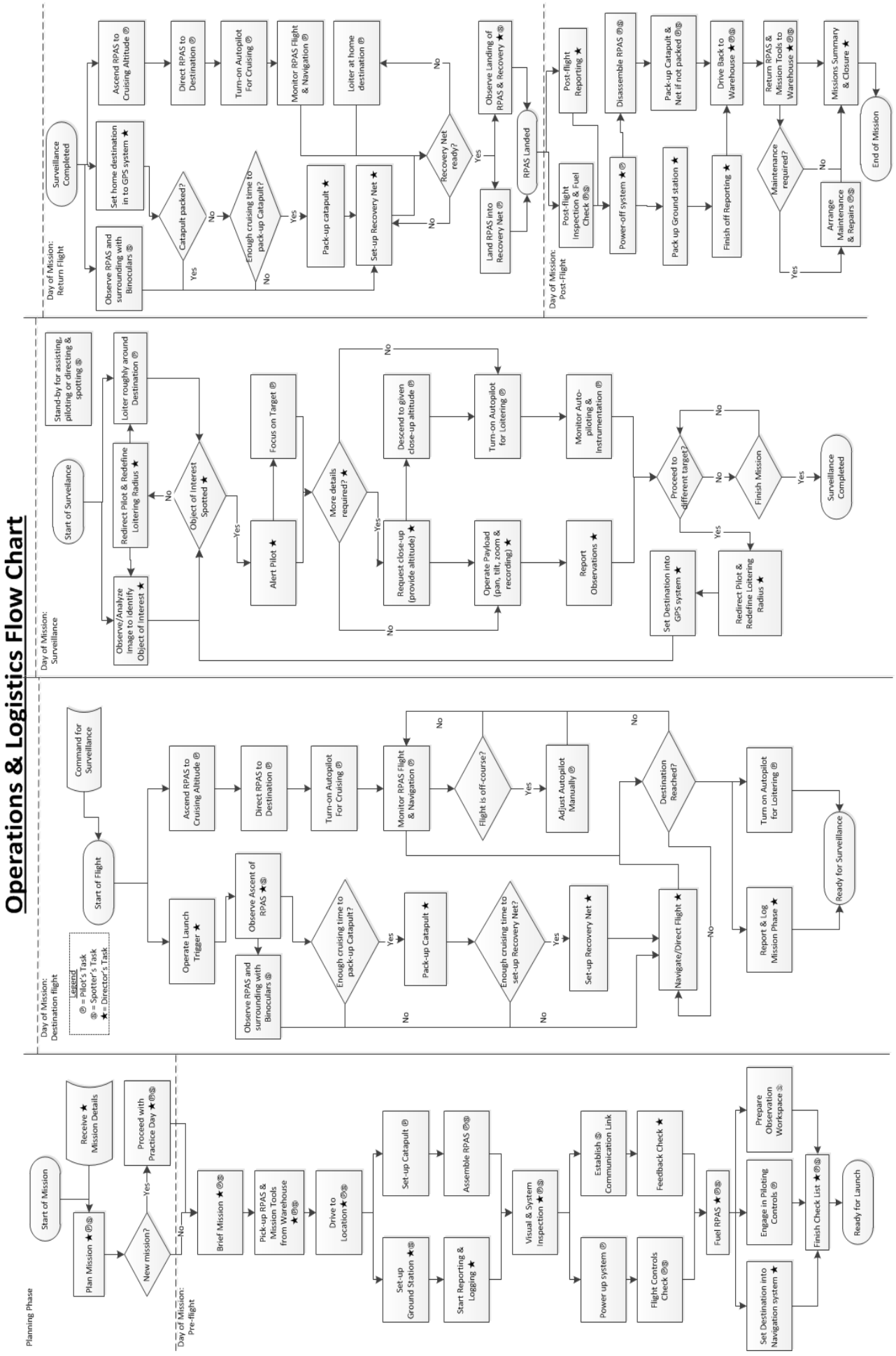

Figure 14.12: Operations and logistics flow diagram

14.4 Deployment

In the end the end-user is only interested in possibilities of deploying the RPAS. Therefore this section displays the steps that needs to be taken before, during, and after deployment.

Mission preparation
Before any mission can be performed, the RPAS have to be prepared for operations. There are multiple types of missions the RPAS could perform, for example operate after call, operate on schedule, or operate on maximum endurance. However every mission needs to be launched at some point, therefore the general mission preparation is explained. Basic steps needs to be taken regarding to the RPAS, mission, and circumstances at mission location. The following steps are essential for a good mission progress:

- Charge the battery
- Save and format content from hard drive
- View weather forecast

After confirmation that all tasks have been completed, the mission can be established. If the RPAS is not on mission location, it will first have to be transported. Once arrived, the next task shall have to be carried out on launch location, the assembly of the RPAS. First the clearance height and distance as described in section 14.1 have to be applicable the launch location. Transmission towers, buildings and other obstructions in the surroundings have to be located. Thus the location has to be satisfied, otherwise a new location must be found.

Assemble the RPAS
Since the earlier stages of the design, mobility of the RPAS is one of the important design criteria. Increasing the mobility of the entire operation will increase the deployability of the RPAS. Transporting a large span RPAS involves multiple logistic difficulties, therefore the RPAS is designed to be modular.

The RPAS can be constructed from three modules; the fuselage, and two half wings. Connections are realised using the wing joint construction as described in section 9.3.4. Both half wings are attached to the fuselage to transfer the loads and connect the electronics. The electronics for the servos and lights are connected, which are located inside the wing to prevent it from any impacts.

Pre-flight check
After assembling the wing the first checks can be performed, the first check is called the pre-flight check. This is a general check to assure the airworthiness of the RPAS for takeoff. The pre-flight check can be divided into two different phases; before power up, and after power up.

Before the propulsion and power systems are initialised, a visual inspection of the airframe has to be performed. This contains looking for damages caused by impacts or cracks. If necessary, remove the dirt from the surface of the wing and fuselage. After that the engine is checked on oil blow-out and other damages. Also there should be looked at the propeller to be sure that the blades are not cracked, bent, or other damages. Next step is to turn the power switch on and initialise the subsystems. An external power supply is provided during such that the battery is still fully charged at the launch

After powering up the system the most intensive phase of the pre-flight check starts. A checklist of the most important tasks is listed below;

- Structure
  - Catapult installation
- Electric power
  - Check battery capacity
- Communication
  - Turn on on-board systems
  - Turn on remote control
  - Obtain connection with ground station
- Control surface
  - Inspect control surfaces on possible deflections
  - Check response of remote control inputs
- Payload
  - Turn on camera
  - Check presence of hard drive
- Propulsion
  - Start engine
  - Check power generator
  - Check fuel system/level
- Navigation and sensing
  - Calibrate sensors
  - Wait for GPS-fix
- Miscellaneous
  - Control autopilot system

Just before launching the RPAS there must be ensured that the clearance is still available and that no people are in the catapult clearance area. If the clearance can be guaranteed the RPAS can be launched.

After take-off
Just after launching the RPAS, the mission for the end-user is started. But to ensure that nothing fails on the RPAS, the RPAS must start circling above the launch location such that the spotter any possible errors can observe. Also the live-video streaming at the ground station should be checked on operation. The final systems of importance in the after take-off check that needs to be checked are the control surfaces and the sensors. If all systems are working correctly the RPAS can continue its mission.

During the mission
After checking all the systems and launching the RPAS, the real mission and all its difficulties start. During the flight the pilot must constantly have control of the aircraft or should be able to take control any time of the mission. The surroundings shall be checked constantly for danger from other objects, in particular other aerial vehicles. Furthermore it can happen that the RPAS may exhibit strange behaviour, this can have various causes. Therefore the RPAS must have to land because of safety reasons, the troubleshooting manual can be found in section 14.5. What also is important, is the constant inspection of the battery and fuel level. Finally, just before the landing using the net capture mechanism, regardless of whether a manual or automated landing takes place, scan always the landing area for potential obstruction hazards.

Post-flight check
Now the RPAS has landed successfully, there are several options to do next. If the mission is completed the normal post-flight check shall be followed. In case the mission is not completed yet and the RPAS has to go airborne again, additional tasks arise. First the the fundamental steps immediately after landing that has to be taken are listed;

1. Turn off engine
2. Turn off communication system
3. Turn off payload camera
4. Save and format hard drive
5. Turn off battery
6. Replace/remove battery
7. Visually check RPAS for damages and wear
8. Refuel/remove fuel
9. Disassemble RPAS if mission is completed
10. Log flight

The engine of the RPAS needs to be turned of to prevent any damages to the engine and propeller. Remove the RPAS from the net capturing mechanism and place it on a flat surface. The post-flight check starts with turning of the subsystems and save the video content from the hard drive and format it afterwards. The next step is to turn the battery off and replace or remove the battery, this depends on the whether a new mission will be performed or not. After the visual check the fuel in the RPAS shall be removed or it could be refuelled. Log the flight in a logbook is the last step of the post-flight check, this step should not be underestimated since this is the input for the maintenance program as is described in section 14.6.

14.5 Troubleshooting

Despite the fact that the RPAS is designed using different safety factors and will be maintained according to schedule as can be seen in section 14.6, still problems and failures may occur to the system. There are many different types of failure that can occur, fatal or failures with less impact. For each possible problem a troubleshooting manual can be distinguished, however only the in general most common failures are discussed in the troubleshooting manual. In each troubleshooting manual the condition, the possible cause, and the solution is stated.

For the electric power, communication, and navigation and sensing there is special return to home protocol. As can be seen in tables 14.4, 14.5, and 14.6, for in flight failure condition this return to home protocol is introduced. This protocol contains a very cautious return to the location where the net capture is located.

Propulsion problems
Problems caused by the propulsion can appear if the RPAS is still on the ground, as well as in the air. Still on the ground the engine can be repaired or replaced for instance, however if it is already in the air additional problems may arise. The propulsion system is one of the most important systems to be checked during deployments and maintenance. The propulsion troubleshooting manual is shown in table 14.3.

Table 14.3: Propulsion troubleshooting manual

	Condition	Possible cause	Solution
On ground	Engine will not start	No fuel feed, engine flooded, engine igniter defect	1. Check fuel feed 2. Check spark plug 3. Return to manufacturer or replace the engine
Airborne	Engine failure	Dirty air/fuel filter, fuel too lean/rich	1. Reignite the engine 2. Start gliding to net capture location or safe location for emergency landing

Electric power problems

In general, a failure in the electric power system can disrupt the entire system. Because almost every sub-system is dependent on a power source, redundant power systems are often installed. Because there is a generator and a battery present in the RPAS, when problems arise the battery source can be switched. The electric power troubleshooting manual is shown in table 14.4.

Table 14.4: Electric power troubleshooting manual

	Condition	Possible cause	Solution
On ground	No electric power available	Battery is off, battery is not charged, battery is defect, engine rpm too low	1. Check battery capacity if required replace it 2. Increase engine rpm 3. Check power generator
Airborne	No power to single subsystem	Power connection interrupted	1. Change power source to battery for single subsystem 2. Start return to home protocol
	No power to total system	Battery defect, power connections damaged, power generator defect	1. Change main power source to battery and start return to home protocol

Communication problems

The communication system of the RPAS has two different tasks during the mission, sending images of the payload to the ground station, and sending and receiving flight data. If the RPAS is still on the ground, the connection can be easily restored. Once in the air, there is a difference in solution. Depending on which part of the communication system fails, there are various solutions such as can be seen in table 14.5.

Table 14.5: Communication troubleshooting manual

	Condition	Possible cause	Solution
On ground	Connection failed	Antenna damage, component failure, signal interference	1. Reconnect to the ground station 2. Replace the communication system or return to manufacturer
Airborne	Payload connection failed	Antenna damage, component failure, signal interference	1. Automatically switch to autonomous flight mode 2. Reconnect with ground station 3. Still no connection, perform a normal return to home
	Flight data connection failed	Antenna damage, component failure, signal interference	1. Automatically switch to autonomous flight mode 2. Reconnect with ground station 3. Still no connection, start return to home protocol

Navigation and sensing

Sensors are generally very influenced by environmental effects, therefore, sensors are often calibrated before they can give reliable measurement results. Sensor calibration is a method of improving the performance of a sensor by removing errors in the sensor outputs. However, there may also arise calibration errors which negatively affect the system. The same can happen with a GPS module that transmits the most accurate approximation of the location. Therefore, the troubleshooting for the failure with a relatively high impact are discussed in table 14.6.

Table 14.6: Navigation and sensing troubleshooting manual

	Condition	Possible cause	Solution
On ground	No GPS fix	GPS signal interference, rain fade, GPS module defect	1. Reinitialize the GPS module 2. If still not working replace the GPS module
	Sensor calibration error	Damaged sensor cable	1. Recalibrate the sensor 2. If still not working replace the sensor
Airborne	No accurate GPS location	GPS signal interference, rain fade, GPS module defect	1. Reinitialize the GPS module 2. Integrate information from accelerometers to obtain temporary position 3. Start return to home protocol

Payload
And finally, the payload troubleshooting manual which is partly dependent on the payload itself and the communication system. In the end the entire mission is all about the payload images for the end-user and it makes not sense to perform a mission without a working camera. Fortunately, the failure of the payload system little to no impact on flight safety of the RPAS. However, the deployment of the RPAS, and therefore the payload camera, strongly dependent on other subsystem are as can be seen in table 14.7.

Table 14.7: Payload troubleshooting manual

	Condition	Possible cause	Solution
On ground	No images on ground station	Connection interrupted, payload camera defect, communication system defect	1. Check communication system and follow the communication troubleshooting manual in table 14.5 2. Check and replace/repair payload camera
Airborne	No images on ground station	Connection interrupted, payload camera defect, communication system defect	1. Check communication system and follow the communication troubleshooting manual in table 14.5 2. Still no images, perform a normal return to home 3. Check and replace/repair payload camera

14.6 Maintenance

Just like all other aircraft, the RPAS needs to be checked whether it still complies with airworthiness regulations. Besides daily checks such as pre- and post-flight checks that mainly checks the exterior of the aircraft for damaged parts, also maintenance has to be performed on the aircraft.

At this time there are no regulations regarding to maintenance programs for RPAS. Often there are maintenance programs set up by the manufacturer that ensure continued airworthiness. For the flying wing the maintenance program besides the daily checks is defined in two different checks, this maintenance program is based on civil aviation maintenance programs. Maintenance on the RPAS can be performed by own staff or certified external companies. The amount of maintenance checks mainly depends on the amount of flight hours performed by the RPAS. Taking into account the daylight camera and the purpose of the mission, the RPAS has to fly the entire time in daylight. According to the Koninklijk Nederlands Meteorologisch Instituut (KNMI), the shortest and longest day in the Netherlands (De Bilt) is 7:43 and 16:33 ($hh:mm$) respectively [118, 119]. Patrol- and surveillance-boats in the port operate 24 hours a day 7 days a week, keeping in mind that the RPAS has to assist, the following maintenance estimations are based on 8 flight hours per day.

Check A
The "A" check (light) maintenance program consist of a next level check and includes the daily check as well. The maintenance shall be performed at a designated maintenance station, where the required test equipment, tooling, and service is available. Check A however, does not involve a detailed dissassembly or removal of subsystems. The RPAS will be out of service every 1.5 - 2 months (350 - 500 flight hours) for 1 - 2 hours depending on the required maintenance if performed by one technician. The following items are included in the "A" check:

- Visual inspection of aircraft structure for damage, corrosion, deformation, and missing parts.

- Check operational lights
- Check engine and propeller
- Check battery capacity

Check B
Check "B" (heavy) involves heavy testing of the structure and subsystems, as well the "A" check and the daily checks. Also the maintenance shall be performed at a designated maintenance station, where the required test equipment, tooling, and service is available. Check B is an extensive test in which the functions and serviceability of individual systems and components will be checked. The RPAS will be out of service once every 1 - 1.5 years for 2 - 3 days depending on the required maintenance if performed by one technician. The following checks are included in the "B" check:

- Fuselage
  - Fabric and skin
  - Flight and engine controls
  - Batteries
  - Fuel tank
  - Launch connection point
- Engine
  - Check for oil, fuel, and hydraulic leaks
  - Ground run-up and functional check
  - Engine mount
- Miscellaneous
  - Autopilot system
- Wing
  - Fabric and skin
  - Internal structure
  - Movable surfaces
- Propeller
  - Propeller assembly
  - Control mechanisms
- Communication and navigation
  - Radio and electronic equipment
  - Check for proper wiring
  - Check antennas

Sustainability
Nowadays, companies are thinking more and more green. However in order to remain sustainable, the operation has to be performed responsible and maintained properly. Therefore, sustainability is often directly linked to the maintenance of the product. With regard to sustainability, there are three different types of maintenance determined; reactive maintenance, preventive maintenance, and condition based maintenance.

Reactive maintenance means that maintenance is performed when subsystems or the RPAS have obvious malfunctions. When maintenance is performed because it's time for the yearly check-up, then it is called preventive maintenance. Condition based maintenance is constantly looking for abnormalities and malfunctions that could have negative impact on the performance of the RPAS.

While setting up the maintenance program, sustainability is explicitly taken into account. In the maintenance program there is a combination of two different types of maintenance; preventive maintenance, and condition based maintenance. The condition based maintenance is performed during each pre- and after flight check, where the preventive maintenance is carried out during the light and heavy maintenance. The combination of those two types of maintenance also increases the safety since the RPAS will be properly maintained.

Availability
Aircraft availability is defined as available days for service as percentage of total days per year. The largest contribution to the days not available is maintenance. The more maintenance is required, the more days the RPAS will not be available. Before and after each mission the RPAS is checked by the so called pre- and after-flight checks. These checks ensure that intermediate inspection is carried out and that early abnormalities are detected. During the year multiple light maintenance are performed to keep the RPAS ready for service. Since the main purpose of the RPAS is be in service the entire year, decreasing availability is expected due to maintenance and unfavoured weather conditions.

There will be multiple (6 - 8) light maintenance and one heavy maintenance performed every year. Light checks can be performed during the night, however for the availability analysis both cases are taken into account. During heavy checks the RPAS will be out of service for 2-3 days once every 1-1.5 years, however also for this availability analysis is assumed that the heavy maintenance could be performed during days with bad weather. The availability due to weather conditions is determined by the intensity of wind gusts at the location where the operations take place. Wind gusts cause high loads on the RPAS for a short period of time. The maximum wind gust the structure of the RPAS can withstand is 20 m/s, as already explained in section 9.2.1. The availability due to wind gust is dependent of the location, however for the port of Rotterdam the 20 m/s maximum gust is equal to an availability of about 90% of the days. After defining the expected weather conditions and maintenance, the availability analysis is performed as can be seen in table 14.8.

Table 14.8: Service availability of the RPAS

Parameter	Value	Unit	Input	Output	Comments
Flight hours	2,922	$[hr]$	X		Flight hours every year (8 hours for 365.25 days)
Gust unavailability	10	[-]	X		Unavailability due to gust in percent
Light maintenance	0-16	$[hr]$		X	Unavailability due to light maintenance
Heavy maintenance	0-40	$[hr]$		X	Unavailability due to heavy maintenance
Availability	0.886-0.9	[-]		X	Availability in percent of days every year
Availability	324-329	$[day]$		X	Available days every year

14.7 Operational costs

Purchasing an RPAS, introduces new costs such as operational costs. The operational costs are estimated in costs per operation, according to 8 flight hours per day as already mentioned in section 14.6.

Fuel
During the mission, the fuel tank will go from full state to almost empty. Taking into account the reserve fuel, a full tank of fuel will be used during the mission of 4 hours. The weight of the fuel tank is determined to be 3.34 kg. The density of gasoline is assumed to lie between 0.71 and 0.77 kg/L, the average will be taken at 0.74 kg/L [45, p. 33]. The cost of a liter of gasoline is estimated to be €1.50. The cost per flight hour and mission can be seen in table 14.9.

Table 14.9: Operational costs of fuel

Parameter	Value	Unit	Input	Output	Comments
Price gasoline	1.50	[€/L]	X		Fuel price depends on country
Fuel weight	3.34	$[kg]$	X		Source: Structures and Materials
Density	0.74	$[kg/L]$	X		Density of gasoline [45, p. 33]
Mission costs	6.77	[€]		X	fuel costs per deployment based on 4 hour endurance
Flight hour costs	1.69	[€/hr]		X	Costs per flight hour

Staff salaries
During the mission there are three people required, a pilot, a backup pilot or spotter, and a camera operator that needs to be hired from external companies or trained. In the labour market, there are currently no vacancies for RPAS pilots since this is a new market. In order to make a reliable salary estimation, foreign labour markets are not taken into account. If local authorities, governments, or port authority want to use their own staff, the staff needs to be trained before they fly the RPAS. RPAS pilot training are given by the Nationaal Lucht- en Ruimtevaartlabouratorium (NLR) in order to get exemption from Inspectie Leefomgeving en Transport (ILT). The costs of an RPAS pilot training is about €4,500 including theory test, technical Review of the RPAS, and practical exam [120].

For a first staff year salary estimation the average income of 2015 in the Netherlands is €34,500 [121]. Since the salary, free days per year, and length of a workweek is dependent on the collective labour agreement, those parameters are estimated using a 36 hour workweek, 52 weeks per year, and free days can be calculated by multiplying weekly work by four [122]. The mission costs are based on the mission endurance of 4 hours, remaining parameters can be seen in table 14.10.

Table 14.10: Operational costs of staff salaries

Parameter	Value	Unit	Input	Output	Comments
Working hours	1,728	$[hr]$	X		Total hours minus free hours
Free hours	144	$[hr]$	X		Weekly hours multiplied by four [122]
Total hours	1,872	$[hr]$	X		Defined as 36 hours multiplied by 52 weeks
Average income	34,500	[€]	X		Average income in the Netherlands [121]
Staff members	3	[-]	X		Pilot, a backup pilot, and a camera operator
Hourly wage	19.97	$[€/hr]$		X	Average income divided by working hours
Flight hour costs	59.90	$[€/hr]$		X	Costs per flight hour
Mission costs	239.58	[€]		X	Staff salary costs per deployment based on 4 hour endurance

Insurance

If a customer purchases a new RPAS, an insurance is recommended. Just as the drone market, also the drone insurance market is growing rapidly. More often accidents occur, however the damages are not refunded since accidents by drones are not included in the policy. There is a legal liability policy available on the on the drone insurance market.

An RPAS operator may consider the legal liability as a minimum. In case of any accident this policy covers the cost to repair property you may damage and the injuries to people. Additionally cover is available that covers physical damage to the RPAS itself. It covers the cost to repair, or the total loss of the RPAS, payload, or ground equipment [123]. The costs for the insurance are about €4,500 every year for flying with 20 UAVs where the cover limit is €1,000,000 [124]. This yearly insurance costs is independent on the amount of flight hours during the year. In table 14.11, the insurance costs per hour and mission are shown.

Table 14.11: Operational costs of insurance

Parameter	Value	Unit	Input	Output	Comments
Insurance costs	4,500	[€]	X		Insurance costs per year
Flight hours	2,922	$[hr]$	X		Flight hours every year (8 hours for 365.25 days)
Costs per flight hour	1.54	$[€/hr]$		X	Insurance costs for each flight hour
Mission costs	6.16	[€]		X	Insurance costs per deployment based on 4 hour endurance

Maintenance

For the costs of the maintenance, the different checks in section 14.6 are an indication for the labour costs and component replacements costs. For each subsystem there is a different expected life time, therefore high risk subsystems with smaller life time should be checked more often depending on the expected life time of the manufacturer.

In section 14.6 the expected hours of maintenance is discussed. Maintenance labour is calculated counting only the actual craft technicians working hours. The maintenance labour costs are based on salary properties as used for determining the staff salaries. The results can be seen in table 14.13. The calculations are based on an "A" check every 1.5 months and a "B" check every 12 months.

The maintenance costs for maintaining the RPAS itself (i.e. material and subsystem replacement costs) are based on the lifetime of specific subsystems and Replacement Asset Value (RAV) based on benchmarks. The maintenance cost as a percentage of replacement asset value is used as a benchmark for the yearly maintenance costs. In general, two stroke engines as installed on the RPAS have a limited lifetime. Since the engine is one of the high asset value subsystems, a separate maintenance cost estimation is performed for the engine. According to the engine manufacturing, there is a warranty of 36 months from the date of purchase or 1,200 operating hours, therefore the expected lifetime of the engine is set equal to the warranty of 1,200 operating hours [125]. For the other subsystems, a maintenance cost as a percentage of replacement asset value of 5% is determined according to benchmarks [126]. These data are collected from section 16 and processed in table 14.12.

Table 14.12: Estimated yearly maintenance costs of individual RPAS subsystems

Subsystem	Asset value [€]	Maintenance costs [€]
Propulsion	1,050.00	2,556.75
Communication	4,372.00	218.60
Payload	8,856.00	442.80
Sensors	6,454.00	322.70
Electric power	610.00	30.50
Control	235.72	11.79
Fuel	180.00	9.00
Frame	80.00	4.00
Wing	684.63	34.23
Materials	5,938.25	296.91
Other	2,000.00	100.00
Total		4,027.28

Combining the labour costs and replacement maintenance costs, in table 14.13 the results can be seen. This is including the labour costs of both checks calculated with all annual checks performed by own staff members.

Table 14.13: Operational costs of maintenance

Parameter	Value	Unit	Input	Output	Comments
Flight hours	2,922	$[hr]$	X		Flight hours every year (8 hours for 365.25 days)
Replacement Asset Value	5	[-]	X		Maintenance cost as percentage of RAV
Hourly wage	19.97	$[€/hr]$	X		Average income divided by working hours
Labour costs "A" check	319.44	[€]		X	Yearly labour cost of "A" checks
Labour costs "B" check	479.17	[€]		X	Yearly labour cost of "B" check
Costs subsystems	4,027.28	[€]		X	Yearly subsystem maintenance costs
Maintenance costs	4,825.89	[€]		X	Maintenance costs per year
Costs per flight hour	1.65	$[€/hr]$		X	Maintenance costs for each flight hour
Mission costs	6.61	[€]		X	Maintenance costs per deployment based on 4 hour endurance

Conclusion

After analysing the fuel, staff salaries, insurance, and maintenance for the RPAS, the expected operational costs can be shown. The operational costs are based on 8 flight hours every day and costs that are not related to the operation itself are not taken into account for the final conclusion. The final conclusions can be seen in table 14.14, where the costs per flight hour, mission and the costs for every mission are mentioned.

Table 14.14: Final conclusion of the operational costs

Parameter	Value	Unit	Comments
Fuel	1.69	$[€/hr]$	Fuel costs per flight hour
Insurance	1.54	$[€/hr]$	Insurance costs per flight hour
Salary	59.90	$[€/hr]$	Staff salaries per flight hour
Maintenance	1.65	$[€/hr]$	Maintenance costs per flight hour
Total per flight hour	64.78	$[€/hr]$	Total costs per flight hour
Total per mission	259.12	[€]	Costs per deployment based on 4 hour endurance
Total per year	189,287.20	[€]	Total costs per year

14.8 Certification and regulation

The certification of an RPAS is different compared to the certification of a general aviation or transport aircraft. Regulations and certifications of an RPAS are based on their weight, the maximum take-off weight is already determined to be 20 kg. According to the regulations of the European Aviation Safety Agency (EASA), non-military governmental RPAS flights and civil RPAS that weight less than 150 kg are regulated by individual member states of the European Union [127]. Therefore the regulations provided by the Dutch Ministry about RPAS have to be followed. There is no difference between commercial or governmental use of the RPAS regarding to the regulations or certification. Next to that the Inspectie Leefomgeving en Transport (ILT) monitors compliance with safety and environmental laws and regulations for aviation. In the Netherlands, there are different classes that distinguish the regulations that have to be followed in the design process of an RPAS. There are two different classes that can be distinguished [10].

Class 1

- Maximum flight altitude is 120 m AGL
- Maximum distance from controller is 500 m
- Fly only in Visual flight rules (VFR) conditions
- Fly only in Visual Line of Sight (VLOS)
- Not fly within 150 m of buildings, traffic, and people

Class2

- Fly above 120 m AGL
- Fly more than 500 m away from controller
- Allowed to fly in Instrument flight rules (IFR) conditions
- Fly out Visual Line of Sight (VLOS)
- Allowed to fly above buildings, traffic, and people

Since the RPAS is designed to fly above ports where people, buildings, and traffic is present, the RPAS is designed for at least class two. Designing for class two requires the RPAS to be designed according to International Civil Aviation Organization (ICAO) requirements [10], therefore the RPAS is designed according to the ICAO regulations.

For the use of certain frequencies in the field of telecommunication, regulations are also available for each country. These are summarised by the ITU in the document [74]. However, for practical use, section 10.7 focuses mainly on the national regulations established by the Dutch ministery of Economic Affairs [75]. In these documents, frequencies are regulated by licenses, application, bandwidth, equivalent isotropic radiated power (EIRP), duty cycle and power density.

15 Performance

This section explains the performance of the RPAS. Firstly the flight profiles are for each mission are analysed. After that the flight performance in terms of climb, manoeuvring, glide ratio, and endurance are elaborated. The main inputs for this section are summarised in table 15.1.

Table 15.1: Inputs of performance

Parameter	Value	Unit	Input	Output	Comments
W	176.6	$[kg]$	X		Maximum Weight (Chapter 9)
A	9.9	[-]	X		Aspect Ratio (Chapter 6)
C_{D0}	0.045	[-]	X		Parasite Drag (Chapter 8)
S	1.1	$[m^2]$	X		Wing area (Chapter 6)
e	0.9	[-]	X		Oswald Factor (Chapter 6)
c_p	$9.8 \cdot 10^{-8}$	$[kg/J]$	X		Brake Specific Fuel Consumption (Chapter 8)
η_p	0.85	[-]	X		Propulsive efficiency (Chapter 8)
n_{max}	5	[-]		X	Maximum Manoeuvring Load (Chapter 9)

15.1 Flight profiles

The RPAS is used for several mission goals. The RPAS primarily has a surveillance purpose. This purpose is divided in three different scenarios. The first one is to observe incidents in seaside recreation. Next the RPAS has to go to anchorages and do inspection flights to observe illegal activities. Finally it has to monitor activists boarding ships. For every mission a separate mission profile is made.

The seaside recreation flight profile is shown in figure 15.1. The RPAS is launched with its goal to loiter at the incident. At location it will keep imaging to help ground officers which attend the scene until the scene is resolved. The mission sections are specified in table 15.2. To observe protesters boarding a ship the same mission profile is the same as shown in figure 15.1. The RPAS is flown to the ship to observe the number and location of protesters by loitering around the ship.

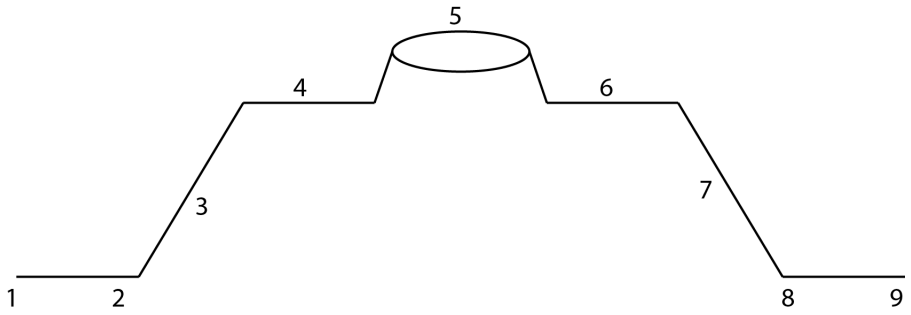

Figure 15.1: Seaside mission profile

Table 15.2: Seaside and protesters mission flight profile

#	Section
1	Pre-flight check
2	Launch
3	Climb
4	Cruise to location
5	Loiter at scene taking images
6	Cruise back to station
7	Descend to net
8	Recovery
9	Post-flight check

The anchorage mission and inspection flight profile is shown in figure 15.2. The anchorage mission is different to the first mission since the RPAS does not fly to a single location to monitor. Instead it is flying a route of way points to detect illegal activities, as specified in table 15.3. In addition to the anchorage mission, an inspection flight can be undertaken. This has the same flight profile shown in figure 15.2. Although the number of way points is decreased to the identified points of interest.

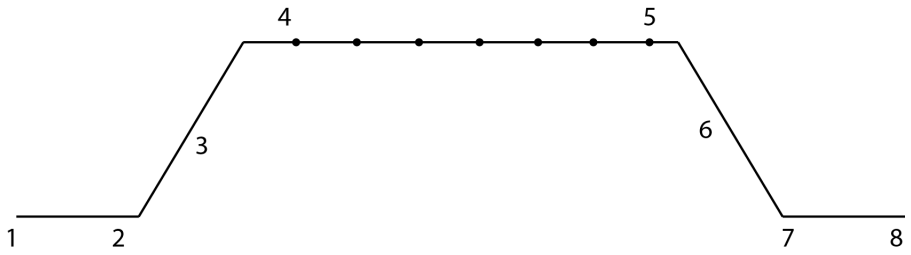

Figure 15.2: Anchorage and inspection flight profile

Table 15.3: Seaside mission profile

#	Section
1	Pre-flight check
2	Launch
3	Climb
4	Cruise to waypoints
5	Cruise back to station
6	Descend to net
7	Recovery
8	Post-flight check

15.2 Climb

High climbing performance increases the manoeuvrability of the RPAS and hence is favourable for its versatility. The RPAS flies at an optimal climb rate its operating altitude. The optimal C_L for climb rate is found using equation 15.2.1 [128].

$$C_L = \sqrt{3C_{D_0}\pi Ae} = \sqrt{3 \cdot 0.045 \cdot \pi \cdot 9.9 \cdot 0.9} = 1.94 \tag{15.2.1}$$

The optimal lift coefficient is higher than $C_{L_{max}}$. Therefore the optimal climb rate is just below $C_{L_{max}}$, such that the RPAS will not stall in climb. Using $C_L = 1.2$ and equation 15.2.3 [128] the climb rate is calculated. The climb rate is determined at 10.8 m/s.

$$C_D = C_{D_0} + \frac{C_L^2}{\pi Ae} = 0.045 + \frac{1.2^2}{\pi \cdot 9.9 \cdot 0.9} = 0.0964 \tag{15.2.2}$$

$$c = \frac{\eta_p P_{br}}{W} - \frac{\sqrt{\frac{W}{S}}\sqrt{2}}{\frac{C_L^{3/2}}{C_d}\sqrt{\rho}} = \frac{0.85 \cdot 2500}{176.58} - \frac{\sqrt{\frac{176.58}{1.1}}\sqrt{2}}{\frac{1.2^{3/2}}{0.0964}\sqrt{1.225}} = 10.8[m/s] \tag{15.2.3}$$

15.3 Manoeuvring

The manoeuvrability of the RPAS is dependent on the velocity of the RPAS. This performance is expressed as limit manoeuvring load. Equation 15.3.1 [128] is used to determine the relation between the speed and manoeuvring load for the given power available of the engine. However not every speed and load is feasible, due to the computed stall characteristics. The maximum manoeuvring load with respect to the $C_{L_{max}}$ is expressed by equation 15.3.2.

$$\frac{\eta_p P_{br}}{W} = \frac{C_{D_0} \frac{1}{2}\rho V^3}{W/S} + \frac{W}{S}\frac{n_{\max}^2}{\pi A e \frac{1}{2}\rho V} \tag{15.3.1}$$

$$n_{max} = \frac{\frac{1}{2}\rho V^2 S C_{L_{max}}}{W} \tag{15.3.2}$$

Figure 15.3 displays the relation of maximum manoeuvring load of the RPAS in respect to its velocity. One can observe that the RPAS is most manoeuvrable at a speed of 32 m/s with a manoeuvring load of 4.7. Moreover the RPAS is designed for a limit load of 10 (Chapter 9) and ultimate load of 15, which indicates the RPAS could even withstand higher manoeuvring loads in case the power available is higher.

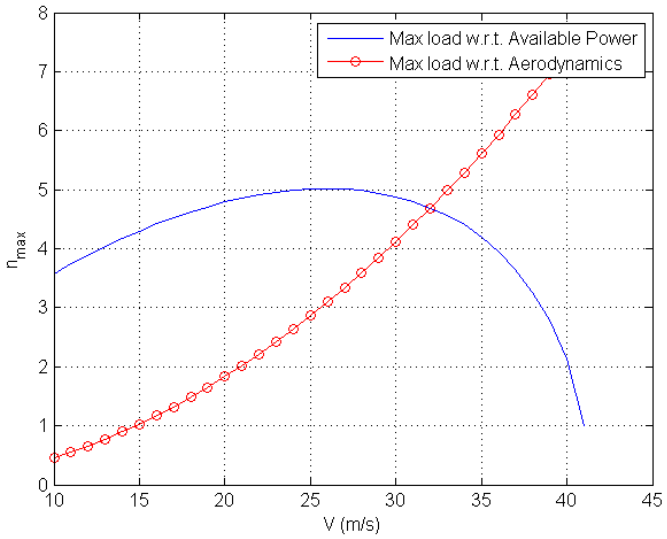

Figure 15.3: Maximum manoeuvring load in respect to velocity

15.4 Time

Time is an important factor in this mission. The RPAS will fly to a certain destination where it is surveying. For all missions time to get to cruise altitude is essential to know. The fastest time to get to a cruise altitude of 200 m is calculated using formula 15.4.1.

$$T_3 = \frac{h}{c} = \frac{200}{10.8} = 18.5\ [s] = 0.3\ [min] \tag{15.4.1}$$

When cruise altitude is reached, the time to get to destination is a meaningful parameter. Equation 15.4.2 is used to compute the time to get to the edge of the maximum range of 20 km. This furthest destination can be reached in 12 min. Hence for an incident at 20 km distance the operational time of reaching destination and back to recovery is roughly 25 min plus the surveying time.

$$T_{4,6} = \frac{d}{V} = \frac{20,000}{28} = 714.3\ [s] = 12\ [min] \tag{15.4.2}$$

15.5 Glide ratio

An interesting property of the RPAS is its glide ratio. If the propulsion subsystem fails the RPAS will glide down to Earth. In this case the RPAS needs to fly at highest aerodynamic efficiency. This efficiency is calculated using formula 15.5.1. This gives the characteristic relation between the angle of attack it has to fly for a specific lift coefficient to have maximum aerodynamic efficiency. This relation is shown in figure 15.4a. A parasite drag of 0.045 is used, for which the propulsion system is designed. This parasite drag is estimated to be slightly high. Thus the RPAS is likely to have an even better glide ratio.

$$\frac{L}{D} = \frac{C_L}{C_{D0} + \frac{C_L^2}{\pi A e}} \tag{15.5.1}$$

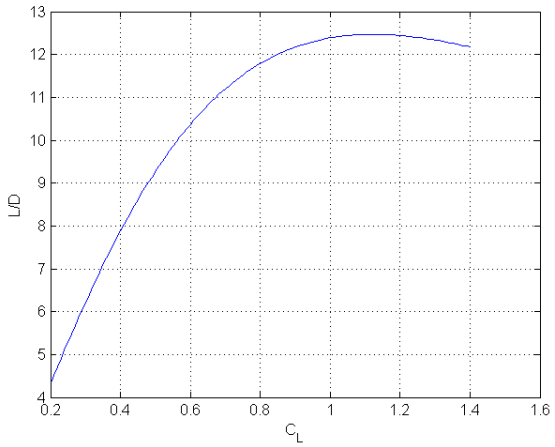

(a) Gliding ratio w.r.t. the lift coefficient

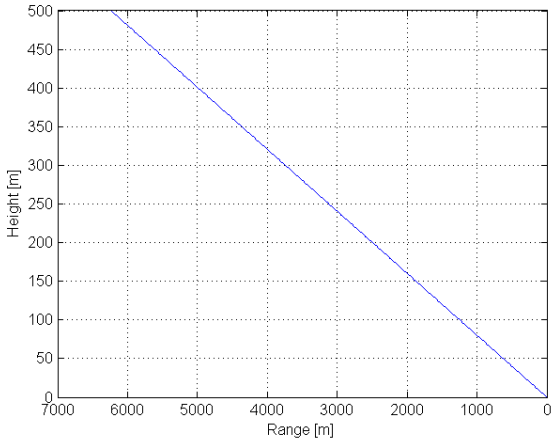

(b) Glide range w.r.t. the height

Figure 15.4: Gliding ratio and range

Using the maximum aerodynamic efficiency of 12.5 the gliding distance could be evaluated for every height. This relation is calculated using formula 15.5.2 and shown in figure 15.4b

$$R = \frac{L}{D}\Delta h \ [m] \tag{15.5.2}$$

15.6 Endurance

The endurance of the RPAS is one of the most important characteristic of the RPAS and is determined using the Breguet equation 15.6.1. This equation is dependent on the motor characteristics, the aerodynamic efficiency, and fuel fraction. Since the endurance is dependent on many other factors as well, the computed value is considered as a rough estimate.

$$E = \left(\frac{\eta_p}{V g c_p}\right) \cdot \left(\frac{L}{D}\right) \cdot \ln\left(\frac{W}{W - W_f}\right) \tag{15.6.1}$$

The specific fuel consumption is first converted to SI units, $C_p = 0.58\ [lbs/hp/hr] = 9.8 \cdot 10^{-8}\ [kg/J]$. The total fuel of the RPAS is 3.34 kg. Only 3 kg is assumed to be used for endurance, due to the fact the motor generates power for other systems as well. The RPAS can reach high aerodynamic efficiency due to its aerodynamic design. The zero lift drag of 0.045, which is used to determine the thrust of the RPAS. Using figure 15.4a an aerodynamic efficiency of 10 is taken, because the RPAS will probably not fly constant when observing the surroundings. The RPAS is likely to turn a lot, which reduces the overall efficiency for a longer time span. Finally the endurance is calculated to be 16 hours as shown in equation 15.6.2.

$$E = \left(\frac{0.85}{28 \times 9.81 \times 9.8 \cdot 10^{-8}}\right) \cdot 10 \cdot \ln\left(\frac{18}{18 - 3}\right) = 57,571\ [s] = 16\ [h] \tag{15.6.2}$$

16 Costs

The budget for production of the RPAS is set to €100,000 by customer requirements. Operations costs are explained in chapter 14. The cost budget can be split up into several components as shown in figure 16.1.

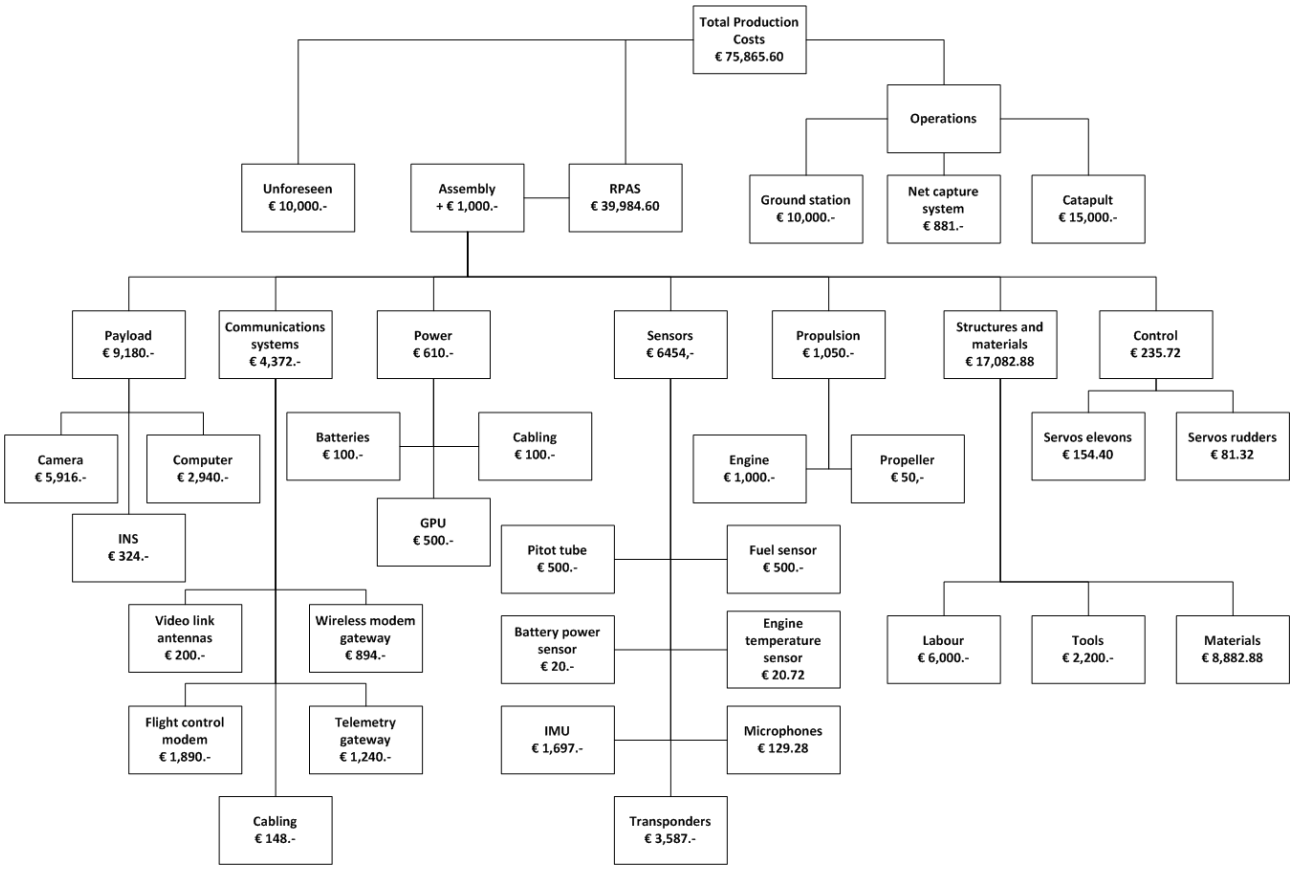

Figure 16.1: Breakdown structure of the production costs

The total costs of the subsystems, parts, and production are summarised in table 16.1. A total production cost of €75,886 can be extracted. This budget is round up to €80,000 to account for a contingency of approximately 5%. This means the budget requirement is easily met. In this way the HERON is a good competitor in the market for surveillance drones in maritime environment. The main cost savings are due to payload selection and using simple structural shapes and cheap materials to lower manufacturing costs.

Table 16.1: Costs

System	**Costs [€]**
Communications	4,372
Payload	9,180
Sensors	6,454
Power	610
Propulsion	1,050
Control	236
Structures	17,083
Ground Station	10,000
Assembly	1,000
Operations	15,881
Unforeseen	10,000
Total	75,866

17 Risk Analysis

With all designs comes risk, and this must be discussed for the flying wing. Risks can be divided into three main aspects, technical performance risk, schedule risk, and cost risk, which will all be discussed for the flying wing. The risks are plotted in their respective place in table 17.1 and are elaborated on in table 17.2. On the x-axis the probability of occurrence is split into low, mediocre, and high. Similarly the y-axis is split into low, mediocre, and high impact of the particular risk.

Table 17.1: Technical risks for the flying wing

High Impact	2	1	
Mediocre Impact	4,8	3	
Low Impact	5,6,7		
	Low Probability	**Mediocre Probability**	**High Probability**

Table 17.2: List of risks

Number	Risk
	Structures
1	Carbon fibre fuselage
2	Modularity
	Propulsion
3	Engine
	Stability and Control
4	Artificial damping
	Operations
5	Catapult launch
6	Net capture
	Navigation & Sensing
7	Autopilot
8	Microphones

All the numbers in table 17.1 are explained in table 17.2. The risks are explained in this section and potential solutions for these risks are elaborated on.

Structures
Certain decisions for the structure have possible risks associated with them, including the carbon fibre fuselage and the wing modularity. The carbon fibre fuselage is relatively weak against impacts due to material properties, which is a risk for technical performance. An unexpected impact that is too high may result in an immediate failure of a structural component. This may be a problem if the RPAS has to be recovered at a higher speed than designed for. Aramid fibre resist impact much better, which may be a better choice. However the strength properties of carbon fibre with respect to it's density are better as a lightweight design is preferred. Furthermore, the carbon fibre can induce interference for the antenna. Communication signals are heavily affected by carbon fibre. Although the antenna's are placed outside the fuselage, the carbon fibre may still interfere. Carbon fibre is chosen due to the fact it has higher strength properties compared to glass fibre which does not induce interference in communication signals. Another risk for the RPAS is due to the modularity of the wings. Both wings can be removed and attached to the fuselage. This connection is a weak point in the structure and a point with higher stress concentrations that incurs a technical risk. Sustaining fatigue for the lifetime of the RPAS is difficult with these high stress concentrations. To counteract this, it is decided to do periodic maintenance and inspection of these connection points as well as possible reinforcement of these locations.

Propulsion
The main risk associated with using the current propulsion system is due to the engine potentially not being able to satisfy sustainability requirements due to the fact that the engine uses internal combustion. Furthermore there may be slight risks with safety, but not more than other forms of propulsion. While the reliability of this

engine is high, there is always the chance with internal combustion engines that something goes wrong. The effects of a failure with this engine may cause significant damage to the RPAS. Impurities in the engine or combustion errors may lead to fire in the RPAS or even small explosions. To counteract this, maintenance and inspection of the engine should occur on a regular basis.

Stability and control
Technical performance risks incurred from stability and control are due to the RPAS being designed with artificial damping. Artificial damping of the RPAS causes technical risk. This system makes sure that an acceptable level of stability is kept during flight. If this artificial damping system fails during the mission, it will not be possible to meet the stability requirements for the imaging system. To reduce this, it is important to make the damping system as reliable as possible to avoid potential failures during flight.

Operations
Risks during operations can be associated with the launch and recovery systems. Firstly, the risks involved with using a catapult system are slightly higher than using a conventional launching method. These risks are induced by the complexity of the launch mechanism and the low popularity of this type of launch system. A catapult system is a way more complex launching method than using a runway, meaning there is a higher chance of an error occurring that can lead to damages. Incorrect air pressure can lead to too little final velocity and the RPAS not being able to sustain flight. A fault in the rail may lead to the carriage jamming during launch, which may induce unsustainable g-forces. Checks and maintenance before each launch should be done to decrease risk of this system. Cost risk of this launch system is also high. From the UAV Factory [112] and ELI catapults[1], an estimate of €15,000 is taken for the launch system. This is higher than initially budgetted and other systems should be analysed if the price is too high. Secondly, there is definitely risk involved in using a net capture method for the recovery system. Fast deceleration is a very important aspect that gives the method a high risk. If the net is too tight or too slack, the RPAS may sustain damage. The propeller is located at the rear of the RPAS, which will not hinder with the net and decreases the risk of this system. The net can also be calibrated before each recovery to make sure that the RPAS will be captured optimally.

Navigation and sensing
Although the NAVIO+ autopilot will work easily with its own integrated sensors, some work needs to be done to make it work with the additional sensors proposed for the RPAS. However, because most of the proposed sensors are common additions to the standard NAVIO+ sensor package, there is typically readily available software to integrate these sensors. Naturally, integration of these sensors and the addition of this software does require additional verification and validation procedures.

Although measures have already been accounted for to mitigate the vibrations present in the RPAS, the problem might still occur, as it is a very often occurring problem and difficult to mitigate. Tests should be performed with flying the RPAS in safe areas to determine with sufficient certainty that the vibrations have been sufficiently mitigated.

The microphones installed on the RPAS are rather unconventional, and therefore need special attention during the development phase. Sufficient verification and validation of the system should take place. Special care must be taken with respect to whether the positioning of the microphones is sufficient for all-round detection, whether the noise of the RPAS itself can sufficiently be filtered out such that other sounds may be detected, and whether the surrounding sound can be detected from a sufficient distance.

Reliability and safety
Throughout the design process, it was important to design subsystem characteristics while taking into account the reliability and safety of the RPAS. To mitigate the risk of the RPAS as a whole, subsystems were designed with safety factors and redundancies in mind. This was applied to most if not all of the subsystems. Redundancy can be found in control, power, communication, and navigation. Double actuators are present to ensure control of the RPAS is possible if one of them fails. Extra batteries are placed on board as a redundancy for the power generator so that the RPAS can fly back to the ground station from a distance of 20 km. All communications antennas have a backup in case one of the communications antennas happens to malfunction. Finally, navigation has multiple systems to determine the position and orientation of the RPAS, which can all satisfy navigation requirements if one fails. On top of these redundancies, safety factors were applied to load factors, power requirements, aerodynamic coefficients, and more to ensure safe use of the RPAS if there happens to be exceptional situations.

[1]Values acquired through personal email communication

18 Conclusion and Recommendations

18.1 Conclusion

Starting with the project description, an analysis of the mission was performed, leading to the necessary requirements for the RPAS. Customer requirements that had been set, such as an endurance of 4 hours, an operating radius of maximum 20 km, and inherent safety, were key. Following these requirements, several conceptual designs were thought of and subsequently analysed for their feasibility. Four preliminary designs, the flying wing, conventional configuration, airship, and kite, were designed to a higher level of detail. After defining relevant criteria needed for the detailed design and weighing them using the analytical hierarchy process, a trade-off could be executed. The trade-off concluded a qualitative 'win' for the conventional concept, but aerodynamic efficiency and innovation of the flying wing design led to proceeding to the detailed design phase with this concept instead.

Many subsystems are integrated together during the detailed design phase of the HERON, as is illustrated using an N^2 chart. This phase included lots of communication between departments for iteration purposes. The aerodynamics department and stability and control department cooperated to determine the airfoil, which was chosen to be the NACA 22115 due to its reflex generating a positive pitching moment coefficient. Controlability of the RPAS is fulfilled by elevons and rudders that give it level 1 handling capabilities. The wing, spanning 3.57 m, is made of a foam core covered in 4 layers of carbon fibre at 0.5 mm thickness. This structure will support an ultimate loading factor of 15 due to the high wing gusts, which include a safety factor of 1.5. The fuselage is a simple cylinder made of carbon fibres, manually lain-up at 0° and 90°, to satisfy the expected bending forces. Carbon fibre was chosen as it is a sustainable material that can be recycled after the lifetime of the RPAS. To propel the aircraft a single cylinder, two-stroke piston engine was chosen. The power subsystem required a power generator, limiting the engine choice to the 3W 28i, which delivers 3.35 hp and 100W of electrical power. Cruise flight is performed at 6700RPM and for highest efficiency the largest diameter propeller was chosen, which is the 18 x 10.

To perform the mission, electronic subsystems, including communications, navigation, and payload, were designed. Two data links ensure that live video streaming and control of the RPAS are on separate channels and do not interfere. Microphones and transponders are on-board to ensure detection and avoidance capabilities of dynamic objects. The imaging system is a camera from Sony that is integrated into a gimbal system to allow for continuous pan and tilt at a rate of 100° per second. A video processing unit is on-board in the case that the data rate is too high. To power these subsystems a power generator on the engine will be used as well as a backup battery that can power all systems for a maximum return flight of 20 km.

The RPAS operations were analysed, which include launch, recovery, maintenance, costs, and certification. The HERON complies with ICAO class II regulations as needed by the requirements. Using a catapult system, it is not limited by a single launch location. Furthermore, the recovery is innovative as the net capture system allows for a transportable recovery method. Post mission inspections will be performed to check for defects. Additionally, light and heavy checks will be completed every 1-1.5 months and 1.5-2 years respectively. Once operational, the RPAS will incur fuel, staff salaries, insurance, and maintenance as its main costs, which equate to €259 per mission.

The maritime flyer has now been designed in detail for every one of its subsystems. The HERON RPAS is a flying wing that is capable of flying 28 m/s, suitable for the maritime environment, delivers a live video stream over a 10 kilometer range, and has an endurance of at least 4 hours. The HERON can be deployed and captured from various locations and is able to assist local police and harbour authorities in handling scenarios such as kite-surfers in need, illegal waste dumping, and protesters boarding a ship.

18.2 Recommendations

While the design is completed, the HERON RPAS is still far from being able to complete its mission in the Port of Rotterdam. Some necessary steps that have to be taken are scale model testing, validation of this data, full scale model testing, and finally production. For subsystems such as propulsion, structures, and aerodynamics, theoretical values are not always reliable. With scale model testing, it will be possible to validate the data for aerodynamic coefficients, propulsive power needed, and weight of the structure. From this, design iterations can

be made to optimise the design to its fullest potential. Further validation can be done after a full scale model of the RPAS is made. This will also make it possible to test the suitability of the RPAS in maritime environments and give an idea of the errors that will be encountered. Once this design has been optimised, production of the RPAS can start. Contact with the customer is essential to make sure that all requirements are being satisfied during the design process.

Post-DSE Activities

Project design and development logic with flow diagram in figure 18.1 and the Gannt chart is shown in figure 18.2.

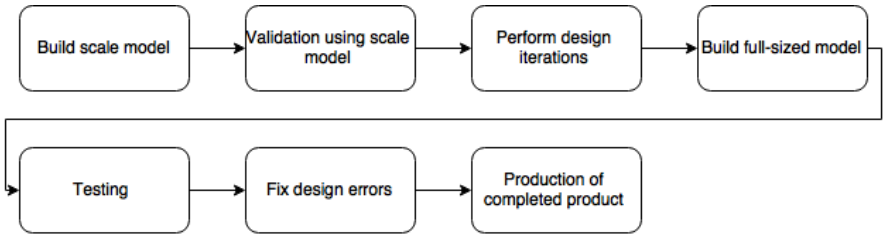

Figure 18.1: Post DSE activities diagram

ID	Task Name	Duration	Start	Finish
1	Final review	0 days	Thu 25-6-15	Thu 25-6-15
2	Iterate design	20 days	Mon 6-7-15	Fri 31-7-15
3	Build full-size model	20 days	Mon 3-8-15	Fri 28-8-15
4	Validation scale model	5 days	Mon 31-8-15	Fri 4-9-15
5	Perform design iterations	40 days	Mon 7-9-15	Fri 30-10-15
6	Build full-size model	40 days	Mon 2-11-15	Fri 25-12-15
7	Testing	30 days	Mon 28-12-1	Fri 5-2-16
8	Fix design errors	30 days	Mon 8-2-16	Fri 18-3-16
9	Production of completed produ	50 days	Mon 21-3-16	Fri 27-5-16
10	Final product	0 days	Fri 27-5-16	Fri 27-5-16

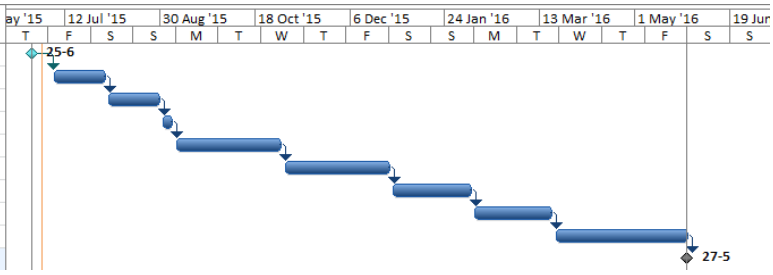

Figure 18.2: Post DSE Gannt Chart

Bibliography

[1] E. v. Kampen, "Project guide design synthesis exercise - maritime flyer," 2015.

[2] P. Pulleman, "To drone, or not to drone?." http://denms.nl/wp-content/uploads/2015/04/To-drone-or-not-to-drone-EN-def.pdf, 2014. Accessed: 29 April 2015.

[3] R. Curran and W. Verhagen, "Risk management & reliability, lecture 8 notes [lecture slides]."

[4] R. Austin, "Unmanned aicraft systems, uavs design, development and deployment," 2010.

[5] CybAero, "Apid one ranger - cybaero ab." http://cybaero.se/en/products-applications/apid-one-ranger. Accessed: 28 April 2015.

[6] Insitu Inc., "Scaneagle_subfolder-digital." http://www.insitu.com/images/uploads/product-cards/ScanEagle_Subfolder-Digital.pdf. Accessed: 28 April 2015.

[7] Pang, K., "Uav sales and training — hornbillsurveys.com." http://hornbillsurveys.com/equipment/. Accessed: 28 April 2015.

[8] Draganfly Innovations Inc., "Draganfly.com uav news rss feed." http://www.draganfly.com/uav-airplane/tango/. Accessed: 28 April 2015.

[9] Insitu Inc., "Integrator_subfolder_digital_pr041615_1." http://www.insitu.com/images/uploads/product-cards/Integrator_SubFolder_Digital_PR041615_1.pdf. Accessed: 28 April 2015.

[10] Inspectie Leefomgeving en Transport, "Informatiebulletin lichte onbemande luchtvaartuigen (uas) unmanned aircraft systems." http://www.ilent.nl/Images/Informatiebulletin%20lichte%20onbemande%20luchtvaartuigen%20januari%202015_tcm334-362146.pdf, 2015. Accessed: 30 April 2015.

[11] J. Roskam and C. Lan, *Airplane Aerodynamics and Performance*. DARcorporation, 1997.

[12] L. J. L.K. and S. H.A., *Aerodynamic Characteristics of 15 NACA Airfoil Sections at seven Reynolds Numbers*. National Advisory Committee for Aeronautics, 1949.

[13] D. Steenhuizen, "Aerospace Design and Systems Engineering Elements II, AE2101, Wing Design Part 1 [lecture slides]," 2013.

[14] "Airfoil tools." http://airfoiltools.com/index. Accessed: 12 May 2015.

[15] Clarkson University, "Finite wing corrections." http://people.clarkson.edu/~pmarzocc/AE429/AE-429-4.pdf. Accessed: 2 June 2015.

[16] Timmer, W.A., "Two-dimensional low-reynolds number wind tunnel results for airfoil naca 0018," *Wind Engineering*, vol. 32, no. 6, 2008.

[17] D. Steenhuizen, "Aerospace Design and Systems Engineering Elements II, AE2101, Wing Design Part 2 [lecture slides]," 2013.

[18] Traub, L.W. and Botero, E. and Waghela R., Callahan R. and Watson, A., "Effect of taper ratio at low Reynolds number," *AIAA Journal*, vol. 52, no. 3, 2015.

[19] E. Obert, R. Slingerland, D. Leusink, T. van den Berg, J. H. Koning, and M. van Tooren, *Aerodynamic Design of Transport Aircraft*. IOS Press.

[20] M. H. Sadraey, *Aircraft Design: A Systems Engineering Approach*. Wiley Publications, 2012.

[21] D. Steenhuizen, "Aerospace Design and Systems Engineering Elements II, AE2101, Wing Design Part 3 [lecture slides]," 2013.

[22] International RPAS community, *RPAS, remotely piloted aircraft systems*. rue Michel-Ange, Paris: Blyenburgh & co, 2013/2014.

[23] A. Braslow, "A history of suction-type laminar-flow control with emphasis on flight research," *Monographs in Aerospace History*, no. 13, 1999.

[24] Popov, A.V. and Botez, R.M. and Labib, M., "Transition point detection from the surface pressure distribution for controller design," *Journal of aircraft*, vol. 45, no. 1, 2008.

[25] XFLR5, "Xflr5." http://www.xflr5.com/xflr5.htm. Accessed: 19 May 2015.

[26] M. Napolitano, *Aircraft Dynamics From Modelling to Simulation*. Wiley, 2011.

[27] G. Rocca, "Requirement analysis and design principles for a/c stability & control (part 2) [lecture slides]," 2015.

[28] W. Durham, *Aircraft Flight Dynamics and Control*. Wiley, 2013.

[29] J. Mulder, W. Van Staveren, J. van der Vaart, E. de Weerdt, C. de Visser, A. in 't Veld, and E. Mooij, "Flight dynamics lecture notes," 2013.

[30] Costa, A.J. and Koopman, F. and Soboleski, C. and Trieu, T.B. and Duquette, J. and Krause, S. and Susko, D. and Trieu, T., "Design and construction of a remote piloted flying wing." http://nix.larc.nasa.gov/search.jsp?R=19950006282&qs=N%3D4294946712%2B4294924922. Accessed: 1 June 2015.

[31] M. Mulder, B. Lubbers, P. Zaal, M. van Paassen, and J. Mulder, "Aerodynamic hinge moment coefficient estimation using automatic fly-by-wire control inputs," *AIAA Journal*, 10 - 13 August 2009.

[32] "TGY-306G Ultra Fast/High Torque MG Digital Alloy Cased Servo 3kg / .06sec / 21g." http://www.hobbyking.com/hobbyking/store/__22687__TGY_306G_Ultra_Fast_High_Torque_MG_Digital_Alloy_Cased_Servo_3kg_06sec_21g.html. Accessed: 16 June 2015.

[33] "Turnigy TGY-589MG HV Digital Metal Cased High Torque Servo 40g/8kg/0.09sec." http://www.hobbyking.com/hobbyking/store/__62609__Turnigy_TGY_589MG_HV_Digital_Metal_Cased_High_Torque_Servo_40g_8kg_0_09sec.html. Accessed: 27 June 2015.

[34] C. Perkins and R. Hage, *Airplane performance stability and control*. John Wiley & Sons, 1949.

[35] L. Nicolai and G. Carichner, *Fundamentals of Aircraft and Airship Design*, vol. I. American Institute of Aeronautics and Astronautics, 2010.

[36] R. Carpenter and H. Diederichs, *Internal combustion engines, their history, construction and operation*. Van Nostrand, 1909.

[37] M. Sadraey, *Aircraft Performance: Analysis*. VDM, 2011.

[38] P. E. Tulapurkara, "Drag polar." http://nptel.ac.in/courses/101106041/Chapter%203%20Lecture%2010%2020-12-2011.pdf. Accessed: 10 June 2015.

[39] "Ngh gt25 25cc gas engine with rcexl cdi ignition (2.7hp) (eu warehouse)." http://www.hobbyking.com/hobbyking/store/uh_viewItem.asp?idProduct=73114. Accessed: 11 June 2015.

[40] "Towerhobbies.com — o.s. 95ax ringed w/muffler." http://www3.towerhobbies.com/cgi-bin/wti0001p?&I=LXXMU4&P=ML. Accessed: 11 June 2015.

[41] "Dle gasoline engines - dle-20ra gasoline engine." http://www.dle-engines.com/dleg0420.html. Accessed: 11 June 2015.

[42] "Rcg 26cc gas engine w/ cd-ignition 2.6hp/1.95kw (eu warehouse)." http://www.hobbyking.com/hobbyking/store/uh_viewItem.asp?idProduct=31284. Accessed: 11 June 2015.

[43] "O.s. gt22 gas engine." http://www.hobbyking.com/hobbyking/store/__63151__O_S_GT22_Gas_Engine.html. Accessed: 11 June 2015.

[44] J. Hebert, "Brake specific fuel consumption - moderated discussion areas." http://continuouswave.com/ubb/Forum4/HTML/004149.html. Accessed: 9 June 2015.

[45] Y. Demirel, *Energy Production, Conversion, Storage, Conservation, and Coupling*. Springer, 2012.

[46] "3w 28i." http://uavfactory.com/product/27. Accessed: 18 June 2015.

[47] R. E. Ltd, "rcv flyer." http://www.rcvengines.com/documents/rcv%20flyer.pdf. Accessed: 18 June 2015.

[48] Air BP Norway AS, "Jet a-1 - product information." http://www.statoilaviation.com/en_EN/pg1332347009500/ar1334072083204/SFRAviation/fuel_jeta1.html. Accessed: 19 June 2015.

[49] P. Carpenter, "Rc airplane propeller size guide." http://www.rc-airplane-world.com/propeller-size.html. Accessed: 8 June 2015.

[50] HARTZELL PROPELLER INC., "Technical questions — hartzell propeller inc.." http://hartzellprop.com/faq/technical-questions/. Accessed: 22 June 2015.

[51] M. Hepperle, "How a propeller works." http://www.mh-aerotools.de/airfoils/propuls4.htm. Accessed: 22 June 2015.

[52] Modellbau Piechowski, "2 blade cfk propeller 18 x 10 pusher."

[53] A. Abdel-Rahman, "On the emissions from internal-combustion engines: a review," *International Journal of Energy Research*, vol. 22, pp. 483–513, 1998.

[54] A. Mohanty, M. Misra, and L. Drzal, "Sustainable bio-composites from renewable resources: Opportunities and challenges in the green materials world," *Journal of Polymers and the Environment*, vol. 10, 2002.

[55] M. Sadraey, "Aircraft performance analysis." http://faculty.dwc.edu/sadraey/V-n%20diagram.pdf, 2009.

[56] KNMI, "Knmi - daggegevens van het weer in nederland - download." http://www.knmi.nl/klimatologie/daggegevens/download.html, 2009.

[57] "Mechanical properties of carbon fibre composite materials." http://www.performance-composites.com/carbonfibre/mechanicalproperties_2.asp. Accessed: 16 June 2015.

[58] Carbon Winkel, "Rohacell 31 ig-f 1250 x 625 mm - carbonwinkel.nl." http://www.carbonwinkel.nl/nl/schuim-foam/55444867-rohacell-rhc-51f-pmi-schuim.html. Accessed: 23 June 2015.

[59] E. Meier, "Obeche — the wood database - lumber identification (hardwoods)." http://www.wood-database.com/lumber-identification/hardwoods/obeche/. Accessed: 22 June 2015.

[60] A. Bedford and W. Fowler, *Engineering Mechanics: Dynamics, 5th edition.* 23/25 First Lok Yang Road, Jurong Singapore: Pearson Education, 2008.

[61] J. Sinke, "Part 1 - chapter 5 processes for composites," 2015.

[62] R. Hibbeler, *Mechanics of Materials, 7th edition.* 23/25 First Lok Yang Road, Jurong Singapore: Pearson Education, 2008.

[63] Tonca Trading BV., "Aluminiumshop.nl - aluminium profielen, aluminium buizen, aluminium strips, aluminium platen en meer." http://www.aluminiumshop.nl. Accessed: 18 May 2015.

[64] HobbyKing, "Radio control planes, helicopters, cars, boats, fpv and quadcopters - hobbyking." http://www.hobbyking.com/hobbyking/store/index.asp. Accessed: 18 May 2015.

[65] CarbonWinkel composite materials, "Carbonwinkel.nl." http://www.carbonwinkel.nl. Accessed: 23 June 2015.

[66] Van Der Horst BV, "Fijnhout drenthe." http://www.fijnhoutdrenthe.nl. Accessed: 18 May 2015.

[67] Evonik Industries AG, "Environment and safety - rohacell - high-performance structural foam cores." http://www.rohacell.com/product/rohacell/en/about/environment-safety/pages/default.aspx. Accessed: 26 June 2015.

[68] N. Benvenuto, R. Corvaja, and L. N. Erseghe, T., *Communication Systems, Fundamentals and Design Methods.* WILEY, 2007.

[69] L. I. Couch, *Digital and Analog Communication Systems, Seventh Edition.* Pearson Education, 2007.

[70] "Comparing Media Codecs for Video Content." http://www.media-matters.net/docs/resources/Digital%20Files/General/Comparing%20Media%20Codecs%20for%20Video%20Content.pdf. Accessed: 15 June 2015.

[71] J. Griggs, "Human Figure average measurements." http://www.fas.harvard.edu/~loebinfo/loebinfo/Proportions/humanfigure.html, 2001. Accessed: 26 June 2015.

[72] Kitefly.de GbR, "Kites — Kitesurfen." http://www.kitefly.de/kites-c-29-1.html. Accessed: 26 June 2015.

[73] Z MARINE, "Zodiac Nautic." http://www.zodiac-nautic.de/. Accessed: 26 June 2015.

[74] ITU, "Frequency Allocation Table - October 2010." https://www.itu.int/ITU-D/asp/CMS/Events/2010/SMS4DC/SMS4DC2_AllocationsV2.pdf. Accessed: 27 June 2015.

[75] Agentschap Telecom, "Vergunningsvrije Radiotoepassingen." https://www.agentschaptelecom.nl/sites/default/files/brochure-vergunningsvrije-radiotoepassingen.pdf/. Accessed: 27 June 2015.

[76] A. Cervone, "Ae2111-ii lecture 09 telecommunications [lecture slides]." Lecture notes for the course AE2111-II accessed on 27 June 2015.

[77] "Ubiquiti Networks - Nano Station M." https://www.ubnt.com/airmax/nanostationm/.

[78] "Ubiquiti Networks - Nano Bridge M." https://www.ubnt.com/airmax/nanobridgem/.

[79] "Adcon Telemetry - A440 Wireless Modem." http://www.adcon.at/index.php?option=com_hikashop&ctrl=product&task=show&cid=94&name=a440-wireless-modem&Itemid=219&lang=en#technical-data.

[80] "Adcon Telemetry - A850 Telemetry Gateway." http://www.adcon.at/index.php?option=com_hikashop&ctrl=product&task=show&cid=57&name=a850-telemetry-gateway&Itemid=219&lang=en.

[81] "Adcon Telemetry - A733 addWAVE Funkstation." http://www.adcon.at/index.php?option=com_hikashop&ctrl=product&task=show&cid=6&name=a733-addwave-funkstation&Itemid=218&lang=de.

[82] Informatie Rijksoverheid, "wetten.nl - Wet- en regelgeving - Binnenvaartpolitiereglement - BWBR0003628." http://wetten.overheid.nl/BWBR0003628/volledig/geldigheidsdatum_15-06-2015#Bijlage1.

[83] "DINED Anthropometric Database." http://dined.io.tudelft.nl/dined/nl. Accessed: 15 June 2015.

[84] "Cm100 data sheet." http://uavvision.com/wp-content/uploads/2015/05/UAV_VISION_CM100.pdf. Accessed: 15 June 2015.

[85] "Hitachi di-sc120r camera data sheet." http://www.hitachi.eu/chassiscameras/download/DI-SC120R.pdf. Accessed: 15 June 2015.

[86] "Cloudcap tase310 data sheet." http://www.cloudcaptech.com/images/uploads/documents/TASE310_Data_Sheet.pdf. Accessed: 15 June 2015.

[87] "Nextvision stabalized systems." http://nextvision-sys.com. Accessed: 15 June 2015.

[88] "Sony fcbex980sp product detail page." https://pro.sony.com/bbsc/ssr/cat-camerasindustrial/cat-ciblockcameras/product-FCBEX980SP/. Accessed: 15 June 2015.

[89] "Btc-101 product page." http://www.microuav.com/btc-101.html. Accessed: 15 June 2015.

[90] "Sony fcbex11d product detail page." http://pro.sony.com/bbsc/ssr/cat-camerasindustrial/cat-ciblockcameras/product-FCBEX11D/. Accessed: 15 June 2015.

[91] "Uav gimbal specter 360 pro." http://www.atmolab.eu/uav-gimbal-specter-360.html. Accessed: 15 June 2015.

[92] "Vtulapvo s120 image." http://aa4cc.dce.fel.cvut.cz/sites/default/files/images/IMG_4681%20kopie.jpg.

[93] A. Blake, G. Winstanley, and W. Wilkinsin, "Displacement from accelerometer." http://cmis.mis.brighton.ac.uk/staff/gw4/papers/Displacement%20from%20Accelerometer.pdf. Accessed: 30 June 2015.

[94] I. Roselli, P. Testa, G. Caronna, and A. Barbagelata, "Acoustic system for aircraft detection and tracking based on passive microphones arrays," *The journal of the Acoustical Society of America*, 2004.

[95] "How to measure state-of-charge." http://batteryuniversity.com/learn/article/how_to_measure_state_of_charge. Accessed: 16 June 2015.

[96] UAV Navigation, "Vector autonomous flight control unit — uav navigation." http://www.uavnavigation.com/products/uav-autopilot-vector. Accessed: 19 June 2015.

[97] "Ardupilot — open source autopilot." http://ardupilot.com/. Accessed: 19 June 2015.

[98] "Paparazziuav." https://wiki.paparazziuav.org/wiki/Main_Page. Accessed: 19 June 2015.

[99] RobotShop inc., "Navio+ autopilot kit for raspberry pi a+/b+ - robotshop." http://www.robotshop.com/en/navio-autopilot-kit-raspberry-pi-a-b.html. Accessed: 19 June 2015.

[100] "Pixhawk autopilot - px4 autopilot project." https://pixhawk.org/modules/pixhawk. Accessed: 19 June 2015.

[101] I. Analog Devices, "Adis16485 — datasheet and product info tactical grade six degrees of freedom mems inertial sensor — analog devices." http://www.analog.com/en/products/sensors/isensor-mems-inertial-measurement-units/adis16485.html#product-overview. Accessed: 19 June 2015.

[102] UAV Factory, "UAV Factory – Unmanned Platforms and Subsystems." http://uavfactory.com/product/12. Accessed: 23 June 2015.

[103] K. W. Headquarters, "Knowles :: MR series." http://www.knowles.com/eng/Products/Microphones/Waterproof/MR-series. Accessed: 24 June 2015.

[104] C. Corperation, "Sagetechmodestransponderebrochure." http://api.ning.com/files/36zE12PBn9ar3R5QR9NJyShAq52sqOF42HwOlVC4zaTaGEIDS33py-hQ8oP2Nx-oQQ2NEdOL4UxGjWLNTfbn*o8E3Te4XzB1/SagetechModeSTranspondereBrochure.pdf. Accessed: 24 June 2015.

[105] Alibaba.com Hong Kong Lt. and UAV Flight Control System Ltd., "Uav fuel level gauge, view uav, bmp product details from beijing micropilot uav control system ltd. on alibaba.com." http://uavstar.en.alibaba.com/product/544344696-213422877/UAV_Fuel_level_gauge.html. Accessed: 19 June 2015.

[106] B. Scheidegger, "Performance characterization of high energy commercial lithium-ion cells." http://ntrs.nasa.gov/archive/nasa/casi.ntrs.nasa.gov/20110003627.pdf. Accessed: 23 June 2015.

[107] UAV Factory USA LLC., "Uav factory – unmanned platforms and subsystems." http://www.uavfactory.com/product/75. Accessed: 28 April 2015.

[108] "Hitec stall current specs."

[109] M. Kazimierczuk, "Pulse-width modulated dc-dc power converters." Accessed: 27 June 2015.

[110] Arcturus UAV, "Pls spec ver 0.1." http://www.arcturus-uav.com/docs/PLS%20Spec%20ver%200.1.pdf. Arcturus Portable Launching System, accessed on 2 June 2015.

[111] ELI Military Simulations, "Products - eli military simulations." http://eli.ee/products/7/uav-pneumatic-catapult. Accessed: 2 June 2015.

[112] UAV Factory, "Uav factory – unmanned platforms and subsystems." http://www.uavfactory.com/product/21. Accessed: 2 June 2015.

[113] Embention SI SL, "Nm& l200." http://products.embention.com/nmand-l200.html. Accessed: 2 June 2015.

[114] M. Ashby, *Material Selection in Mechanical Design*. Butterworth Heinenmann, 2 ed., 1999.

[115] X. Tan, Y. Xu, J. Wang, R. Curran, S. Raghunathan, D. Gore, and J. Doherty, "Life cycle assessment of aluminium for engineering application," *American Institute of Aeronautics and Astronautics*, 2008.

[116] Fall Protection Pros.com, Inc., "4100400 - dbi-sala adjust-a-net personnel netting system - 15 ft. x 30 ft.." http://www.fallprotectionpros.com/dbi-sala-adjust-a-net-system.html. Accessed: 21 June 2015.

[117] Wisselkoers.nl, "Wisselkoers." http://www.wisselkoers.nl. Accessed: 21 May 2015.

[118] KNMI, "Knmi kortste dagen." http://www.knmi.nl/cms/content/22497/kortste_dagen. Accessed: 18 June 2015.

[119] KNMI, "Knmi langste dag." http://www.knmi.nl/cms/content/57100/langste_dag. Accessed: 18 June 2015.

[120] NLR, "Ontheffing voor vliegen met een drone (rpas)." http://www.nlr.nl/NL/capabilities-ii/ontheffing-vliegen-met-een-drone/index.html. Accessed: 18 June 2015.

[121] C. Planbureau, "Kerngegevenstabel 2012-2015 voor het centraal economisch plan 2014 — www.cpb.nl." http://www.cpb.nl/cijfer/kerngegevenstabel-2012-2015-voor-het-centraal-economisch-plan-2014. Accessed: 17 June 2015.

[122] Rijksoverheid, "Op hoeveel vakantiedagen en vakantiegeld heb ik recht? — vraag en antwoord — rijksoverheid.nl." http://www.rijksoverheid.nl/onderwerpen/verlof-en-vakantie/vraag-en-antwoord/op-hoeveel-vakantiedagen-en-vakantiegeld-heb-ik-recht.html. Accessed: 18 June 2015.

[123] S. IO, "Uas insurance — skyward." http://skyward.io/uas-insurance/. Accessed: 18 June 2015.

[124] E. v. Kampen. personal communications. Date: 18 June 2015.

[125] W. M. GmbH, "All engines : 3w-28i : Katalog: 3w modellmotoren - modellmotoren und flugzeuge." http://www.3w-modellmotoren.com/katalog/motoren-alle-motoren-84/3w-28i.html. Accessed: 8 June 2015.

[126] T. Wireman, *Benchmarking Best Practices in Maintenance Management*. Industrial Press Inc., 2004.

[127] European Aviation Safety Agency (EASA), "Unmanned aircraft systems (uas) and remotely piloted aircraft systems (rpas) — easa." https://easa.europa.eu/unmanned-aircraft-systems-uas-and-remotely-piloted-aircraft-systems-rpas, 2015. Accessed: 30 Apr 2015.

[128] G. L. Rocca, "AE1201 Wing loading Thrust loading (II) [lecture slides]," 2013.

[129] Aeronautics Defense Systems, "Orbiterbrochure_2013a." http://www.aeronautics-sys.com/_Uploads/dbsAttachedFiles/OrbiterBrochure_2013A.pdf. Accessed: 18 May 2015.

[130] Insitu Inc., "Scaneagle2_productcard_pr102114sm." http://www.insitu.com/images/campaigns/scaneagle2/Scaneagle2_ProductCard_PR102114_sm.pdf. Accessed: 19 May 2015.

[131] C-ASTRAL d.o.o., "Bramor rtk — c-astral." http://www.c-astral.com/en/products/bramor-rtk#specs. Accessed: 18 May 2015.

[132] C-ASTRAL d.o.o., "Bramor c4eye — c-astral." http://www.c-astral.com/en/products/bramor-c4eye#specs. Accessed: 18 May 2015.

[133] Bluebird Aero Systems LTD, "sod_bluebird." http://sibat.mod.gov.il/NR/rdonlyres/5BED14A6-1B5E-47F6-A108-A683B7C67A2C/0/sod_bluebird.pdf. Accessed: 17 May 2015.

[134] E. Jacobs, R. Pinkerton, and H. Greenberg, "Tests of related forward-camber airfoils in the variable-density windtunnel," Tech. Rep. 610, National Advisory Committee for Aeronautics, 1937.

[135] E. Jacobs and A. Sherman, "Airfoil section characteristics as affected by variations of the reynolds number," Tech. Rep. 586, National Advisory Committee for Aeronautics, 1937.

A Flying wing reference RPAS

Name	Ceiling [m]	V [m/s]	MTOW [kg]	Payload [kg]	Endurance [hrs]	b [m]	Length [m]	λ	Λ [°]	AR	S $[m^2]$
Orbiter Mini UAV [129]	609.6	$< 15.4, 36.01 >$	10	1.5	3.5	2.2	1	0.48	34.6	10.4	0.5
ScanEagle [6]	5950	$< 25.7, 30.9 >$	22	3.4	24	3.11	1.71	0.80	22.8	14	
ScanEagle 2 [130]	5950	$< 25, 30 >$	23.5	3.5	16	3.11	1.71				0.7
rTK UAS [131]		16	3.8	0.6	2.5	2.3	0.96	0.51	28.51		
C4EYE [132]		16	4.5	0.8	3	2.3	0.96	0.53		8	0.7
Bluebird Boomerang [133]	600	$< 16.7, 30.56 >$	9	1	9	2.75	1.1				

B NACA Validation Data

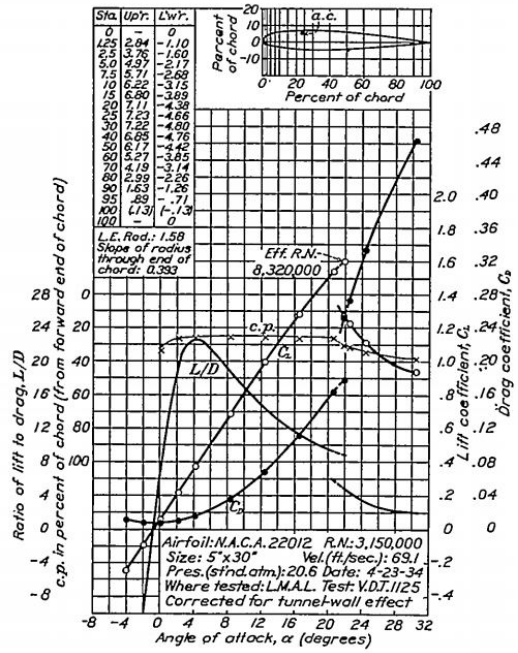

Figure B.1: NACA 22012 Test Data [134]

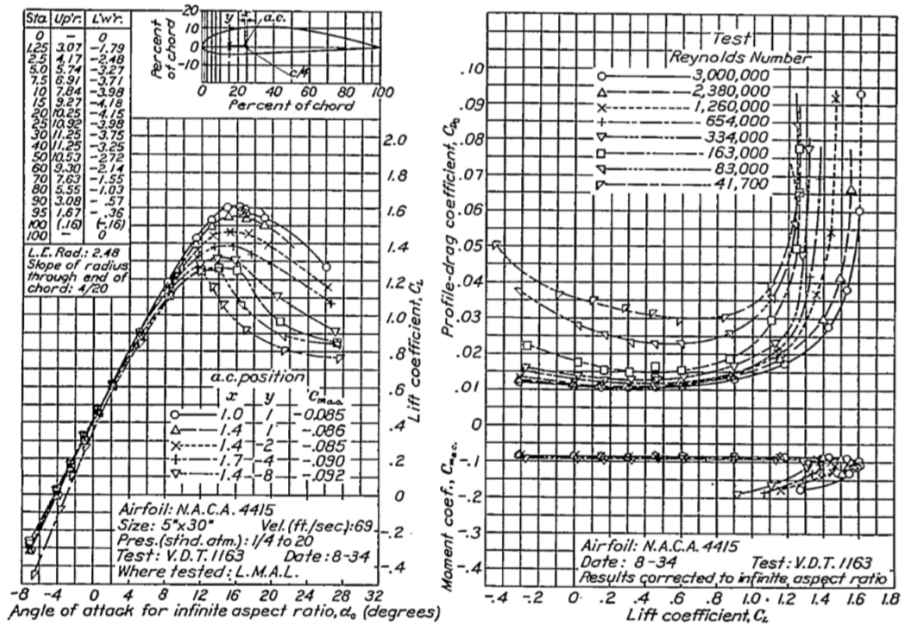

Figure B.2: NACA 4415 Test Data [135]